CENTER FOR COMPOSITES MANUFACTURING FINAL REPORT FTA PROJECT AL-26-7022-02

March 2007

CENTER FOR

COMPOSITES MANUFACTURING

FINAL REPORT

MARCH 2007

FTA PROJECT NUMBER FTA-AL-26-7022-02

CENTER FOR
COMPOSITES MANUFACTURING
FINAL REPORT

MARCH 2007

Prepared by

Uday K. Vaidya, Selvum Pillay, Haibin Ning, Gregg M. Janowski,
and Krishnan Chawla
University of Alabama at Birmingham (UAB)
1150 10th Avenue South
Birmingham, AL 35294

Prepared for

Federal Transit Administration
U.S. Department of Transportation
Washington, DC 20590
http://fta.dot.gov

Available from

National Technical Information Service (NTIS)
5285 Port Royal Road
Springfield, Virginia 22161

703-605-6000
Fax

Email [orders@ntis.fedworld.gov]REPORT DOCUMENTATION PAGE

Form Approved
OMB No. 0704-0188

maintaining the data needed, and completing and reviewing this collection of information. Send comments regarding this burden estimate or any other aspect of this collection of information, including suggestions for reducing this burden to Department of Defense, Washington Headquarters Services, Directorate for Information Operations and Reports (0704-0188), 1215 Jefferson Davis Highway, Suite 1204, Arlington, VA 22202-4302. Respondents should be aware that notwithstanding any other provision of law, no person shall be subject to any penalty for failing to comply with a collection of information if it does not display a currently valid OMB control number. **PLEASE DO NOT RETURN YOUR FORM TO THE ABOVE ADDRESS.**

1. REPORT DATE *(DD-MM-YYYY)*	2. REPORT TYPE	3. DATES COVERED *(From - To)*
03-31-2007	FINAL	From 8-01-05 to 03-31-2007

4. TITLE AND SUBTITLE
Center for Composites Manufacturing

5a. CONTRACT NUMBER

5b. GRANT NUMBER
FTA-AL-26-7022-00

5c. PROGRAM ELEMENT NUMBER

6. AUTHOR(S)
Uday K. Vaidya, Selvum Pillay, Haibin Ning, Gregg M. Janowski and Krish Chawla

5d. PROJECT NUMBER

5e. TASK NUMBER

5f. WORK UNIT NUMBER

7. PERFORMING ORGANIZATION NAME(S) AND ADDRESS(ES)

University of Alabama at Birmingham
1150 10th Avenue South
Birmingham, AL 35294

8. PERFORMING ORGANIZATION REPORT NUMBER

9. SPONSORING / MONITORING AGENCY NAME(S) AND ADDRESS(ES)

10. SPONSOR/MONITOR'S ACRONYM(S)

11. SPONSOR/MONITOR'S REPORT NUMBER(S)

12. DISTRIBUTION / AVAILABILITY STATEMENT

13. SUPPLEMENTARY NOTES

14. ABSTRACT The objective of this project is to continue to develop thermoplastic composite materials and product forms and to develop and demonstrate fabrication methods for molding these materials into components for use in buses and other mass transit applications. These technologies are projected to provide lower cost, lighter weight, and improved performance structures for mass transit applications.

This report details work done in design, analysis, mechanical testing & characterization, prototyping, processing, manufacturing, processing of a air conditioning (AC) cover door for the roof of an articulated mass transit bus using advanced thermoplastic composites. Innovative thermoplastic composites materials and thermoforming processing technology has been demonstrated to form an AC door that has an outer skin on thermoplastic polyolefin (TPO) and an inner rib-stiffened lightweight lofted polypropylene liner. The thermoplastic AC doors are 40% lighter than the metal counterpart and can be readily molded in a mass-produce able cost-effective manner.

This report also details continuation of previous work in long fiber thermoplastic (LFT) composites materials and performance assessment. The vibration damping, fatigue and ultraviolet (UV) environmental degradation of LFTs has been investigated and reported.

15. SUBJECT TERMS
long fiber thermoplastic composite, thermoforming, mass transit, bus technology

16. SECURITY CLASSIFICATION OF:			17. LIMITATION OF ABSTRACT	18. NUMBER OF PAGES	19a. NAME OF RESPONSIBLE PERSON
a. REPORT	b. ABSTRACT	c. THIS PAGE			19b. TELEPHONE NUMBER *(include area code)*

Standard Form 298 (Rev. 8-98)
Prescribed by ANSI Std. Z39.18

Notice

This document is disseminated under the sponsorship of the U.S. Department of Transportation in the interest of information exchange. The United States Government assumes no liability for its contents or use thereof.

The United States Government does not endorse manufacturers or products. Trade names appear in the document only because they are essential to the content of the report.

METRIC/ENGLISH CONVERSION FACTORS

ENGLISH TO METRIC

LENGTH (APPROXIMATE)

1 inch (in) = 2.5 centimeters (cm)
1 foot (ft) = 3.0 centimeters (cm)
1 yard (yd) = 0.9 meter (m)
1 mile (mi) = 1.6 kilometers (km)

AREA (APPROXIMATE)

1 square inch (sq in, in^2) = 6.5 square centimeters (cm^2)
1 square foot (sq ft, ft^2) = 0.09 square meter (m^2)
1 square yard (sq yd, yd^2) = 2.6 square kilometers (km^2)
1 acre = 0.4 hectares (he) = 4,000 square meters (m^2)

MASS - WEIGHT (APPROXIMATE)

1 ounce (oz) = 28 grams (gr)
1 pound (lb) = .45 kilogram (kg)
1 short ton = 2,000 pounds (lb) = 0.9 tonne (t)

VOLUME (APPROXIMATE)

1 teaspoon (tsp) = 5 milliliters (ml)
1 tablespoon (tbsp) = 15 milliliters (ml)
1 fluid ounce (fl oz) = 30 milliliters (ml)
1 cup (c) = 0.24 liter (l)
1 pint (pt) = 0.47 liter (l)
1 quart (qt) = 0.96 liter (l)
1 gallon (gal) = 3.8 liters (l)
1 cubic foot (cu ft, ft^3) = 0.03 cubic meter (m^3)
1 cubic yard (cu yd, yd^3) = 0.76 cubic meter (m^3)

TEMPERATURE (EXACT)

$[(x - 32)(5/9)]°F = y°C$

METRIC TO ENGLISH

LENGTH (APPROXIMATE)

1 millimeters (mm) = 0.04 inch (in)
1 centimeters (cm) = 0.4 inch (in)
1 meter (m) = 2.2 feet (ft)
1 meter (m) = 1.1 yards (yd)
1 kilometer (km) = 0.6 mile (mi)

AREA (APPROXIMATE)

1 square centimeter (cm^2) = 0.16 square inch (sq in, in^2)
1 square meter (m^2) = 1.2 square yards (sq yd, yd^2)
1 square kilometer (km^2) = 0.4 square mile (sq mi, mi^2)
1 hectares (he) = 10,000 square meters (m^2) = 2.5 acres

MASS - WEIGHT (APPROXIMATE)

1 gram (gr) = 0.036 ounce (oz)
1 kilogram (kg) = 2.2 pounds (lb)
1 tonne (t) = 1,000 kilograms (kg) = 1.1 short tons

VOLUME (APPROXIMATE)

1 milliliters (ml) = 0.03 fluid ounce (fl oz)
1 liter (l) = 2.1 pints (pt)
1 liter (l) = 1.06 quarts (qt)
1 liter (l) = 0.06 gallon (gal)
1 cubic meter (m^3) = 36 cubic feet (cu ft, ft^3)
1 cubic meter (m^3) = 1.3 cubic yards (cu yd, yd^3)

TEMPERATURE (EXACT)

$[(9/5)(y + 32)]°C = x°F$

QUICK INCH-CENTIMETER LENGTH CONVERSION

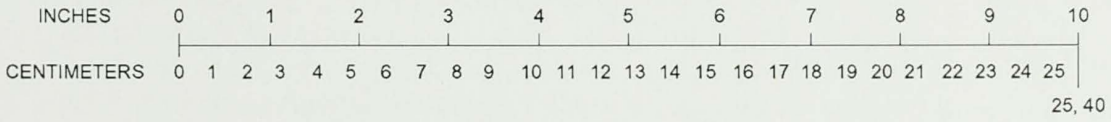

QUICK FAHRENHEIT-CELCIUS TEMPERATURE CONVERSION

For more exact and or other conversion factors, see NBS Miscellaneous Publication 286, Units of Weights and Measures. Price $2.50. SD Catalog No. C1310286.

Acknowledgments

The authors wish to express their appreciation to the Federal Transit Administration for the support of this work. We thank North American Bus Industries (NABI), Anniston, Alabama for their guidance in component selection and design guidelines. At NABI, we like to acknowledge Dan Allen, Robert Ngu, Ronnie O'Byrne. We acknowledge the following for their contributions to the technical effort of this project; Juan Serrano, George Husman, Andy Grabany, Krishnan Balaji Thattaiparthasarathy, Ashutosh Goel, Rahul Kulkarni and Venkata Chevali from the University of Alabama at Birmingham (UAB); Pritam Das and Harry Couch from the National Composites Center (NCC), Kettering, Ohio. We are also grateful to the assistance provided by Portage Molding and Castings (PMC), Wisconsin in the manufacturing and tooling issues.

Table of Contents

Notice 3
Acknowledgments 5
List of Figures 9
List of Tables 15
Executive Summary 16
I. Introduction 17
II. Task Description 20
2.0 Project Management 20
2.1 Materials and Product Forms Technology 20
2.2 Continuing Materials Studies (From 2004-2005 effort) 20
2.3 Fatigue behavior of LFTs 21
2.3.1 Introduction (Fatigue) 21
2.3.2 Results (Fatigue) 22
2.3.2.1 Microstructural Characterization (LFT) 22
2.3.2.2 Tensile Tests (LFT) 22
2.3.2.3 Fatigue Tests (LFT) 23
2.3.2.4 Temperature rise (Fatigue) 27
2.3.3 Discussion (Fatigue) 31
2.3.4 Conclusions (Fatigue) 32
2.4 Flexural creep testing of neat and fiber reinforced thermoplastics 33
2.4.1 Introduction (Creep) 33
2.4.2 Materials and Methods 35
2.4.3 Results and Discussions (Creep) 36
2.4.3.1 Flexural Creep 36
2.4.3.2 Empirical Modeling 38
2.4.3.3 Dynamical Mechanical Analysis 40
2.4.4 Conclusions (Creep) 41
2.5 UV degradation of LFT 41
2.5.1 Introduction 41
2.5.2 Results (UV) 42
2.5.2.1 Visual appearance 42
2.5.2.2 Optical Microscopy 42
2.5.2.3 Scanning Electron Microscopy (SEM) 44
2.5.2.4 Nanoindentation 48
2.5.2.5 Fourier Transform Infrared (FTIR) Spectroscopy 52
2.5.2.6 Modulus measurement of LFT 54
2.5.3 Discussion (UV) 54
2.5.4 Conclusions (UV) 55
2.6 Characterization of candidate thermoplastic materials for the AC door 55
2.6.1 Introduction (AC door) 55
2.6.2 TPO 56
2.6.2.1 DSC and TGA 56
2.6.2.2 Flexural testing 57
2.6.2.3 Tensile testing 59

2.6.3 Lightweight reinforced thermoplastic composites (LWRT) 61
2.6.3.1 Tensile testing 61
2.6.3.2 Damping response of LWRT 66
2.7 Long fiber thermoplastic (LFT)/metal laminate (LML) composite 67
III. Processing Technology 68
3.1 Thermoforming Process 68
3.1.1 Vacuum Forming process 69
3.1.2 Pressure forming process 69
3.1.3 Thermoforming materials 69
3.1.3.1 GE Plastics/Azdelite 72
3.1.3.2 Quadrant Composites/Symalite 74
3.1.4 Finishing operations 74
3.1.5 Class A finish on thermoformed parts 74
3.2 Twin sheet thermoforming troubleshooting 77
3.2.1 Precise mold alignment 77
3.2.2 Compensation for compression 77
3.2.3 Cooling and venting 77
3.2.4 Draw ratio limits 78
3.2.5 Elimination of shadowing 78
3.2.6 Sheet thickness compatibility 78
3.3 Quickstep Technology 78
3.3.1 Thermoplastic processing at the Quickstep Machine 80
IV. Component Demonstration 82
4.1. Component selection, and design for manufacturing 82
4.1.1 Natural Gas Tank Cover, NABI Ref 801-1511-001 83
4.1.2 Thermoplastic composite concept 84
4.1.3 Design for manufacturing (AC Door) 84
4.1.3.1 AC door/cover, NABI Ref 61A-7119-001 85
4.1.3.2 Structural design 89
4.1.4 Design optimization 95
4.1.5 Tool Design for the AC Cover Door 97
4.1.5.1 Tool 97
4.1.6 Tool Fabrication 98
V. Component Demonstration 100
5.1 Component Fabrication 100
5.1.1 Twin sheet thermoforming 101
5.1.2. Manufacturing option 2 104
5.1.2.1 Compression molding of thermoplastic composite sheet 105
5.1.2.2 Thermoforming of thermoplastic olefin (TPO) sheet 107
5.1.2.3 Joining of the compression molded thermoplastic sheet and thermoformed TPO sheet 109
5.2 Component Verification for AC Door 112
5.2.1 Testing 112
5.2.1.1 Damping 112
5.2.1.2 Deflection Testing 113
5.2.2 Design Verification (AC Door) 117

5.2.3 Weight Evaluation 120
5.2.4 Fitment trials at NABI, Anniston 120
VI. Summary and Conclusions 123
References 125

List of Figures

Figure 1.1- 1 Overview of the UAB Composites Development Effort. 17

Figure 1.1- 2 Tasks designation 2005-2006 period. 18

Figure 1.1- 3 Task description and duration 2005-2006 period. 19

Figure 2.3- 1 A representative micrograph of LFT. It can be seen that most of the fibers are parallel to the extrusion direction. 22

Figure 2.3- 2 S-N curves for samples sectioned along longitudinal and transverse direction at a frequency of 10 Hz. Longitudinal samples shows better fatigue resistance as compared to transverse samples. 23

Figure 2.3- 3 S-N curves for samples sectioned along longitudinal and transverse direction at a frequency of 15 Hz. Longitudinal samples shows better fatigue resistance as compared to transverse samples. 24

Figure 2.3- 4 S-N curves for samples sectioned along longitudinal and transverse direction at a frequency of 20 Hz. Longitudinal samples shows better fatigue resistance as compared to transverse samples. 24

Figure 2.3- 5 S-N curves normalized with longitudinal and transverse modulus of LFT at a frequency of 10 Hz. Normalized curves for longitudinal and transverse LFTs overlap..... 25

Figure 2.3- 6 S-N curves normalized with longitudinal and transverse modulus of LFT at a frequency of 15 Hz. Normalized curves for longitudinal and transverse LFTs overlap..... 25

Figure 2.3- 7 S-N curves normalized with longitudinal and transverse modulus of LFT at a frequency of 20 Hz. Normalized curves for longitudinal and transverse LFTs overlap..... 26

Figure 2.3- 8 S-N curves for longitudinal samples tested at frequencies of (a) 10 Hz, (b) 15 Hz, and (c) 20 Hz. Fatigue life decreases with increasing frequency. 26

Figure 2.3- 9 S-N curves for transverse samples tested at frequencies of (a) 10 Hz, (b) 15 Hz, and (c) 20 Hz. Fatigue life decreases with increasing frequency. 27

Figure 2.3- 10 Temperature rise vs. no. of cycles to failure curves for sample tested at a frequency of 10 Hz at stress amplitudes of (a) 35 MPa, (b) 27 MPa, and (c) 21 MPa. At higher stress amplitude temperature rises faster and leads to early failure of the sample. 28

Figure 2.3- 11 Temperature rise vs. no. of cycles to failure curves for sample tested at a frequency of 15 Hz and at stress amplitudes of (a) 35 MPa, and (c) 21 MPa. At higher stress amplitude temperature rises faster and leads to early failure of the sample. 28

Figure 2.3- 12 Temperature rise vs. no. of cycles to failure curves for sample tested at a frequency of 20 Hz and at stress amplitudes of (a) 35 MPa, (b) 27 MPa and (c) 21 MPa. At higher stress amplitude temperature rises faster and leads to early failure of the sample. 29

Figure 2.3- 13 Temperature rise vs. no. of cycles to failure curves for sample tested at a stress amplitude of 35 MPa and at frequencies (a) 20 Hz, (b) 15 Hz, and (c) 10 Hz. At higher frequency temperature rises faster and leads to early failure of the sample. 29

Figure 2.3- 14: Temperature rise vs. no. of cycles to failure curves for sample tested at a stress amplitude of 27 MPa and at frequencies (a) 20 Hz, (b) 15 Hz, and (c) 10 Hz. At higher frequency temperature rises faster and leads to early failure of the sample. 30

Figure 2.3- 15 Temperature rise vs. no. of cycles to failure curves for sample tested at a stress amplitude of 21 MPa and at frequencies (a) 20 Hz, (b) 15 Hz, and (c) 10 Hz. At higher frequency temperature rises faster and leads to early failure of the sample. 30

Figure 2.4- 2 Flexural creep testing apparatus was (a) designed and modeled in Pro/Engineer, and (b) fabricated at the UAB machine shop. 35

Figure 2.4- 3 A decrease in the creep compliance recorded at 10 hours of testing with an increase in the fiber weight percentage was recorded. Neat nylon 6/6 showed the highest creep compliance when tested at 23 °C and 27.7 MPa. 36

Figure 2.4- 4 Creep data for 10 and 40 wt.% glass fiber reinforced nylon 6/6 compare the effect of fiber volume fraction, stress level (nominal 50 and 70 MPa) and temperature (room temperature and 120 °C) on the creep resistance of the material. 37

Figure 2.4- 5 Creep data for specimens from the parallel and perpendicular flow directions show the development of a possible preferable fiber orientation during processing. 37

Figure 2.4- 6 Neat nylon 6/6 shows non-linearity with respect to time and applied stress. 38

Figure 2.4- 7 The four parameter empirical model provides a good data fit for the non-linear behavior of the LFT composite (nylon 6/6 + 40 w. % E-glass fibers, 23 °C, 56 MPa)..... 39

Figure 2.4- 8 Macro photograph showing crazing and plasticity in TPO specimens after testing at a constant load of 147 N. 40

Figure 2.4- 9 WLF superposition principle was used to generate the master creep curve for 40 wt.% glass fiber reinforced nylon 6/6 generated by superposing short term creep data at each 5 °C in the 35 °C to 160 °C range in an DMA. A reference temperature T_S= 100 °C (T_g+ 50 °C) was used to shift the curves 40

Figure 2.5- 2 Image of the polished cross-section of the LFT exposed to UV for 100 hours. Surface cracks begins to form. 43

Figure 2.5- 3 Image of the polished cross-section of the LFT exposed to UV for 400 h. Degraded matrix layer can be easily seen due to easily distinguishable contrast between the degraded layer and the unaffected layer. Surface crack density increases as compared to the density at 100 h. 43

Figure 2.5- 4 Image of the polished cross-section of the LFT exposed to UV for 1600 h. Surface crack density is the maximum for the sample exposed for 1600 h. 44

Figure 2.5- 5 LFT unexposed to UV radiation. Glass fibers are well bonded with the matrix. 45

Figure 2.5- 6 LFT exposed for 100 h. Most of cracks run along the fiber length. Short transverse cracks connect the long ones. 45

Figure 2.5- 7 (a): LFT exposed for 200 hours in UV radiation. Matrix damage in the form of cracks (long ones along the fiber length and short transverse cracks) can be seen, (b): An area of (a) at higher magnification. 46

Figure 2.5- 8 (a): LFT exposed for 1600 hours in UV radiation. Most of the matrix in the surface region has disappeared and exposed fibers can be seen, (b): LFT exposed for 1600 hours in UV light at higher magnification. The cracks present in the matrix and the exposed fibers can be seen clearly. 47

Figure 2.5- 9 Image of the polished cross-section of the LFT exposed to UV for 1600 hours with nanoindentation marks on it (encircled). Several indentations were done at varying distances from the surface. 48

Figure 2.5- 10 Typical Load-displacement curves during nanoindentation of the PP matrix after (a) 0 h, (b) 200 h, (c) 400 h, and (d) 1600 h of UV exposure. The sample exposed to UV for 1600 h shows higher load at the same displacement as compared to other samples..... 49

Figure 2.5- 11 A representative modulus vs. displacement curves for indentation done on the degraded region of the LFT sample exposed to UV radiation for (a) 200 h, (b) 400 h, and (c) 1600 h. The curve for indentation done on the unexposed sample (0 h) is also shown. It can be seen that the sample exposed to 1600 h shows the highest modulus..... 50

Figure 2.5- 12 A representative hardness vs. displacement curves for indentation done on the degraded region of the LFT sample exposed to UV radiation for (a) 200 h, (b) 400 h, and (c) 1600 h. The curve for indentation done on the unexposed sample (0 h) is also shown. It can be seen that the sample exposed to 1600 h shows the maximum hardness..... 50

Figure 2.5- 13 Modulus vs. distance from the surface plots for the samples exposed to UV for (a) 200 h, (b) 400 h, and (c) 1600 h. Modulus was determined, for each indentation, from plots looking similar to Fig. 2.5-11. Each point in the plot is the average modulus of ten indentations done on the matrix, at a given distance from the surface. Near the surface, the higher the exposure time, the higher the modulus. 51

Figure 2.5- 14 Hardness vs. distance from the surface plots for the samples exposed to UV for (a) 200 h, (b) 400 h, and (c) 1600 h. Hardness was determined, for each indentation, from plots looking similar to Fig. 2.5-12. Each point in the plot is the average modulus of ten indentations done on the matrix, at a given distance from the surface. Near the surface, the higher the exposure time, the higher the hardness. 51

Figure 2.5- 15 Intensity of carbonyl band increases with time. Notice that carbonyl band was not present for the LFT unexposed to UV. 52

Figure 2.5- 16 Intensity of hydroxyl band increases with time. Hydroxyl band was not present initially for the unexposed LFT. 53

Figure 2.5- 17 Crystallinity increases with UV exposure time..... 53

Figure 2.5- 18 Modulus vs. exposure time for the unexposed and exposed beams. The modulus decreases with exposure time. 54

Figure 2.6- 1 Dynamic scanning calorimetry of TPO..... 56

Figure 2.6- 2 Thermo gravimetrical analysis of TPO. 57

Figure 2.6- 3 Load vs. apparent displacement curves for TPO. 58

Figure 2.6- 4 Stress vs. apparent strain curves for TPO. Displacement rate was 6 mm/min. UTS values between 17.5 to 19.8 MPa. 59

Figure 2.6- 5 Stress vs. strain curves for TPO. Displacement rate was 6 mm/min. 60
Figure 2.6- 6 Elastic modulus and stress vs. strain plot for Azdelite (1400gsm 55% GF) compressed to 2 mm. 62
Figure 2.6- 7 Elastic modulus and stress vs. strain plot for Azdelite (1400 gsm 55% GF) compressed to 3 mm. 63
Figure 2.6- 8 Elastic modulus and stress vs. strain plot for Quadrant (1600 gsm 55% GF) compressed to 2 mm. 64
Figure 2.6- 9 Elastic modulus and stress vs. strain plot for Quadrant (1600 gsm 55% GF) compressed to 3 mm. 65
Figure 2.6- 10 Setup for the determination of damping ratio of composite materials. 66
Figure 2.6- 11 Damping ratio vs. frequency for Aluminum (baseline design), and LWRT materials (new design). 67
Figure 3.1- 1 Thermoforming: Vacuum forming process and pressure forming process (www.geimd.com). 68
Figure 3.1- 2 Detail on a pressure forming box and corresponding mold (www.geimd.com). 69
Figure 3.1- 3 Crash performance of thermoplastic composite thermoformed hoods (black) and steel hood (silver). 72
Figure 3.1- 4 Manufacturing process of Azdelite (from AZDEL, proprietary information). 73
Figure 3.1- 5 Lofting of Azdelite (from AZDEL, proprietary information) 73
Figure 3.1- 6 Manufacturing process using Symalite INTRA (From Quadrant Composites) 74
Figure 3.1- 7 MCC spoiler plus roof module (Senoplast, 2005) and thermoformed bumper fascia (GMC, 2005). 75
Figure 3.1- 8 Multilayer thermoformable sheet for class A finish parts (GM, 2005) 76
Figure 3.3- 1 Quickstep process [50]. 79
Figure 3.3- 2. Twintex weaves. 80
Figure 3.3- 3 Consolidation of Twintex weaves. 80
Figure 3.3- 4 Temperature profile of an 8 ply twintex weave. 81
Figure 3.3- 5 Thermoplastic composite consolidated panels made with the process of Quickstep. 81
Figure 3.3- 6 Bubbles on the surface of the thermoplastic color film. 82
Figure 4.1- 1 CNG roof door. 82
Figure 4.1- 2 CNG cover solid model and steel frame skeleton generated in Pro E Wildfire 83
Figure 4.1- 3 Thermoplastic composite multi layer sheet concept. 84
Figure 4.1- 4 AC tank door on 60 BRT bus 84

Figure 4.1- 5 AC door in the open position. Note extender arm, welded stiffener and hardware. 85

Figure 4.1- 6 Existing manufacturing process algorithm for aluminum AC door. 86

Figure 4.1- 7 Proposed manufacturing process algorithm for thermoplastic AC door. 86

Figure 4.1- 8 Conceptual thermoplastic AC door solid model and detail on twin sheet concept. 87

Figure 4.1- 9 External view and internal view of sine-hat stiffened concept for thermoplastic AC cover (solid model) 88

Figure 4.1- 10 Boundary Conditions for structural analysis of AC cover. Translation constraints in blue, rotation constraints in white, Direction of inertial loading in cyan. 91

Figure 4.1- 11 Deformation convergence for UAB concept model of AC cover 91

Figure 4.1- 12 Deformation convergence plot for baseline design of AC cover. 92

Figure 4.1- 13 Contours of free-standing deflection of baseline design and UAB thermoplastic concept. 93

Figure 4.1- 14 Deformation versus total mass for baseline and UAB concepts of AC cover. 95

Figure 4.1- 15 The hinge plate and prop bonded on door shell 96

Figure 4.1- 16 The hinge plate and prop bolted on door shell. Note the flat rib area for the bolting. 96

Figure 4.1- 17 Twin sheet thermoforming of thermoplastic composite and TPO sheets. 97

Figure 4.1- 18 (A) Placement of preheated thermoplastic composite sheet between the wooden plug assist tool and heated aluminum male tool, (B) Heated aluminum male tool compression molds the heated thermoplastic composite sheet, (C) Compression molded ribbed structure is formed 98

Figure 4.1- 19 Female aluminum tool, for thermoforming of TPO exterior section. 99

Figure 4.1- 20 Male aluminum tool for thermoforming or compression molding of interior azdellite section 99

Figure 4.1- 21 Wooden female tool for compression molding of azdellite inner section. 100

Figure 5.1- 1 Four-station rotary thermoforming machine at Portage Cast and Mold. 102

Figure 5.1- 2 TPO sheet heated, moved onto the forming station and ready for tools to close and sheet to be thermoformed 102

Figure 5.1- 3 TPO sheet thermoformed and azdel sheet ready to be formed and twinned to the TPO sheet. 103

Figure 5.1- 4 Twin sheet formed part, showing sink marks on the exterior TPO side. 104

Figure 5.1- 5 (A) Placement of preheated thermoplastic composite sheet between the wooden tool and heated aluminum male tool, (B) Heated aluminum male tool compression molds the heated thermoplastic composite sheet, (C) Compression molded ribbed structure is formed 105

Figure 5.1- 6 Azdelite sheet transferred to forming station after heating and ready to be compression molded. 106

Figure 5.1- 7 Compression molded part, after opening of tools, being air cooled. 106

Figure 5.1- 8 Part being removed at the loading/unloading station. 107

Figure 5.1- 9 TPO sheet at compression molding station ready for vacuum thermoforming. ... 108

Figure 5.1- 10 TPO sheet during thermoforming. 108

Figure 5.1- 11 TPO sheet at unloading station after thermoforming. 109

Figure 5.1- 12 Primer being applied to formed azdel composite part (after hand trimming). 110

Figure 5.1- 13 Primer being applied to thermoformed TPO part (after hand trimming) 110

Figure 5.1- 14 3M VHB tape applied to composite sheet and being hand rolled. 111

Figure 5.1- 15. Bonded parts ready for CNC trimming. 111

Figure 5.2- 1 A schematic of the experimental setup for vibration testing in free-free boundary conditions. 112

Figure 5.2- 2 Damping comparison chart for different materials. TPO-Azdel combine shows the highest damping while Aluminum shows the lowest 113

Figure 5.2- 3 AC door mounted on a frame for the deflection testing 114

Figure 5.2- 4 AC door at closed position, open at 45° angle and 75° angle (fully open) position. 115

Figure 5.2- 5 AC door testing. (a) The deflection was measured with the help of an LVDT mounted on a trolley. (b) The maximum deflection measured at the corner of the unsupported side. 116

Figure 5.2- 6 AC door under its self weight and door handle weight at an angle of 45°. 117

Figure 5.2- 7 The boundary and loading conditions for the fully open AC door. 118

Figure 5.2- 8 The deflection contour resulted from the boundary and loading conditions as shown in Fig. 5.2-7. 119

Figure 5.2- 9. The comparison among the baseline Al shell and truss, the composites door in experimental and FEA results for four loading cases. 119

Figure 5.2- 10 Assembly of the thermoplastic composite door on the NABI Altoona 60 BRT articulated bus. 121

Figure 5.2- 11 Thermoplastic composite door on the NABI Altoona 60 BRT articulated bus in its open position. Note: Details of ribbing of the door inside visible 121

Figure 5.2- 12 Person stepping on the thermoplastic composite door on the NABI Altoona 60 BRT articulated bus. 122

Figure 5.2- 13 Thermoplastic composite door on the NABI Altoona 60 BRT articulated bus in its open position. Note: Door has excellent rigidity at the unsupported end. 122

List of Tables

Table 2.3- 1 Summary of tensile test of LFT. 23

Table 2.6- 1 Tabulated data from flexural testing of TPO 58

Table 2.6- 2 Measured elastic modulus of TPO (calculated based on data from Fig 2.2.5) 60

Table 3.1- 1 Some engineering polymers for thermoforming and their general characteristics 71

Table 3.1- 2 Some commodity polymers for thermoforming and their general characteristics 71

Table 4.1- 1 CNG Cover manufacturing parameters* 83

Table 4.1- 2 Existing aluminum AC Cover parameters* 85

Table 4.1- 3 Thermoplastic AC Cover parameters* 89

Table 4.1- 4 Calculated deflections for different beam sections under an assumed flexural loading regime 90

Table 4.1- 5 List of parameters and material properties used for simulations 94

Table 5.2- 1 Materials properties used for finite element analysis 118

Table 5.2- 2 Weight evaluation for the composites AC door 120

Executive Summary

The objective of this project is to develop thermoplastic composite materials and product forms and to develop and demonstrate fabrication methods for molding these materials into components for use in buses and other mass transit applications. The ultimate purpose is to demonstrate that these technologies can provide lower cost, lighter weight, and improved performance structures for mass transit applications.

A series of candidate bus components were selected after a visit to NABI, Anniston by the UAB investigators. Based upon discussions with NABI, an air conditioning (AC) cover/roof door was selected for demonstration of advanced thermoplastic composites technologies for the 2005-2006 project.

This report details work done in design, analysis, mechanical testing & characterization, prototyping, processing, manufacturing, processing of the AC cover door for the roof of an articulated mass transit bus using advanced thermoplastic composites. Innovative thermoplastic composites materials and thermoforming processing technology has been demonstrated to form an AC door that has an outer skin on thermoplastic polyolefin (TPO) and an inner rib-stiffened lightweight lofted polypropylene liner. The thermoplastic AC doors are 40% lighter than the metal counterpart and can be readily molded in a mass-producible cost-effective manner.

This report also details continuation of previous work in long fiber thermoplastic (LFT) composites materials and performance assessment. Fatigue, creep, and ultraviolet (UV) environmental degradation of LFTs has been investigated and reported.

I. Introduction

The objective of this project is to develop thermoplastic composite materials and product forms and to develop and demonstrate fabrication methods for molding these materials into components for use in buses and other mass transit applications. The ultimate purpose is to demonstrate that these technologies can provide lower cost, lighter weight, and improved performance structures for mass transit applications[1-5].

The work described in this report is being performed under a Cooperative Agreement with the U.S. Department of Transportation, Federal Transit Administration (FTA), FTA C-7, Project number: AL-26-7001-02.

The National Composite Center (NCC) is involved in the manufacturing support on the effort.

Figure 1.1-1 gives an overview of the evolution of the UAB effort from 2002 to the present time. Throughout the project there is a demonstrated development of materials and manufacturing technology, and each year specific mass transit components are selected for applications demonstration. In the first year a lightweight, low cost long fiber thermoplastic bus seat was successfully demonstrated. In the second year, an innovative thermoplastic tape form bus floor design was demonstrated. The work performed during the third year demonstrated a prototype frame and body panel segment of continuous fiber thermoplastic materials. The work performed during the fourth year of the project demonstrated the feasibility of long fiber thermoplastic composite technology for the replacement of a battery box access door for an articulated bus. The focus of these demonstrations is to reduce weight and cost of the overall bus structure which would result in lower fuel consumption, less road wear, lower axle weight among other benefits.

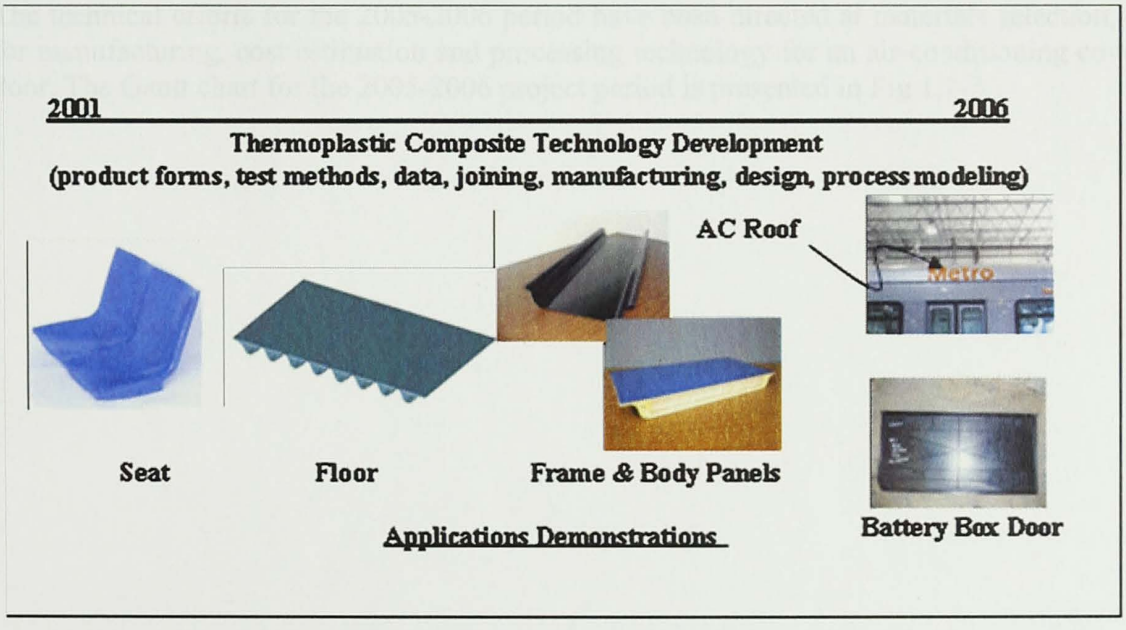

Figure 1.1- 1 Overview of the UAB Composites Development Effort.

Figure 1.1-2 shows a more detailed overview of the tasks scheduled for the 2005-2006 effort. The work is divided into subtasks for basic technology development in materials and manufacturing and tasks for component design and fabrication.

Ongoing Technology Development

Task I:	Materials Technology
	Material & Product Form Development
	Material Evaluation and Test Technique
	Material Selection for AC Door
Task II:	Process Technology
	Technology Selection
	Process Evaluation and Development
	Technology Demonstration
Task III:	Component Demonstration
	Component Selection
	Component Design
	Tool Design
	Tool Manufacturing
	Component Fabrication
	Component Evaluation

Figure 1.1- 2 Tasks designation 2005-2006 period.

The technical efforts for the 2005-2006 period have been directed at materials selection, design for manufacturing, cost estimation and processing technology for an air-conditioning cover roof door. The Gantt chart for the 2005-2006 project period is presented in Fig 1.1-3.

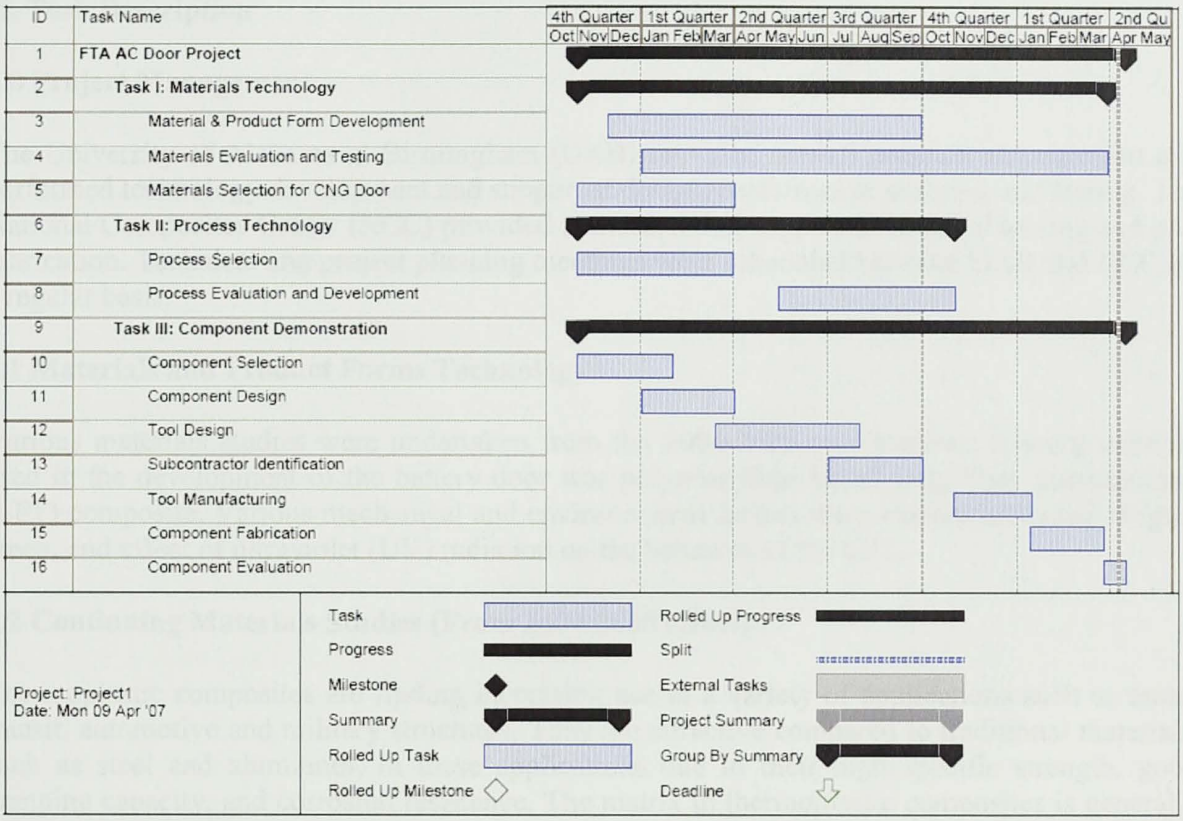

Figure 1.1- 3 Task description and duration 2005-2006 period.

II. Task Description

2.0 Project Management

The University of Alabama at Birmingham (UAB) provided overall program management and performed technology development and supported design, performance analysis, and testing. The National Composites Center (NCC) provided manufacturing support in terms of tooling and part fabrication. Technical and project planning meetings were scheduled between UAB and NCC on a regular basis.

2.1 Materials and Product Forms Technology

Various materials studies were undertaken from the 2004-2005 year's effort. Primary material used in the development of the battery door was polypropylene based long fiber thermoplastic (LFT) composite. Various mechanical and environmental factors were studied including fatigue, creep, and effect of ultraviolet (UV) radiation on the behavior of the LFT.

2.2 Continuing Materials Studies (From 2004-2005 effort)

Thermoplastic composites are finding increasing use in a variety of applications such as mass-transit, automotive and military structures. They are attractive compared to traditional materials, such as steel and aluminum, in these applications due to their high specific strength, good damping capacity, and corrosion resistance. The matrix in thermoplastic composites is generally comprised of polypropylene (PP), polyethylene (PE), nylon or other inexpensive polymers. E-glass fiber is a commonly used reinforcing material [6]. Long fiber thermoplastic (LFT) composites have seen one of the highest growth rates, approximately 30%, in the plastic industry over the last five years [7]. Currently, short glass fibers are predominantly used as reinforcement in polypropylene in the automotive industry. The full strength of the reinforcing fiber is not realized, however, due to its low fiber aspect ratio. The fibers in LFTs have large fiber aspect ratio (ratio of length (ℓ) to diameter (d)), often exceeding ℓ/d of 2000 and thus take full advantage of the reinforcing fiber strength [8]. Starting fiber lengths are typically greater than 13 mm, and depend on desired properties, fiber volume fraction, and processing technique. The aspect ratio of a long-fiber is typically an order of magnitude greater than that of a short fiber. While short fiber reinforced thermoplastics realize substantial gain in mechanical properties over that of the neat material the full strength of the reinforcement cannot be realized because the fiber is below a critical length. The critical fiber length (ℓ_c) can be obtained from the following equation [8]:

$$\frac{\ell_c}{d} = \frac{\sigma_{max}}{2\tau_i} \qquad (1)$$

Considering the glass fiber diameter, d = 15 μm, fiber fracture strength, σ_{max} = 2000 MPa, and the glass-PP interface strength, τ_i= 4 MPa [9] an ℓ_c of about 3.75 mm is calculated. It can be seen that the length of fibers in the case of LFT is much higher than the critical length. Hence the fiber can be loaded to its maximum strength.

2.3 Fatigue behavior of LFTs

2.3.1 Introduction (Fatigue)

LFTs are frequently used for structural applications which are often subjected to cyclic loading. Thus, characterizing the fatigue behavior of LFTs is of great importance. Many factors govern the fatigue behavior of discontinuous fiber reinforced polymer-matrix composites (PMC) system such as LFTs. Some of these are: processing conditions, type of fiber, length of the fiber, orientation of the fiber with respect to the loading axis, properties of the matrix, interfacial properties, and testing conditions. Some common methods of making composites such as LFTs include extrusion-compression molding or injection molding. Fibers tend to orient in the flow direction in such composites, which leads to superior mechanical properties along the flow direction. As the fiber misorientation from the loading axis increases the strength of the composite will be increasingly dominated by the matrix and the interfacial properties [10]. Fiber length also plays an important role in the fatigue sensitivity of discontinuous fiber reinforced composites. Long fibers carry a significantly higher fraction of the load compared to short fibers. Also, for a given fiber volume fraction, there are less stress concentration sites (fiber ends) for long fibers as compared to short fibers [8].

Fatigue of polymer and PMCs also depend greatly on the frequency, cyclic amplitude, and viscoelastic nature of the polymer matrix. One of the important aspects of fatigue in polymers is hysteretic heating due to the visoelastic and insulating nature of the polymer leading to temperature rise and possible softening of the polymer. This becomes important at high frequency because not enough time is available for temperature equilibrium with surroundings [10-12]. Another source of temperature rise in fiber reinforced composites is the frictional sliding between the fiber and matrix.

A lot of work has been done in the past on continuous and short glass-fiber reinforced polypropylene [13-16]. It has been reported that continuous fibers composites show better performance than short fiber composites. But, the strength of discontinuous fiber composites approaches the strength of continuous fiber composites when the fiber length is substantially above the critical length [8]. In the current work we show the results of effect of long fibers in the fatigue behavior of LFT (PP/20 vol. % E-glass), made by extrusion-compression molding process, in terms of S–N or Wöhler curves. We studied the fatigue behavior in terms of processing induced fiber-orientation and the effect of frequency on the fatigue life of LFT.

2.3.2 Results (Fatigue)

2.3.2.1 Microstructural Characterization (LFT)

A representative micrograph of the LFT is shown in Fig. 2.3-1. It can be seen that most of the fibers are aligned along the extrusion direction. The extrusion direction is parallel to the samples sectioned along the length of the plate while it is perpendicular to the samples sectioned along the transverse direction. When the sample is loaded in tension or fatigue, most of the fibers in the longitudinal samples are loaded to its maximum strength while in the transverse only a low fraction of the fibers are loaded to its maximum strength. Thus, longitudinal samples are expected to show better performance in tension and fatigue as compared to the transverse samples.

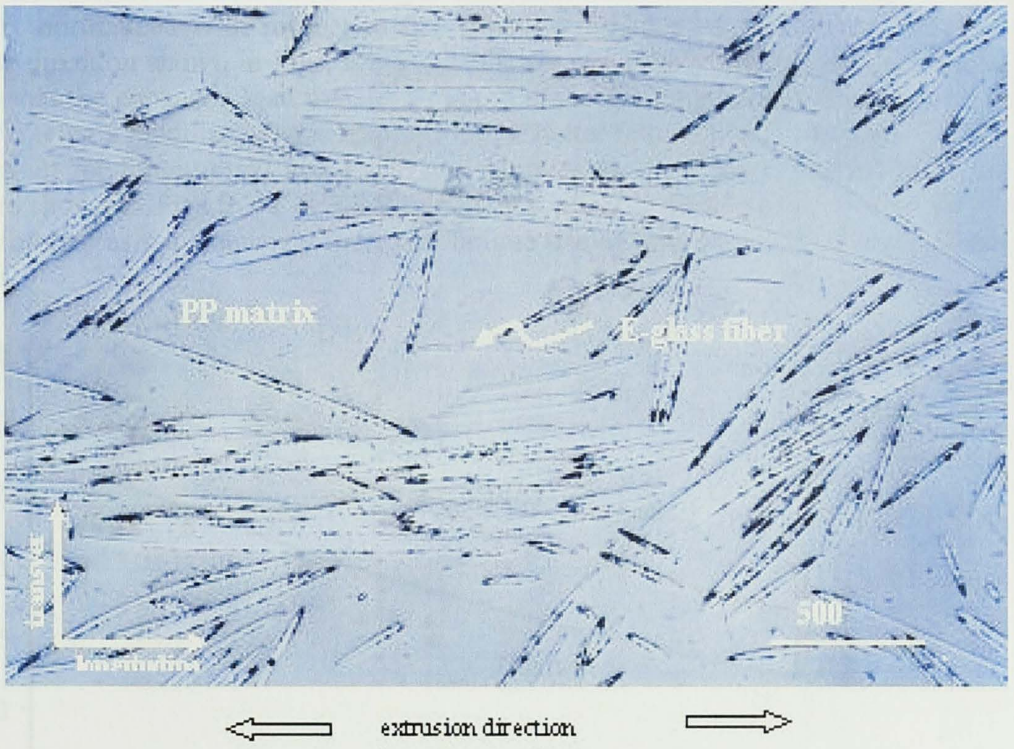

Figure 2.3- 1 A representative micrograph of LFT. It can be seen that most of the fibers are parallel to the extrusion direction.

2.3.2.2 Tensile Tests (LFT)

Results of the tensile test are summarized in Table 2.3-1. It can be seen that longitudinal LFTs have higher ultimate tensile strength (UTS) and modulus values as compared to the transverse LFTs.

Table 2.3- 1 Summary of tensile test of LFT.

LFT	UTS(MPa)		Modulus (GPa)	
	Mean	St. dev.	Mean	St. dev.
Longitudinal	113.8	14.3	6.5	1.0
Transverse	68.2	10.2	5.0	0.5

2.3.2.3 Fatigue Tests (LFT)

Results of the fatigue tests of samples along longitudinal and transverse direction at frequencies of 10, 15 and 20 Hz are shown in Figs. 2.3-2 – 2.3-4. We can clearly see from these plots that longitudinal samples showed better fatigue resistance than the transverse samples. When these results are normalized with respect to the Young's modulus of LFT in the longitudinal and transverse direction shown in Figs. 2.3-5 – 2.3-7, we can clearly see that the plots overlap. This indicates that the enhanced load transfer to the fibers in the longitudinal direction, which results in higher Young's modulus, also is responsible for better fatigue life. Figs. 2.3-2 – 2.3-4 are then plotted again for longitudinal and transverse samples to show the effect of frequency. These results are shown in Figs 2.3-8 & 2.3-9. Frequency effect is clearly evident from the plot and it can be seen that as the frequency increases fatigue life of both longitudinal and transverse LFT decreases.

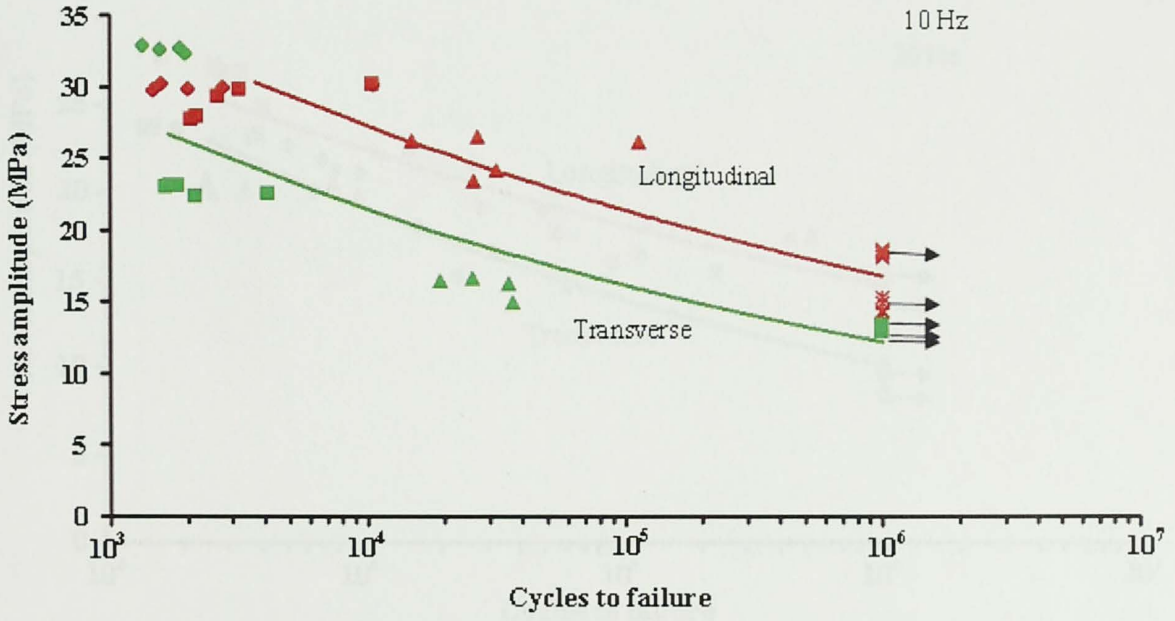

Figure 2.3- 2 S-N curves for samples sectioned along longitudinal and transverse direction at a frequency of 10 Hz. Longitudinal samples shows better fatigue resistance as compared to transverse samples.

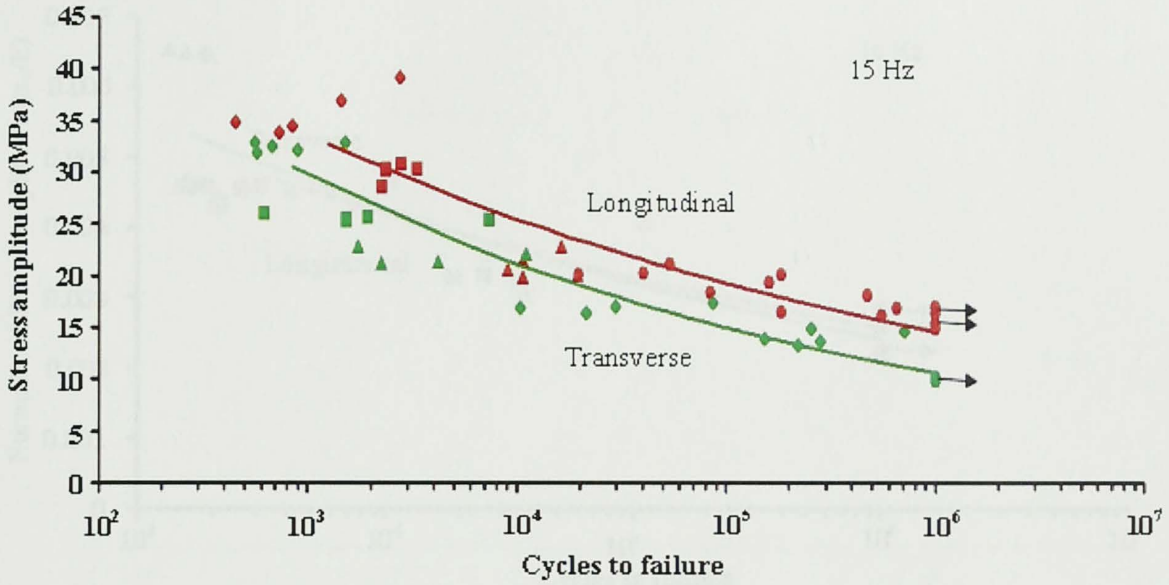

Figure 2.3- 3 S-N curves for samples sectioned along longitudinal and transverse direction at a frequency of 15 Hz. Longitudinal samples shows better fatigue resistance as compared to transverse samples.

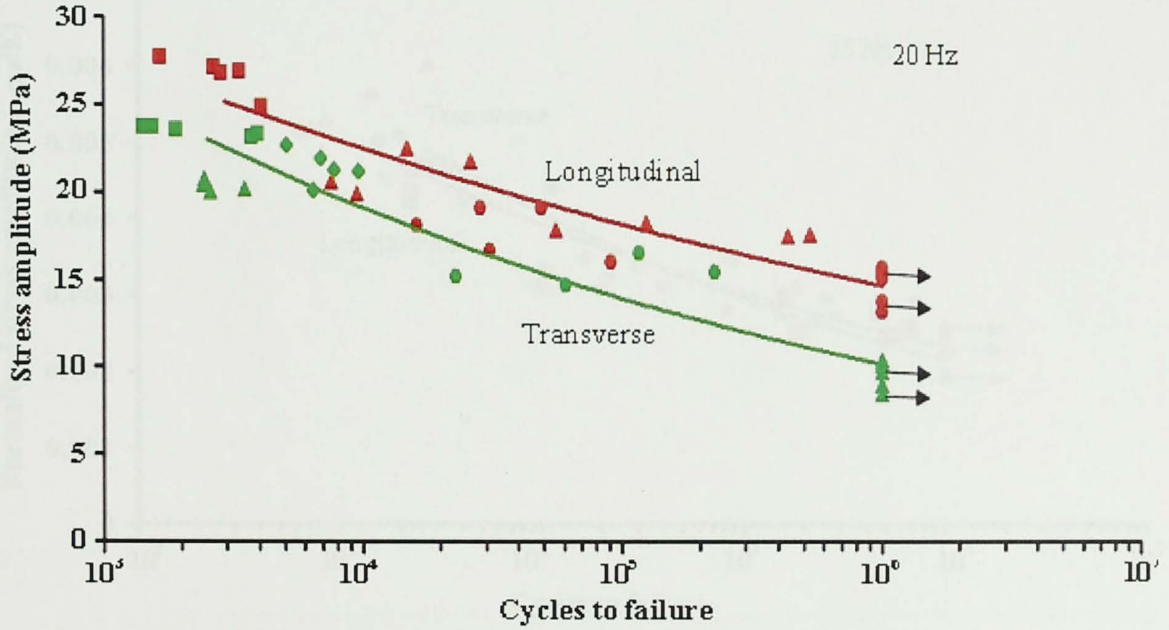

Figure 2.3- 4 S-N curves for samples sectioned along longitudinal and transverse direction at a frequency of 20 Hz. Longitudinal samples shows better fatigue resistance as compared to transverse samples.

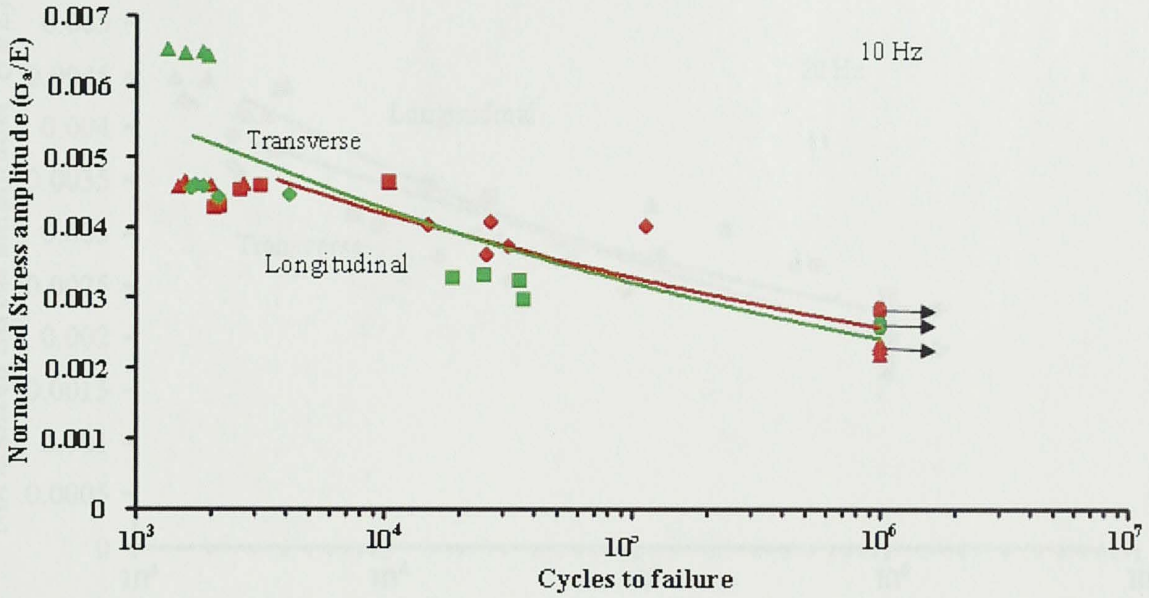

Figure 2.3- 5 S-N curves normalized with longitudinal and transverse modulus of LFT at a frequency of 10 Hz. Normalized curves for longitudinal and transverse LFTs overlap.

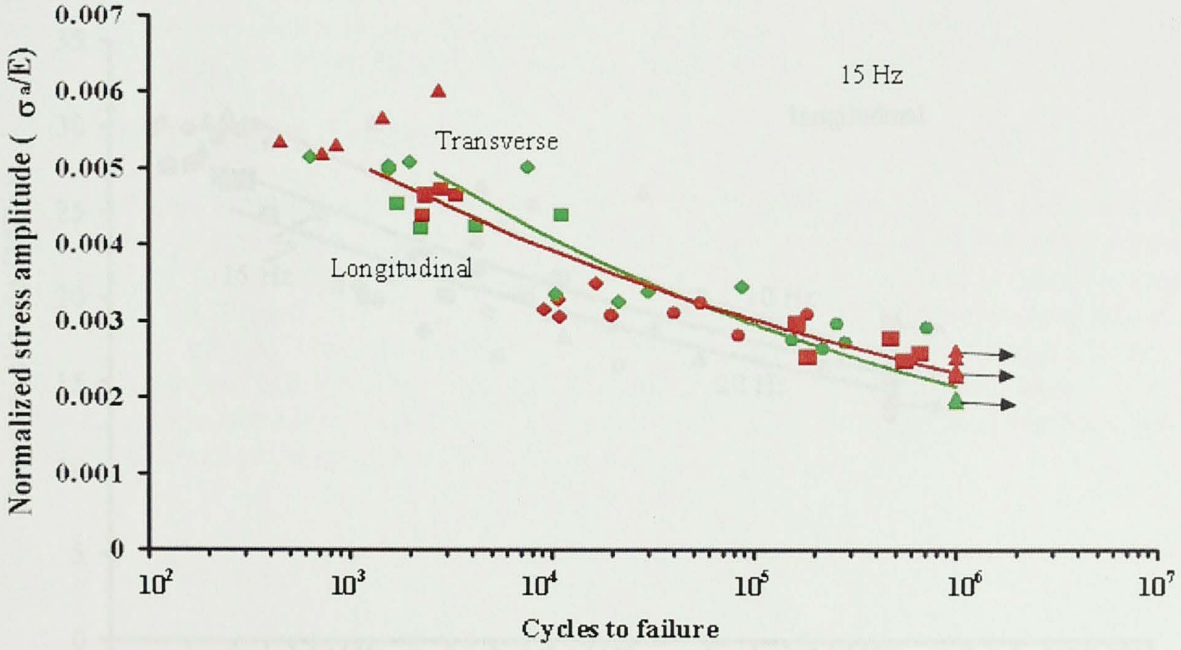

Figure 2.3- 6 S-N curves normalized with longitudinal and transverse modulus of LFT at a frequency of 15 Hz. Normalized curves for longitudinal and transverse LFTs overlap.

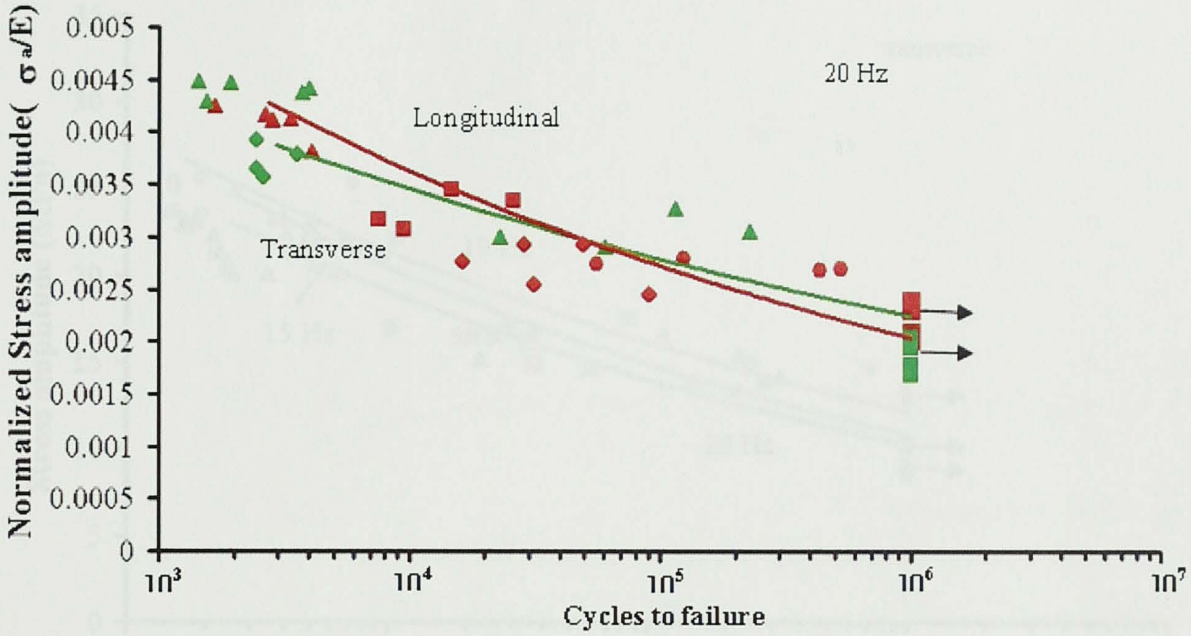

Figure 2.3- 7 S-N curves normalized with longitudinal and transverse modulus of LFT at a frequency of 20 Hz. Normalized curves for longitudinal and transverse LFTs overlap.

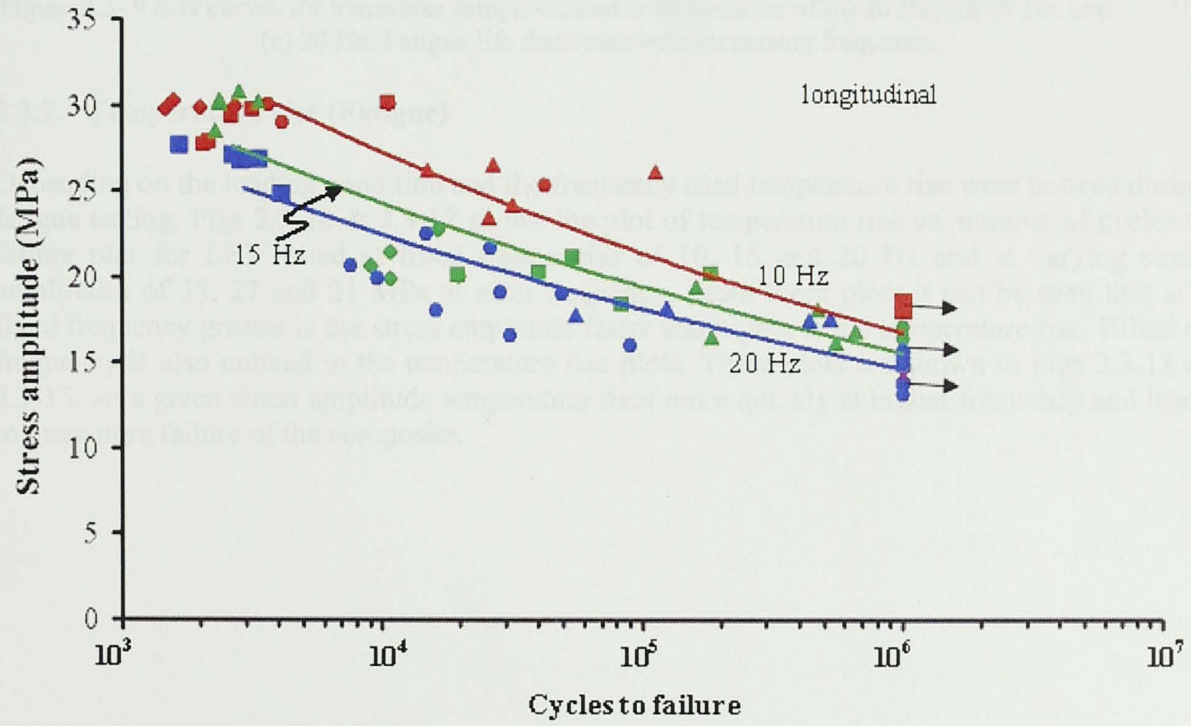

Figure 2.3- 8 S-N curves for longitudinal samples tested at frequencies of (a) 10 Hz, (b) 15 Hz, and (c) 20 Hz. Fatigue life decreases with increasing frequency.

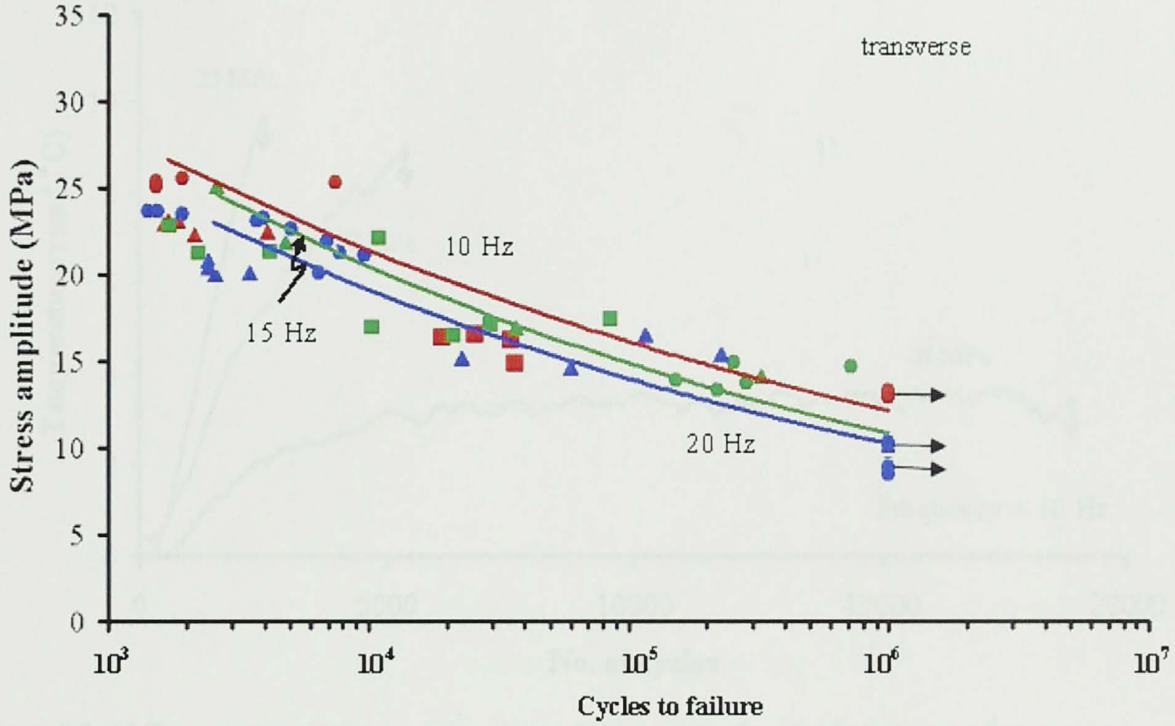

Figure 2.3- 9 S-N curves for transverse samples tested at frequencies of (a) 10 Hz, (b) 15 Hz, and (c) 20 Hz. Fatigue life decreases with increasing frequency.

2.3.2.4 Temperature rise (Fatigue)

Depending on the loading condition and the frequency used temperature rise were noticed during fatigue testing. Figs 2.3-10 & 2.3-12 shows the plot of temperature rise vs. number of cycles to failure plot for LFT tested at fixed frequencies of 10, 15 and 20 Hz and at varying stress amplitudes of 35, 27 and 21 MPa at each frequency. From these plots it can be seen that at a fixed frequency greater is the stress amplitude faster and higher is the temperature rise. Effect of frequency is also noticed in the temperature rise plots. These plots are shown in Figs 2.3-13 & 2.3-15. At a given stress amplitude temperature rises more quickly at higher frequency and leads to premature failure of the composite.

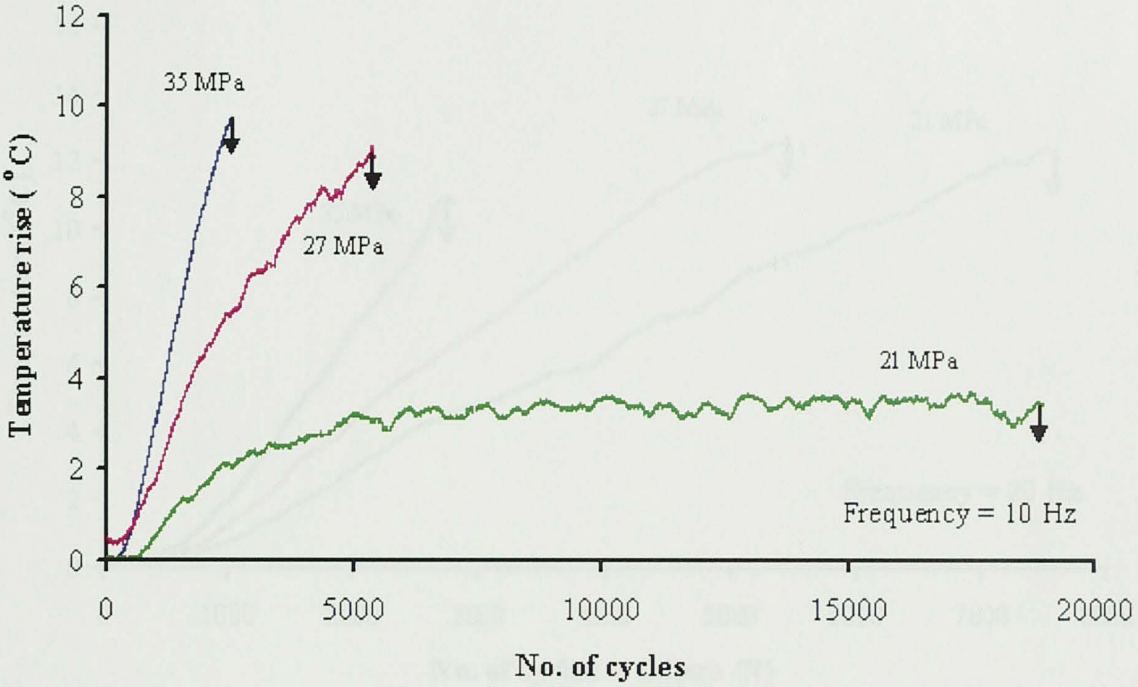

Figure 2.3- 10 Temperature rise vs. no. of cycles to failure curves for sample tested at a frequency of 10 Hz at stress amplitudes of (a) 35 MPa, (b) 27 MPa, and (c) 21 MPa. At higher stress amplitude temperature rises faster and leads to early failure of the sample.

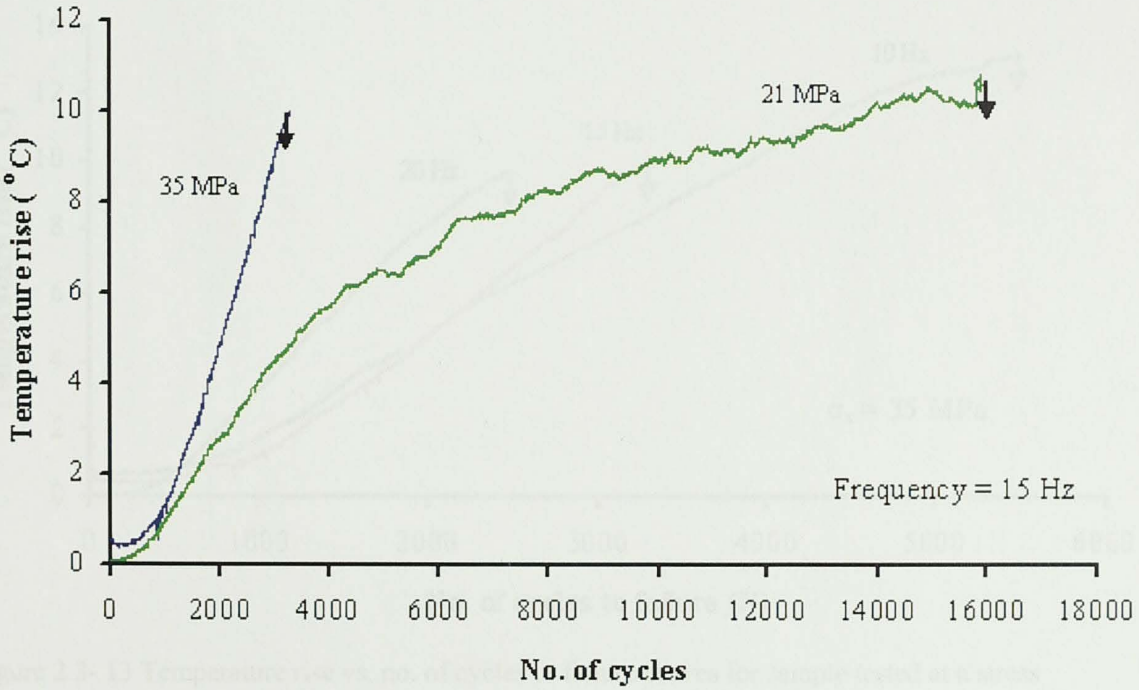

Figure 2.3- 11 Temperature rise vs. no. of cycles to failure curves for sample tested at a frequency of 15 Hz and at stress amplitudes of (a) 35 MPa, and (c) 21 MPa. At higher stress amplitude temperature rises faster and leads to early failure of the sample.

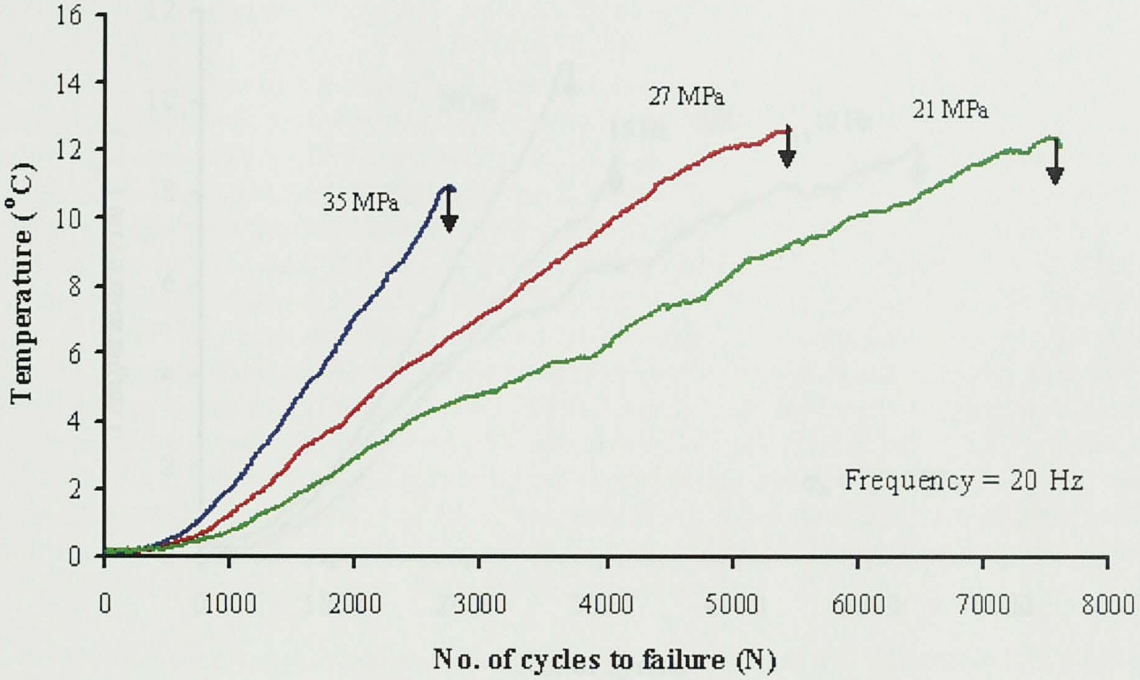

Figure 2.3- 12 Temperature rise vs. no. of cycles to failure curves for sample tested at a frequency of 20 Hz and at stress amplitudes of (a) 35 MPa, (b) 27 MPa and (c) 21 MPa. At higher stress amplitude temperature rises faster and leads to early failure of the sample.

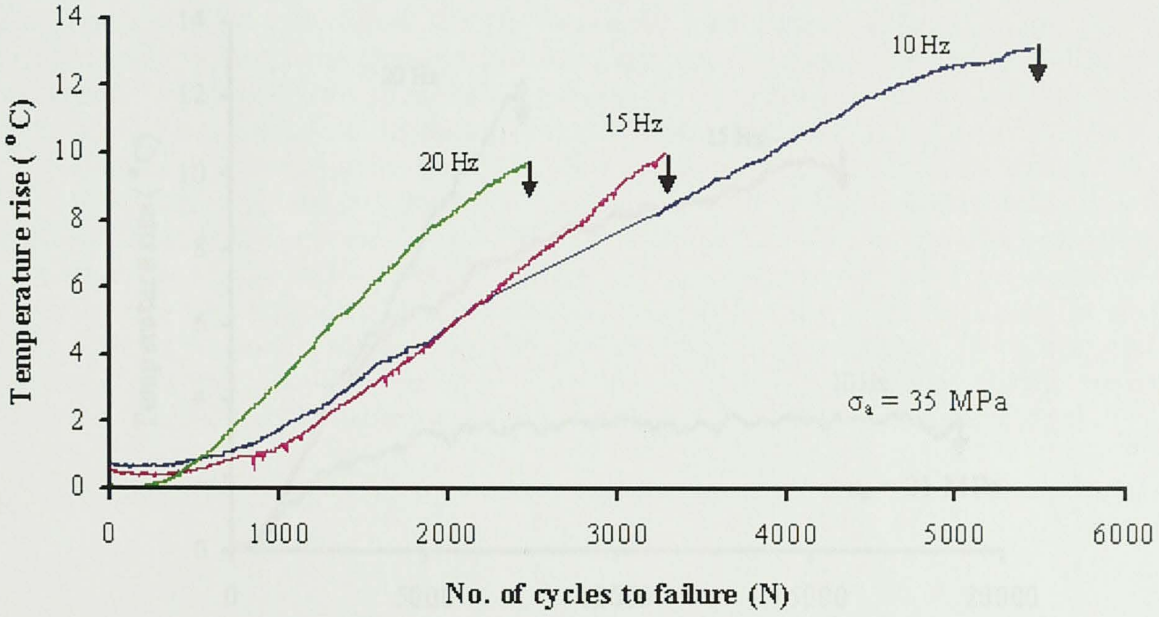

Figure 2.3- 13 Temperature rise vs. no. of cycles to failure curves for sample tested at a stress amplitude of 35 MPa and at frequencies (a) 20 Hz, (b) 15 Hz, and (c) 10 Hz. At higher frequency temperature rises faster and leads to early failure of the sample.

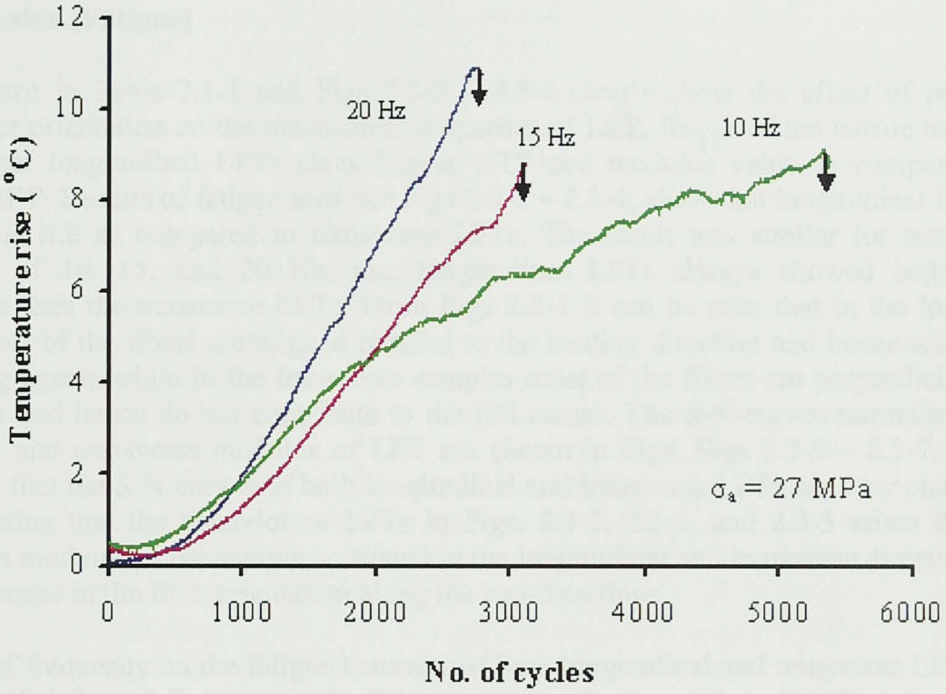

Figure 2.3- 14: Temperature rise vs. no. of cycles to failure curves for sample tested at a stress amplitude of 27 MPa and at frequencies (a) 20 Hz, (b) 15 Hz, and (c) 10 Hz. At higher frequency temperature rises faster and leads to early failure of the sample.

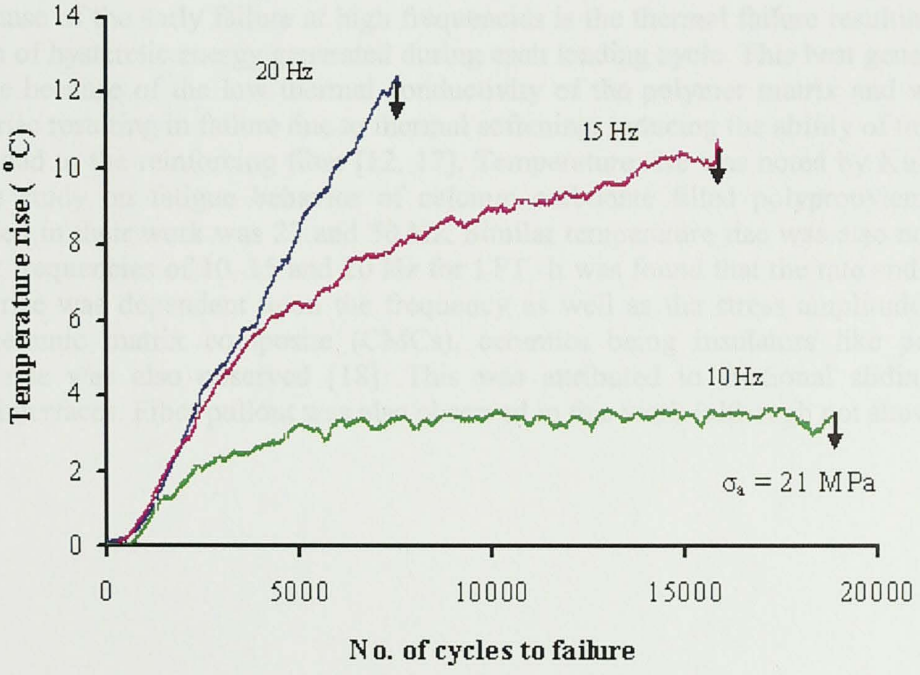

Figure 2.3- 15 Temperature rise vs. no. of cycles to failure curves for sample tested at a stress amplitude of 21 MPa and at frequencies (a) 20 Hz, (b) 15 Hz, and (c) 10 Hz. At higher frequency temperature rises faster and leads to early failure of the sample.

2.3.3 Discussion (Fatigue)

Results shown in Table 2.1-1 and Figs 2.3-2 – 2.3-4 clearly show the effect of processing-induced fiber orientation on the mechanical properties of LFT. Result of the tensile tests (Table 1) shows that longitudinal LFTs show higher UTS and modulus value as compared to the transverse LFT. Results of fatigue tests see Figs 2.3-2 – 2.3-4; show that longitudinal LFTs have better fatigue life as compared to transverse LFTs. The result was similar for tests done at frequencies of 10, 15, and 20 Hz, i.e., longitudinal LFTs always showed better fatigue performance than the transverse LFTs. From Figs 2.3-1 it can be seen that in the longitudinal samples, most of the fibers are aligned parallel to the loading direction and hence are the main load bearing agents while in the transverse samples most of the fibers are perpendicular to the loading axis and hence do not contribute to the full extent. The S-N curves normalized by the longitudinal and transverse modulus of LFT are shown in Figs. Figs 2.3-5 – 2.3-7. It can be clearly seen that the S-N curves of both longitudinal and transverse LFTs are very close to each other indicating that the behavior of LFTs in Figs. 2.3-3, 2.3-4, and 2.3-5 arises due to the difference in modulus of the sample sectioned in the longitudinal and transverse direction caused by the difference in the fiber orientation along the two directions.

The effect of frequency on the fatigue behavior of both longitudinal and transverse LFTs can be seen in Figs. 2.3-8 – 2.3-9, respectively. With increasing frequency there is a decrease in fatigue life of both longitudinal and transverse LFTs. The mechanical work done during fatigue cycling of the polymer involves molecular processes leading to microscopic deformation modes such as formation of crazes, shear bands, voids or microcracks. A part of the mechanical work done is converted to heat which is particularly evident at high stress amplitudes and at high frequencies. The major cause of the early failure at high frequencies is the thermal failure resulting from the accumulation of hysteretic energy generated during each loading cycle. This heat generated stays in the sample because of the low thermal conductivity of the polymer matrix and will lead to temperature rise resulting in failure due to thermal softening, reducing the ability of the matrix to transfer the load to the reinforcing fiber [12, 17]. Temperature rise was noted by Kultrual et al. [12] in their study on fatigue behavior of calcium carbonate filled polypropylene. But the frequency used in their work was 23 and 50 Hz. Similar temperature rise was also noted in this work even at frequencies of 10, 15 and 20 Hz for LFT. It was found that the rate and amount of temperature rise was dependent upon the frequency as well as the stress amplitude. In cyclic fatigue of ceramic matrix composite (CMCs), ceramics being insulators like polymers, a temperature rise was also observed [18]. This was attributed to frictional sliding between fiber/matrix interfaces. Fiber pullout was also observed in this work (although not shown).

Fig. 2.3-5 shows the temperature rise vs. number of cycles to failure curves for sample tested at 10 Hz and at stress amplitudes of 35, 27 and 21 MPa. It can be seen that although the sample tested at 35 and 27 MPa showed similar temperature rise, the rate of temperature rise is faster in the case of sample tested at 35 MPa. Not much temperature rise can be seen in the case of sample tested at 21 MPa. Sample showed some initial temperature increase but later temperature becomes constant and it can be believed that failure occurs not because of hysteretic heating but conventional form of fatigue crack nucleation and propagation. Similar results were obtained for the samples tested at 15 and 20 Hz and similar stress amplitudes (Fig. 2.3-11 and 2.3-12). In Fig. 2.3-12 it can be seen that a continuous temperature rise takes place even at lower stress amplitudes. This is probably because of the high frequency of 20 Hz in this case. Therefore, in this case failure occurs due to accumulation of heat. Figures 2.3-13, 2.3-14, and 2.3-15 show the effect of frequency on the behavior of temperature rise at a given stress amplitude. From Fig. 2.3-13 it can be seen that at 35 MPa the sample tested at 20 Hz survives the least number of fatigue cycles while the one tested at 10 Hz survived the most number of fatigue cycles. In the case of sample tested at 20 Hz temperature rises very fast which lead to thermal failure of the LFT. Thermal failure was dominant in all the samples because of very high stress amplitude. Fig. 2.3-14 shows similar behavior as that of Fig. 2.3-13 because 27 MPa is still large stress amplitude for LFT. From Fig. 2.3-15 it is clear that sample tested at 21 MPa and at 20 Hz shows a significant temperature rise while the sample tested at the same stress amplitude but at 10 Hz shows only slight temperature rise and later temperature becomes constant. In the former, failure is dominated by hysteretic heating phenomenon while in the later it is the conventional form of fatigue crack propagation was the main reason for the failure of the sample.

2.3.4 Conclusions (Fatigue)

Fiber orientation developed during processing played an important role in the fatigue and tensile properties of LFT. Longitudinal LFT showed better tensile and fatigue behavior than the transverse LFTs. Samples tested at lower frequency showed higher fatigue life, compared to the samples tested at higher frequency. This is because of the hysteretic heating phenomenon taking place at high frequencies and also due to the low thermal conductivity of the polymer matrix. At higher frequency less time is available for the heat dissipation to the surroundings which lead to temperature rise and failure of the sample.

2.4 Flexural creep testing of neat and fiber reinforced thermoplastics

2.4.1 Introduction (Creep)

Dimensional stability is based on the constancy of the material to retain its original dimensions with progressing time, not exceeding the tolerance level specified in design, and is subject to intrinsic material properties and external agencies, which affect material performance [19]. Viscoelasticity and its theories describe dimensional stability related time-dependent material behavior that conjoins characteristic liquid like viscous properties and solid like elastic properties that are also dependent on (or combination of) of temperature (T), frequency (ω) and stress (σ) or strain (ε) rate [20]. Automobile semi-structural parts often see constant loads, which cause constant stresses and concomitant creep strains. Data from creep tests are necessary to predict the decrease in creep modulus and strength of the material under long-term loads and predict dimensional changes that occur because of such loads. Not only these stresses cause dimensional instability, they also trigger material defects and degradation of mechanical properties. Composites are non-linear viscoelastic in nature, i.e. the strain produced in composite specimens is not a linear variant in time or stress, and require testing at various temperatures, because they operate around 200K around the glass transition temperature of the matrix [21].

Dynamic mechanical analysis (DMA) for polymers is a method to measure linear viscoelastic properties where a sinusoidal force causes deformation in the specimens, lagging by a phase angle δ [22]. Strganac and Golden investigated the nonlinear viscoelasticity of thin film polyethylene as a combination of creep and dynamic mechanical tests and speculated its validity over different material systems [22]. Yang and Chin investigated the tensile creep of long aligned glass fiber reinforced polypropylene and found a high variation in the times to rupture of specimens [23]. Kim et al. indicated the usage of a higher molecular weight polymer and longer fiber reinforcement to improve creep reinforced in long fiber thermoplastics [19]. Investigation of flexural creep in neat and reinforced thermoplastic resins is equally necessary, due to an early onset of the non-linear viscoelastic regime, could be carried out more accurately in a flexural creep apparatus in the time domain rather than in a DMA, which is based on damping response of the solid polymer or composite.

Flexural creep is the transient deformation of a material in three-point or four-point bending loading condition [24]. The maximum stress produced on the material is a function of the geometry of the specimen and the applied load and is described by Eq. 2.

$$\sigma = \frac{3}{2}\frac{Pl}{bd^2} \tag{2}$$

where σ (MPa) is the maximum stress due to the load P (N), on a specimen having support span l (mm), width b (mm) and depth d (mm). This stress occurs at the surface and is referred to as the fiber stress. The maximum strain is produced at the mid-line of the specimen and is given by the Eq. 3.

$$\varepsilon(t) = \frac{6D(t)d}{l^2} \tag{3}$$

where ε(t) is the maximum strain produced due to the application of stress and D(t) (mm) is the instantaneous deflection in the mid-span at time t. This testing configuration can be represented as in Fig. 2.4-1.

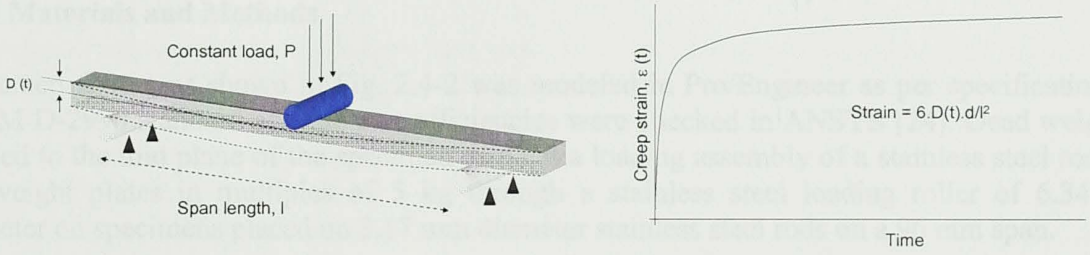

Figure 2.4- 1 The application of a constant load, P (N) produces a stress σ (MPa) which causes deformation (strain, ε(t)) in the material with progressing time.

The transient creep modulus E(t) (MPa) is the ratio of the maximum fiber stress and instantaneous strains mathematically given by Eq. 4.

$$E(t) = \frac{Pl^3}{4bd^3} \cdot \frac{1}{D(t)} \tag{4}$$

The reciprocal of creep modulus is termed the creep compliance J (1/MPa). It is the time dependent strain per unit stress and is a common descriptor of the creep process.

Dynamic mechanical analysis (DMA) measures damping as a function of frequency [20]. The strain produced in the polymer is a function of the frequency and is represented by the complex modulus, which is a sum of the storage modulus and the loss modulus of the material. In DMA, oscillatory deformation and phase lag are measured in sweeps of different frequencies. The behavior is described by the following set of equations.

$$e = e_0 \sin \omega t \tag{5}$$

$$\sigma = \sigma_0 \sin(\omega t + \delta) \tag{6}$$

where ω is the angular frequency and δ is the phase lag between stress and strain. Storage and loss moduli are designated G1 and G2, respectively, and are given mathematically by Eqs. 7 and 8.

$$G_1 = \frac{2E}{e_0^2} \tag{7}$$

$$G_2 = \frac{2E}{\pi e_0^2} \tag{8}$$

$$G_2/G_1 = \tan\delta = \frac{\Delta E}{2\pi E} \tag{9}$$

where E is the maximum stored elastic energy and tan δ is the phase lag. Viscoelastic compliance J (1/MPa) is a frequency dependent quantity, constant at very low and high frequencies, and varies at intermediate frequencies.

2.4.2 Materials and Methods

The creep fixture as shown in Fig. 2.4-2 was modeled in Pro/Engineer as per specifications in ASTM D-2990 standard and the part efficiencies were checked in ANSYS [24]. Dead weight is applied to the mid plane of the specimen through a loading assembly of a stainless steel rod and flat-weight plates in multiples of 5 kg through a stainless steel loading roller of 6.34 mm diameter on specimens placed on 3.17 mm diameter stainless steel rods on a 96 mm span.

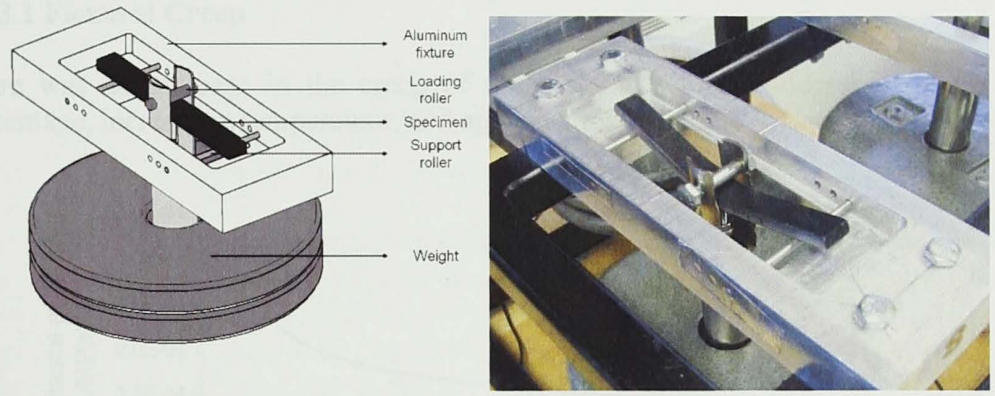

Figure 2.4- 2 Flexural creep testing apparatus was (a) designed and modeled in Pro/Engineer, and (b) fabricated at the UAB machine shop.

A linear variable displacement transducer (LVDT) was coaxially positioned in each loading assembly of loading assembly. The coaxial position ensures the detection of the mid-line deflection because of its symmetry and would reduce the error in measurement. Flexural creep testing was done on a fixture based on three point bending (ASTM D-790). The strain in the specimen is measured by a linear variable displacement transducer positioned coaxially with the loading assembly.

Nylon 6/6 and polypropylene based long fiber thermoplastics were obtained in pellet form as compounded by the vendor and extruded in a low-shear twin-screw extruder and compression molded in 400 ton press as plates. Sequel® thermoplastic olefins, which are used for large exterior automotive applications such as bumper fascias, were obtained as molded plates. Transient creep specimens were machined from plates to 127 mm x 12.7 mm x 6.34 mm coupons as specified in ASTM D-2290. The specimens were conditioned as specified in ASTM D-618 to eradicate strain history. The dynamic creep specimens were made to the size 35.4 mm x 12.7 mm x 1.6 mm as required by the dynamic mechanical analyzer (DMA). All specimens were ground to remove surface roughness and unevenness before conditioning.

Flexural creep specimens were loaded after the LVDTs were stabilized in order to reduce noise in data. The specimens were heated in an environmental chamber, and loaded with the dead weights. Total creep strain data was recorded against time in a chosen time interval through a data acquisition system and analyzed using Microsoft Excel.

Creep time temperature superposition data was generated in frequency sweeps with a frequency range of 0.1 to 100 Hz and amplitude of 100 μm. Short-term tests were done at temperatures ranging from 35 °C to 160 °C in 5 °C step size on a DMA, and the master curve was generated using the TA data analysis software.

2.4.3 Results and Discussions (Creep)

2.4.3.1 Flexural Creep

There was an increase in the creep of the material with the decrease in the fiber volume percentage, increase in temperature, and applied stress (Fig. 2.4-3.).

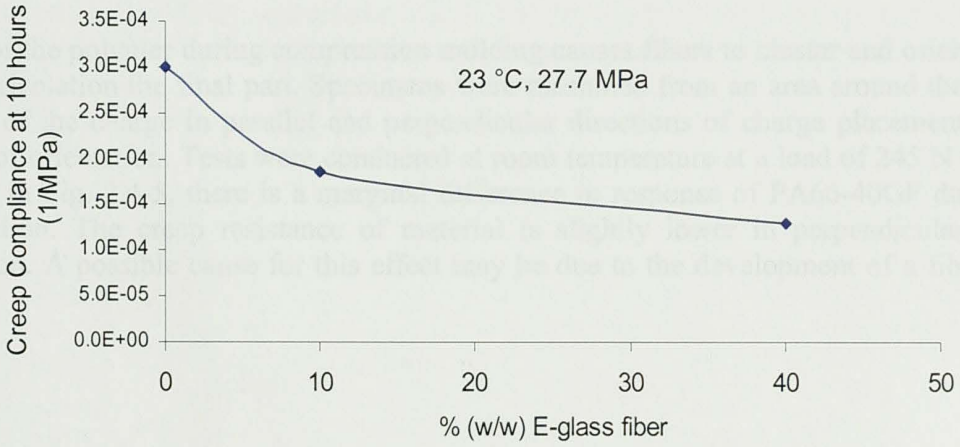

Figure 2.4- 3 A decrease in the creep compliance recorded at 10 hours of testing with an increase in the fiber weight percentage was recorded. Neat nylon 6/6 showed the highest creep compliance when tested at 23 °C and 27.7 MPa.

Creep compliances of composites with different fiber loading at temperatures on either side of the glass transition temperature (50 °C) of nylon 6/6 show that the higher fiber loading causes higher amount of load transfer from the matrix to fiber and constricts the matrix to deformation (Fig. 2.4-4.).

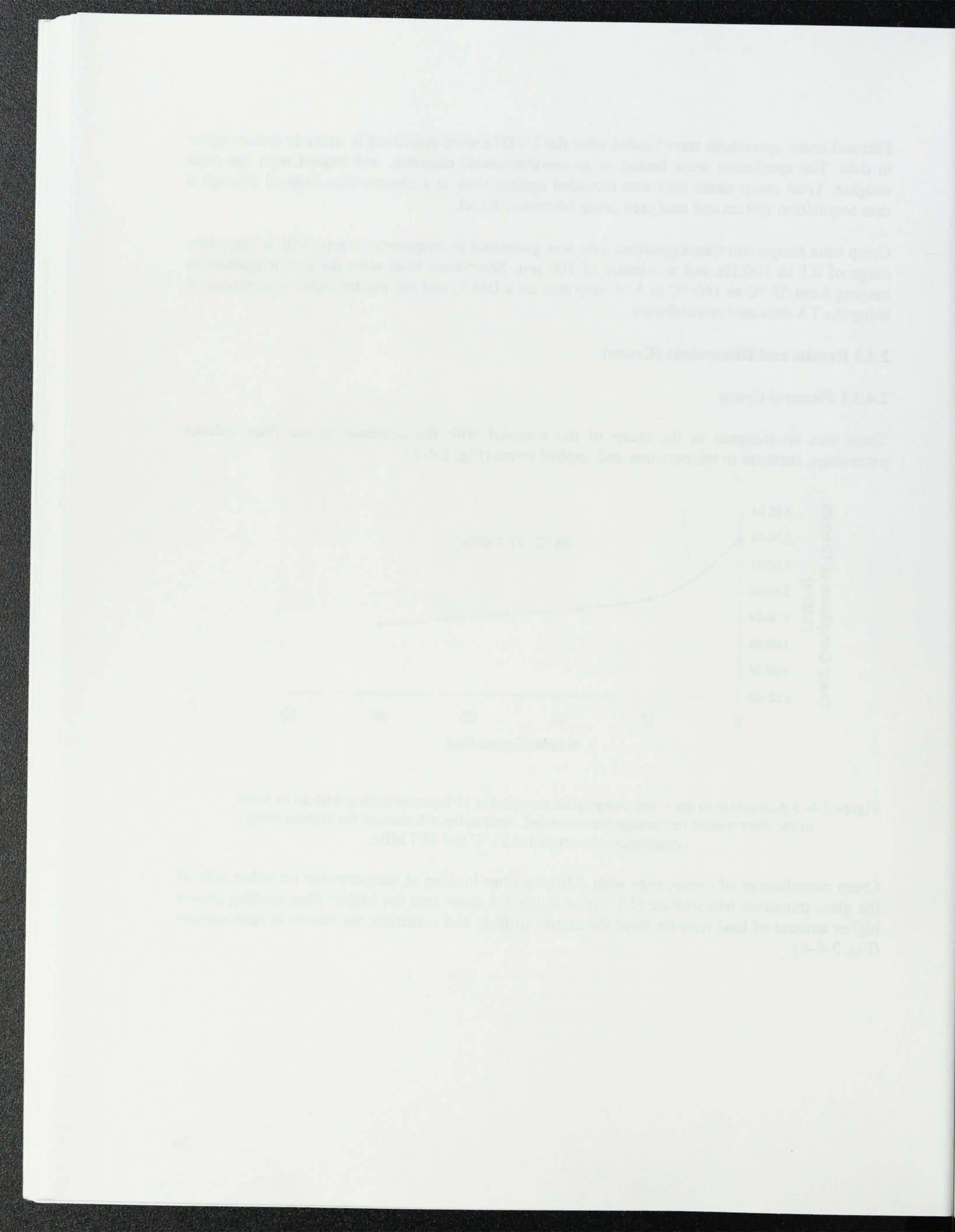

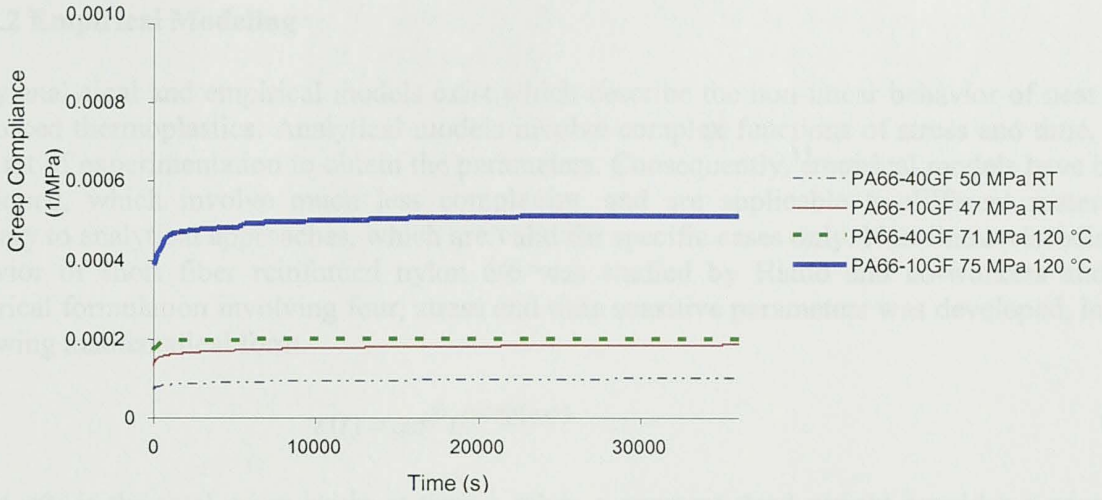

Figure 2.4- 4 Creep data for 10 and 40 wt.% glass fiber reinforced nylon 6/6 compare the effect of fiber volume fraction, stress level (nominal 50 and 70 MPa) and temperature (room temperature and 120 °C) on the creep resistance of the material.

Flow of the polymer during compression molding causes fibers to cluster and orient leading to a fiber orientation the final part. Specimens were machined from an area around the approximate center of the charge in parallel and perpendicular directions of charge placement to study the effect of orientation. Tests were conducted at room temperature at a load of 245 N (70 MPa). As shown in Fig. 2.4-5, there is a marginal difference in response of PA66-40GF due to the flow orientation. The creep resistance of material is slightly lower in perpendicular to the flow direction. A possible cause for this effect may be due to the development of a fiber orientation [25].

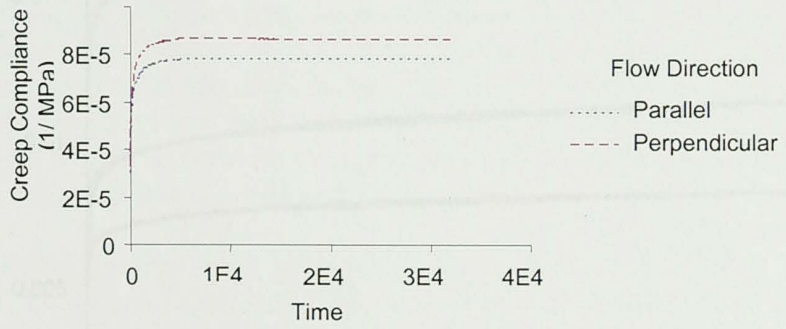

Figure 2.4- 5 Creep data for specimens from the parallel and perpendicular flow directions show the development of a possible preferable fiber orientation during processing.

2.4.3.2 Empirical Modeling

Many analytical and empirical models exist which describe the non-linear behavior of neat and reinforced thermoplastics. Analytical models involve complex functions of stress and time, and need lot of experimentation to obtain the parameters. Consequently, empirical models have been developed, which involve much less complexity, and are applicable to different materials, contrary to analytical approaches, which are valid for specific cases only. Non-linear viscoelastic behavior of short fiber reinforced nylon 6/6 was studied by Hadid and co-workers and an empirical formulation involving four, stress and time sensitive parameters was developed, in the following mathematical form.

$$\varepsilon(t) = a\sigma^{b} t^{c.\exp(e.\sigma)} \tag{10}$$

where $\varepsilon(t)$ is the total creep strain at time t, when a constant dead weight provides a constant stress σ. This four parameter empirical model was found to provide accurate fits to experimental data. As expected, neat nylon 6/6 showed non-linearity, and was modeled by the above-mentioned model to a good approximation. The adjustable parameters are sensitive to changes in temperature and intrinsic mechanisms. Fig. 2.4-6 shows representative experimental data and an empirical data fit for extrusion/ compression molded nylon 6/6 tested at 23 °C and three applied stresses.

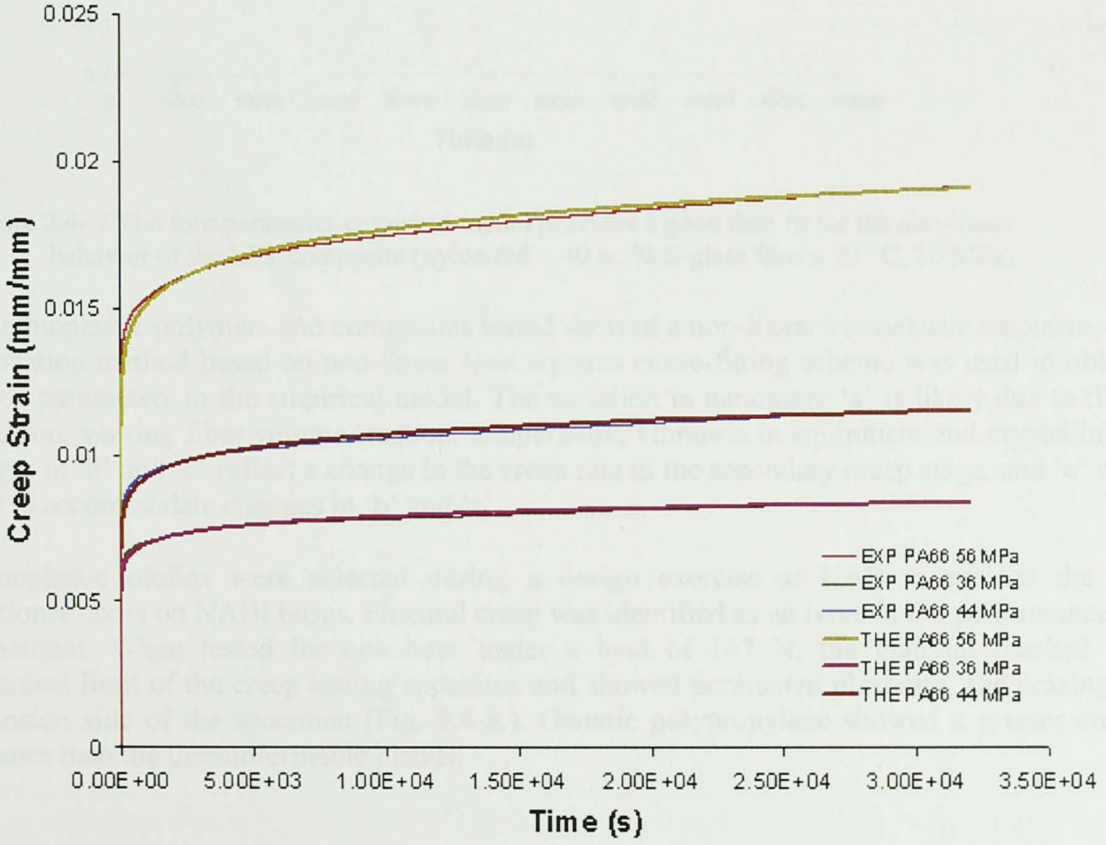

Figure 2.4- 6 Neat nylon 6/6 shows non-linearity with respect to time and applied stress.

The effect of adding fiber reinforcements to the neat resin to decrease the creep rate and to increase the overall stiffness and strength of the composite was realized with the addition of 40 wt. % long (12.7 mm) E-glass fiber by weight. This modification in the material to obtain the long fiber thermoplastic composite can cause complicated results due to an unpredictable fiber orientation, effective fiber length and fiber fraction, which are hard to control in the processing stage. Fig. 2.4-7 shows a similar non-linear viscoelastic response for the LFT composite, the addition of fiber bringing about a decrease in the secondary creep rate and the immediate elastic response on loading.

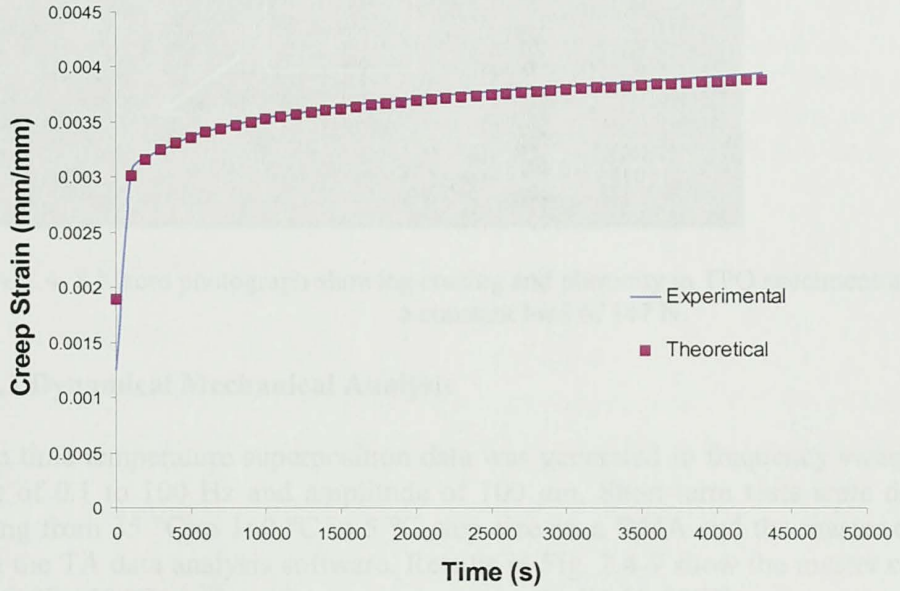

Figure 2.4- 7 The four parameter empirical model provides a good data fit for the non-linear behavior of the LFT composite (nylon 6/6 + 40 w. % E-glass fibers, 23 °C, 56 MPa).

All thermoplastic polymers and composites tested showed a non-linear viscoelastic response. An optimization method based on non-linear least squares curve-fitting scheme was used to obtain the four parameters in the empirical model. The variation in parameter 'a' is likely due to fiber orientation, varying fiber volume fraction, temperature, vibration in equipment and crystallinity. Changes in 'b' and 'c' reflect a change in the creep rate in the secondary creep stage, and 'e' will adjust to accommodate changes in 'b' and 'c'.

Thermoplastic olefins were selected during a design exercise at UAB to replace the air conditioner doors on NABI buses. Flexural creep was identified as an issue in the performance of the material. When tested for one hour under a load of 147 N, the material reached the mechanical limit of the creep testing apparatus and showed permanent plasticity, and crazing in the tension side of the specimen (Fig. 2.4-8.). Generic polypropylene showed a greater creep resistance than the thermoformable blends.

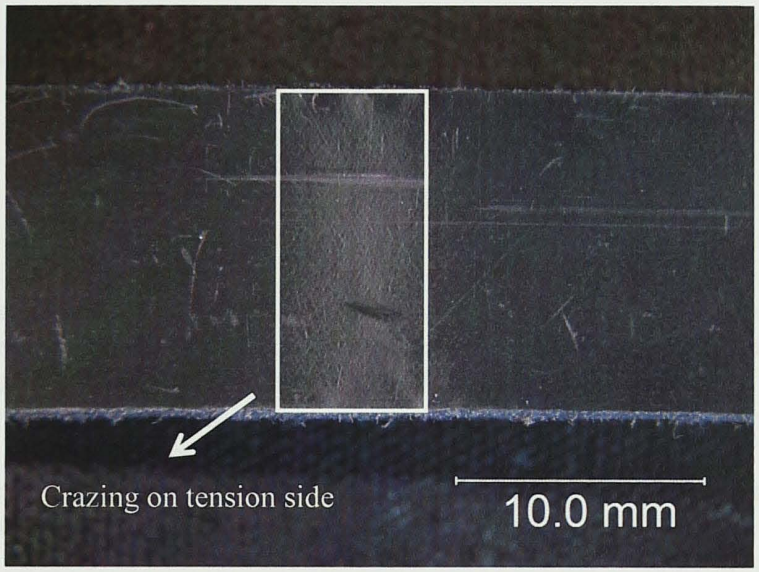

Figure 2.4- 8 Macro photograph showing crazing and plasticity in TPO specimens after testing at a constant load of 147 N.

2.4.3.3 Dynamical Mechanical Analysis

Creep time temperature superposition data was generated in frequency sweeps with a frequency range of 0.1 to 100 Hz and amplitude of 100 μm. Short-term tests were done at temperatures ranging from 35 °C to 160 °C in 5 °C step size on a DMA and the master curve was generated using the TA data analysis software. Results in Fig. 2.4-9 show the master curve generated with 100 °C (T_g+50 °C) as the reference temperature for PA66-40GF.

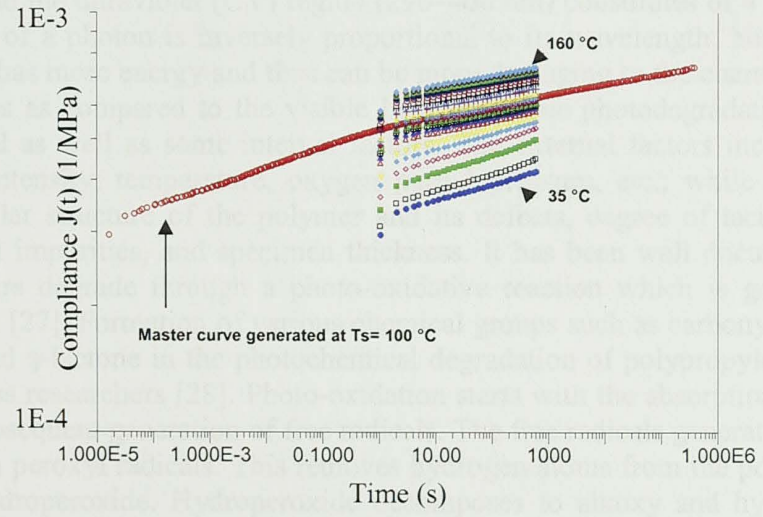

Figure 2.4- 9 WLF superposition principle was used to generate the master creep curve for 40 wt.% glass fiber reinforced nylon 6/6 generated by superposing short term creep data at each 5 °C in the 35 °C to 160 °C range in an DMA. A reference temperature T_S= 100 °C (T_g+ 50 °C) was used to shift the curves

The data from DMA was close to flexural creep data for the first four decades of time. This is probably due to linear viscoelastic (low stresses and infinitesimal strains) regime of testing in DMA and the actual flexural tests that makes the two comparative.

2.4.4 Conclusions (Creep)

A flexural creep testing apparatus was fabricated to test flexural creep response of neat and reinforced thermoplastics in the non-linear viscoelastic regime. The usage of LVDTs reduces error in measurements due to a coaxial location within the loading assembly. Flexural creep measurements indicate that an increase in reinforcements improves creep resistance while an increase in temperature, stress or both can accelerate the creep process, and the affect of flow orientation remains marginal, and consistent with DMA method. Non-linear viscoelasticity in neat and long fiber reinforced thermoplastics was modeled by a four-parameter model, which gave good mathematical data fits to the experimental data, and shows stress and time-sensitivity of the creep process.

2.5 UV degradation of LFT

2.5.1 Introduction

LFTs are frequently used for outdoor structural applications and are exposed to UV radiation. Hence, it is important to determine the effect of UV exposure on mechanical properties of these materials. LFTs provide enhanced stiffness to the structural part due to the reinforcing fiber. An obvious disadvantage of using these composites in outdoor applications, however, is their susceptibility to environmental degradation especially due to solar radiation. The wavelength of solar radiation ranges from 290-1400 nm. The infrared region (780–1400 nm) comprises approximately 53% of the spectrum, while the visible region (400–780 nm) comprises of about 43% and the ultraviolet (UV) region (290–400 nm) constitutes of 4 % of the total radiation. The energy of a photon is inversely proportional to its wavelength; hence the low wavelength UV region has more energy and thus can be more damaging to the chemical structure of the polymer matrices as compared to the visible light [26]. The photodegradation of polymers depends on external as well as some internal factors. The external factors include wavelength, irradiation time, intensity, temperature, oxygen partial pressure, etc.; while the internal factors include molecular structure of the polymer and its defects, degree of tacticity, fabrication procedure, internal impurities, and specimen thickness. It has been well documented in the literature that polymers degrade through a photo-oxidative reaction which is governed by the diffusion of oxygen [27]. Formation of various chemical groups such as carbonyl, hydroperoxide, carboxylic acid and γ-lactone in the photochemical degradation of polypropylene have been confirmed by previous researchers [28]. Photo-oxidation starts with the absorption of photons by the polymer and subsequent generation of free radicals. The free radicals generated rapidly react with oxygen to form peroxyl radicals. This removes hydrogen atoms from the polymer to form alkyl radicals and hydroperoxide. Hydroperoxide decomposes to alkoxy and hydroxyl. These very reactive radicals further remove hydrogen atoms from the polymer to yield new alkyl radicals [26].

Work has been done previously on the UV degradation of the neat PP [27-32] and some work on the reinforced PP [30]. Most of the past work has focussed on studying the mechanism of photodegradation of PP and related the mechanical property changes with the changes in crystallinity and the surface cracking of the matrix. According to these authors [27-32], chemicrystallization, which is the rearrangement of broken polymer chains into crystalline phase, causes an increase in crystallinity. This was the main mechanism of photodegradation of PP. Chemicrystallization causes surface cracks which is the primary cause for degradation of bulk mechanical properties. Not much work has been done to study the effect of UV exposure on the changes in mechanical properties of the LFT. Also detailed characterization of the mechanical properties of the degraded surface layer, formed due to UV exposure, has not been done. The aim of the current work was to investigate the effect of UV exposure on the mechanical properties of LFT (E-glass (20 vol. %)/PP) produced by the extrusion-compression molding process. In particular, we studied the local changes taking place in the mechanical properties of the degraded layer formed due to UV exposure by nanoindentation and Fourier Transform Infrared (FTIR) spectroscopy.

2.5.2 Results (UV)

2.5.2.1 Visual appearance

The visual appearance of the LFT beams changed as a result of UV exposure. The color of the exposed surface changed from light green to chalky white (Fig. 2.5-1). Surface damage in the form of matrix loss and extensive fiber exposure can be seen.

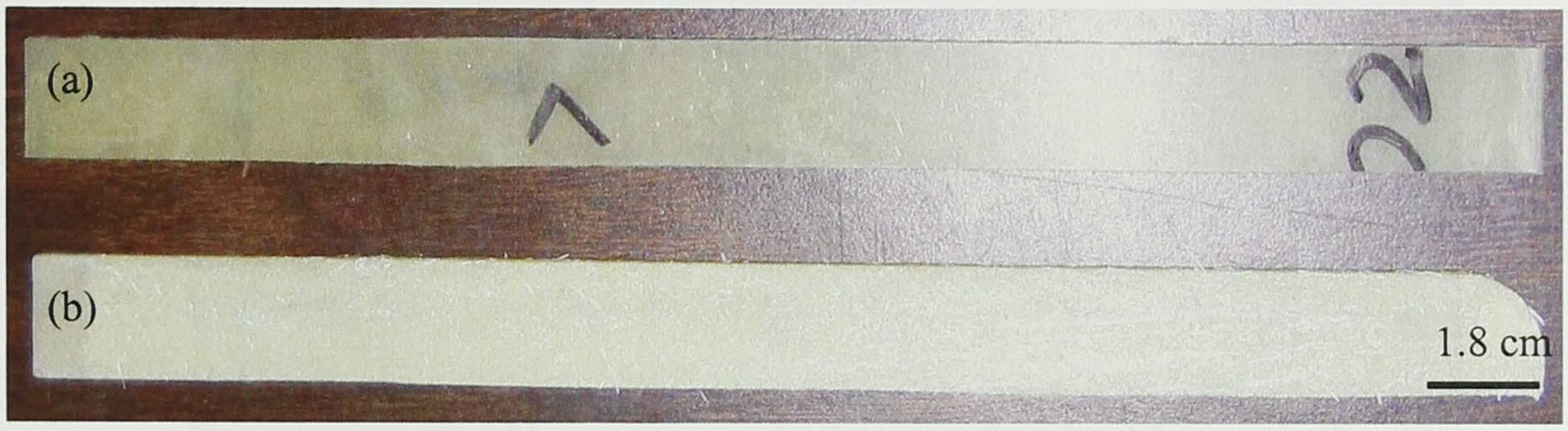

Figure 2.5- 1 (a) Unexposed beam and (b) UV exposed beam. Damage caused by UV can be seen in the form of many fibers exposed at the surface.

2.5.2.2 Optical Microscopy

Images of the polished cross section of the UV exposed LFT at different stages of exposure are shown in Figs. 2.5-2 – 2.5-4. The damage progression can be easily seen. From these micrographs the difference in contrast between the degraded layer and the unexposed layer is evident. The difference in contrast is indicative of the changes taking place in the matrix due to UV exposure. The increase in crack density with the exposure time can also be seen.

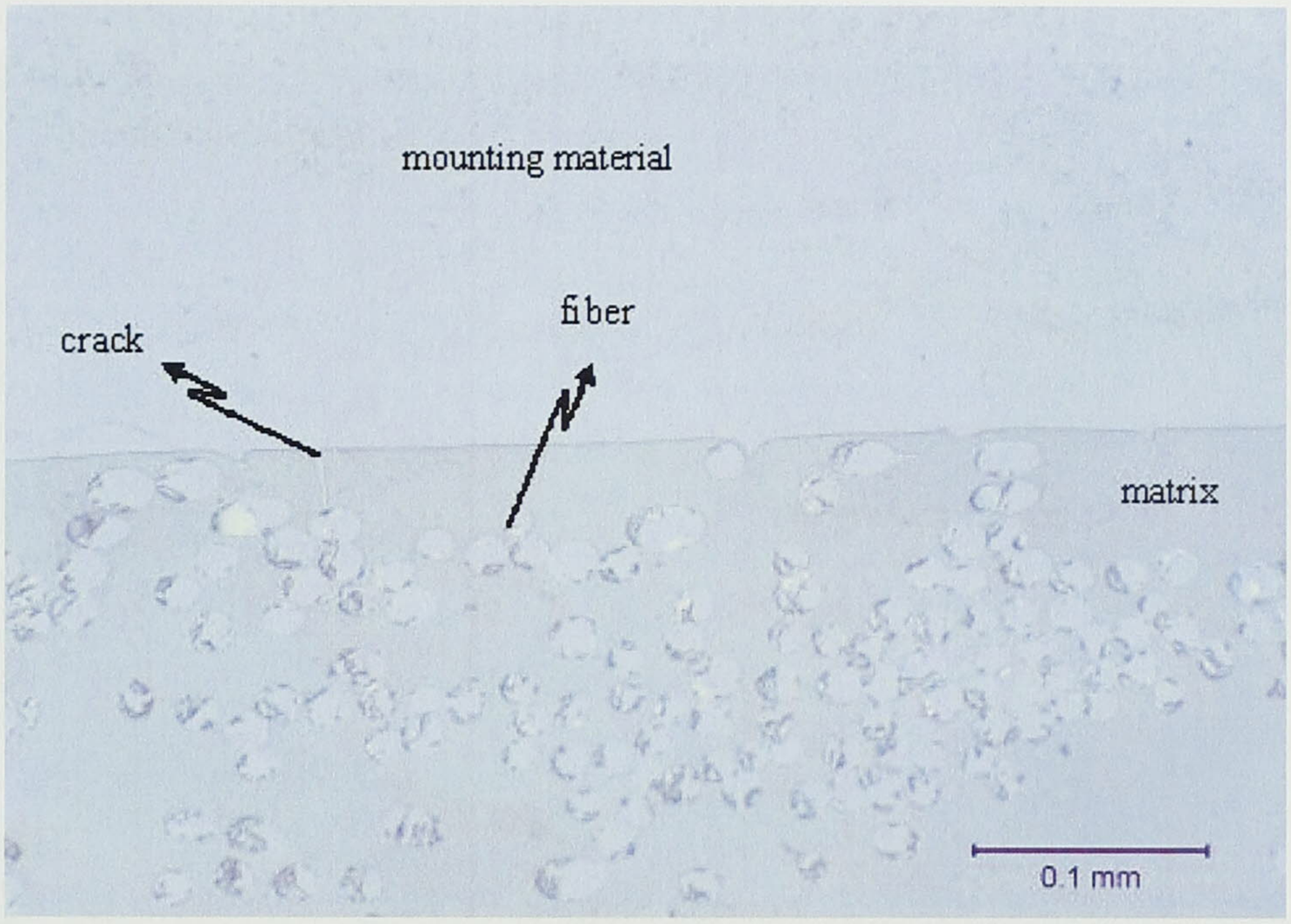

Figure 2.5- 2 Image of the polished cross-section of the LFT exposed to UV for 100 hours. Surface cracks begins to form.

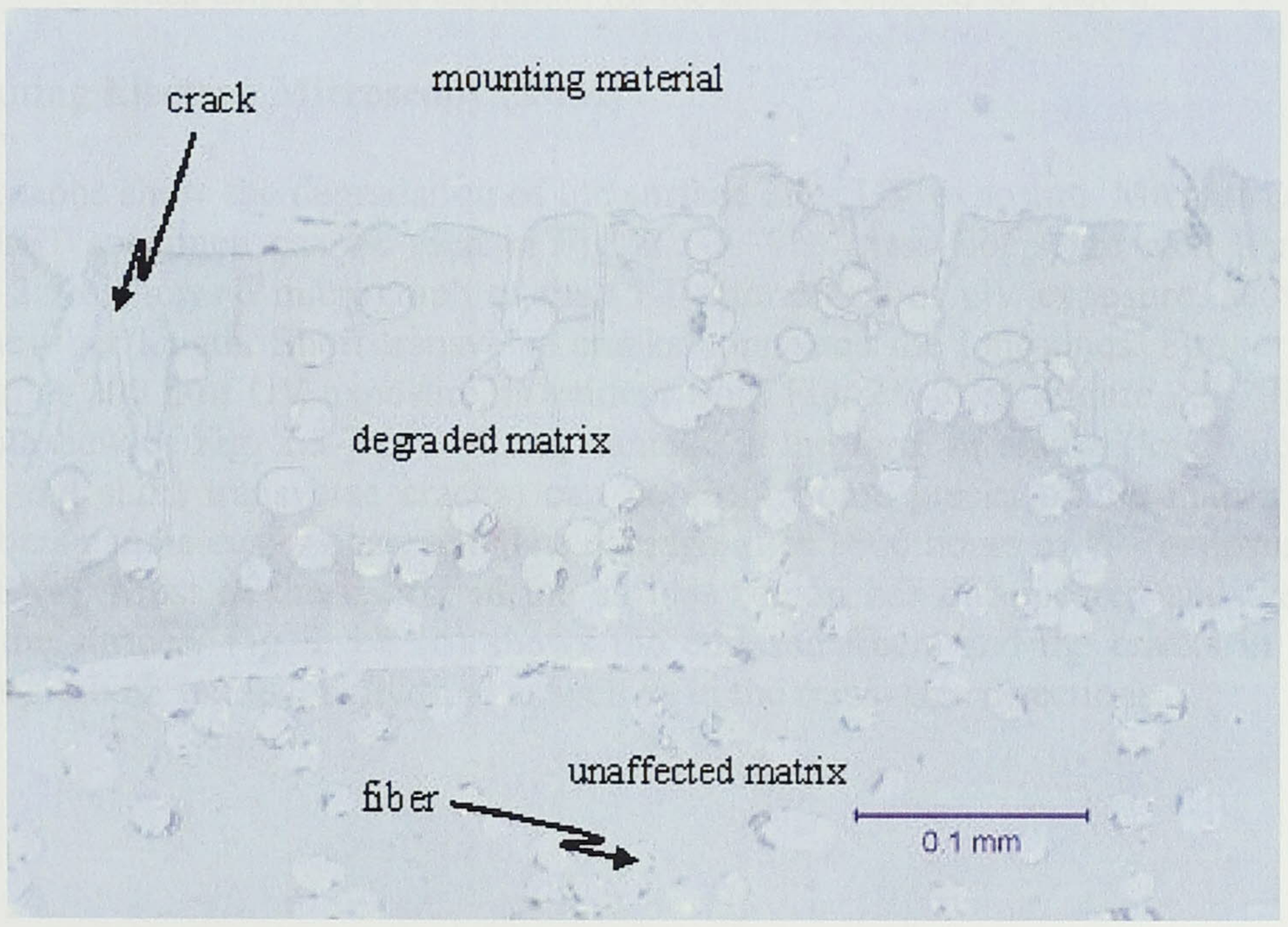

Figure 2.5- 3 Image of the polished cross-section of the LFT exposed to UV for 400 h. Degraded matrix layer can be easily seen due to easily distinguishable contrast between the degraded layer and the unaffected layer. Surface crack density increases as compared to the density at 100 h.

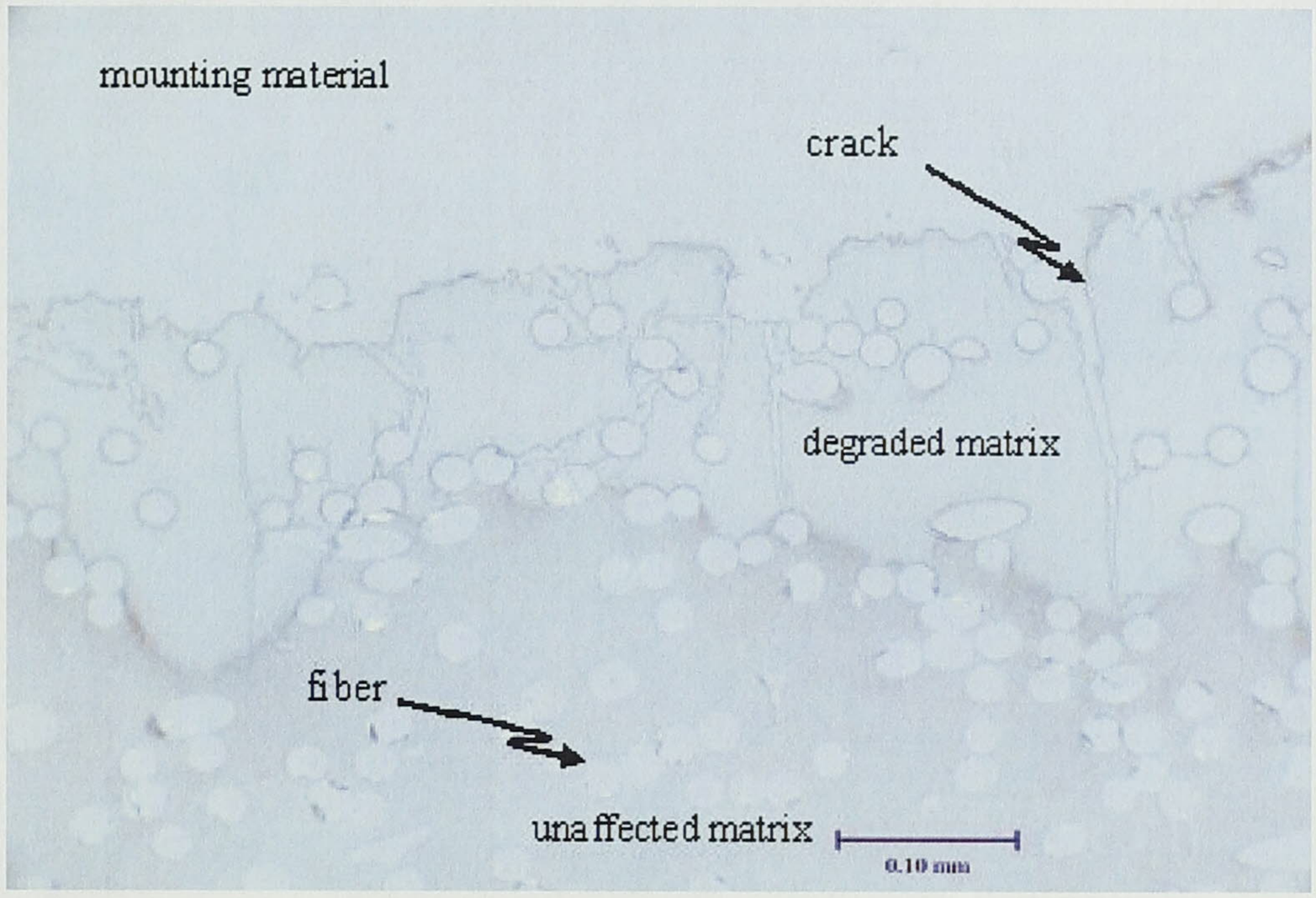

Figure 2.5- 4 Image of the polished cross-section of the LFT exposed to UV for 1600 h. Surface crack density is the maximum for the sample exposed for 1600 h.

2.5.2.3 Scanning Electron Microscopy (SEM)

SEM micrographs show the degradation of the surface after UV exposure. Microstructure of the unexposed LFT specimen can be seen in Fig. 2.5-5. The glass fibers are well bonded to the matrix. Fig. 2.5-6 shows a micrograph of the LFT after 100 h of UV exposure. Most of cracks ran along the fiber length. Short transverse cracks connected the long ones. Further damage in the matrix, after 200 h of UV exposure, is evident from Fig. 2.5-7 (a). Figure 2.5-7 (b) is a high magnification view of Fig. 2.5-7 (a). Matrix damage in the form of cracks (long ones along the fiber length and short transverse cracks) can be seen. Some pieces of the matrix as well as debonded fibers can be easily observed. The damage after 1600 hours of UV exposure is shown in Fig. 2.5-8 (a). Most of the matrix in the surface region has disappeared and the fibers are exposed to the surface. Fig. 2.5-8 (b) shows the exposed fibers and the cracks in the matrix. These cracks are both in the longitudinal as well as in the transverse directions.

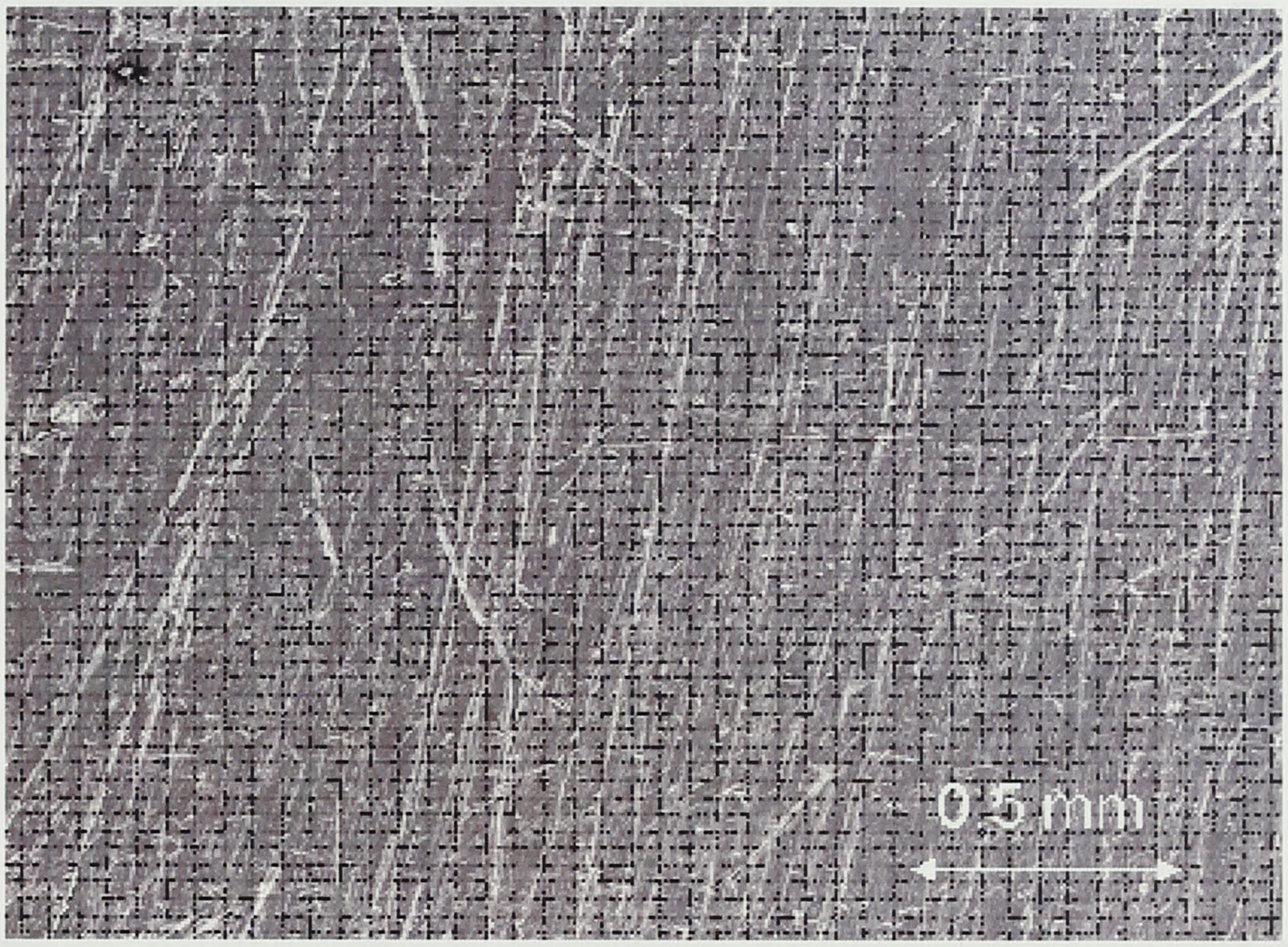

Figure 2.5- 5 LFT unexposed to UV radiation. Glass fibers are well bonded with the matrix.

Figure 2.5- 6 LFT exposed for 100 h. Most of cracks run along the fiber length. Short transverse cracks connect the long ones.

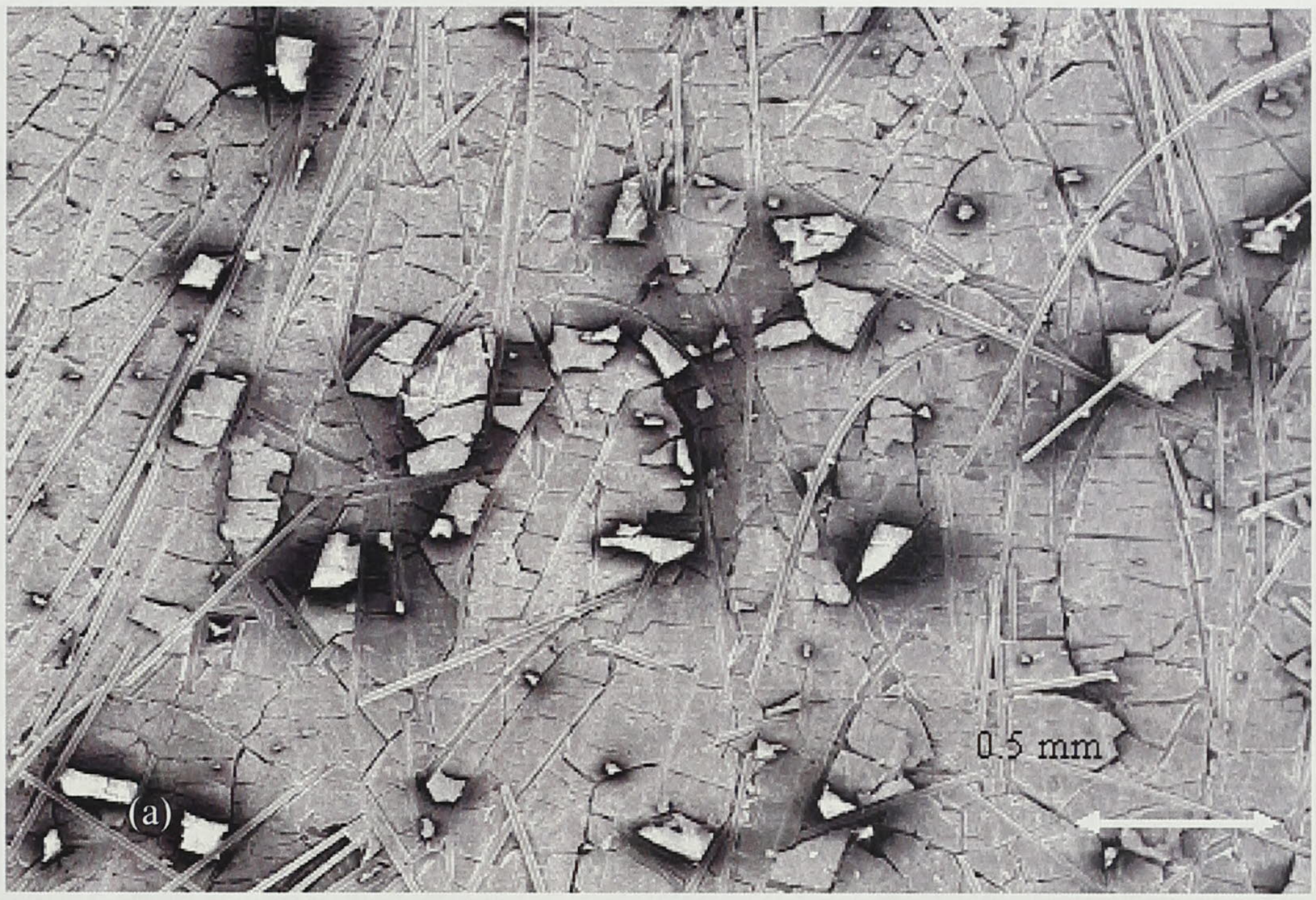

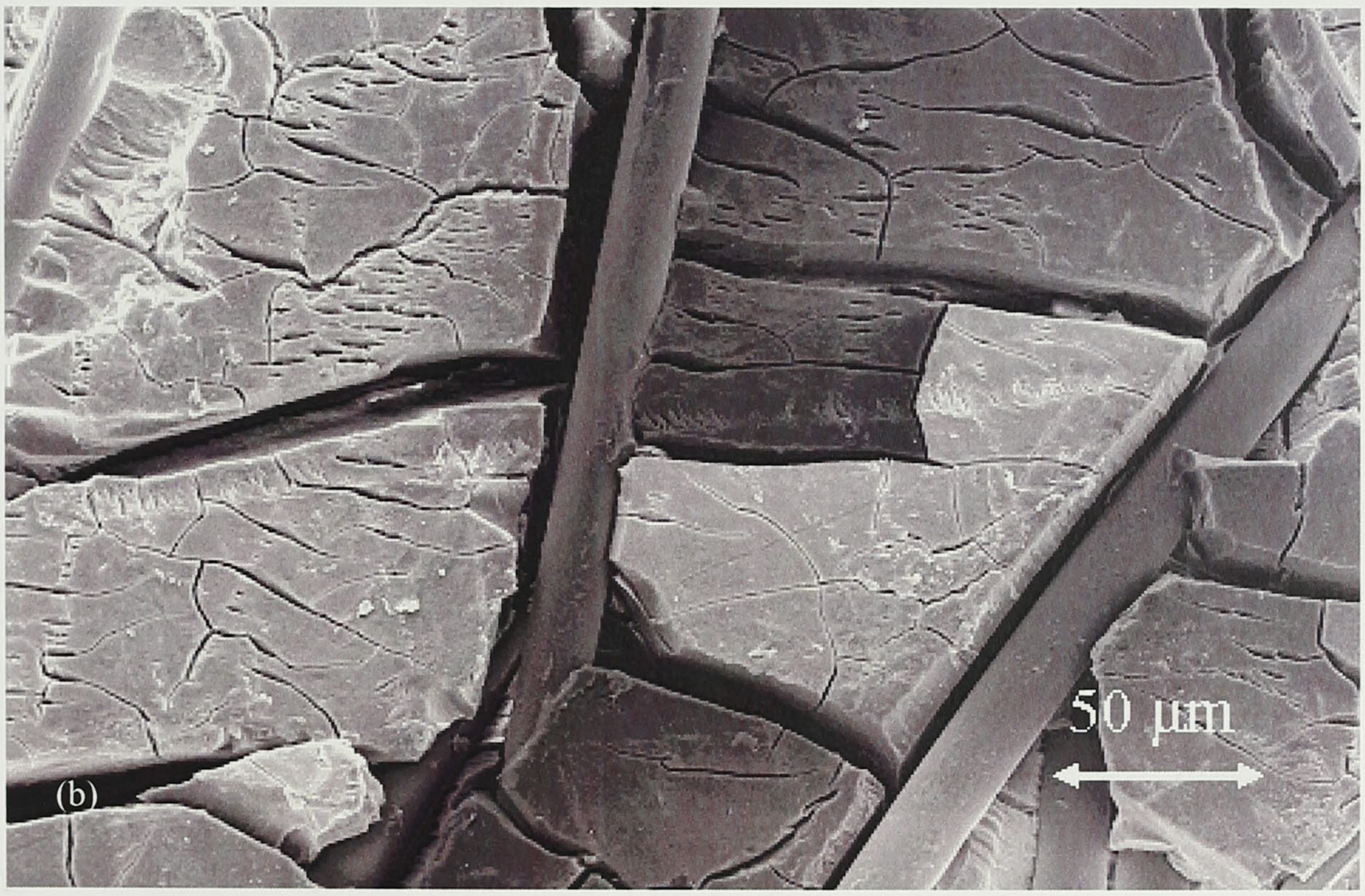

Figure 2.5- 7 (a): LFT exposed for 200 hours in UV radiation. Matrix damage in the form of cracks (long ones along the fiber length and short transverse cracks) can be seen, (b): An area of (a) at higher magnification.

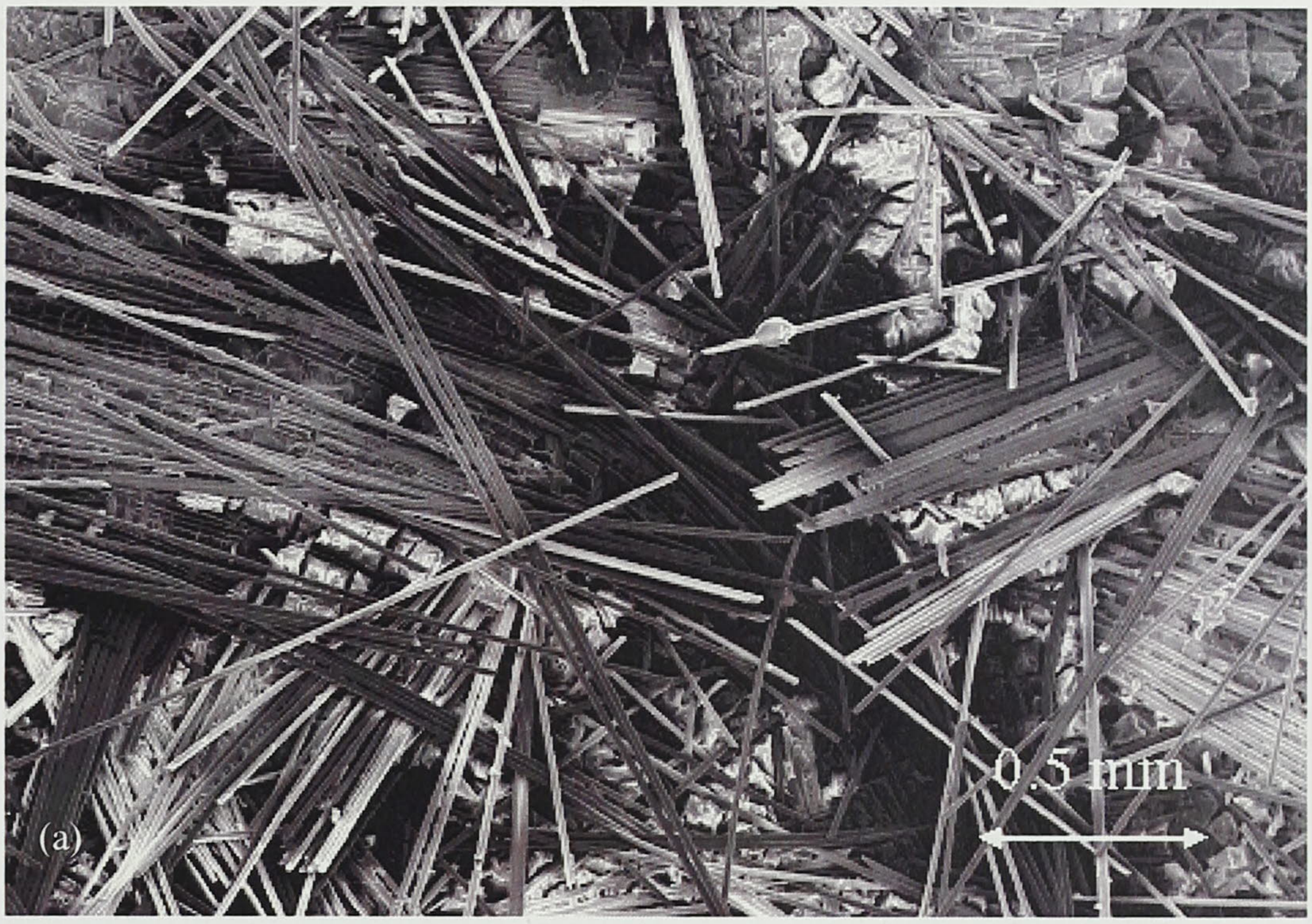

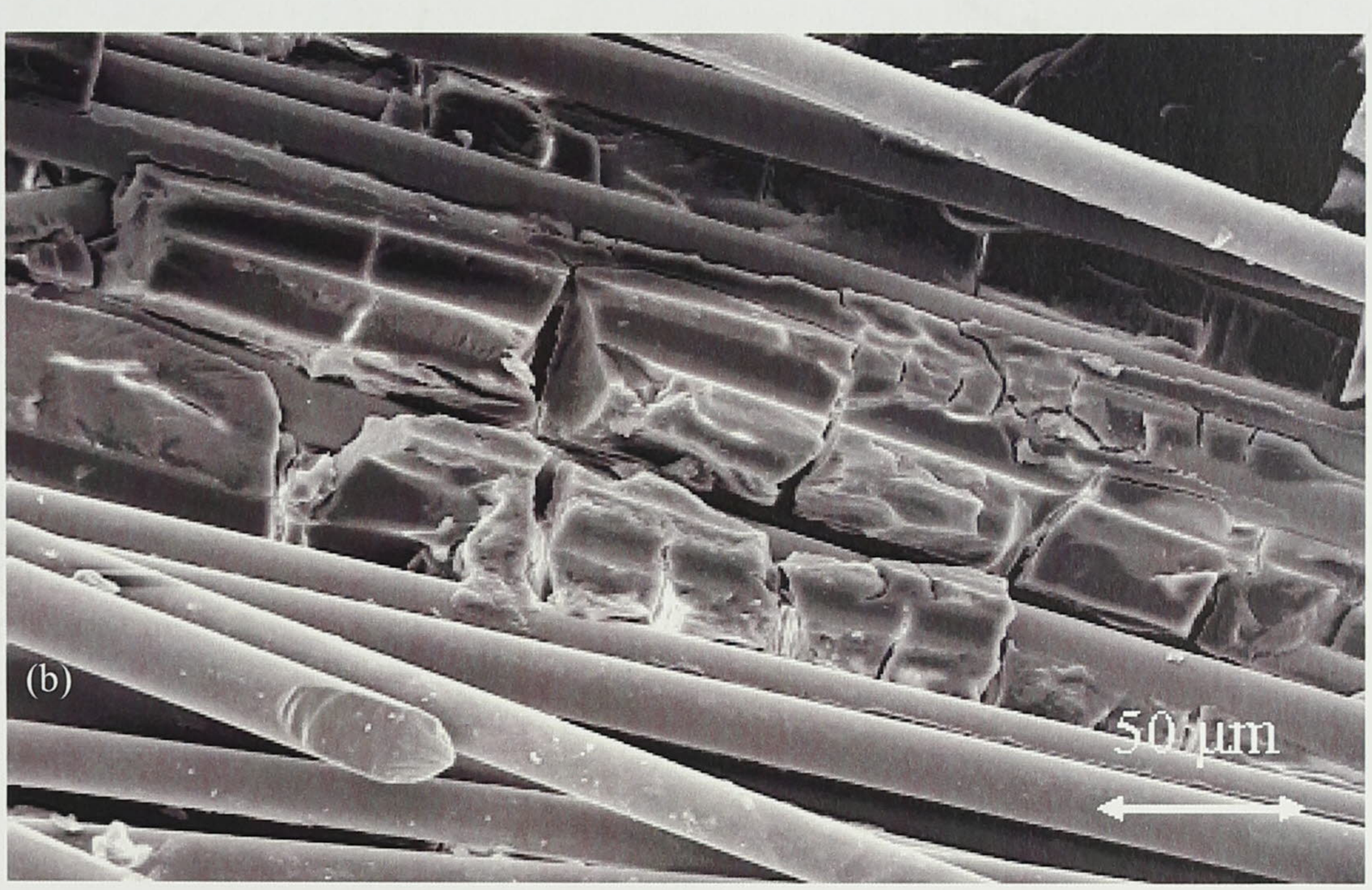

Figure 2.5- 8 (a): LFT exposed for 1600 hours in UV radiation. Most of the matrix in the surface region has disappeared and exposed fibers can be seen, (b): LFT exposed for 1600 hours in UV light at higher magnification. The cracks present in the matrix and the exposed fibers can be seen clearly.

2.5.2.4 Nanoindentation

An optical micrograph of the cross-section of the LFT exposed to LFT for 1600 hours is shown in Fig. 2.5-9. The nanoindentation was done at different depths from the surface both in the degraded as well as the unexposed region.

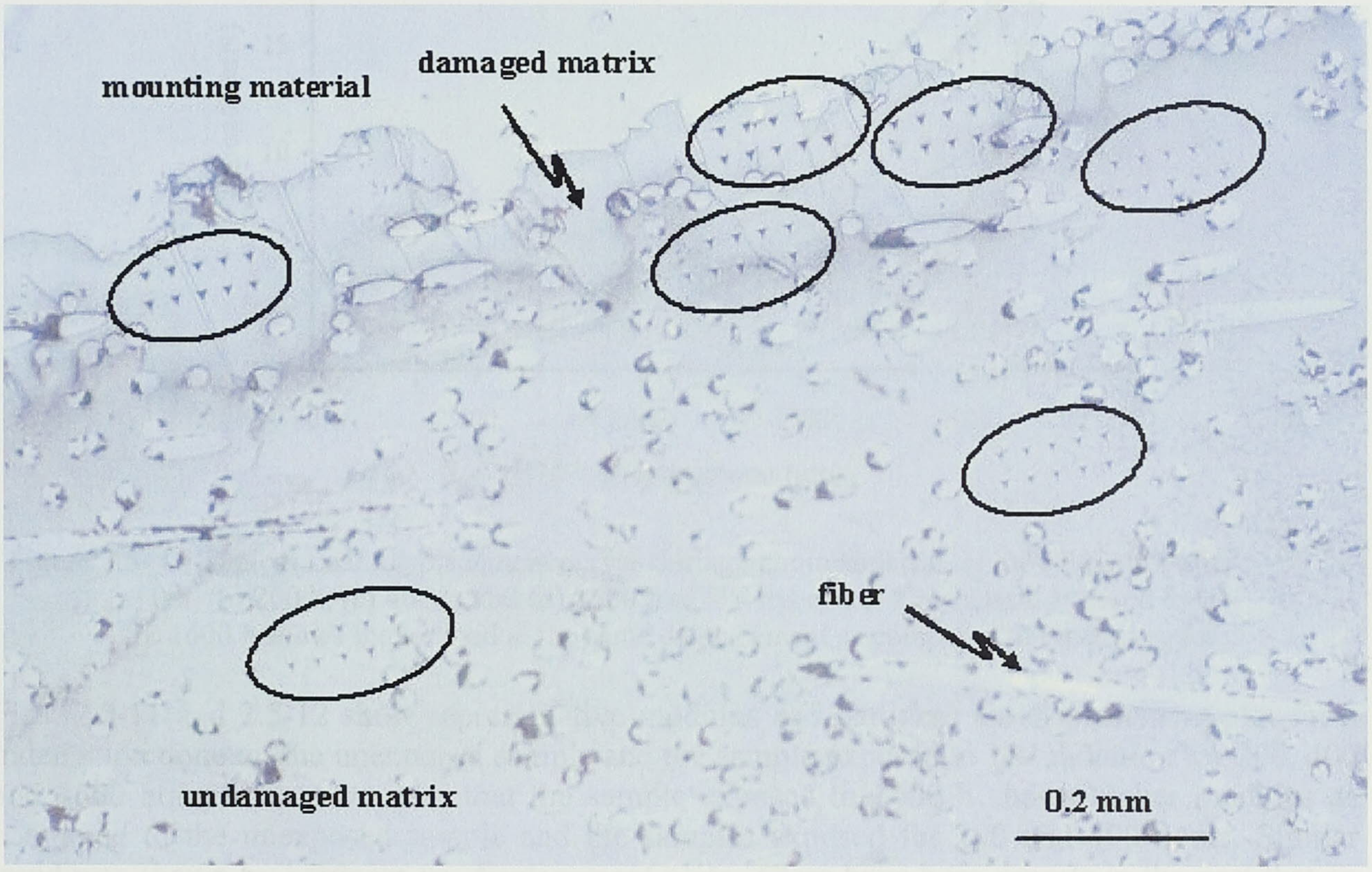

Figure 2.5- 9 Image of the polished cross-section of the LFT exposed to UV for 1600 hours with nanoindentation marks on it (encircled). Several indentations were done at varying distances from the surface.

Fig. 2.5-10 shows typical load-displacement curves of the PP matrix. The sample exposed to UV for 1600 h shows higher load at the same displacement as compared to the samples exposed to UV for lesser time.

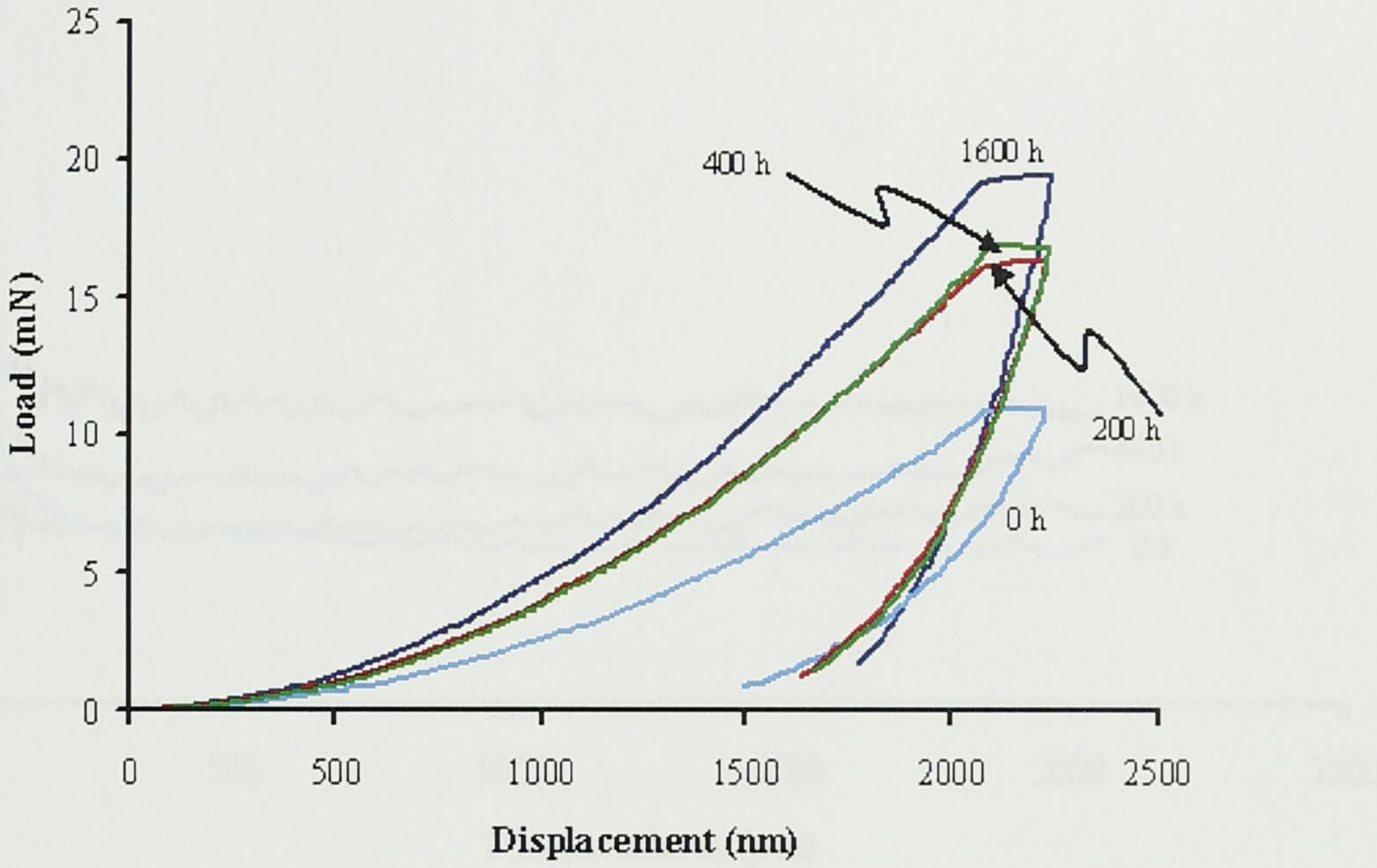

Figure 2.5- 10 Typical Load-displacement curves during nanoindentation of the PP matrix after (a) 0 h, (b) 200 h, (c) 400 h, and (d) 1600 h of UV exposure. The sample exposed to UV for 1600 h shows higher load at the same displacement as compared to other samples.

Figs. 2.5-11 and 2.5-12 show representative modulus and hardness vs. displacement plot for a indentation done on the unexposed sample and the sample exposed to UV radiation for 200, 400 and 1600 hours. It can be seen that the sample exposed to 1600 h shows higher modulus as compared to the unexposed sample and the samples exposed for 200 and 400 hours. Similar trend was shown by hardness vs. displacement plots. There have been reports in the past that an accurate estimation of modulus of polymers could be difficult by nanoindentation since the polymers are soft and the material response cannot be measured due to low system compliances. And also that since all the analysis is based on elasticity, which when applied to viscoelastic materials could lead to large uncertainties in the calculated values of modulus [33, 34]. The results here are useful to indicate relative change in mechanical properties of LFT due to UV exposure for different times.

Figs. 2.5-13 and 2.5-14 show the modulus and hardness vs. distance from the surface plot. Each point in the plot is the average of ten indentations done on the matrix, at a given distance from the surface. It can be seen from the plots that at a given distance, the sample exposed to UV for more time has higher modulus and hardness values as compared to the samples exposed for lesser time. But, as we go deeper into the sample the modulus and hardness for all the samples shows similar values. Thus, it is evident that the damage layer formed due to UV degradation is confined, only, to few hundred micrometers from the surface while the material underneath the degraded layer remained unaffected.

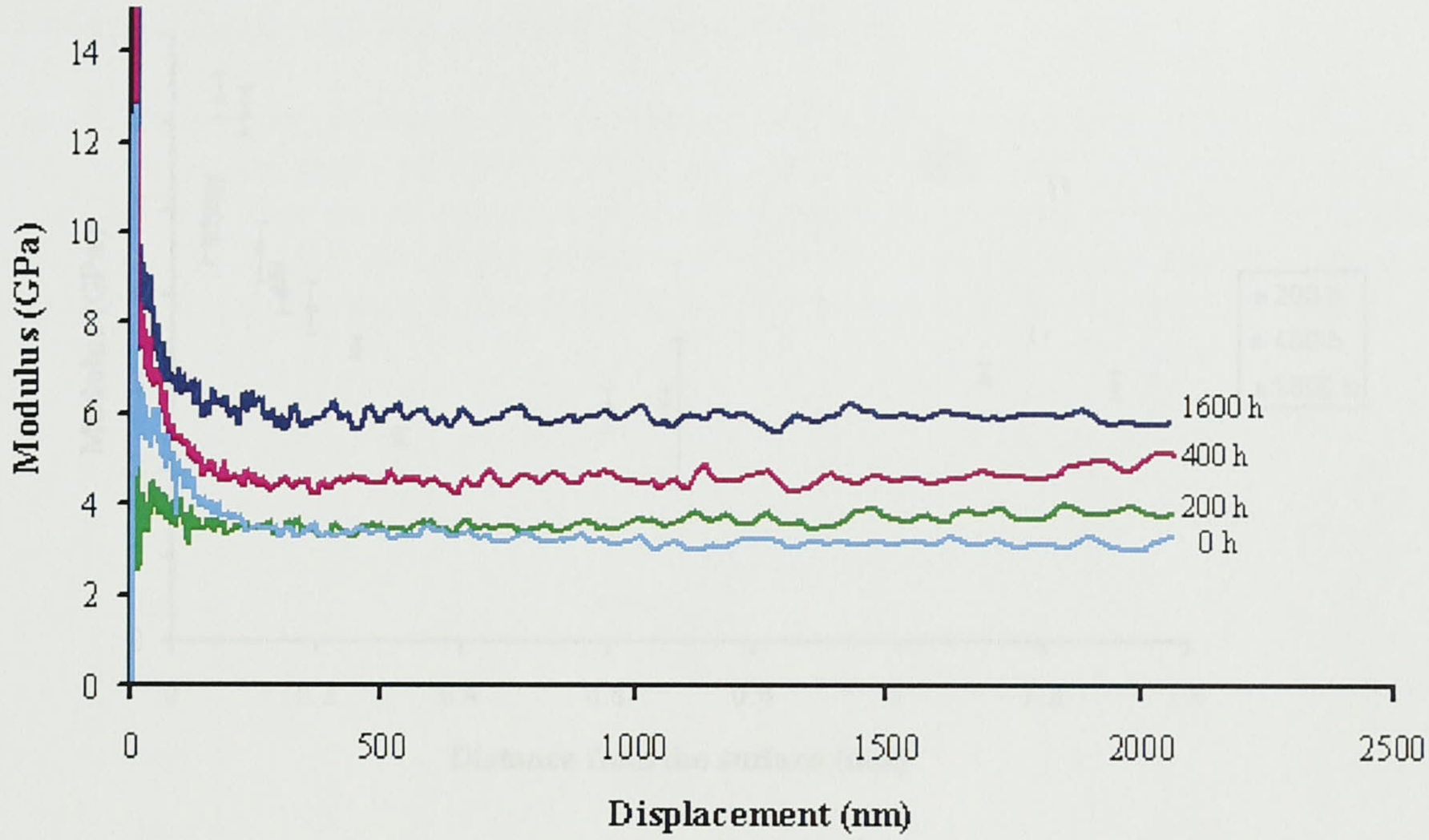

Figure 2.5- 11 A representative modulus vs. displacement curves for indentation done on the degraded region of the LFT sample exposed to UV radiation for (a) 200 h, (b) 400 h, and (c) 1600 h. The curve for indentation done on the unexposed sample (0 h) is also shown. It can be seen that the sample exposed to 1600 h shows the highest modulus.

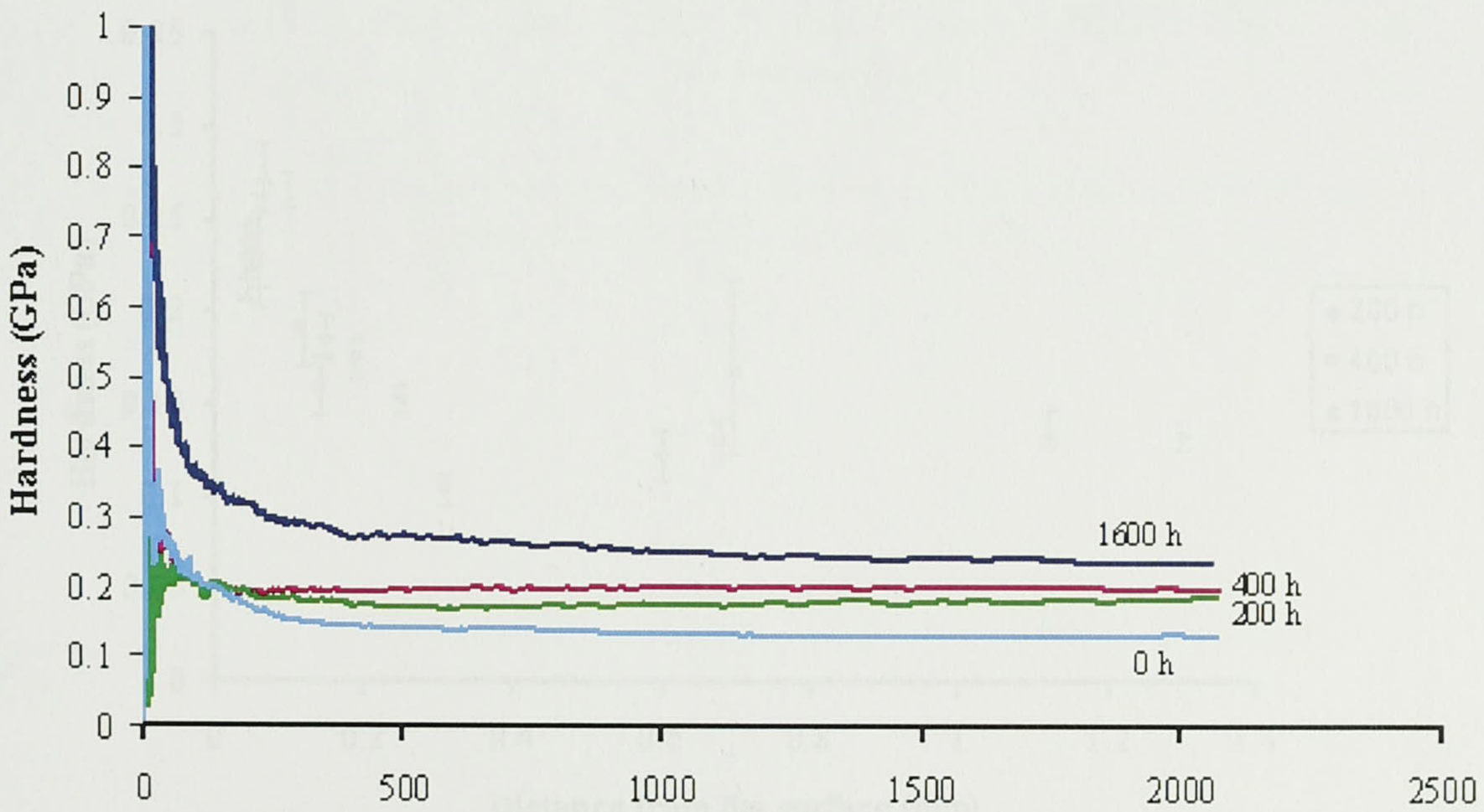

Figure 2.5- 12 A representative hardness vs. displacement curves for indentation done on the degraded region of the LFT sample exposed to UV radiation for (a) 200 h, (b) 400 h, and (c) 1600 h. The curve for indentation done on the unexposed sample (0 h) is also shown. It can be seen that the sample exposed to 1600 h shows the maximum hardness.

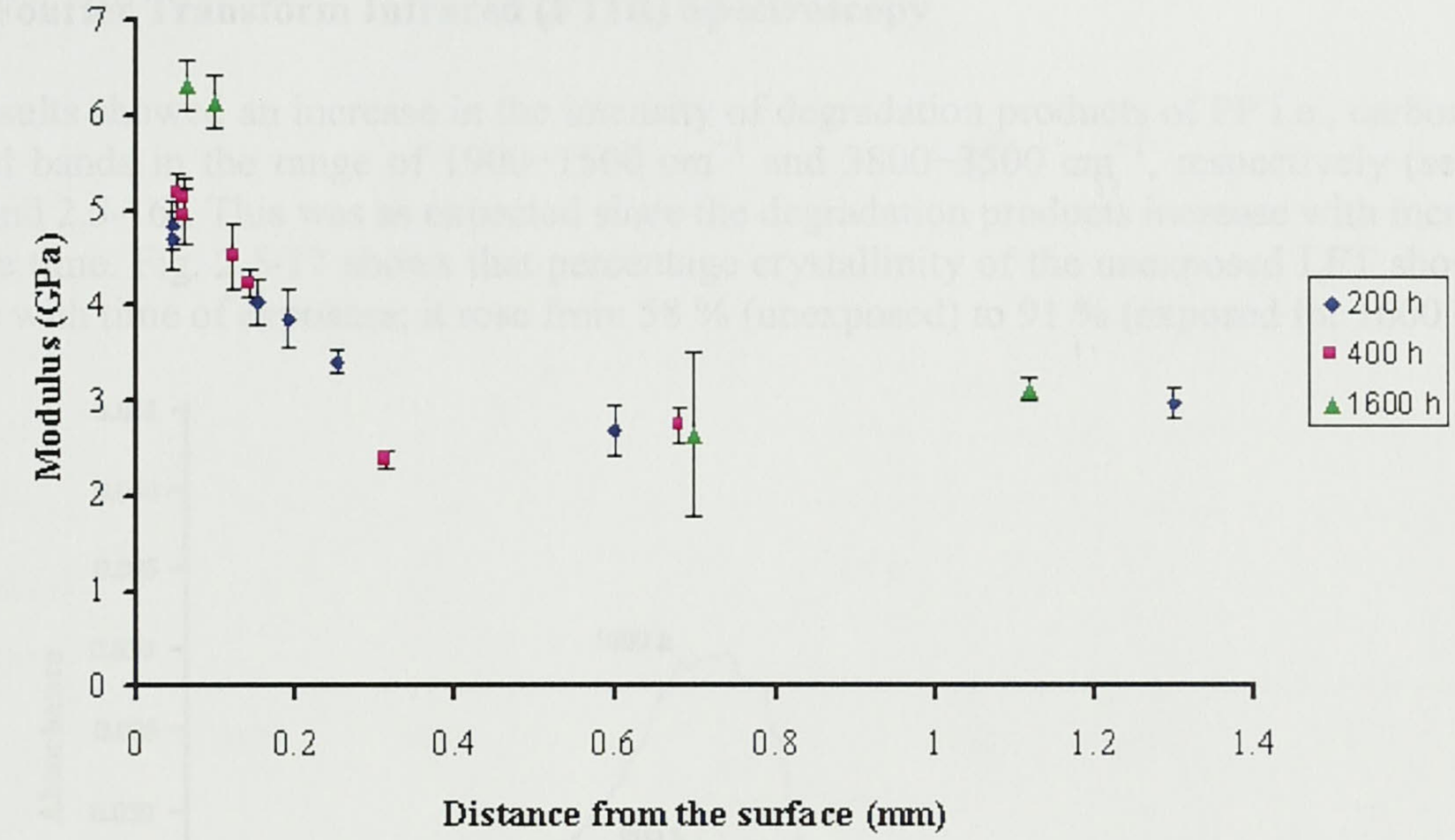

Figure 2.5- 13 Modulus vs. distance from the surface plots for the samples exposed to UV for (a) 200 h, (b) 400 h, and (c) 1600 h. Modulus was determined, for each indentation, from plots looking similar to Fig. 2.5-11. Each point in the plot is the average modulus of ten indentations done on the matrix, at a given distance from the surface. Near the surface, the higher the exposure time, the higher the modulus.

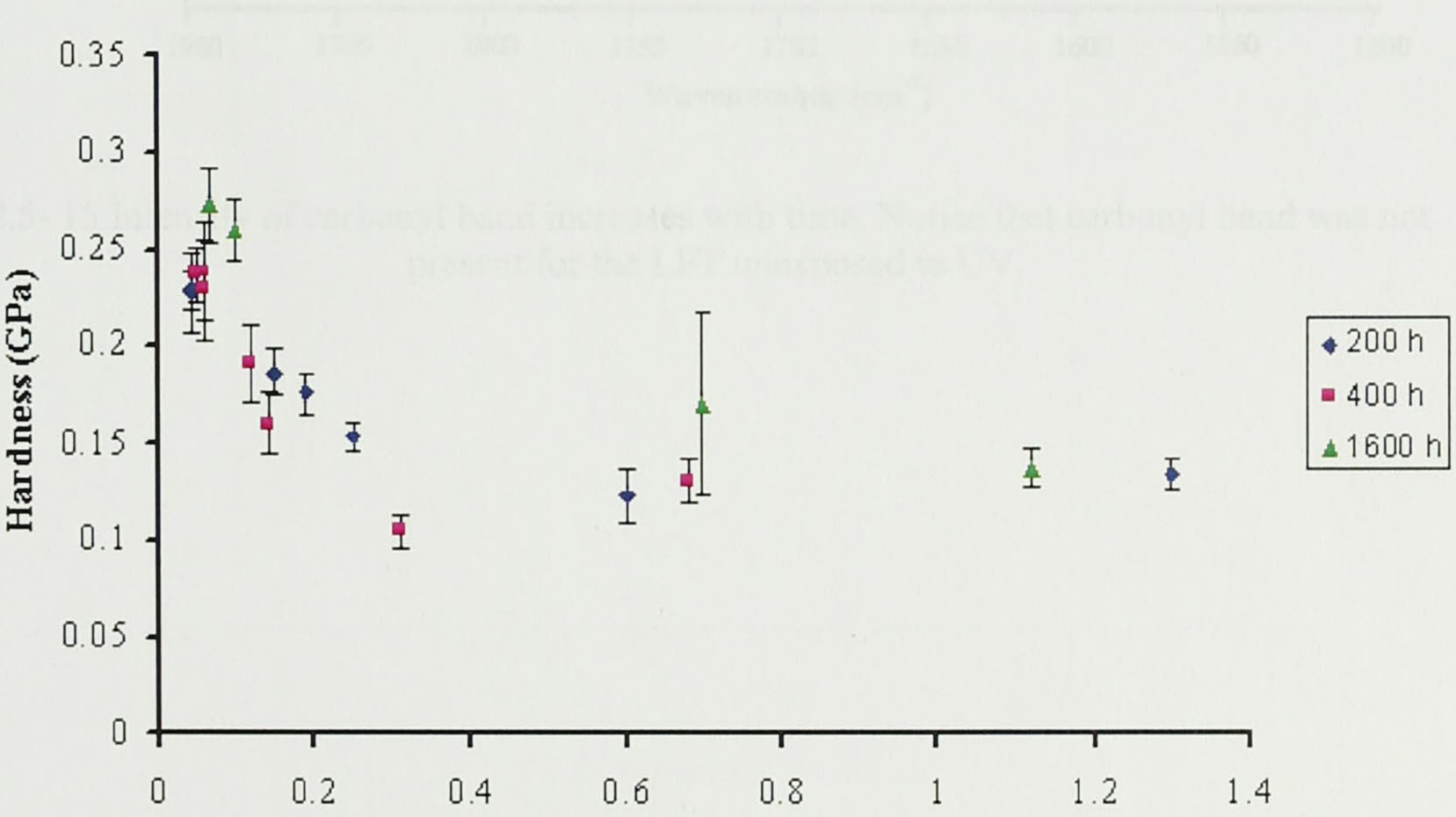

Figure 2.5- 14 Hardness vs. distance from the surface plots for the samples exposed to UV for (a) 200 h, (b) 400 h, and (c) 1600 h. Hardness was determined, for each indentation, from plots looking similar to Fig. 2.5-12. Each point in the plot is the average modulus of ten indentations done on the matrix, at a given distance from the surface. Near the surface, the higher the exposure time, the higher the hardness.

2.5.2.5 Fourier Transform Infrared (FTIR) Spectroscopy

FTIR results showed an increase in the intensity of degradation products of PP i.e., carbonyl and hydroxyl bands in the range of 1900−1500 cm^{-1} and 3800−3500 cm^{-1}, respectively (see Figs. 2.5-15 and 2.5-16). This was as expected since the degradation products increase with increase in exposure time. Fig. 2.5-17 shows that percentage crystallinity of the unexposed LFT showed an increase with time of exposure; it rose from 58 % (unexposed) to 91 % (exposed for 1600 h).

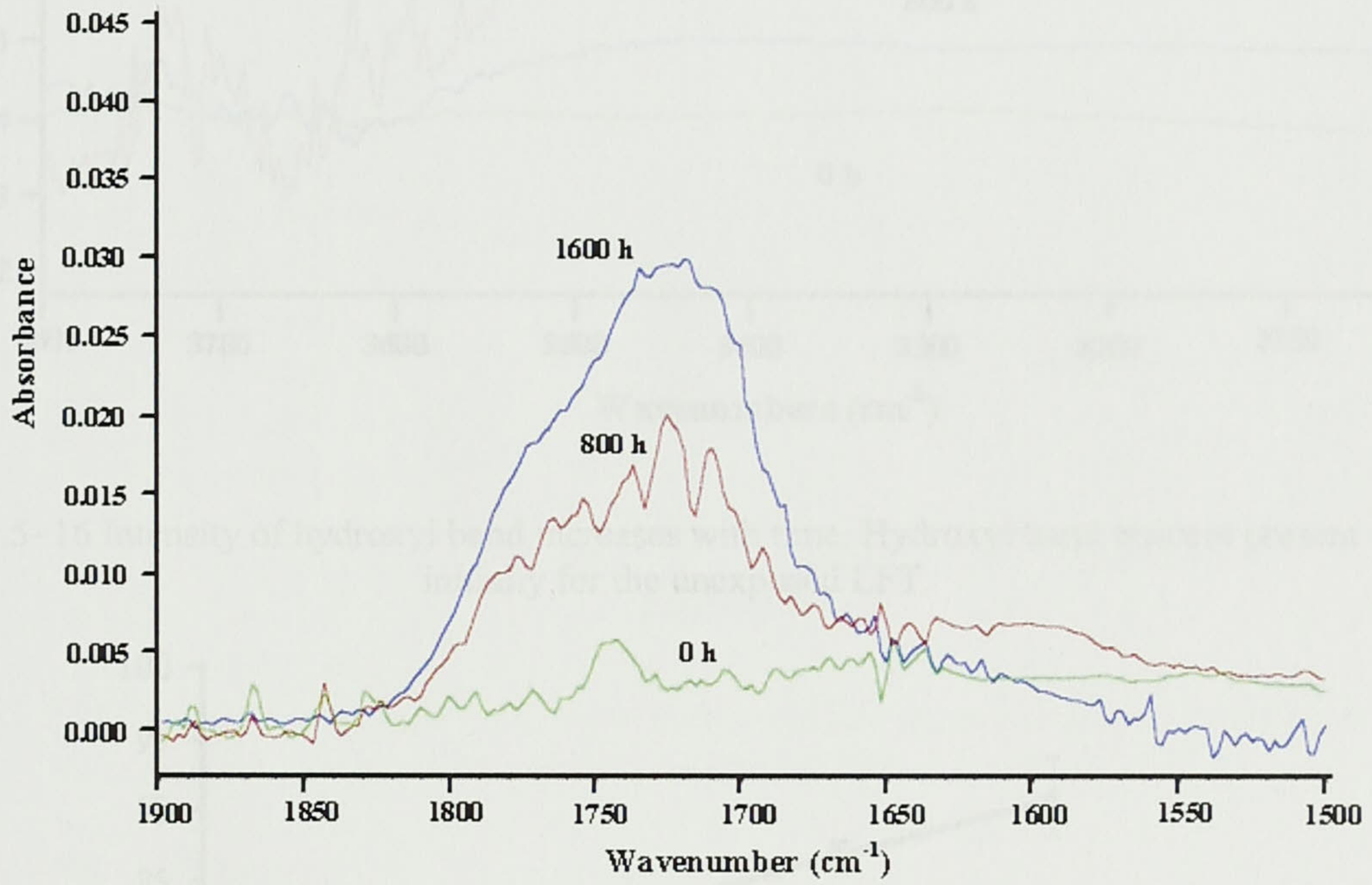

Figure 2.5- 15 Intensity of carbonyl band increases with time. Notice that carbonyl band was not present for the LFT unexposed to UV.

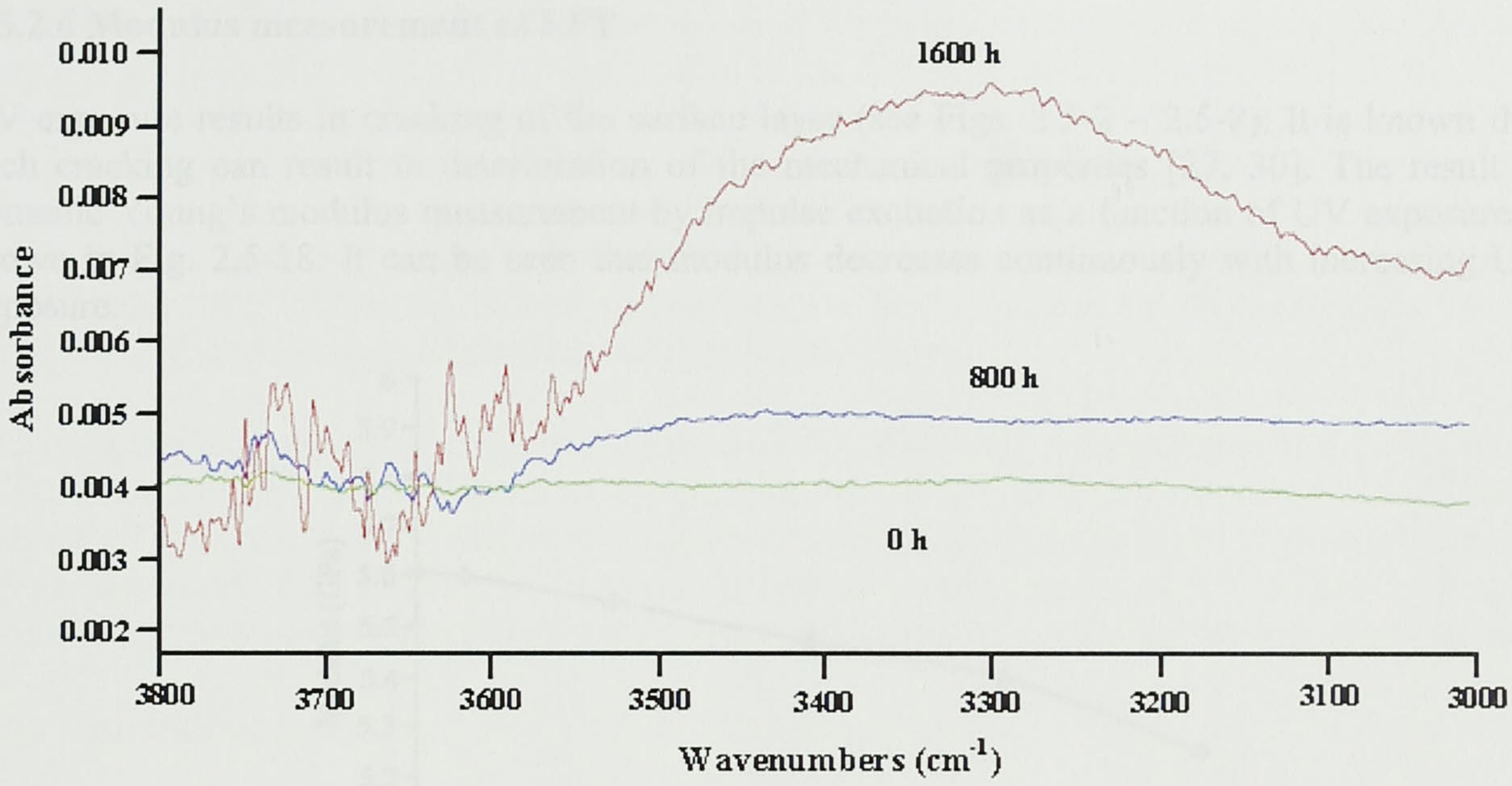

Figure 2.5- 16 Intensity of hydroxyl band increases with time. Hydroxyl band was not present initially for the unexposed LFT.

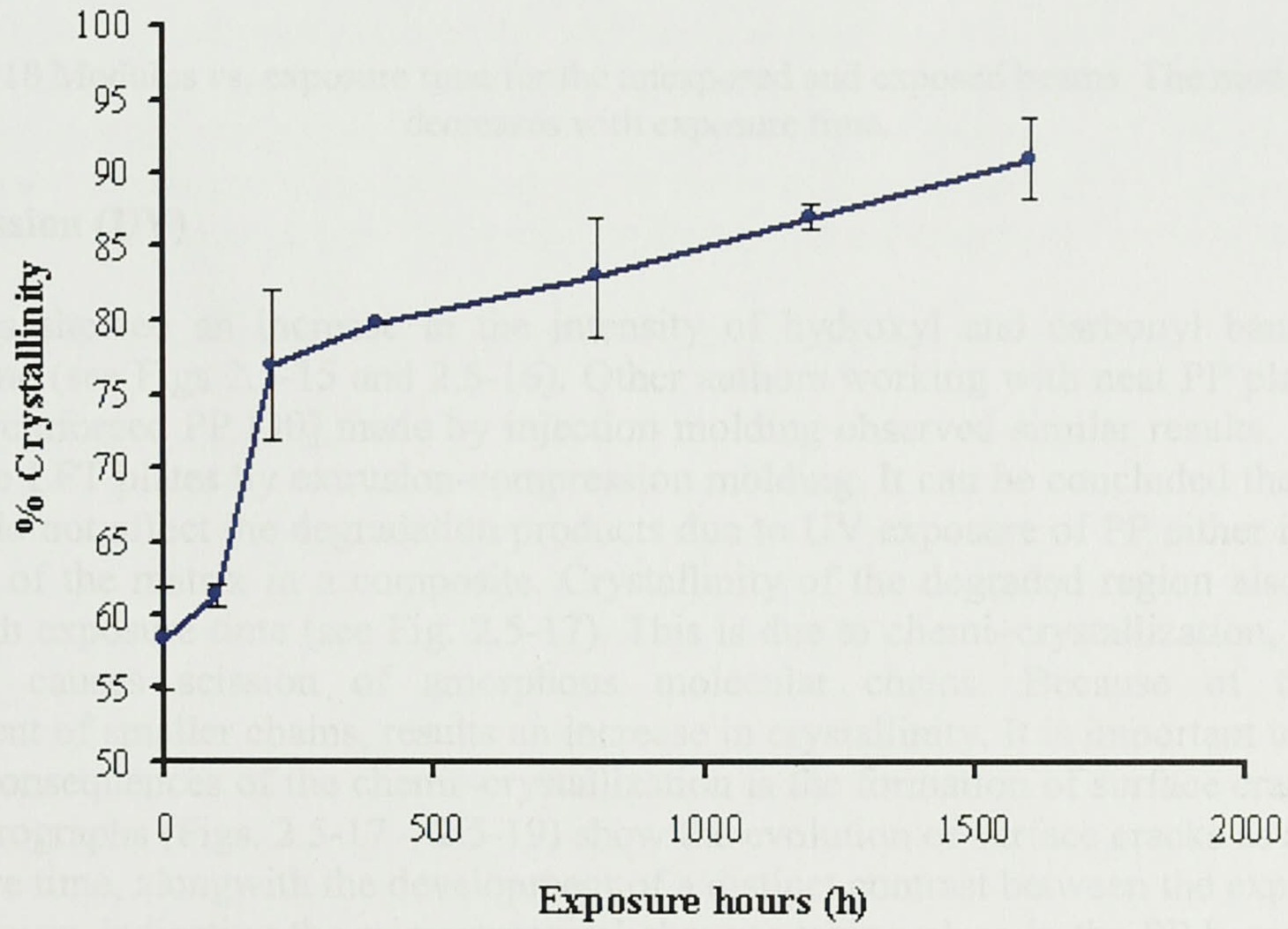

Figure 2.5- 17 Crystallinity increases with UV exposure time.

2.5.2.6 Modulus measurement of LFT

UV exposure results in cracking of the surface layer (see Figs. 2.5-2 – 2.5-8). It is known that such cracking can result in deterioration of the mechanical properties [27, 30]. The result of dynamic Young's modulus measurement by impulse excitation as a function of UV exposure is shown in Fig. 2.5-18. It can be seen that modulus decreases continuously with increasing UV exposure.

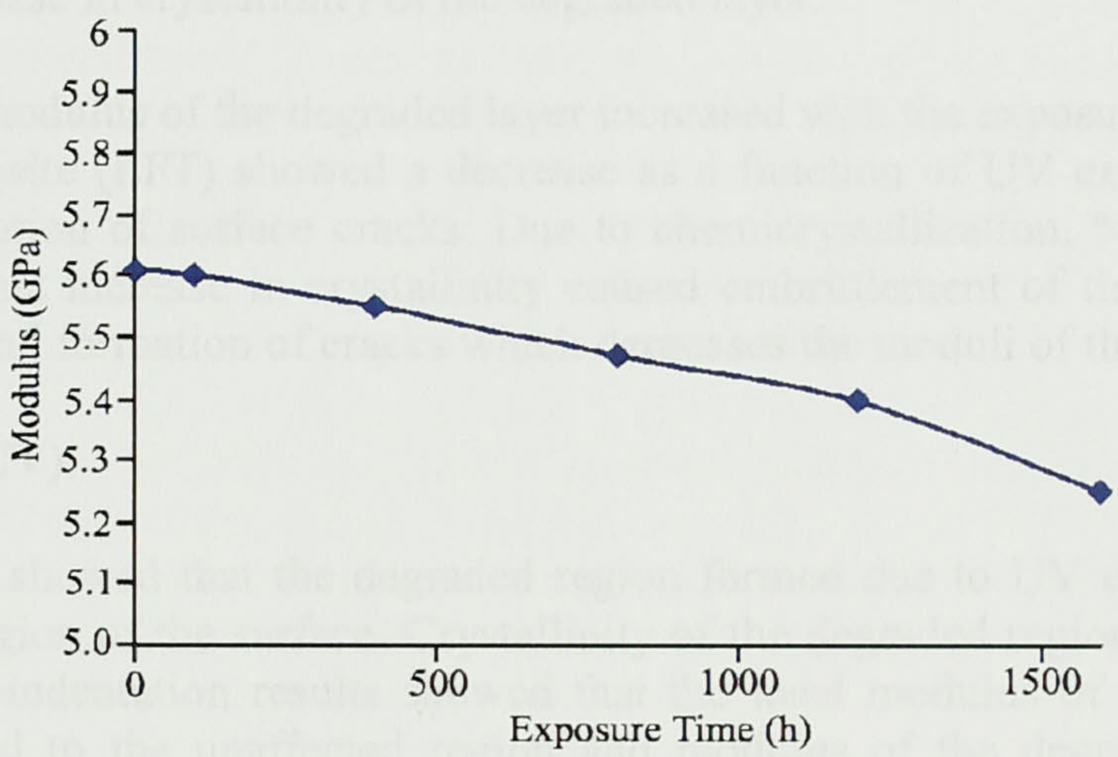

Figure 2.5- 18 Modulus vs. exposure time for the unexposed and exposed beams. The modulus decreases with exposure time.

2.5.3 Discussion (UV)

FTIR results showed an increase in the intensity of hydroxyl and carbonyl bands with UV exposure time (see Figs 2.5-15 and 2.5-16). Other authors working with neat PP plates [35] and glass-fiber reinforced PP [30] made by injection molding observed similar results. In this work we made the LFT plates by extrusion-compression molding. It can be concluded that processing conditions do not affect the degradation products due to UV exposure of PP either in neat PP or in the form of the matrix in a composite. Crystallinity of the degraded region also showed an increase with exposure time (see Fig. 2.5-17). This is due to chemi–crystallization, wherein UV degradation causes scission of amorphous molecular chains. Because of the ease of rearrangement of smaller chains, results an increase in crystallinity. It is important to realize that one of the consequences of the chemi–crystallization is the formation of surface cracks [29, 30]. Optical micrographs (Figs. 2.5-17 – 2.5-19) show the evolution of surface cracks as a function of UV exposure time, alongwith the development of a distinct contrast between the exposed and the unaffected layer, indicating the microstructural changes taking place in the PP based LFT. SEM micrographs also (see Figs. 2.5-5 – 2.5-8) show the changes taking place on the surface of LFT beam due to UV exposure. Surface cracks along with the fibers exposed on the surface were observed.

The UV degraded regions of the samples exposed for larger time showed higher modulus and hardness than the ones exposed for lesser times (Figs. 2.5-11 – 2.5-12). From Figs. 2.5-13 – 2.5-14 we see that the samples exposed for 1600 h showed the highest modulus and hardness. As the distance from the surface increased the modulus and hardness values attained plateaus of 2.5 GPa and 0.12 GPa, respectively. These results show that the damage due to UV is confined only to thin surface region of thickness between 100 and 200 μm. Thus, results of nanoindentation corroborated the FTIR results indicating that increase in modulus of the degraded layer can be attributed to the increase in crystallinity of the degraded layer.

Although, the local modulus of the degraded layer increased with the exposure time, the modulus of the overall composite (LFT) showed a decrease as a function of UV exposure time. This is because of the formation of surface cracks. Due to chemicrystallization, % crystallinity of the sample increased. This increase in crystallinity caused embrittlement of the surface leading to surface contraction and formation of cracks which decreases the moduli of the overall composite.

2.5.4 Conclusions (UV)

Optical micrographs showed that the degraded region formed due to UV exposure was mostly confined to a thin region of the surface. Crystallinity of the degraded region increased with UV exposure time. Nanoindentation results showed that the local modulus of the degraded region was higher compared to the unaffected region and modulus of the degraded region showed higher values for the samples exposed for longer time. Nanoindentation results showed a good correlation with FTIR results since increase in modulus can be directly attributed to an increase in crystallinity of the degraded region. Although, the local modulus of the degraded layer increased with the exposure time, the modulus of the overall composite (LFT) showed a decrease as a function of UV exposure time. This was attributed to the formation of surface cracks.

2.6 Characterization of candidate thermoplastic materials for the AC door

2.6.1 Introduction (AC door)

Three candidate materials were screened during this phase of the project. The main objective of this task being to experimentally determine the mechanical properties of the candidate materials (TPO, Azdelite, Quadrant Symalite), and to generate a comprehensive material database which later could be used in the design process of the AC cover and other thermoplastic composite components. Thermoplastic Polyolefin (TPO) supplied by Solvay polymers, Azdelite (ref SL551400.109) supplied by Azdel, and Quadrant Symalite (SL100G5516T16S1) supplied by Quadrant composites were tested in accordance to ASTM D638-03 (standard test method for tensile properties of plastics), D790-03 Standard Test Methods for Flexural Properties of Unreinforced and Reinforced Plastics and Electrical Insulating Materials and ASTM E756-98, and Half-Power method for measuring vibration damping properties of materials.

5 mm TPO sheets “as received” from Solvay polymers were cut into test specimens and tested for the different material properties. The flexural properties of this material were reported in the previous quarterly report. The effort of this quarter focused on determination of material properties such as elastic modulus and tensile strength.

Azdelite sheet (ref SL551400.109) was compression molded to 2mm and 3mm and tested under tension and flexure. The evaluated sheet grade corresponds to 55% glass fibers in a PP matrix with an aerial density of 1400 g/m^2. Azdelite was tested under tension, flexure and its damping ratio was determined at different frequencies to demonstrate the added sound absorption benefits of LWRT in comparison with the baseline aluminum door.

Symalite sheet grade SL100G5516T16S1 was supplied by Quadrant Composites. This particular grade tested is a 1600 g/m^2, 55% W_f glass material in a PP matrix. Test plates of 2 mm and 3 mm thickness were molded and tested in tension and flexure. The damping ratio of this material was also measured at different frequencies to determine its damping efficiency against aluminum.

2.6.2 TPO

2.6.2.1 DSC and TGA

The TPO was tested on the DSC to find the polymer melting point and its glass transition temperature. The DSC shows that the TPO has a sharp melt point at 161°C. The glass transition (T_g) temperature is not visually discernible from the plot but from the constituents of the blend (PE and PP) TPO is expected to have a T_g between -10°C and 0°C. The resulting curve is shown in Fig. 2.6-1.

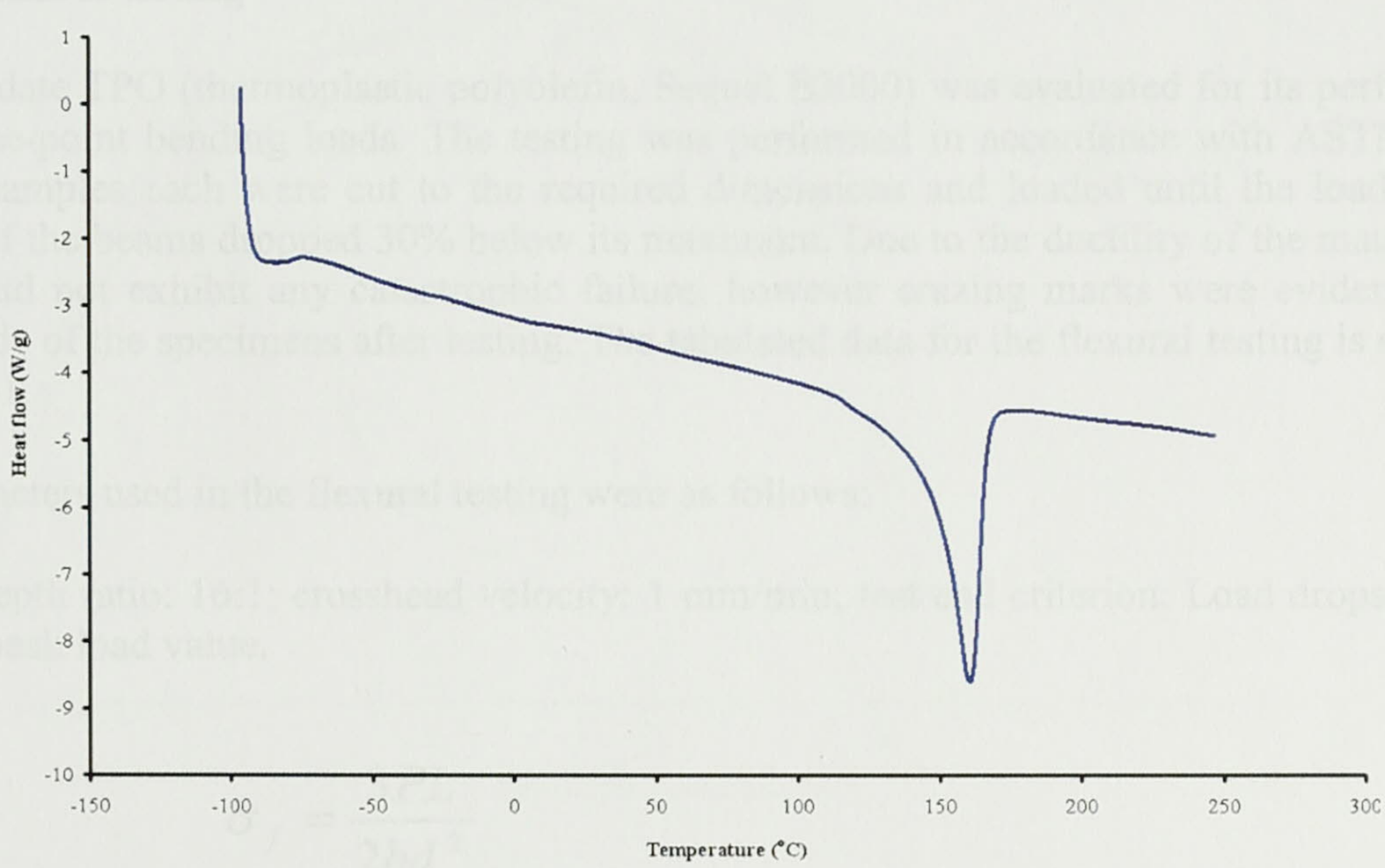

Figure 2.6- 1 Dynamic scanning calorimetry of TPO.

The polymer was also subjected to thermo gravimetrical analysis to find the degradation characteristics of the material. From this plot (Fig 2.6-2) it can be inferred that the polymer degrades at a temperature of 440°C.

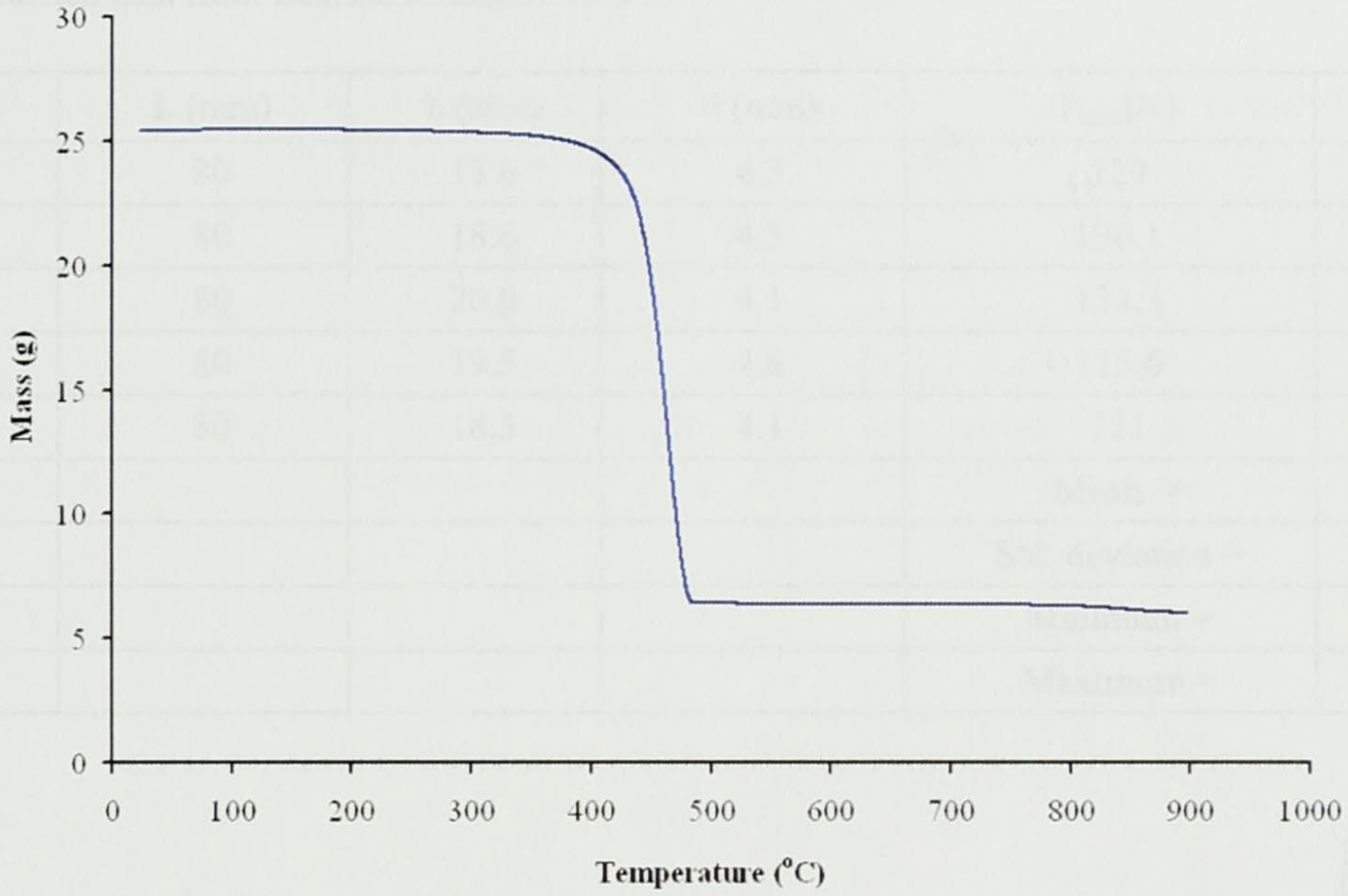

Figure 2.6- 2 Thermo gravimetrical analysis of TPO.

2.6.2.2 Flexural testing

The candidate TPO (thermoplastic polyolefin, Sequel E3000) was evaluated for its performance under three-point bending loads. The testing was performed in accordance with ASTM D790. Five (5) samples each were cut to the required dimensions and loaded until the load bearing capacity of the beams dropped 30% below its maximum. Due to the ductility of the material, the samples did not exhibit any catastrophic failure; however crazing marks were evident on the tension side of the specimens after testing. The tabulated data for the flexural testing is shown in Table 2.6-1.

The parameters used in the flexural testing were as follows:

Span to depth ratio: 16:1; crosshead velocity: 1 mm/min; test end criterion: Load drops by 30% from the peak load value.

$$\sigma_f = \frac{3PL}{2bd^2} \tag{11}$$

where σ_f = Flexural strength (MPa), P = Peak load (N), b = width of the beam tested (mm), and d = thickness of the beam tested (mm).

The mean flexural strength of the material was found to be 43.18 MPa, which corresponds to almost twice of the tensile strength reported by the manufacturer. The load versus displacement curves for the different samples are shown in Fig 2.6-3.

Table 2.6- 1 Tabulated data from flexural testing of TPO

Sample No.	L (mm)	b (mm)	d (mm)	P_{max}(N)	σ_f (MPa)
1	80	18.6	4.3	129	45.01
2	80	18.6	4.3	130.1	45.39
3	80	20.0	4.1	134.3	47.93
4	80	19.5	4.8	115.6	30.87
5	80	18.5	4.1	121	46.69
				Mean =	43.18
				Std. deviation =	6.97
				Minimum =	30.87
				Maximum =	47.93

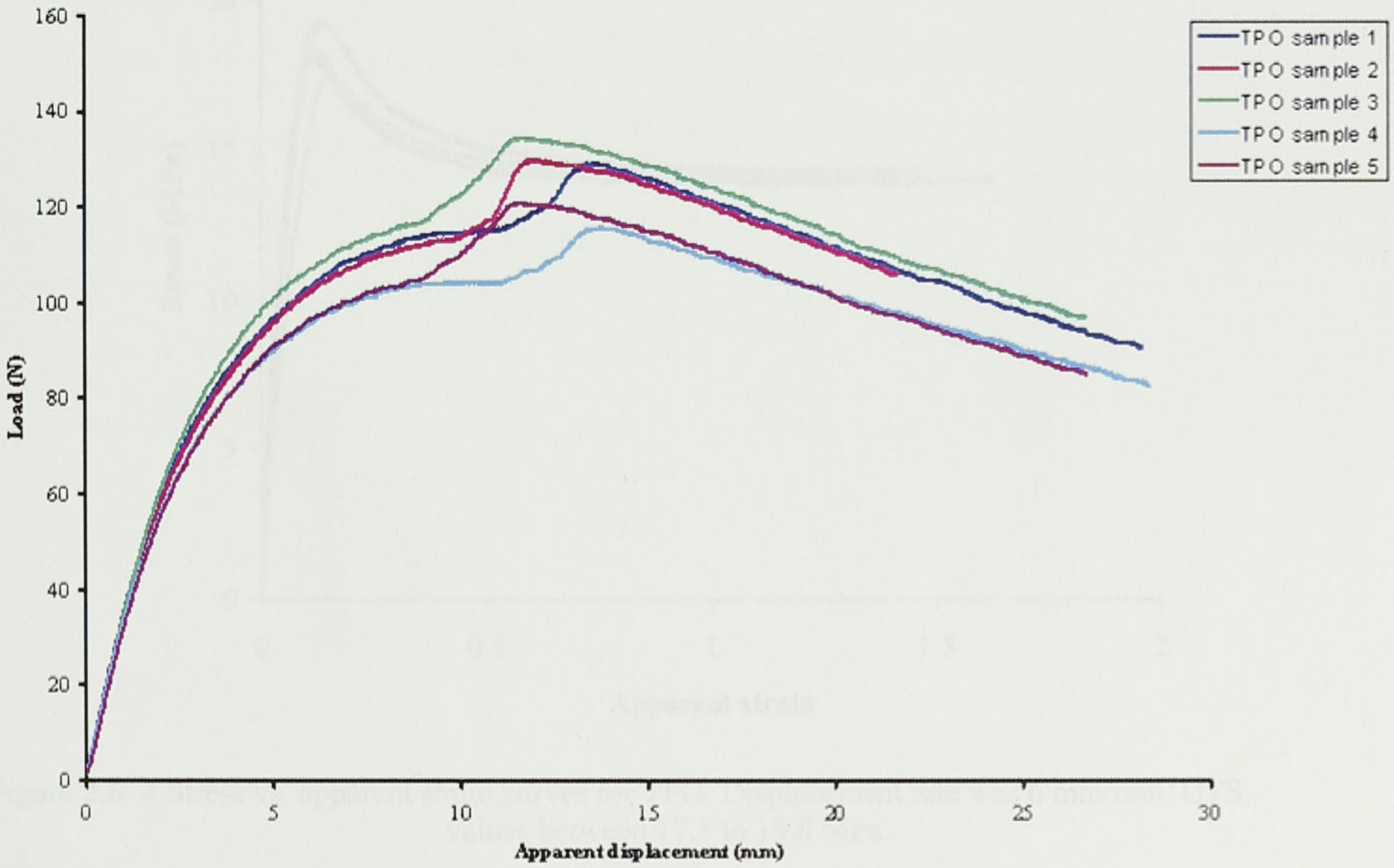

Figure 2.6- 3 Load vs. apparent displacement curves for TPO.

2.6.2.3 Tensile testing

TPO dog-bone coupons were manufactured and tested under tension using a universal loading frame. The resulting stress vs. apparent strain plots for all the TPO samples are shown in Fig. 2.6-4. From these, it can be determined that this material yields between 17 and 18 MPa and then exhibits significant plastic deformation. For the determination of the elastic modulus, an extensometer was attached to the samples in the linear region of the stress vs. strain curve and removed prior to failure. The stress vs. strain data recorded was plotted and is shown in Fig 2.6-5. The tabulated results for the elastic modulus of TPO are listed in Table 2.6-2. The mean measured elastic modulus of TPO was found to be 1.78 GPa with a standard deviation of 0.28 GPa.

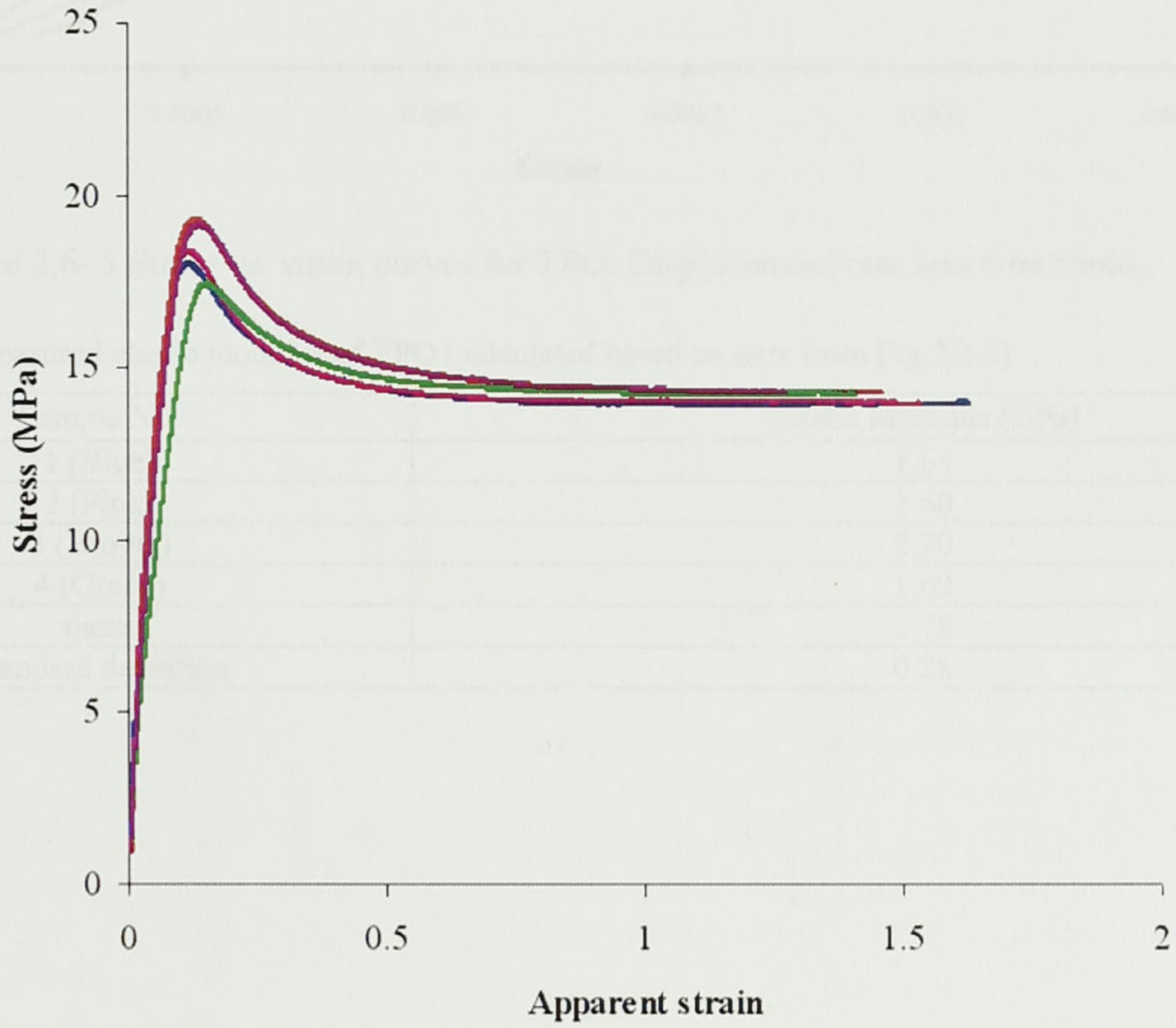

Figure 2.6- 4 Stress vs. apparent strain curves for TPO. Displacement rate was 6 mm/min. UTS values between 17.5 to 19.8 MPa.

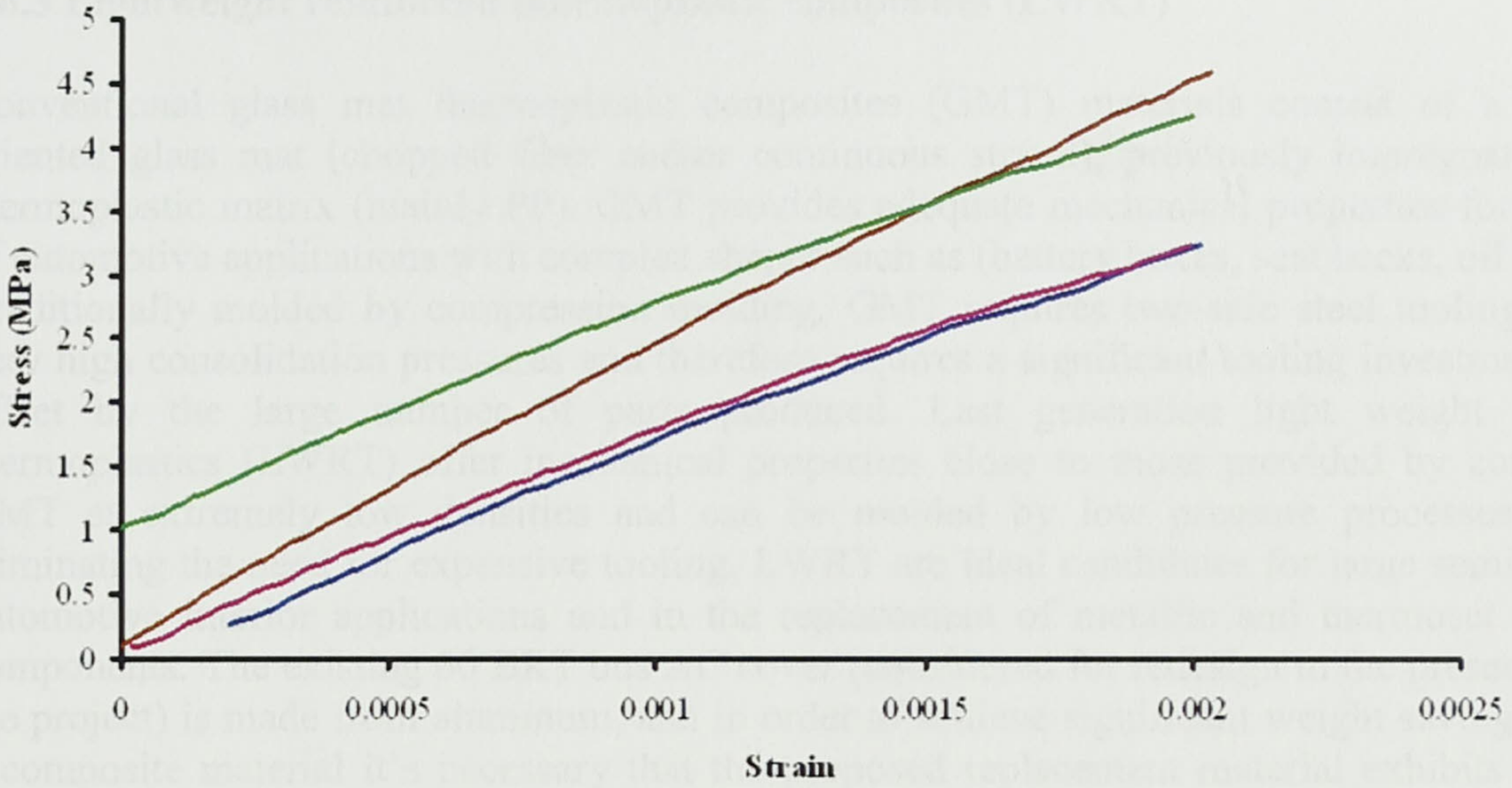

Figure 2.6- 5 Stress vs. strain curves for TPO. Displacement rate was 6 mm/min.

Table 2.6- 2 Measured elastic modulus of TPO (calculated based on data from Fig 2.2.5)

Sample No.	Elastic Modulus (GPa)
1 (Blue)	1.64
2 (Pink)	1.60
3 (Brown)	2.20
4 (Green)	1.69
mean	1.78
Standard deviation	0.28

2.6.3 Lightweight reinforced thermoplastic composites (LWRT)

Conventional glass mat thermoplastic composites (GMT) materials consist of a randomly oriented glass mat (chopped fiber and/or continuous strand), previously impregnated with a thermoplastic matrix (mainly PP). GMT provides adequate mechanical properties for a number of automotive applications with complex shapes such as (battery boxes, seat backs, oil pans etc.). Traditionally molded by compression molding, GMT requires two-side steel tooling rated for very high consolidation pressures and therefore requires a significant tooling investment usually offset by the large number of parts produced. Last generation light weight reinforced thermoplastics (LWRT) offer mechanical properties close to those provided by conventional GMT at extremely low densities and can be molded by low pressure processes therefore eliminating the need for expensive tooling. LWRT are ideal candidates for large semi structural automotive interior applications and in the replacement of metallic and thermoset composite components. The existing 60 BRT bus AC cover (considered for redesign in the present phase of the project) is made from aluminum, and in order to achieve significant weight savings by using a composite material it's necessary that the proposed replacement material exhibits extremely low density and at the same time adequate mechanical properties. Thus, conventional glass based thermoplastic composites are not currently being pursued for this applications since the resulting weight savings would be minimal and the technology shift would not be justifiable. Two different manufacturers of light GMT materials (GE Plastics and Quadrant composites) produce a number of variations of light GMT with an extensive array of proven applications in automotive components. Details on each of the commercially available products are presented below:

2.6.3.1 Tensile testing

Both considered grades of LWRT (Azdelite and Symalite) were tested for the determination of tensile strength, and elastic modulus. The resulting modulus and tensile strength plots are shown in Figs 2.6-6 – 2.6-9. Azdelite exhibited tensile strength of 100 MPa and 64 MPa, and elastic modulus of 8 GPa and 4.8 GPa when molded at 2 mm and 3 mm respectively. Quadrant Symalite exhibited somewhat lower values of strength 75 and 16 MPa, and elastic modulus of 5.33 and 1.63 GPa at the corresponding thicknesses, but unlike the Azdelite material it did not exhibit catastrophic failure.

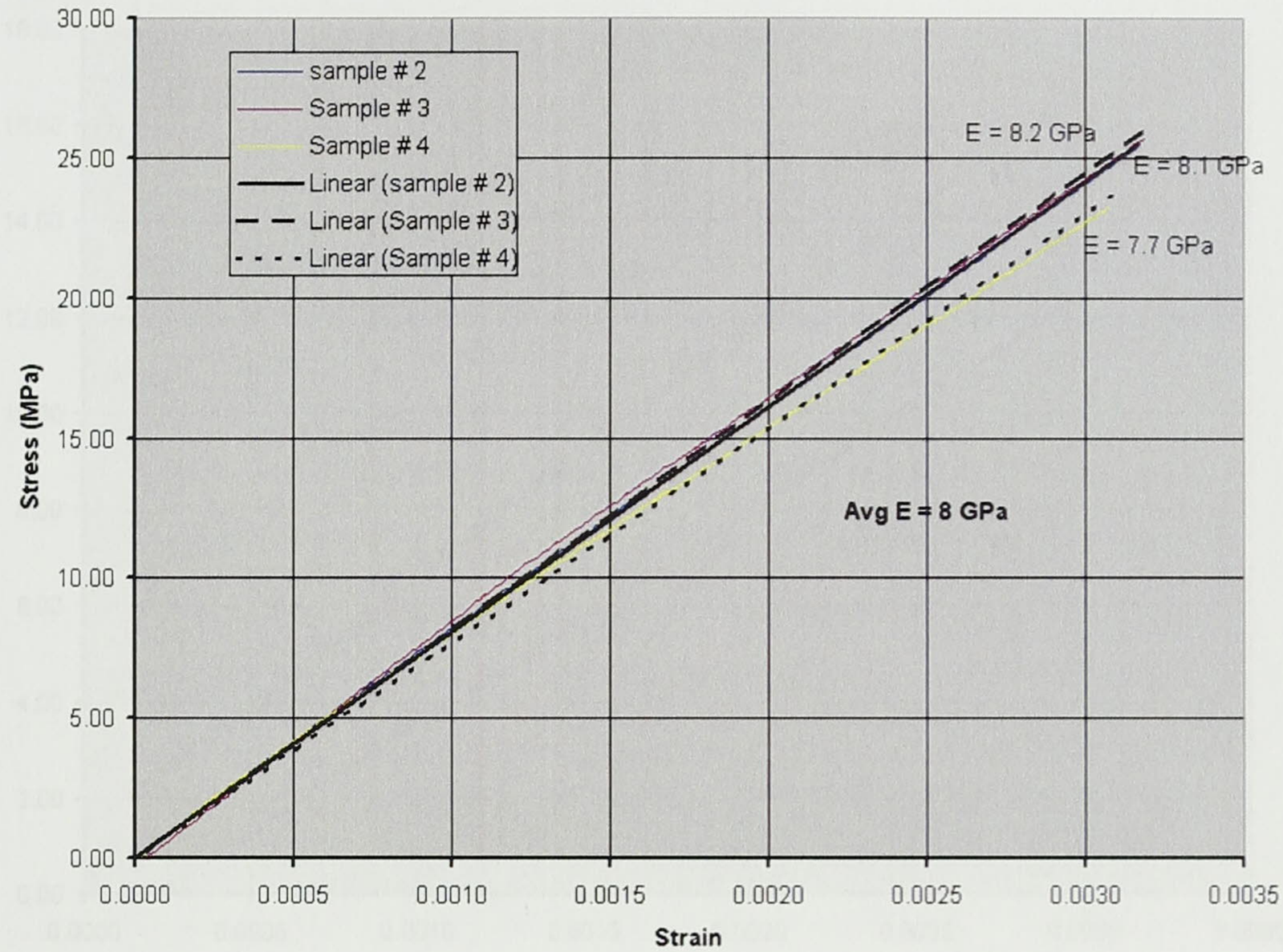

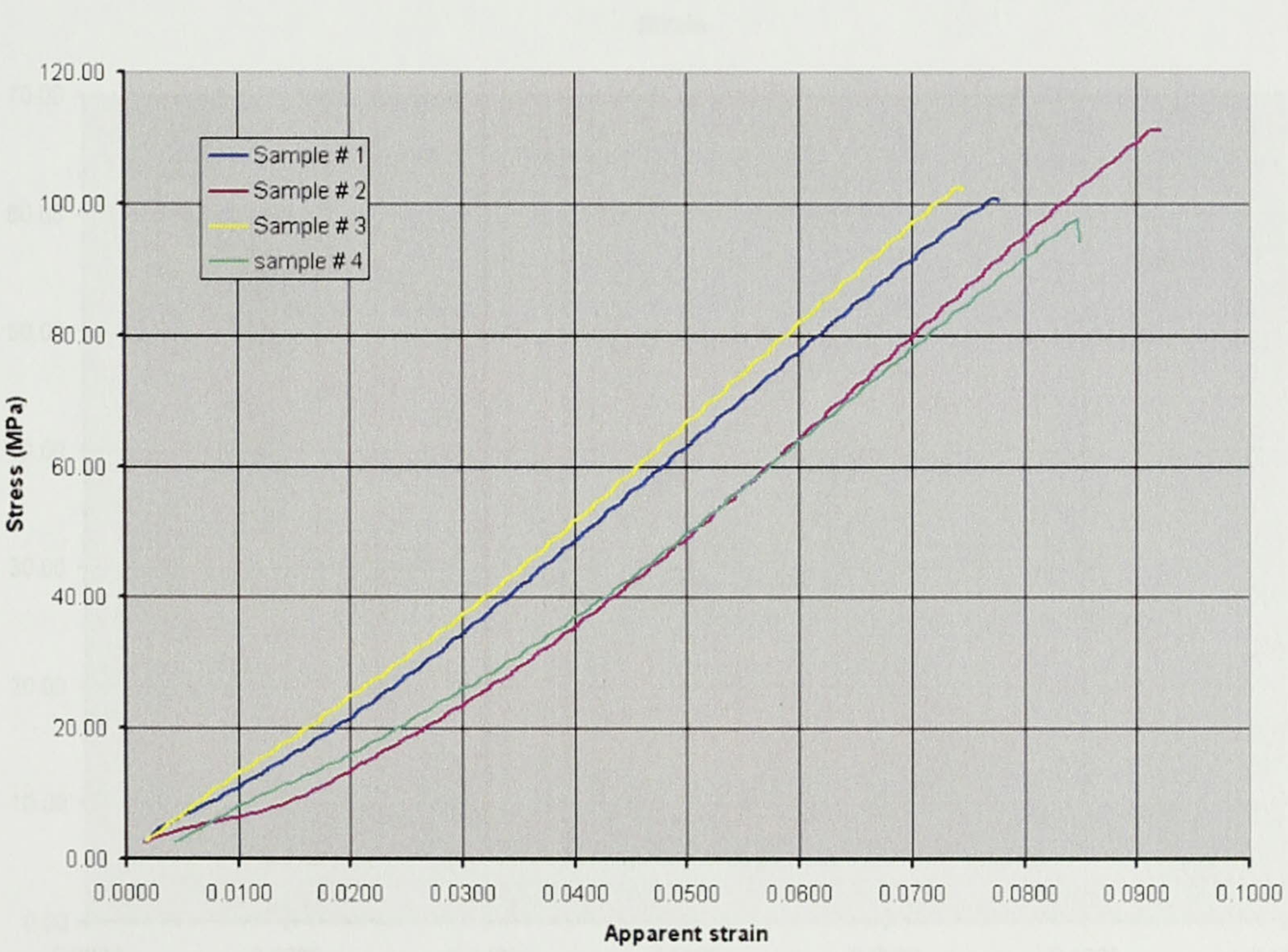

Figure 2.6- 6 Elastic modulus and stress vs. strain plot for Azdelite (1400gsm 55% GF) compressed to 2 mm.

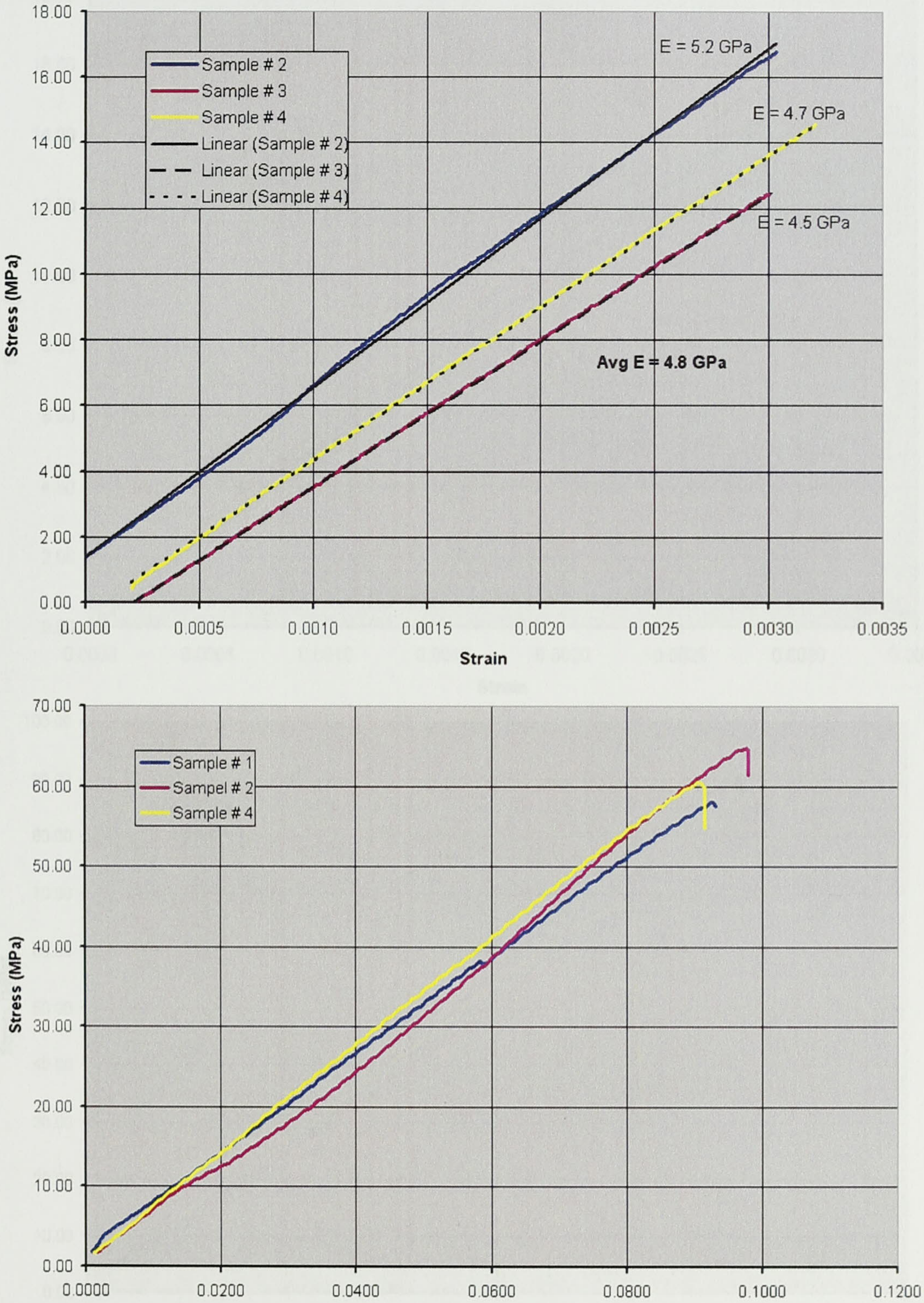

Figure 2.6- 7 Elastic modulus and stress vs. strain plot for Azdelite (1400 gsm 55% GF) compressed to 3 mm.

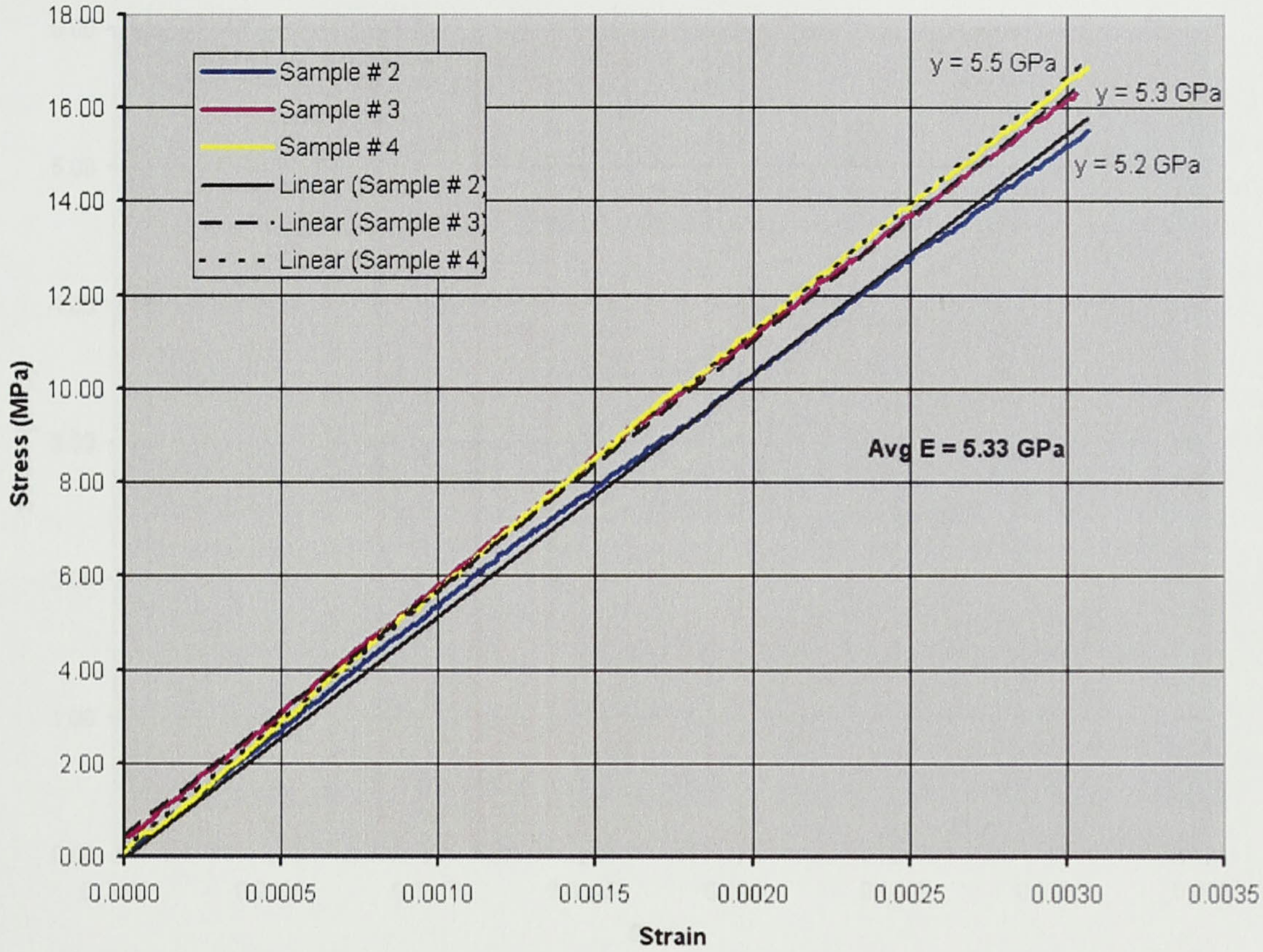

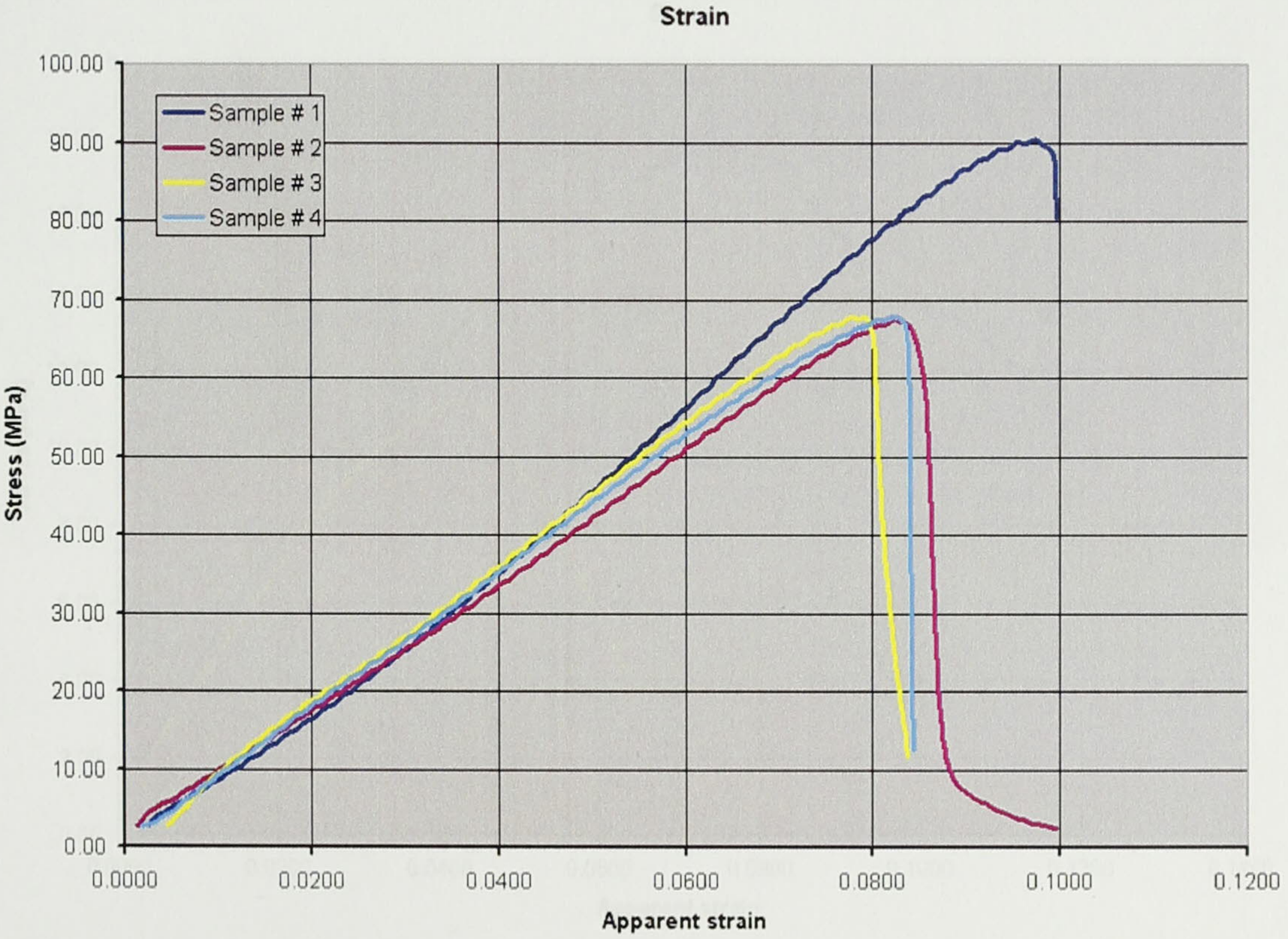

Figure 2.6- 8 Elastic modulus and stress vs. strain plot for Quadrant (1600 gsm 55% GF) compressed to 2 mm.

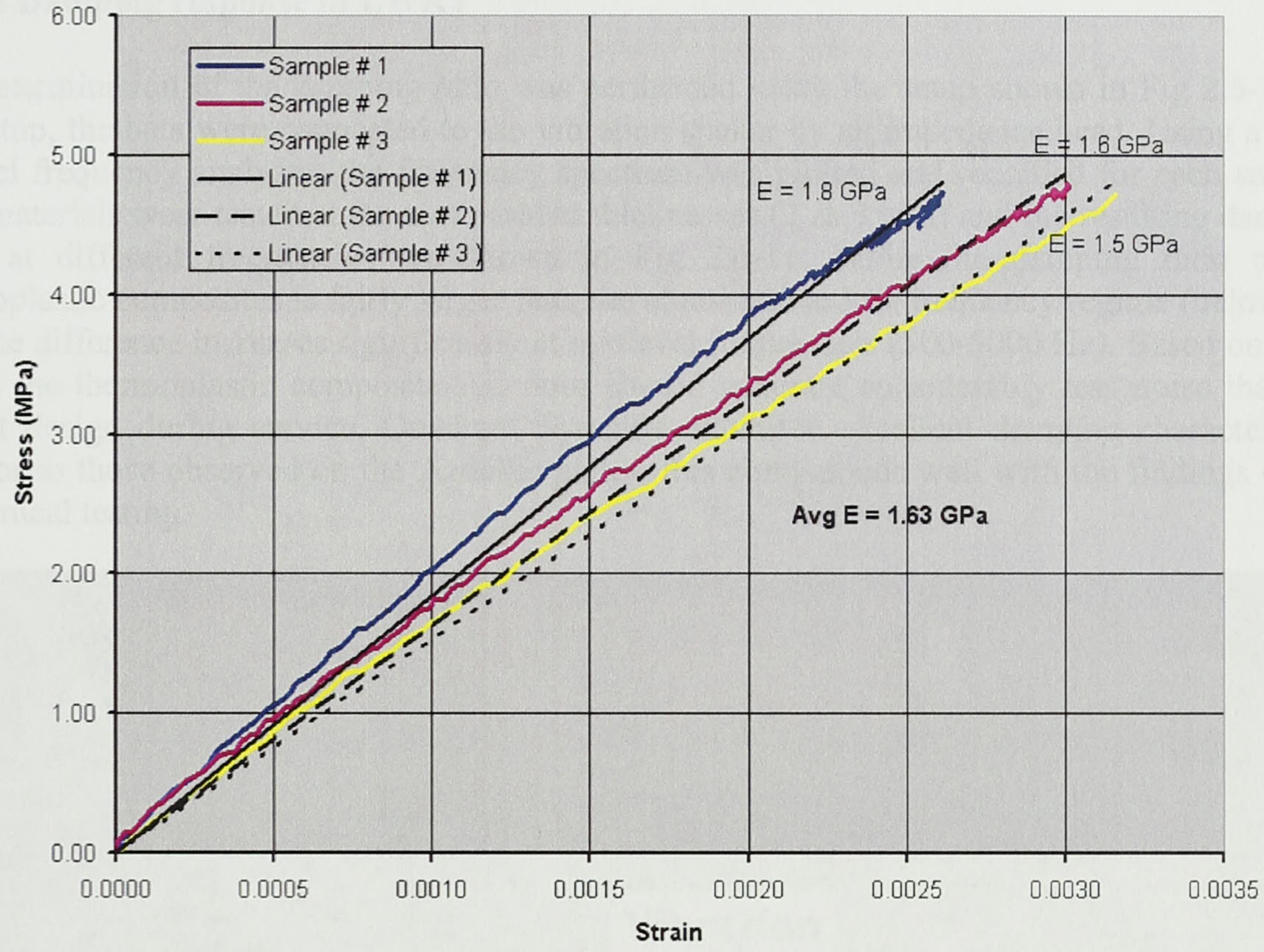

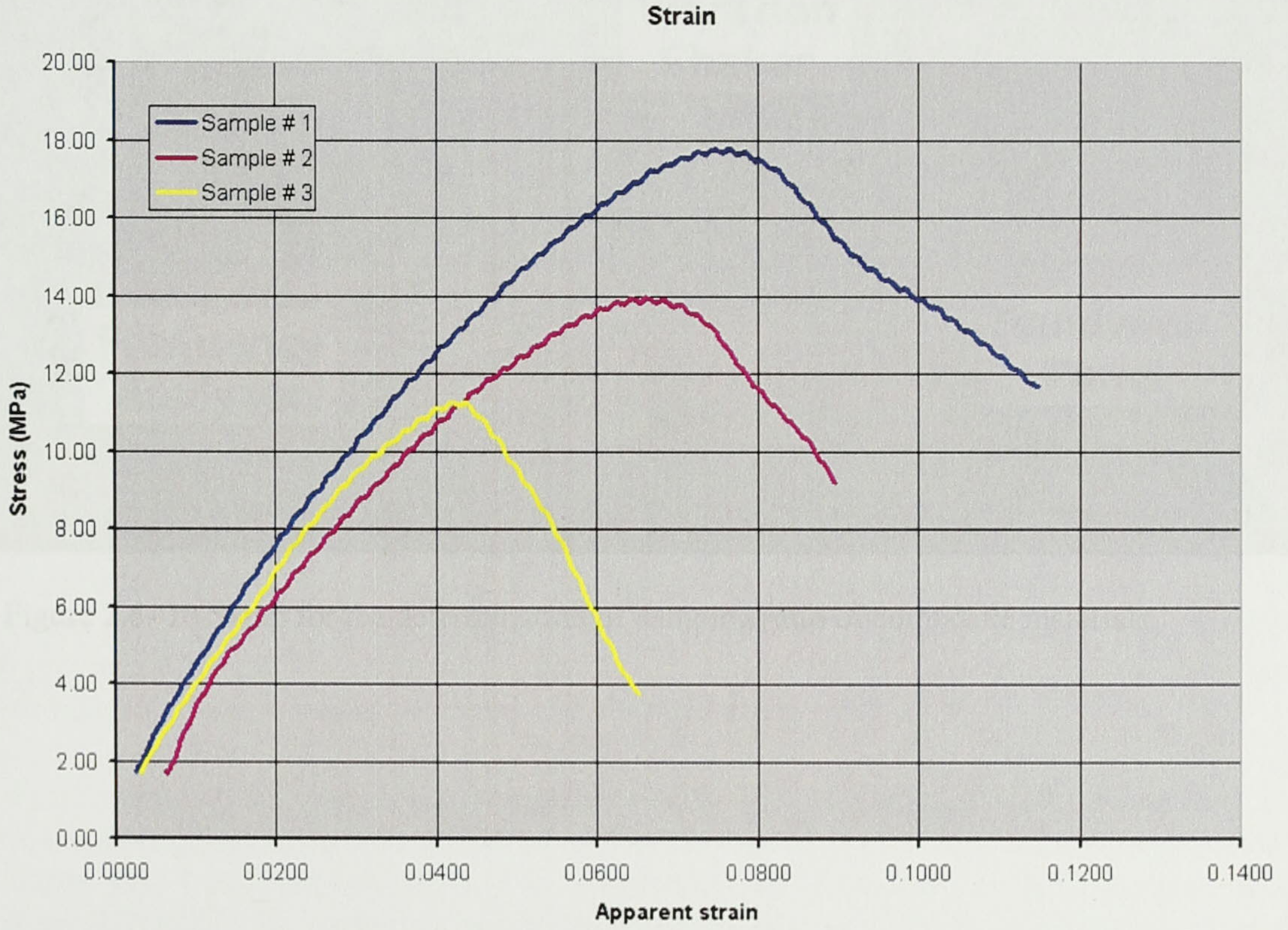

Figure 2.6- 9 Elastic modulus and stress vs. strain plot for Quadrant (1600 gsm 55% GF) compressed to 3 mm.

2.6.3.2 Damping response of LWRT

The determination of the damping ratio was performed using the setup shown in Fig 2.6-10. In this setup, the bars were connected to the vibration shaker by an impedance head. Using a dual-channel frequency analyzer, the frequency spectrum was plotted and recorded for each sample. Both materials were tested at the two molded thicknesses (2 & 3 mm) and the resulting damping ratios at different frequencies are shown in Fig 2.6-11. While the damping ratio of the thermoplastic composites is fairly larger than the aluminum at low frequency regime (below 500 Hz), the difference increases significantly at midlevel frequencies (500-5000 Hz). Based on these results the thermoplastic composite AC door should generate considerably less noise than the current design during service. Quadrant Symalite exhibited excellent damping characteristics superior to those observed on the Azdelite plates, this corresponds well with the findings of the mechanical testing.

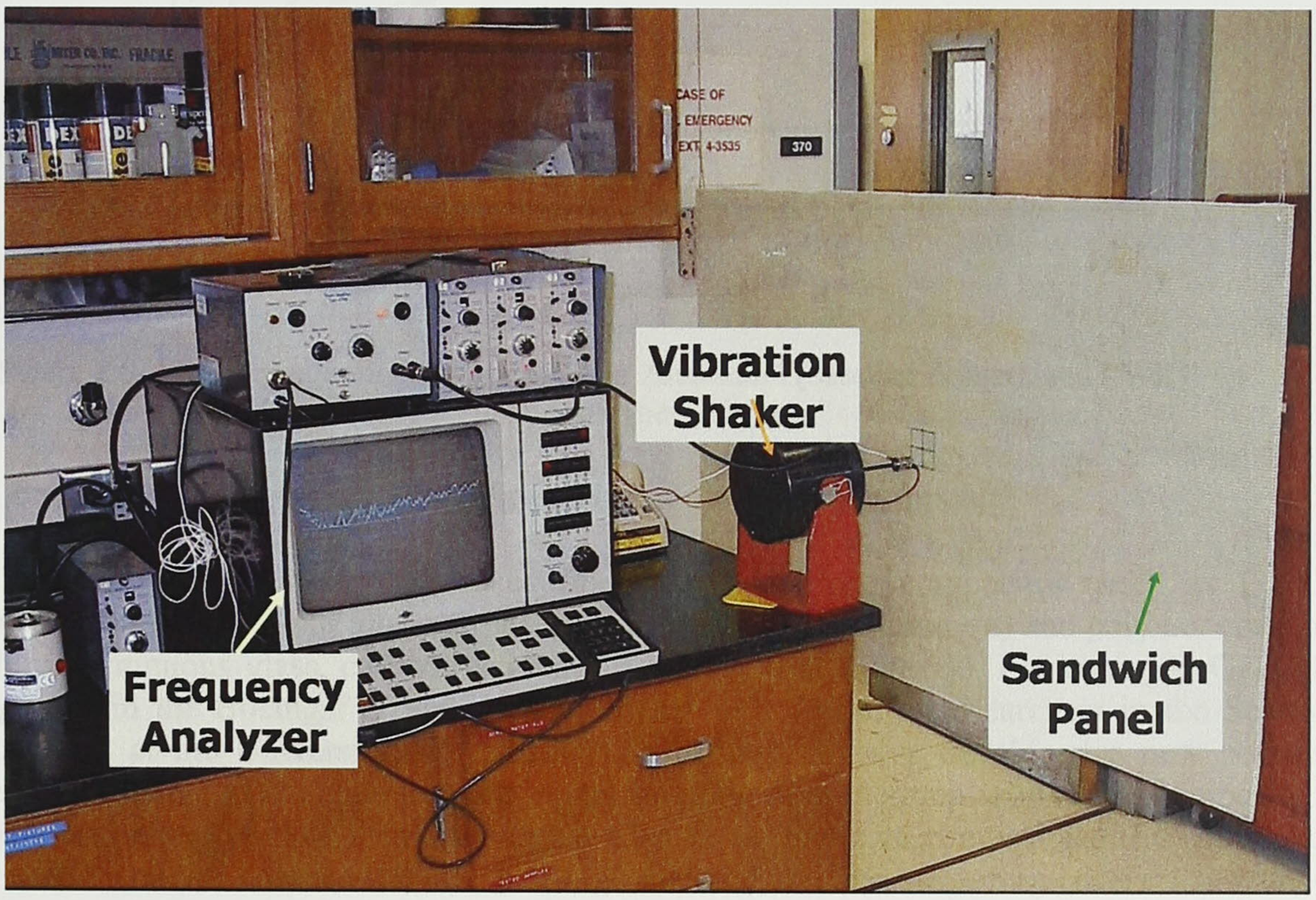

Figure 2.6- 10 Setup for the determination of damping ratio of composite materials.

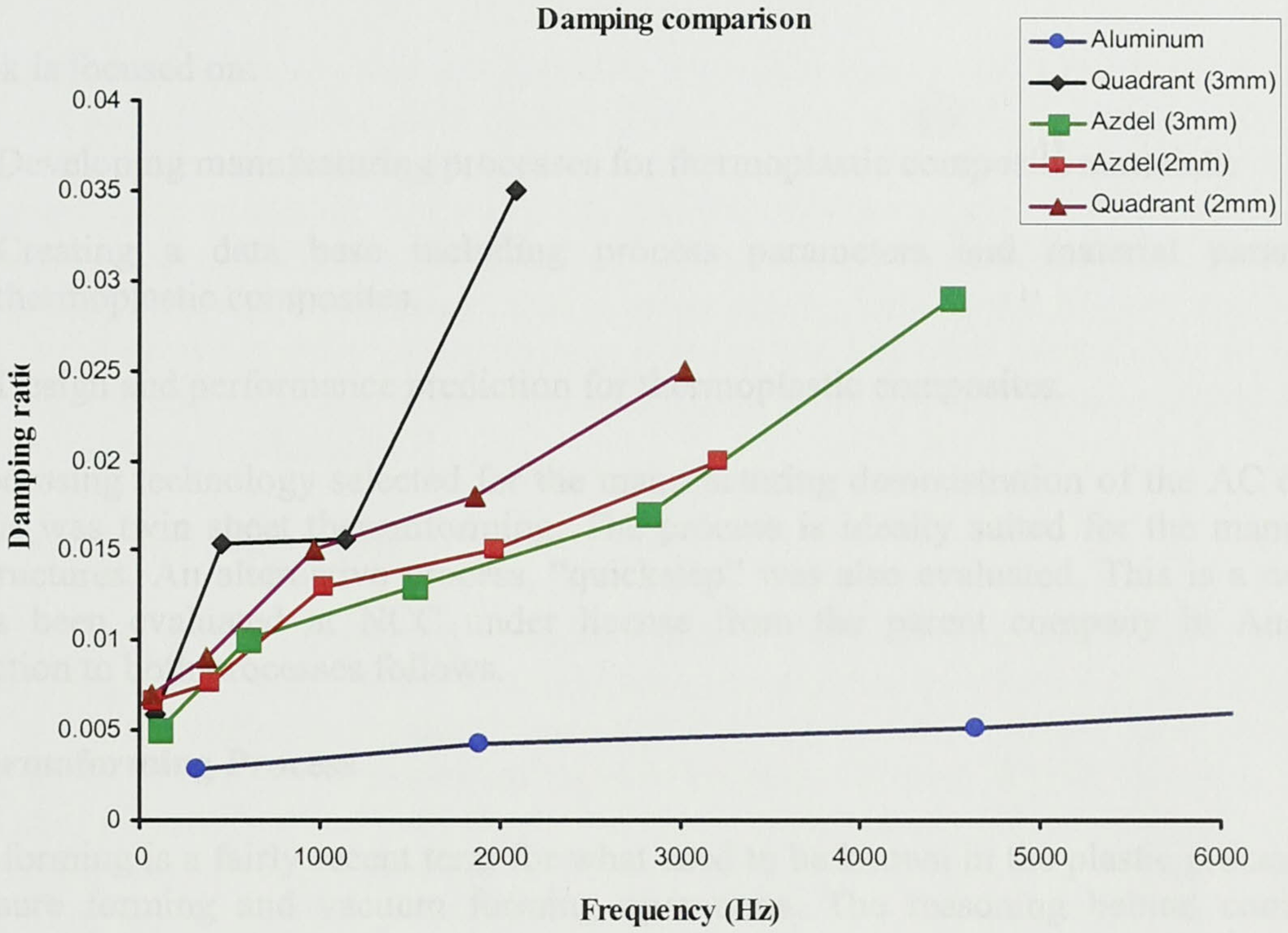

Figure 2.6- 11 Damping ratio vs. frequency for Aluminum (baseline design), and LWRT materials (new design).

2.7 Long fiber thermoplastic (LFT)/metal laminate (LML) composite

The aerospace industry currently uses fiber metal laminate composites (such as GLARE, ARALL, etc.) consisting of alternate sheets of metal (such as aluminum) and polymer composite (such as continuous glass, carbon, or aramid fiber reinforced epoxy). For example, GLARE is being used in the Boeing 777 and Airbus 380 aircrafts [36-41]. Researchers in the School of Engineering at the University of Alabama in Birmingham have developed a new composite material consisting of alternate layers of metal and long fiber thermoplastic (LFT) composite that is more cost-effective than the conventional fiber metal laminate composites. The conventional fiber metal laminate composites, due their high material and manufacturing costs are restricted to the aerospace industries. In contrast, the new composite with a recyclable thermoplastic has low material and manufacturing costs. Such metal/LFT composite laminates will be affordable to the automotive and ground transportation industries. Some of the advantages of this laminate composite include high specific strength, impact resistance, recyclability, etc.

Our research team at UAB is evaluating possibility of intellectual property potential for this laminate technology. As a first step towards filing for a patent, an intellectual property disclosure (IPD) form has been submitted to the University of Alabama at Birmingham Research Foundation (UABRF). A marketing brochure based on this laminate technology has been sent to few companies. The companies have responded positively, as a result of which, the UABRF is preparing to file a provisional patent application.

III. Processing Technology

This task is focused on:

1. Developing manufacturing processes for thermoplastic composite materials.
2. Creating a data base including process parameters and material parameters for thermoplastic composites.
3. Design and performance prediction for thermoplastic composites.

The processing technology selected for the manufacturing demonstration of the AC door for 60 BRT bus was twin sheet thermoforming. The process is ideally suited for the manufacture of large structures. An alternative process, "quickstep" was also evaluated. This is a new process that has been evaluated at NCC under license from the parent company in Australia. An introduction to both processes follows.

3.1 Thermoforming Process

Thermoforming is a fairly recent term for what used to be known in the plastic processing world as pressure forming and vacuum forming operations. The reasoning behind combining the definitions of these two processes into one was that they refer to exactly the same process with the only difference between them being the pressure that is applied to the heated part during forming. In principle, the thermoforming process requires that a plastic sheet be heated uniformly to a temperature that makes it soft enough to be formed by the action of either positive or negative pressure (Fig 3.1-1). Achieving the exact temperature in the sheet can be a challenge since the correct measurement of the temperature of the sheet is difficult to obtain. If the sheet temperature rises above the forming temperature of the material, the material may degrade or sag causing thinning and a possible loss of properties. If on the contrary, the temperature of the sheet is below the forming temperature for the material, the material may cold form, inducing internal stresses in the part that can later precipitate part failure [42].

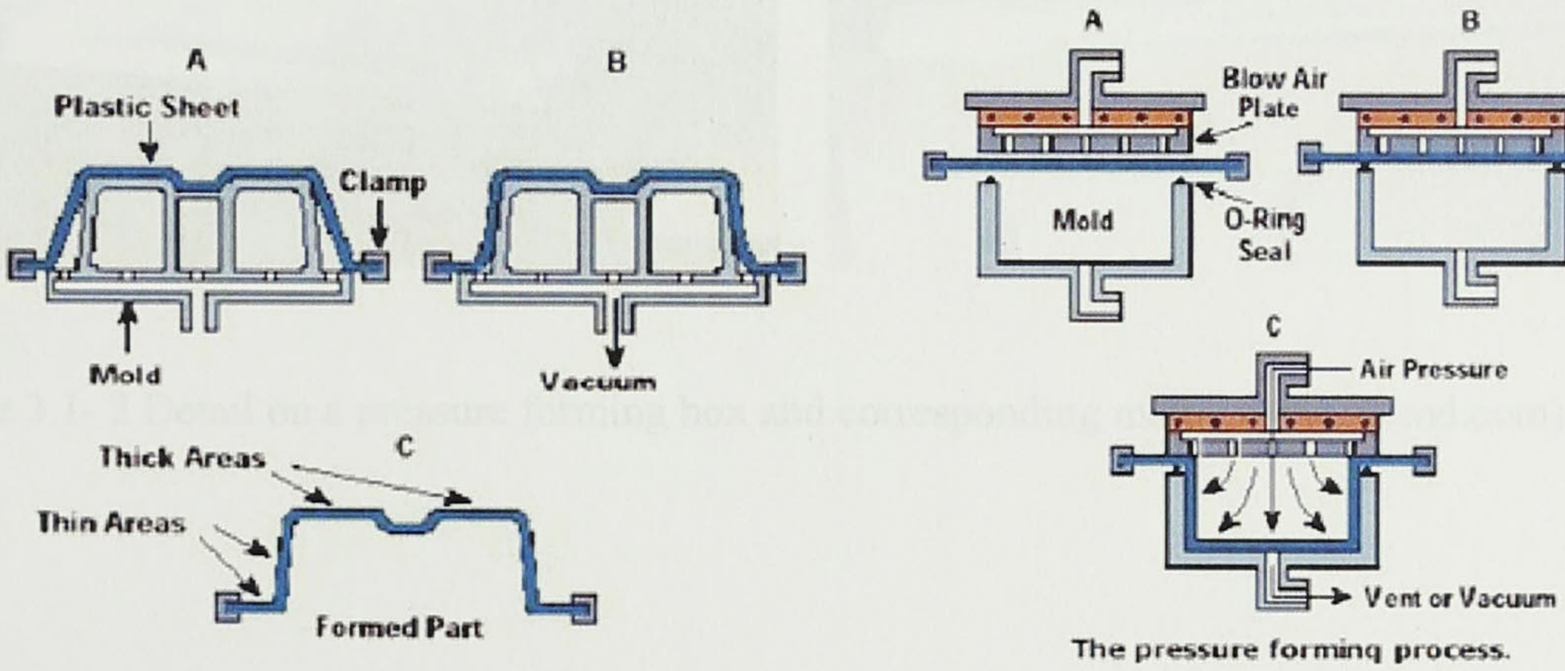

Figure 3.1- 1 Thermoforming: Vacuum forming process and pressure forming process (www.geimd.com).

3.1.1 Vacuum Forming process

Vacuum forming requires a mold connected to a vacuum supply and a system to seal the edges of the mold securely against heated plastic. The seal of system is necessary for the vacuum to build up rapidly between the mold and the heated plastic without leakage. Vacuum leaks can cause trapped air between the mold and hot sheet to cool the plastic sufficiently and prevent it from coming in contact with the mold surface. If the hot plastic becomes chilled before it is fully formed, it may result in a component that is incompletely formed and of poor quality. Vacuum forming is the most common thermoforming process and has been used widely in applications such as sign forming, plastic cup forming, and others. Both male and female molds can be used on vacuum forming machines [43].

3.1.2 Pressure forming process

Pressure forming process requires a pressure box to enclose the mold and create a pressure tight thermoforming area, which allows thermoforming using pressures above 14.7 psi (100 kPa). This process is used for applications that require high definition and detail, and for materials that are too stiff to be formed by conventional vacuum pressure forming. Under the hood automotive components, automotive and industrial machinery body panels and interior components are manufactured using pressure forming. Overall scrap rate and cycle efficiency are improved with pressure forming. Both male and female molds can be used with pressure forming and design of the mold should include the means for generating an adequate seal between the two halves of the mold (Fig 3.1-2) [41]

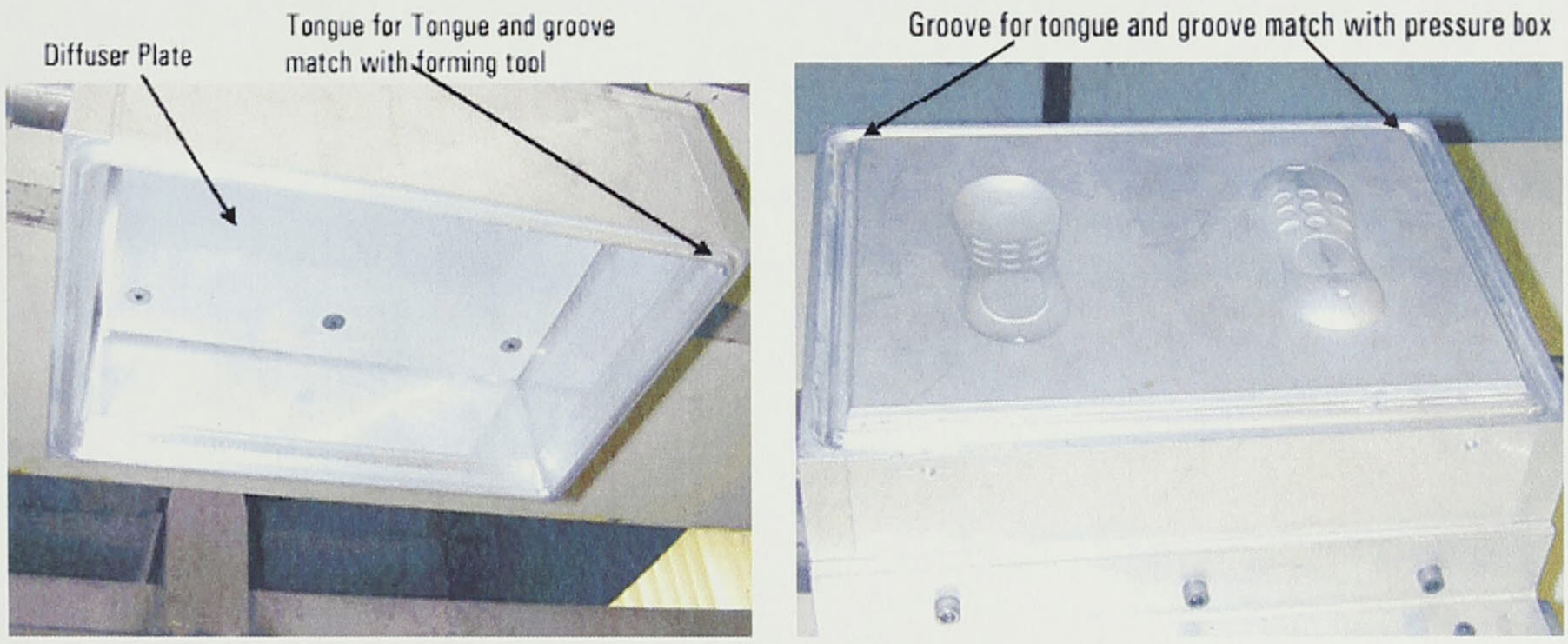

Figure 3.1- 2 Detail on a pressure forming box and corresponding mold (www.geimd.com).

3.1.3 Thermoforming materials

Almost all of the thermoplastic polymers that can be extruded into homogeneous sheets can be formed by thermoforming. Depending on the requirements of the application, the thermoforming materials can range from inexpensive high density polyethylene sheet to high performance engineering resins such as PEEK or PEI. A list of the commodity plastics and the engineering plastics available in sheet form for thermoforming is presented in Tables 3.1-1 and 3.1-2 with some of their general characteristics.

Table 3.1- 1 Some engineering polymers for thermoforming and their general characteristics

Name	Designation	Comparative Cost	Elongation at break %	Maximum service Temperature °C
UHMWPE	Ultra high molecular weight Polyethylene	Moderate	5	93
NYLON 6, 6, 11, 12, 6/16	Polyamides	Moderate	5-60	104
PBT	Polyesters	Moderate	200	110
PTFE	Fluoropolymers, teflon	High	150	260
POM	Acetal	Premium	20-75	98
PEI	Polyetherimide	Premium	60	160
PPS	Polyphenylene sulfide	High	0.7-10	220
PC	Polycarbonate	Moderate	6	130

Table 3.1- 2 Some commodity polymers for thermoforming and their general characteristics

Name	Designation	Comparative Cost	Elongation at break %	Maximum service Temperature °C	Thermoforming temperature° C
PE	High density Polyethylene	Low	1100	65	146
PP	Polypropylene	Low	300	71	154
PET	Polyester	Moderate	50	110	149
RPVC	Rigid Polyvinyl Chloride	Low	30-200	70	118

While there have been several improvements in the automatization of the thermoforming process, there are still several things to be proven in terms of new materials. With the exception of short fiber reinforced polymers, long fiber thermoplastic composites have not been looked at for thermoforming applications, the main limitation being that fiber reinforced composites are high modulus materials and therefore require higher pressures during the forming operation. At the same time, long fiber reinforced sheet material is not yet available commercially. To develop new products which exploit the benefits of thermoplastic composites and thermoforming processes can open a new range of applications in semi structural components previously off limits for thermo formable materials due to their limited structural performance. As an example of the potential of thermoformed thermoplastic composite panels for exterior applications, GE developed a High performance composite hood which weighs 50% that of its equivalent steel component and exhibits better impact performance (Fig 3.1-3)

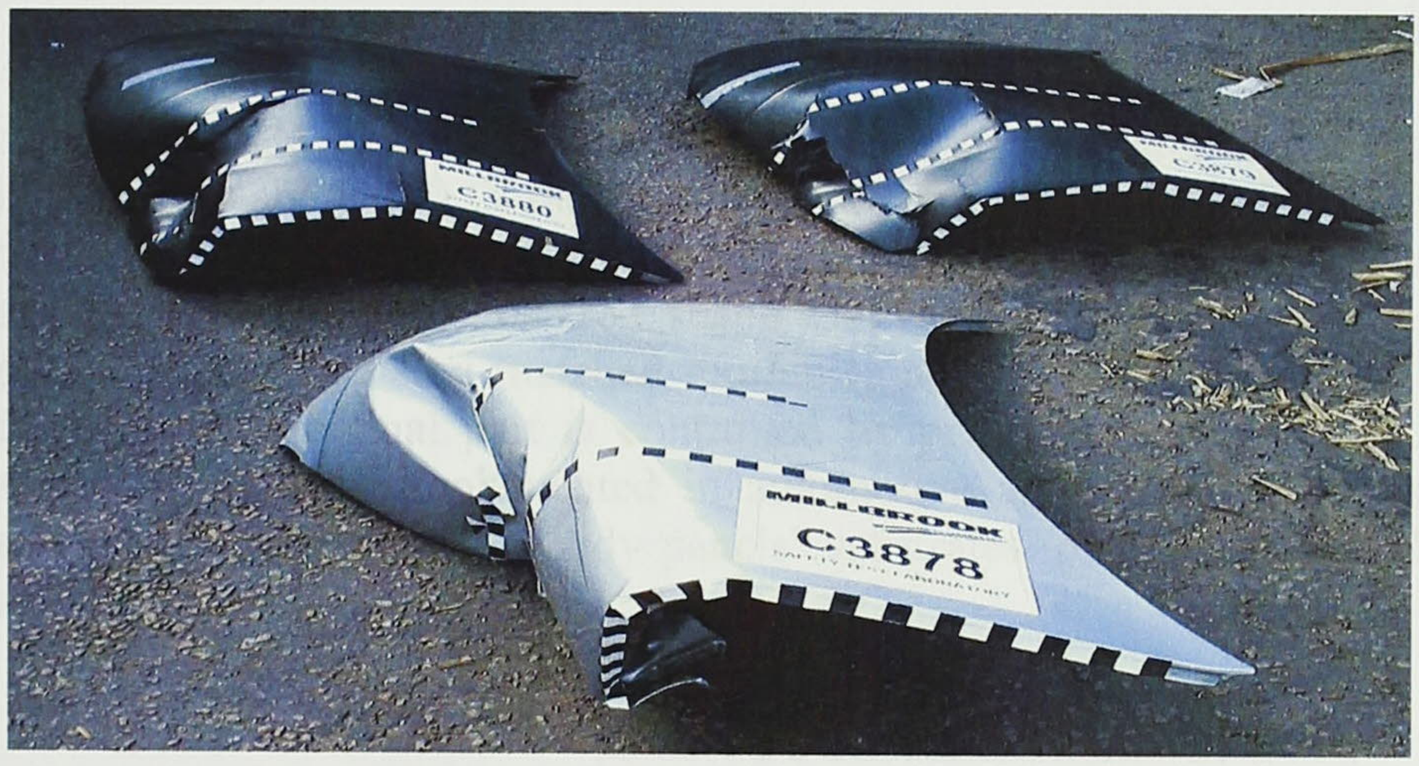

Figure 3.1- 3 Crash performance of thermoplastic composite thermoformed hoods (black) and steel hood (silver).

3.1.3.1 GE Plastics/Azdelite

Azdelite is a low pressure, thermo formable thermoplastic composite made from long chopped glass fibers in a polypropylene matrix. This material can be combined with an array of surface layers such as barrier films, fabrics, felts, carpets or tough polymer films depending on the final application. The material is available in different densities ranging from 600 g/m^2 to 2000 g/m^2 and provides very high strength to weight ratio, high impact tolerance, is fully recyclable, and exhibits very low coefficient of thermal expansion (close to Aluminum). The Azdelite sheets are manufactured by mixing the PP resin with the chopped long fibers into slurry. The slurry is then deposited into a conveyor which transports the material through a vacuum chamber and a hot air drier. The material is then squeezed into the desired thickness by nip rollers and cut to size. The manufacturing process of Azdelite is shown in Fig 3.1-4. [44]

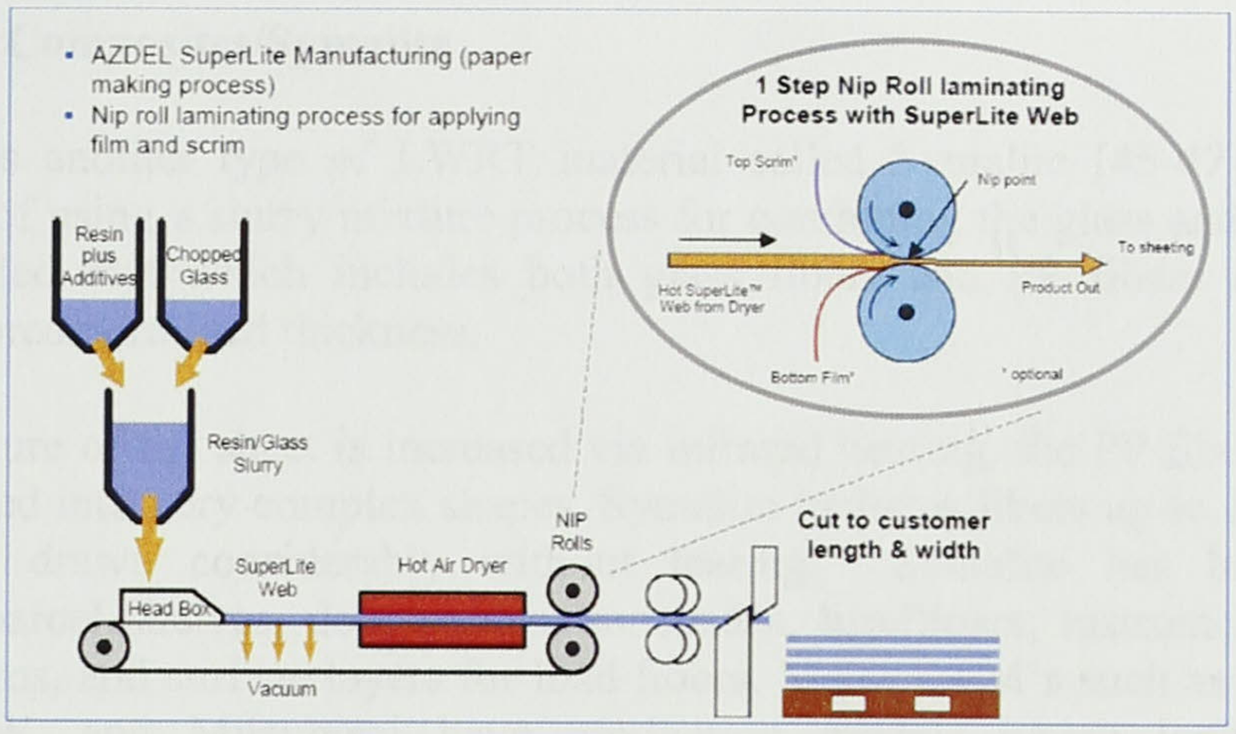

Figure 3.1- 4 Manufacturing process of Azdelite (from AZDEL, proprietary information).

Azdelite sheets exhibit lofting once exposed to heat. When the temperature of the sheet is increased to about 190 C, the sheet expands through its thickness due to the drop in viscosity of the binder resin, which releases the glass fibers (Fig 3.1-5). It is then, when the sheets can be easily molded into the desired shape via vacuum forming (barrier film needed) or by low pressure molding using matched tooling (made from tooling board, wood or aluminum). The thickness of the final part is controlled by press stops previously designed into the tooling. Azdelite has been implemented in automotive applications such as aerodynamic underbody shields, aftermarket parts, body panels' substrates, door panel trim, headliners and sunshades, seat backs, etc.

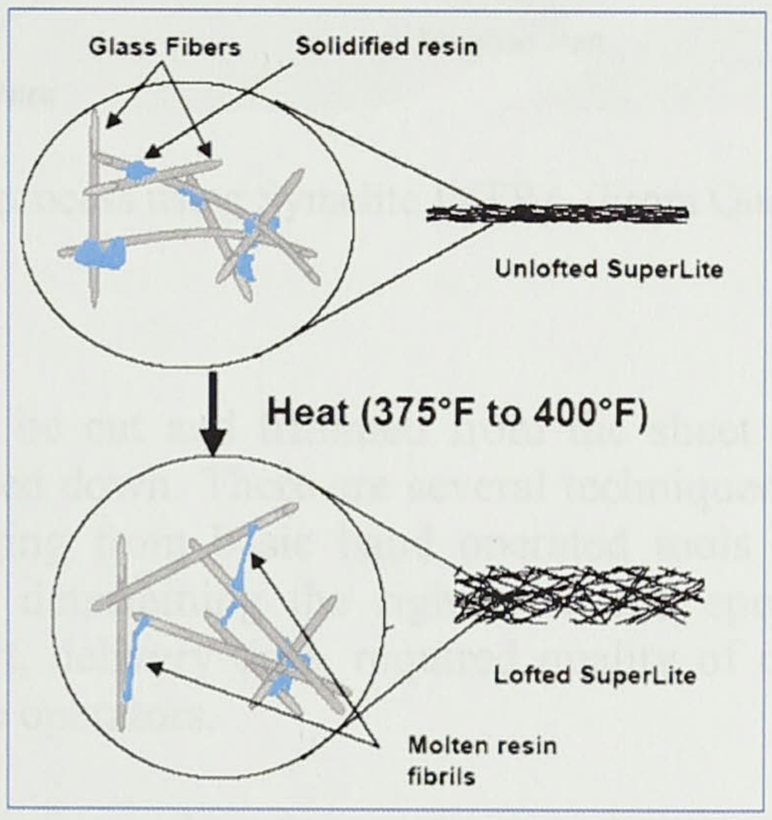

Figure 3.1- 5 Lofting of Azdelite (from AZDEL, proprietary information).

3.1.3.2 Quadrant Composites/Symalite

Quadrant produces another type of LWRT material called Symalite [45-47]. In the case of Symalite, instead of using a slurry mixture process for combining the glass and the PP matrix, a random commingled mat which includes both glass fibers and PP fibers is preheated and consolidated to a predetermined thickness.

Once the temperature of the sheet is increased via infrared heating, the PP fibers soften and the sheet can be molded into very complex shapes. Symalite includes fibers up to 100 mm long and therefore can be drawn considerably without tearing. Symalite has been successfully implemented on parcel shelves, door panels, sunshades, headliners, instrument panels, center consoles, pillar trims, and surface layers for load floors. Major OEM's such as Porsche, IVECO truck, VW, BMW, and Mitsubishi have production models which include components manufactured with Symalite. The manufacturing process of for a typical Symalite based component is shown in Fig. 3.1-6.

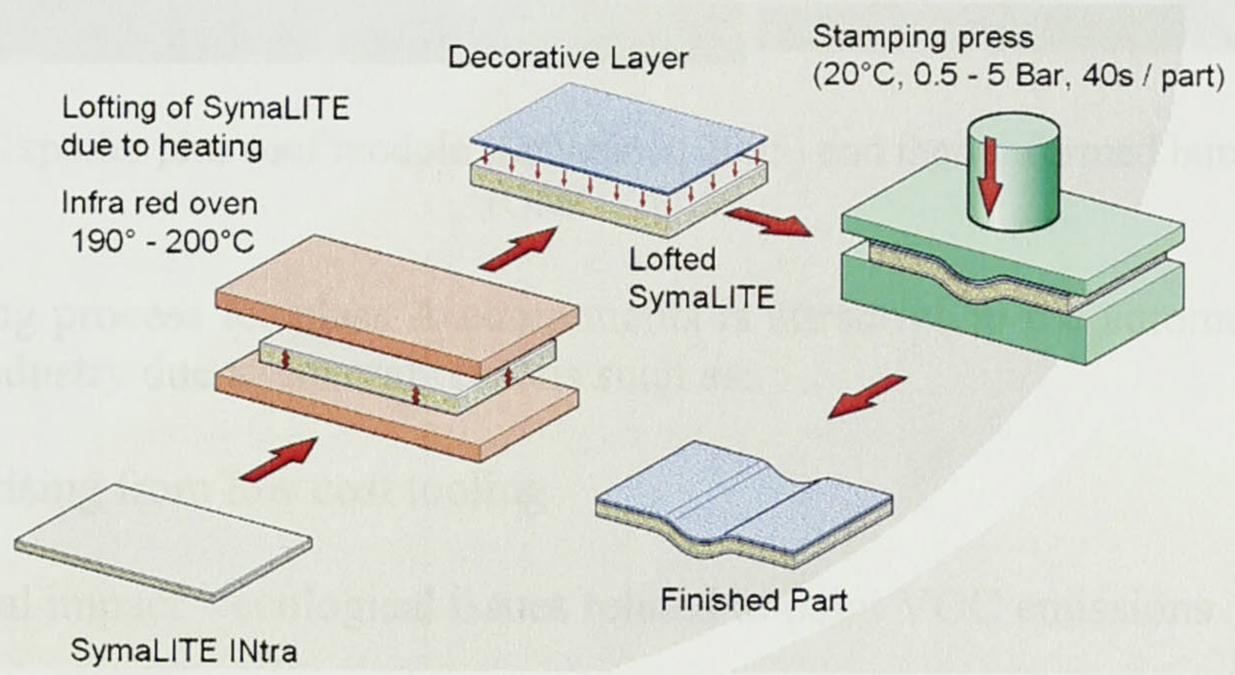

Figure 3.1- 6 Manufacturing process using Symalite INTRA (From Quadrant Composites).

3.1.4 Finishing operations

Thermoformed parts have to be cut and trimmed from the sheet after the molding cycle has finished and the part has cooled down. There are several techniques for trimming the parts once they have been molded ranging from basic hand operated tools to automated trimming and routing systems. Factors for determining the right type and specification of cutting device include initial cost of the part, delivery time, required quality of cut edge, available trimming equipment, and the skill of the operators.

3.1.5 Class A finish on thermoformed parts

Over the last five years several automotive companies have been investigating the use of thermoforming as the manufacturing process for forming "in mold colored" exterior body panels for the automotive industry (Fig. 3.1-7) [48].

Figure 3.1- 7 MCC spoiler plus roof module (Senoplast, 2005) and thermoformed bumper fascia (GMC, 2005).

The thermoforming process for class A components is attractive to the automotive industry and the mass transit industry due to several reasons such as:

Cost reductions arising from low cost tooling

Low environmental impact – ecological issues related to paint VOC emissions

New market requirements (integration)

There are several aspects of the thermoforming process which need to be refined to achieve a high quality class A finish part including:

Gloss: High surface gloss is a requirement for many products including class A automotive panels. Gloss is affected by both composition of the polymer and processing conditions. For a part surface to exhibit high gloss, the surface must be as smooth as possible. Any surface roughness leads to light scattering, thereby reducing surface gloss. Amorphous materials can achieve high gloss levels, and generally by adding rubber particles the gloss reduces significantly. In the case of semi crystalline polymers, the spherulite structure can lead to surface irregularities which can cause light scattering and therefore reduce gloss. By processing semi crystalline materials in such a way that very small spherulites are formed, high gloss surfaces can be achieved as well. Typical high gloss thermoforming materials are: ABS, PC and example of low gloss materials are: HIPS, TPU, PPO, TPO etc.. It is also possible to obtain glossy surfaces on not glossy materials by thermoforming co-extruded sheets. In co-extruded sheets, both the backing material and the surface material are extruded into a layered sheet to exploit the properties of all the layers of the laminate construction.

Multi layer laminate constituents: To achieve both a structurally stable component (low CTE, high elastic modulus) as well as shiny and attractive surface which is protected against weathering effects (UV, H20) it is always necessary to use co-extruded sheets which incorporate all these features. An example of a multi layer thermoformable sheet for class A finish is shown in Fig 3.1-8.

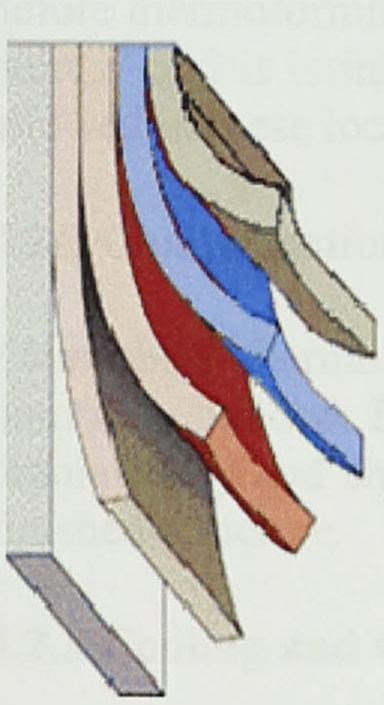

Figure 3.1- 8 Multilayer thermoformable sheet for class A finish parts (GM, 2005).

Besides structural requirements, thermoformed exterior surfaces must:

- Provide chemical resistance (against solvents, oils, etc.)
- Environmental stress cracking resistance
- Electrical conductivity (static electricity build up)
- Surface hardness and scratch resistance

- UV stability and temperature resistance

Other important properties of thermoformable materials include: haze, color retention, and homogeneity of surfaces.

3.2 Twin sheet thermoforming troubleshooting

Twin sheet thermoforming is a promising but challenging process for making hollow double walled industrial parts [49]. The process is increasingly being adopted for a wide variety of applications such as equipment frames, pallets, ducting, and structural chassis parts for medical, printing, and electronic equipment. Generally, in twin sheet thermoforming two sheets are clamped by a double clamp frame with spacers. After heating, the sheets are simultaneously drawn into a female and a male cavity by the action of vacuum pressure, the molds are subsequently closed and the hot sheets are compressed at joining areas designed into the mold. The sheets are thermally bonded to each other into a single part without the need for adhesives or fasteners. However, combining two sheets into a single part is a lot more complicated than forming one sheet. Thermal bonding has to be precise in order to function properly and therefore alignment is critical in the tools.

3.2.1 Precise mold alignment

The need for two matching tools in twin sheet thermoforming requires precise mold alignment before thermoforming trials begin. The points at which the two molds match are known as "press points" and it is in these areas where the thermal bonding occurs. No wiggle room should be allowed in these locations.

3.2.2 Compensation for compression

Twin sheet thermoforming involves 40% to 50% compression of the sheets where they are thermally bonded. In reality after thermal bonding, the thickness of the contact area can reduce dramatically and should be taken into account in determining the mechanical properties of the finished structure.

3.2.3 Cooling and venting

During the process, air gets trapped between the sheets. Upon cooling, the air trapped can collapse the panels. To prevent this, the mold should be designed with vent holes that allow cool air inside the panel. Holes should be sized accordingly to provide enough cooling and avoid marking. In practice, holes are placed on the inside face of the panel so they remain invisible on the outside sheet, when hinges, brackets, or other attachments are to be joined to the thermoformed part, vent holes can be placed in these locations to avoid being easily spotted.

3.2.4 Draw ratio limits

In single sheet thermoforming, it is possible to design parts with 3:1 draw ratios and deep undercuts. What makes this possible is plug assist, which permits material to be mechanically pushed into the mold to reduce wall thinning; however this is not an option in twin sheet thermoforming. This means that twin sheet parts should have generous turning radii at corners and indents and should avoid draw ratios exceeding 2:1.

3.2.5 Elimination of shadowing

Shadowing or visible variation in surface finish occurs at areas adjacent to where the sheets are pressed together. If the panel is to be painted or is a non appearance part, consequences are slight. But if unpainted surface finish is important, shadowing becomes a critical issue. One solution is to bead blast the upper tool so that the entire panel has a textured finish that masks the shadowing. Another answer is to hide the press points as much as possible.

3.2.6 Sheet thickness compatibility

One of the sheets usually is assigned the load bearing role, while the other one present for cosmetic purposes. The difference in sheet thickness should be less than 0.0625 in (1.5875 mm). Greater thickness differentials tend to generate poor parts; the thinner sheet would be subjected to excessive heating and cooling causing excessive sagging and warpage.

3.3 Quickstep Technology

Quickstep, or more specifically, the Quickstep Process, is a range of unique and patented technologies that can be used in the out-of-autoclave manufacture of advanced composite materials [50]. Using balanced pressure and liquid heating and cooling, the Quickstep Process has applications in the aerospace and automotive industries where strength and weight are critical, as well as in many other industries including the mass transit industry seeking to replace metals with composites.

The Quickstep Process involves a unique fluid-filled, balanced pressure, heated floating mould technology for the curing, partial curing and joining of composite materials (Fig. 3.3-1).

It works by rapidly applying heat to the laminate which is trapped between a free floating rigid (or semi-rigid) mould that floats in a Heat Transfer Fluid (HTF). The mould and laminate are separated from the circulating HTF by a flexible membrane or bladder. The temperature and pressure of the HTF behind the mould and flexible membrane stay the same. The Quickstep Process uses balanced pressure, combined with vibration within the HTF and vacuum on the laminate, to remove the air and then compact and heat the laminate to cure the part.

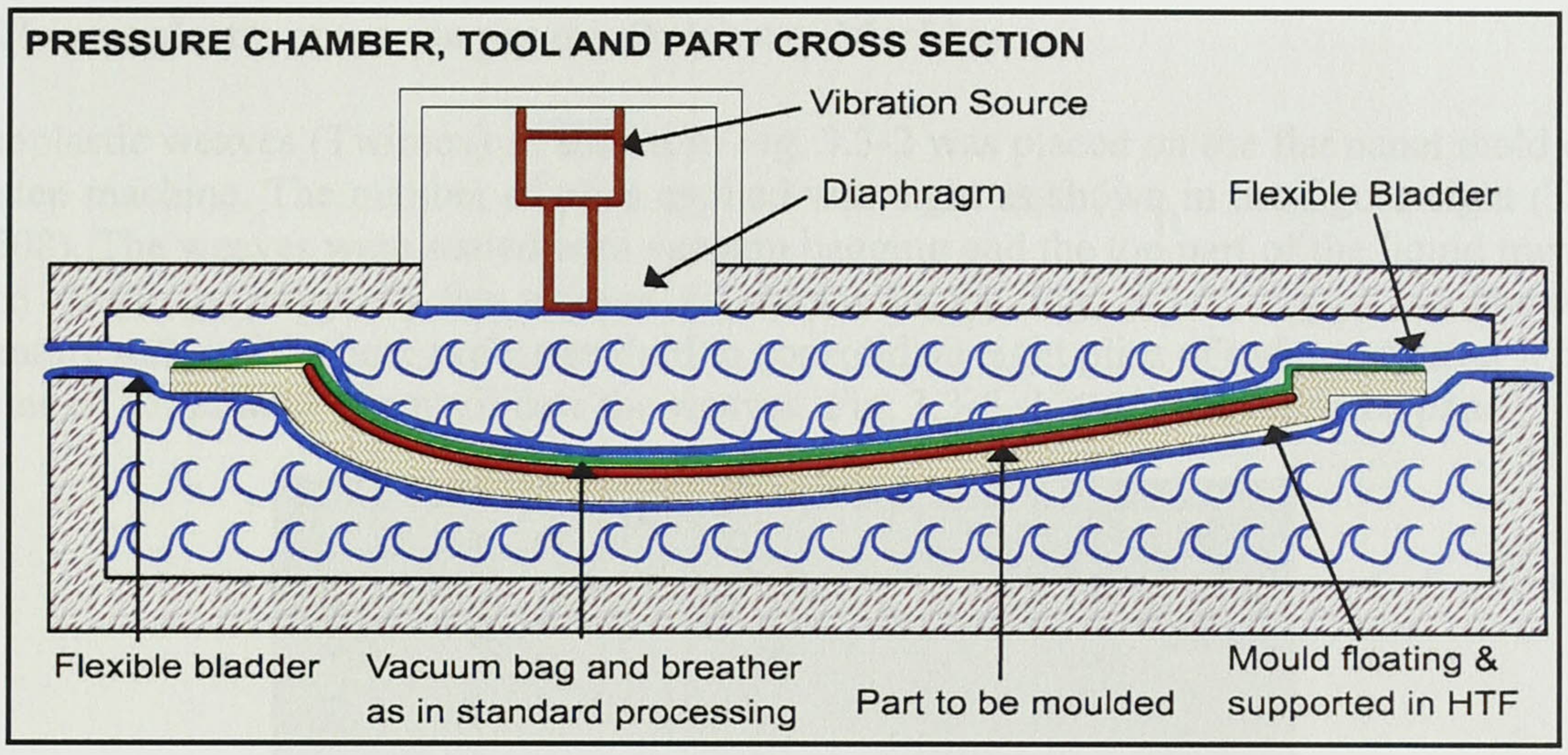

Figure 3.3- 1 Quickstep process [50].

A flexible membrane beneath the mould is bonded into a pressure chamber creating the lower half of a 'clam-shell' like mould set. A second flexible membrane is bonded to a separate pressure chamber creating the upper half of the clam-shell. These HTF filled pressure chambers are clamped together during processing. This permits the laminate to be compressed while the mould is not subject to any distortion or stress as it is floating in a balanced pressure/force environment within the HTF.

The use of fluid to control temperature offers several advantages, including:

Up to 25 times the heat transfer rate of gas systems like autoclave and circulating air ovens, resulting in shorter cycle times

Improved control of part temperature, with fewer hot or cold spots on the mould

Rapid decrease in prepeg resin viscosity, resulting in improved fiber wetting and laminate consolidation without high pressures

The ability to modulate temperature quickly, permitting more accurate injection temperatures or repeatable resin advancement in multi-step cure cycles or in melding of complex components

Reduced exothermic risk as liquid carries away the heat of reaction more efficiently than air or nitrogen

The Quickstep Process achieves this superior performance on larger parts with significantly quicker cycle times at far lower pressures of 1 to 4 psi and lower labor costs than alternative autoclave production systems. Despite the superior performance characteristics, the Quickstep Process is competitive on cost with generic production methodologies like vacuum bag and liquid infusion techniques.

3.3.1 Thermoplastic processing at the Quickstep Machine

Thermoplastic weaves (Twintex) as shown in Fig. 3.3-2 was placed on the flat panel mold of the Quickstep machine. The number of plies applied was eight as shown in the figure eight (TE501 to TE508). The weaves were sealed with vacuum bagging and the top part of the liquid trays was lowered down to compress the weaves as shown in the Fig. 3.3-3. Fig. 3.3-4 shows the temperature ramp of the heat exchange fluid to consolidate eight plies of twintex weave. It took a total time of 17 minutes to consolidate the weaves. Fig. 3.3-5 shows a consolidated panel.

Figure 3.3- 2. Twintex weaves.

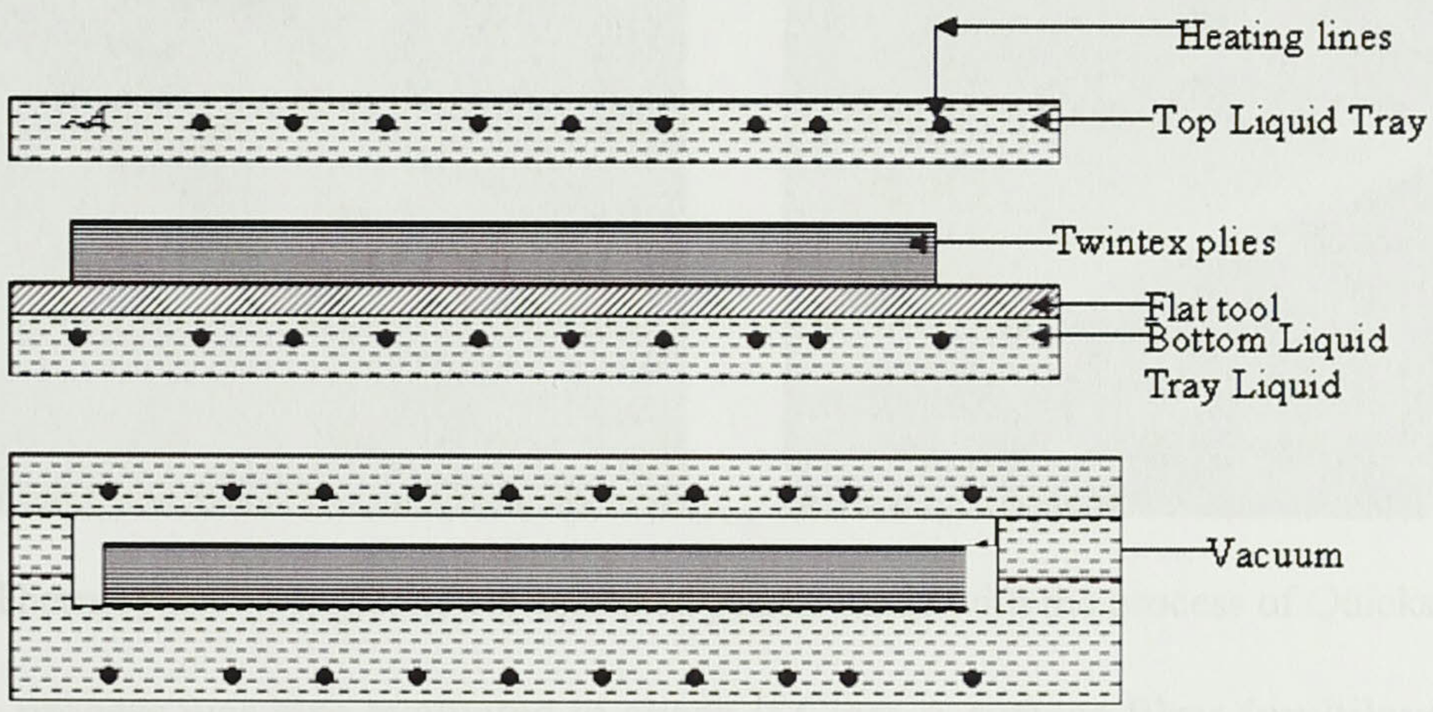

Figure 3.3- 3 Consolidation of Twintex weaves.

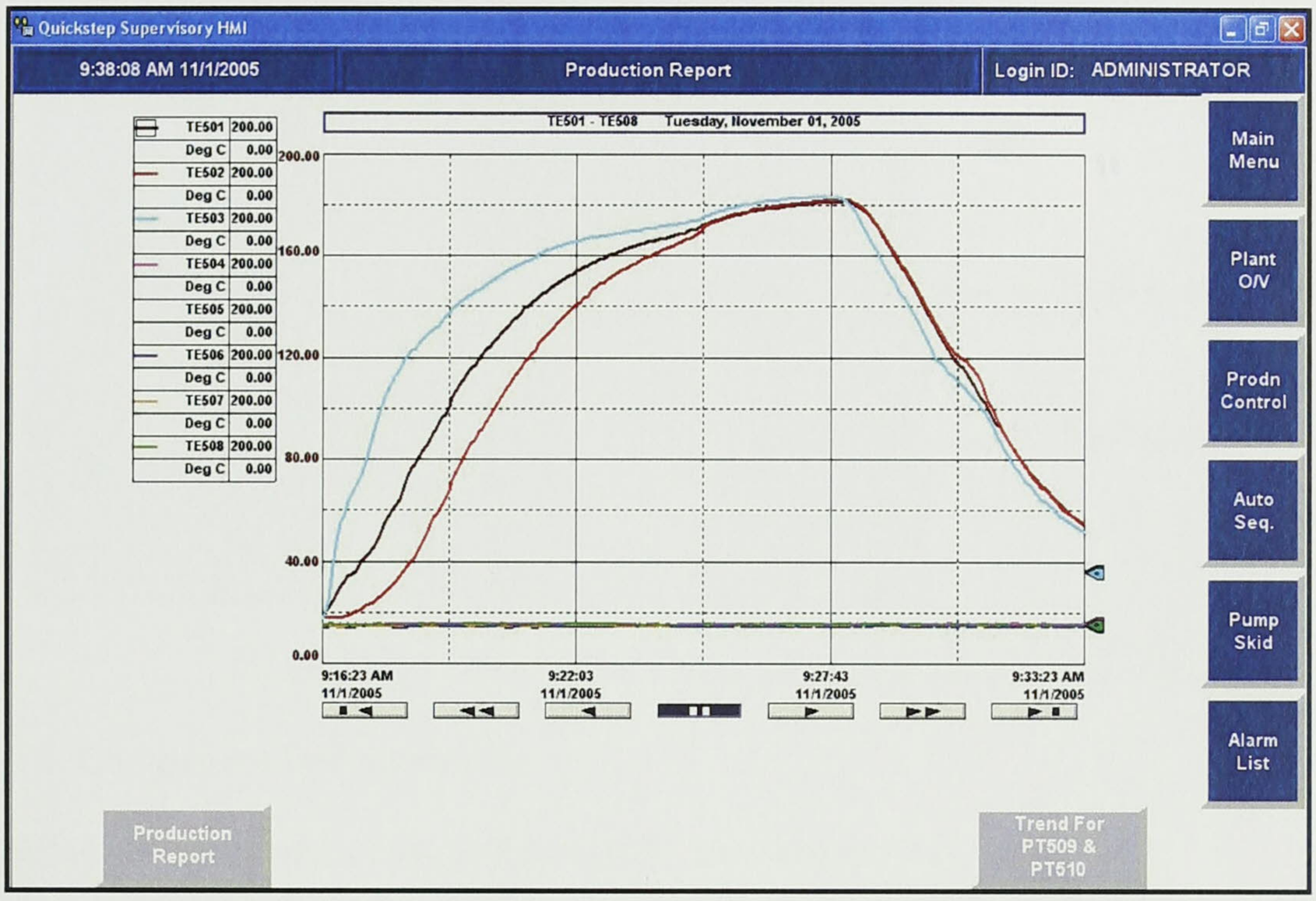

Figure 3.3- 4 Temperature profile of an 8 ply twintex weave.

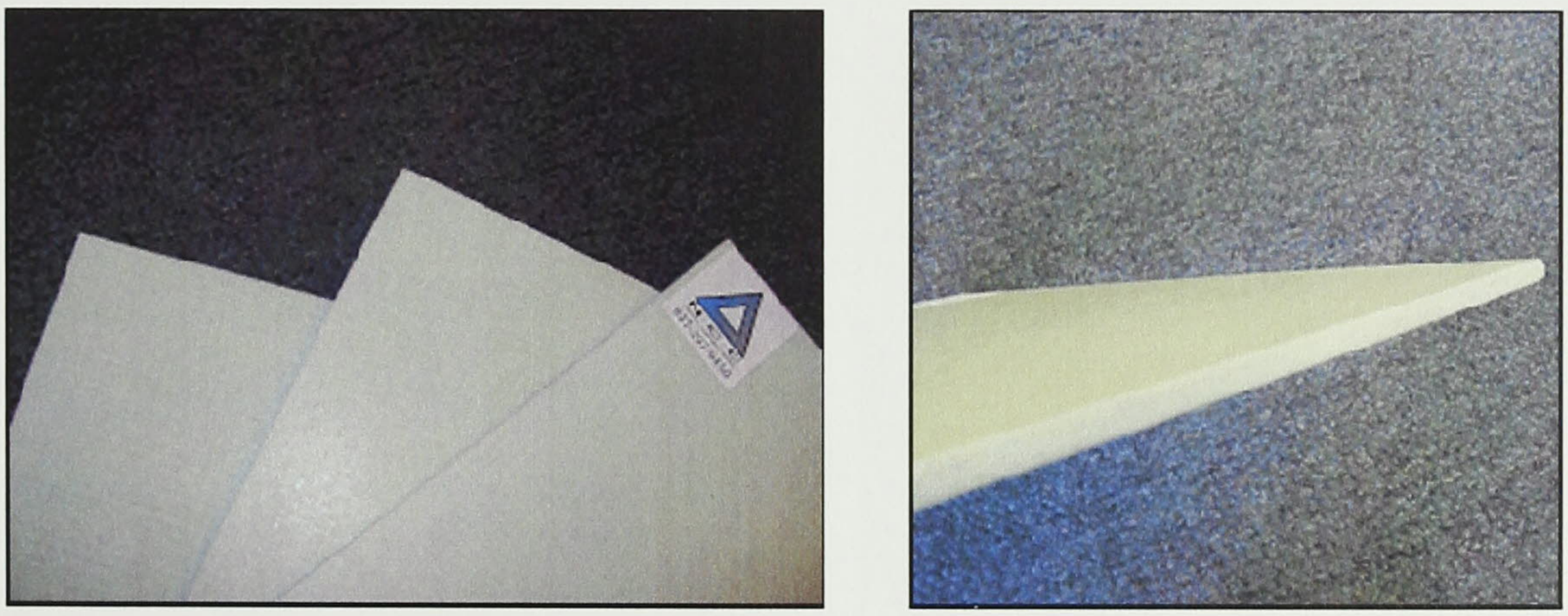

Figure 3.3- 5 Thermoplastic composite consolidated panels made with the process of Quickstep.

The quickstep process was also evaluated to check if Class A surface films (multilayered colored thermoplastic films) can be used to adhere to the thermoplastic composite plies. Instead of eight twintex plies, only one ply was used and an ionomeric film was placed at the top of the ply and the materials were made to go through the same cycle as mentioned in the previous paragraph for the quickstep processing. As shown in the Fig. 3.3-6, the film was not able to survive the consolidation temperature of the thermoplastic composite sheets. Bubbles started appearing on the surface of the film.

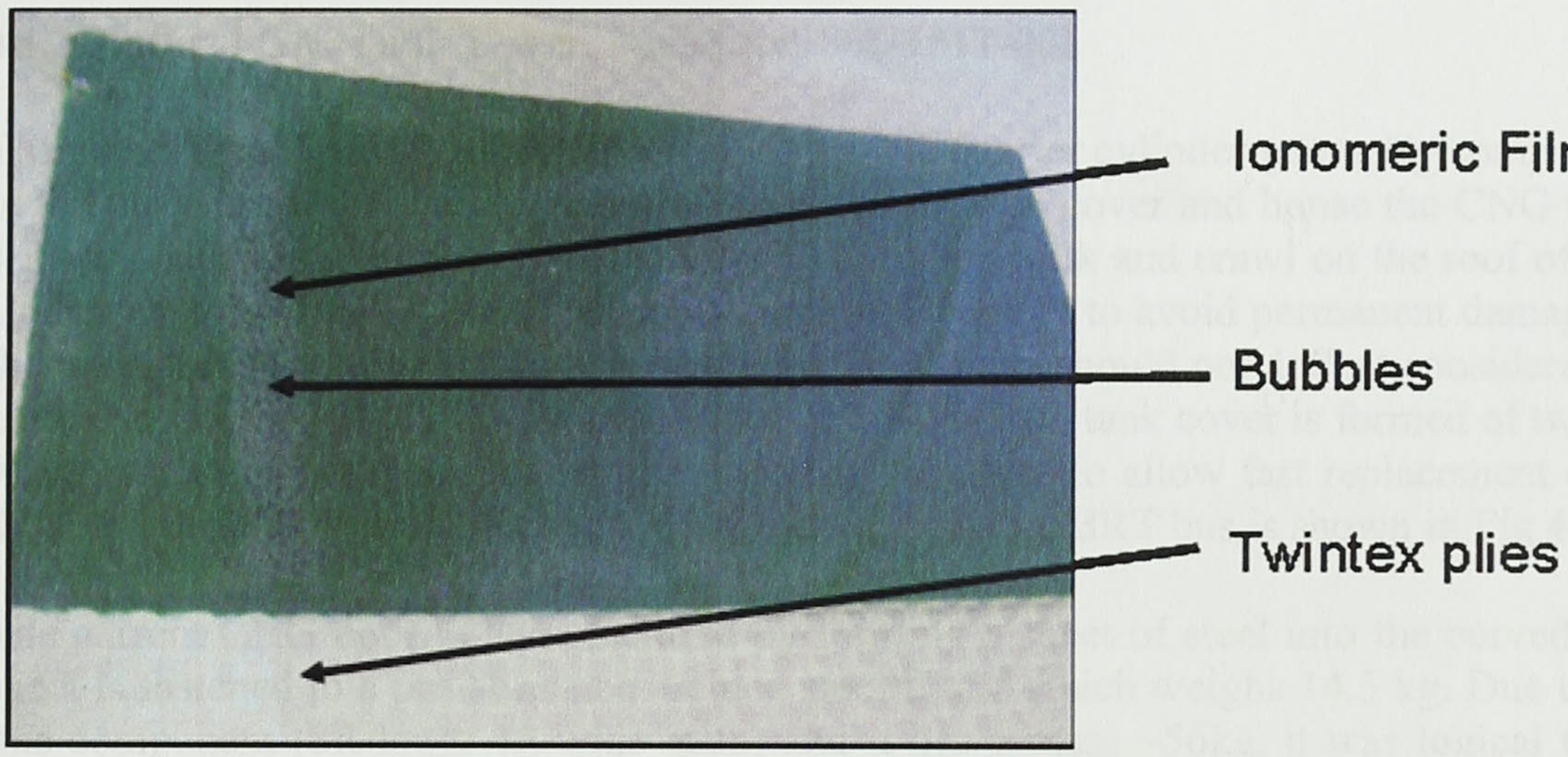

Figure 3.3- 6 Bubbles on the surface of the thermoplastic color film.

IV. Component Demonstration

4.1. Component selection, and design for manufacturing

In the initial discussion with NABI a CNG cover roof door was targeted as a component for the study. Fig. 4.1-1 shows a CNG door which was the target for redesign and manufacturing during this year of the project. This door is part of a series of doors located on the roof top of the bus and provides access to the CNG tank.

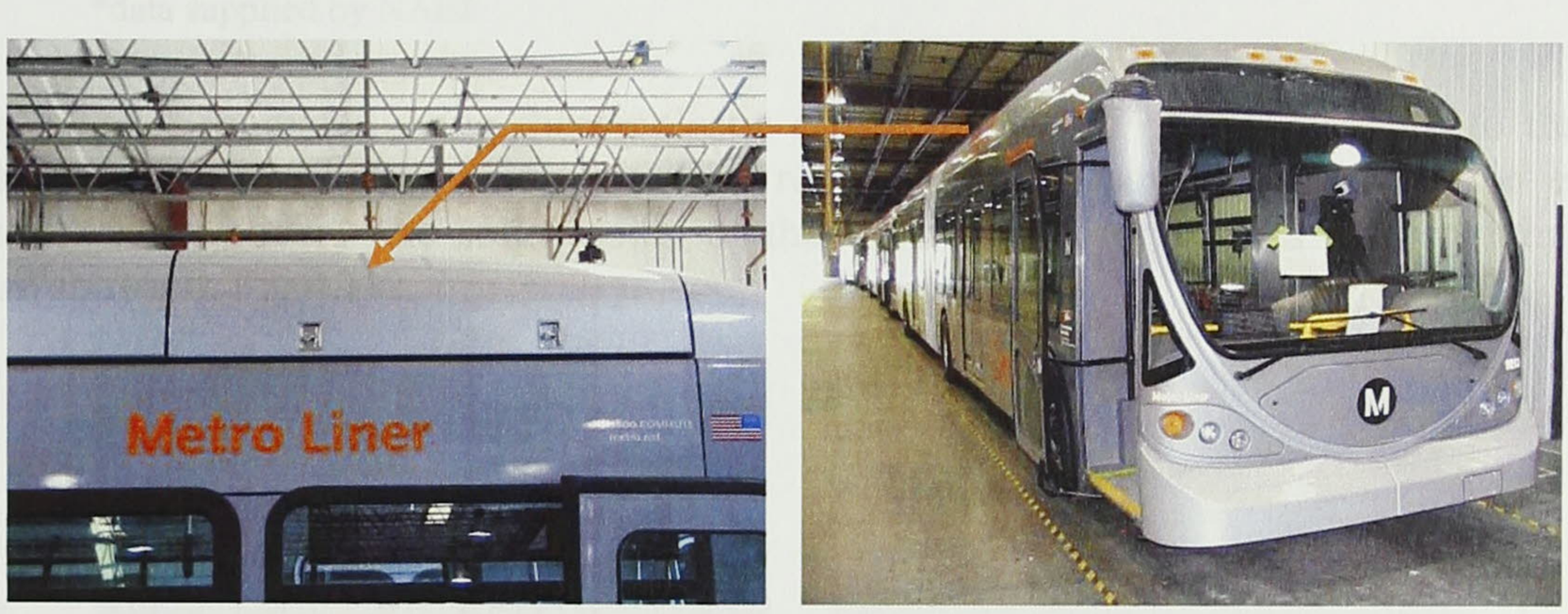

Figure 4.1- 1 CNG roof door.

4.1.1 Natural Gas Tank Cover, NABI Ref 801-1511-001

The compressed natural gas (CNG) tank cover is a quarter cylinder geometry component located in the top part of the bus. Its main function is to protect, cover and house the CNG tank. During service and maintenance of the bus, technicians often walk and crawl on the roof of the vehicle. Under these conditions, the cover needs to be stiff enough to avoid permanent damage caused by the weight of two persons of average weight. The covers should not deflect considerably or come in contact the CNG tank or any adjacent piping. The CNG tank cover is formed of two half shells which meet at the center rib and are hinged at the edges to allow fast replacement or service of the CNG tank. A typical CNG tank door installed on a 60 BRT bus is shown in Fig 4.1-1.

The current CNG door is manufactured by forming a sheet of steel into the curved shape. This sheet is fastened to a prefabricated welded steel frame which weighs 14.5 kg. Due to the size of this component (8ft long, 4ft wide each) and it has a mass ~56kg, it was logical to target this component for weight reduction. Mass and volume data of the current steel CNG tank door shell is presented in Table 4.1-1.

Table 4.1- 1 CNG Cover manufacturing parameters*

	Value	Unit
Current part weight	56	kg
Process used	Sheet metal forming	
Finishing operations	Priming, painting	
Current part volume	0.0072	m^3

*data supplied by NABI

CNG tank cover produced using thermoplastic composite would require changes to the cross sectional geometry, including thickness. The redesign would have to maintain the external appearance of the cover. The solid model of the CNG tank door and its corresponding steel frame are shown in Fig 4.1-2.

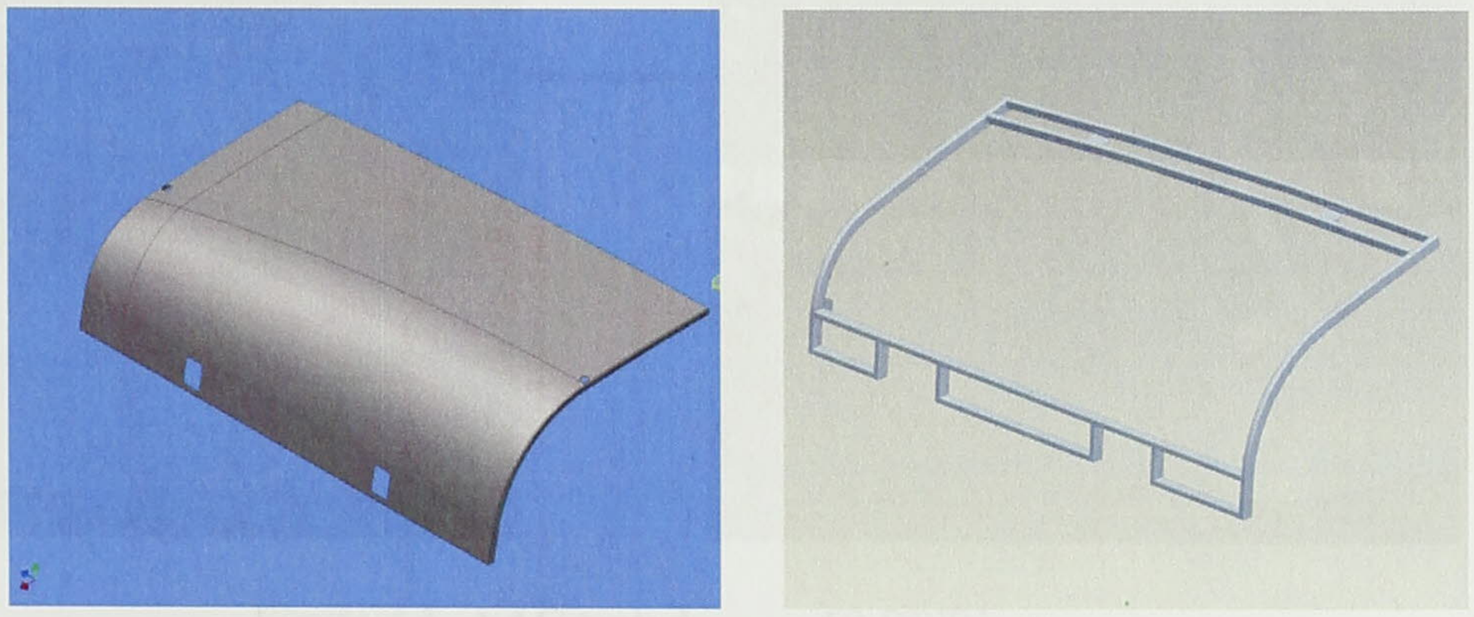

Figure 4.1- 2 CNG cover solid model and steel frame skeleton generated in Pro E Wildfire.

4.1.2 Thermoplastic composite concept

A thermoplastic composite CNG door was conceived to feature multilayered thermoformable sheets which comprise all structural and aesthetical aspects of the doors. An example of this type of architecture is illustrated in Fig. 4.1-3.

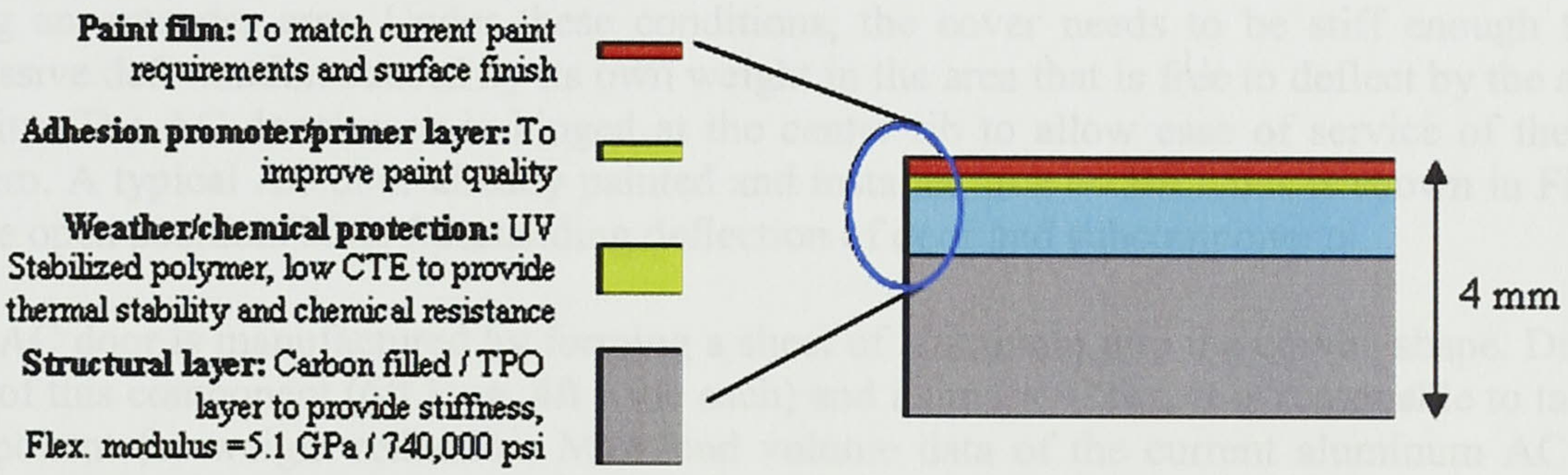

Figure 4.1- 3 Thermoplastic composite multi layer sheet concept.

Such a layered construction has been introduced in [51]. By using a thermoplastic composite alternative, savings of up to 55 % in weight savings can be achieved (based on mass calculations of a CNG door twice the existing thickness (6 mm) and the density of the thermoplastic composite arrangement (~1.5 g/cm^3).

4.1.3 Design for manufacturing (AC Door)

In further discussions with NABI, a decision was made to undertake an AC cover door instead of a CNG cover door, since the AC door is about 2 ft shorter than the CNG door, making tooling and compression molding less expensive and easier. Fig. 4.1-4 (a) shows the AC door which is the candidate part for redesign and manufacturing for the 2005-2006 project. This door is part of a series of doors located in the roof top of the bus and gives access to the HVAC equipment.

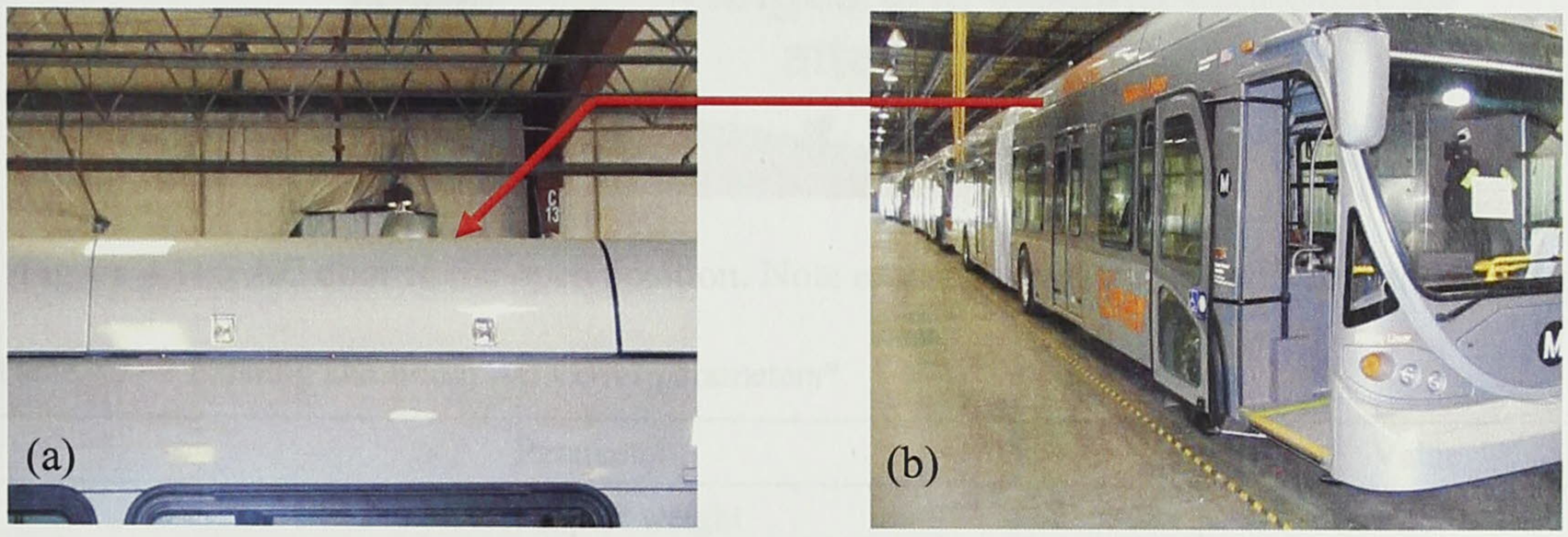

Figure 4.1- 4 AC tank door on 60 BRT bus.

4.1.3.1 AC door/cover, NABI Ref 61A-7119-001

The AC door/cover is a curved geometry component located in the top part of the bus. Its main function is to protect, cover and house the HVAC equipment. The door has a no step requirement, and therefore its structural requirements are much lower than those for the CNG door. During service and maintenance of the bus, technicians open this cover and prop it open using an extender arm. Under these conditions, the cover needs to be stiff enough to avoid excessive deformation caused by its own weight in the area that is free to deflect by the action of gravity. The AC door/cover is hinged at the center rib to allow ease of service of the HVAC system. A typical AC door already painted and installed in a 60 BRT bus is shown in Fig. 4.1-5 in the open position. Note freestanding deflection of door and subcomponents.

The AC door is manufactured by forming a sheet of aluminum into the curved shape. Due to the size of this component (6ft long, 4ft wide each) and its mass ~21kg, it is reasonable to target this component for weight reduction. Mass and volume data of the current aluminum AC door is presented in Table 4.1-2. The existing AC door is assembled to a welded stiffener in the center of the door which stabilizes the sheet metal and improves its bending performance. The process for manufacturing the door includes several labor intensive steps which are listed in Fig. 4.1-6.

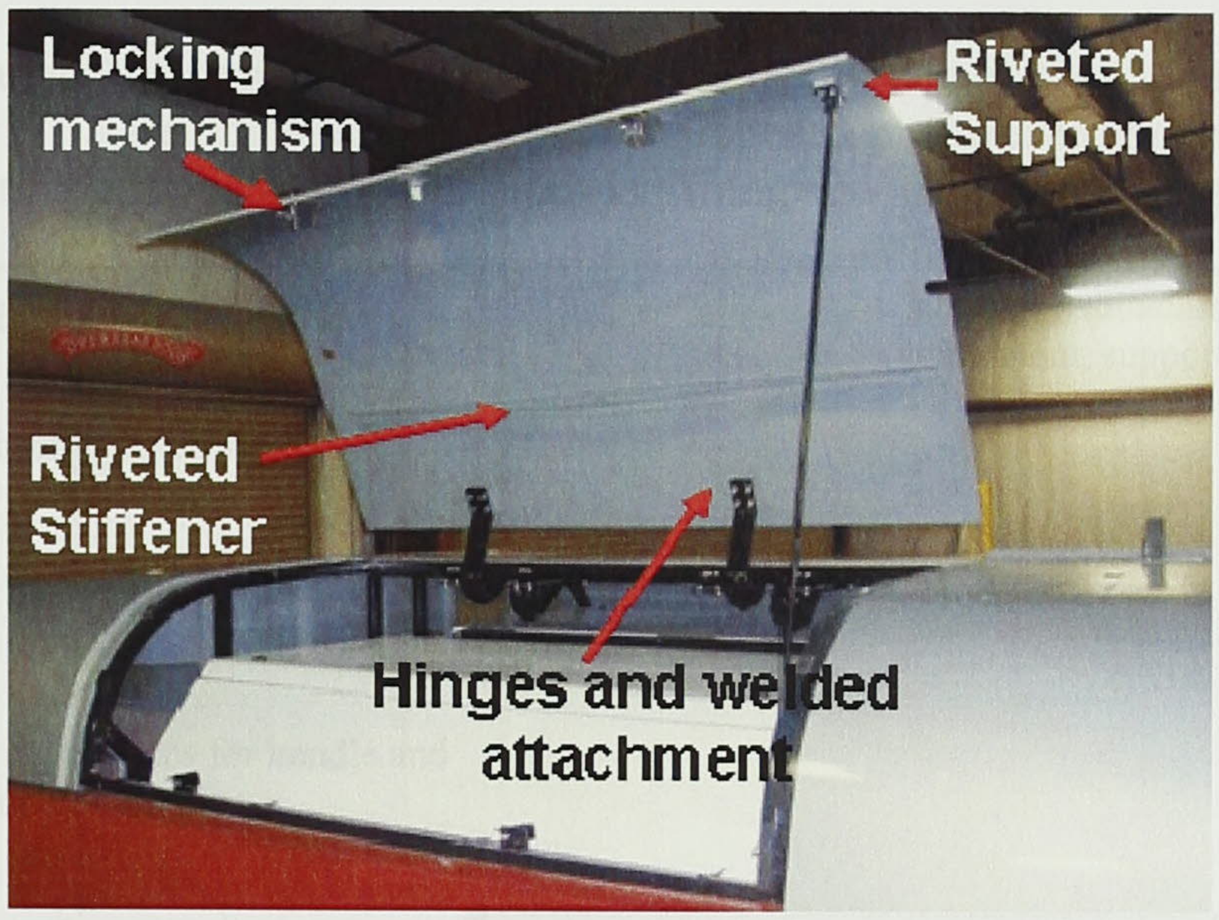

Figure 4.1- 5 AC door in the open position. Note extender arm, welded stiffener and hardware.

Table 4.1- 2 Existing aluminum AC Cover parameters*

Parameter	Value	Unit
Current part weight	20	kg
Current part volume	0.0071	m^3
*data based on original model by NABI		

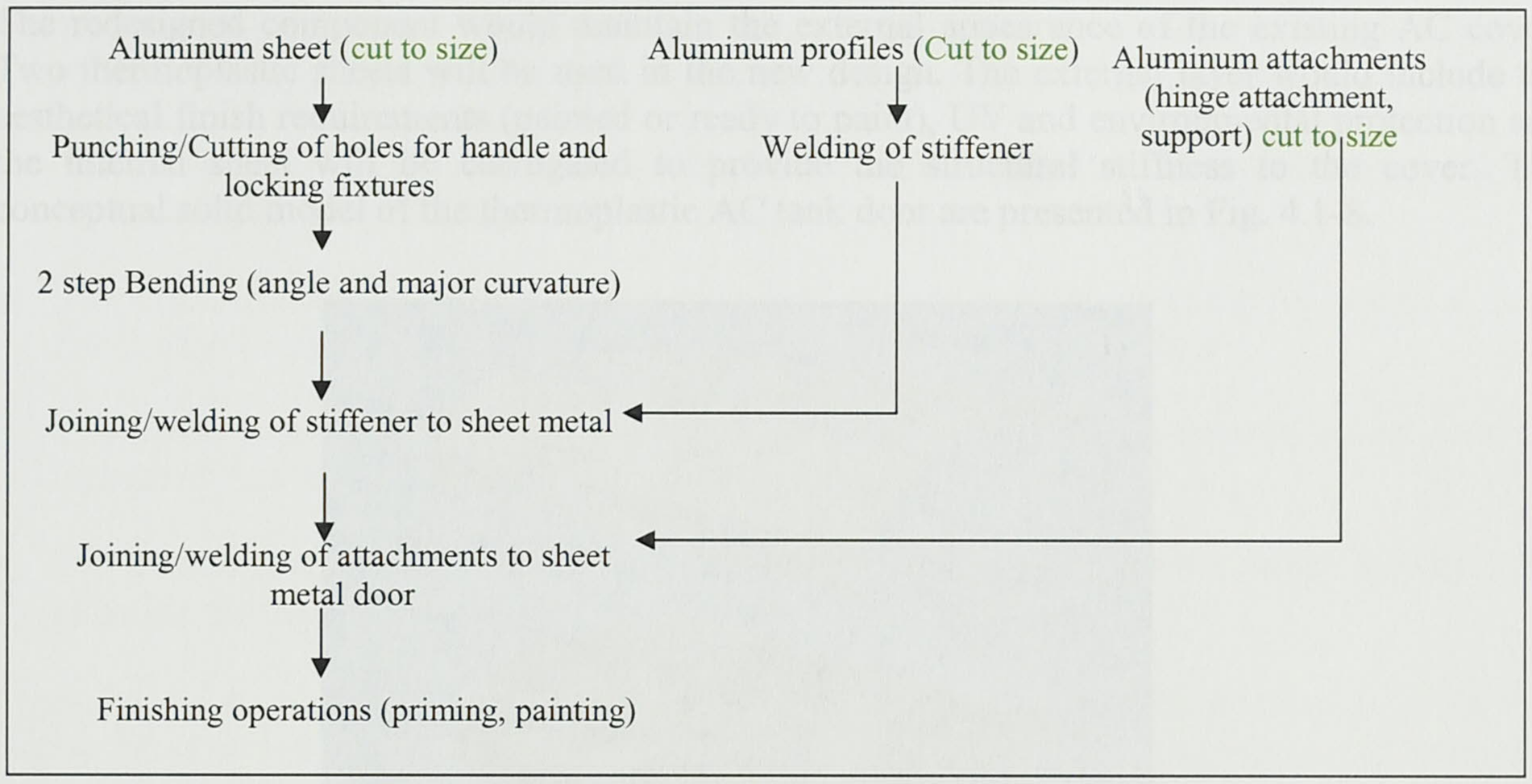

Figure 4.1- 6 Existing manufacturing process algorithm for aluminum AC door.

The proposed manufacturing process algorithm for the fabrication of the thermoplastic AC door is shown in Fig. 4.1-7. The implementation of this proposed manufacturing scheme would save considerable labor time and result in homogeneous, strong and visually pleasing AC covers.

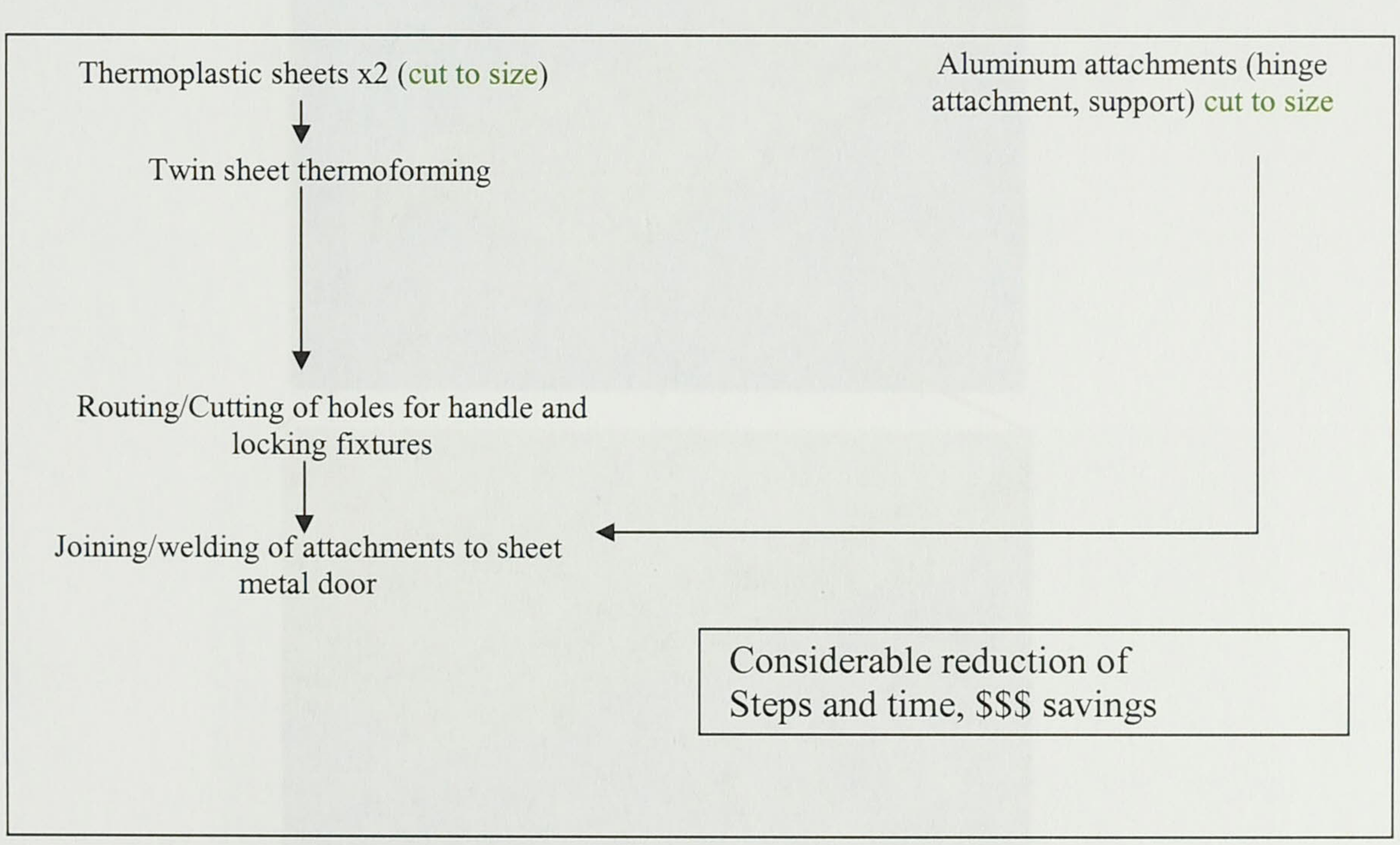

Figure 4.1- 7 Proposed manufacturing process algorithm for thermoplastic AC door.

The redesigned component would maintain the external appearance of the existing AC cover. Two thermoplastic sheets will be used in the new design. The external layer would include the aesthetical finish requirements (painted or ready to paint), UV and environmental protection and the internal sheet will be corrugated to provide the structural stiffness to the cover. The conceptual solid model of the thermoplastic AC tank door are presented in Fig. 4.1-8.

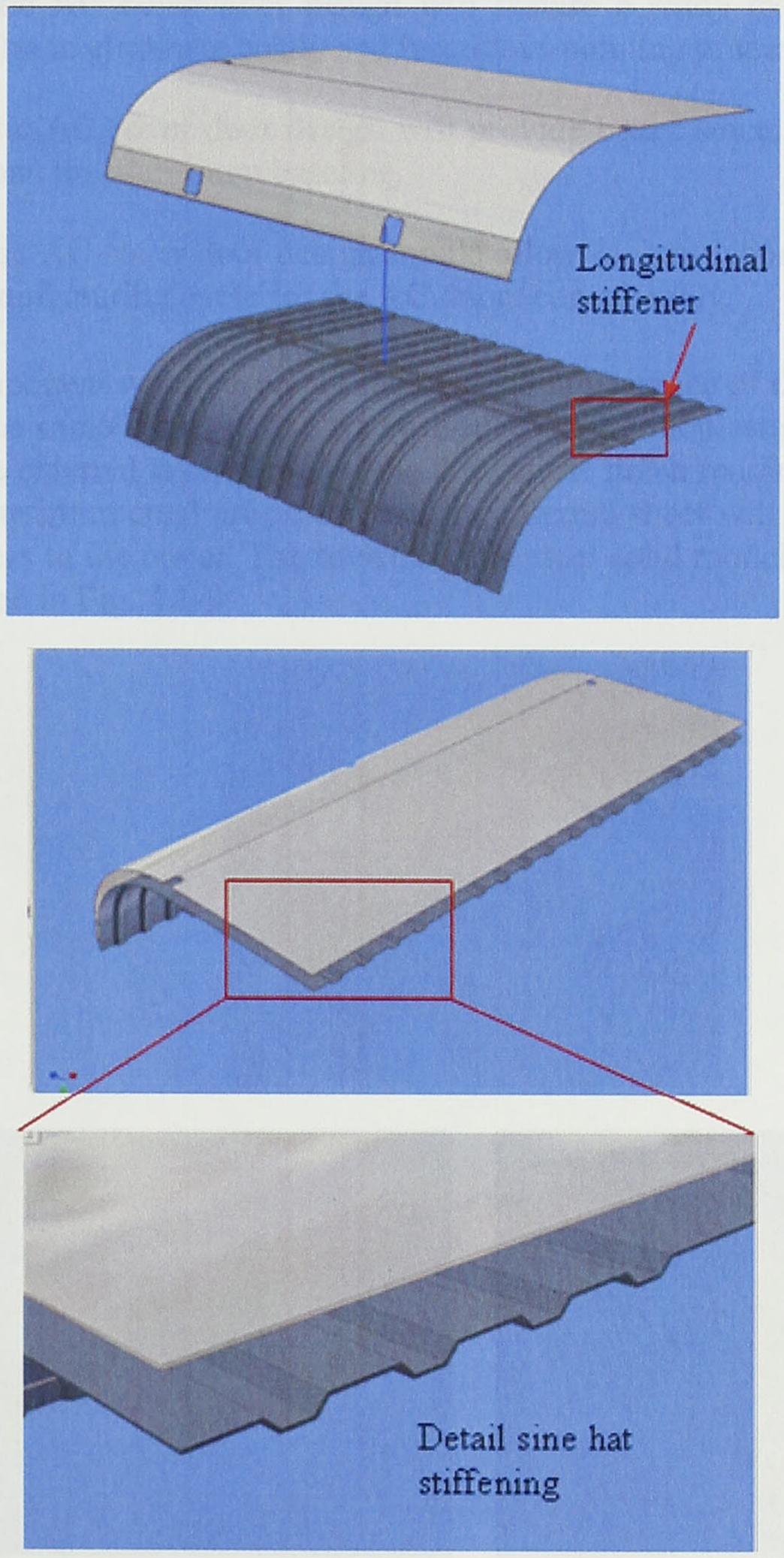

Figure 4.1- 8 Conceptual thermoplastic AC door solid model and detail on twin sheet concept.

- The thermoplastic AC cover door should exhibit substantially less free standing deformation than the current aluminum design, when propped open with the extender arm (see Fig. 4.1-5)
- The thermoplastic AC cover door should provide significant weight savings in comparison to the existing aluminum design (25 kg).
- The thermoplastic AC cover door design will feature a ready to paint surface or a color matched paint film to eliminate costly and hazardous painting processes.
- The thermoplastic AC cover door design will provide better sound absorption and damping characteristics than the aluminum baseline.
- The thermoplastic AC cover door design should allow for less labor intensive manufacturing reducing the manufacturing cycle for the AC doors considerably.

The redesigned component would preserve the external appearance of the existing AC cover and will be fitted with the same hardware presently used. Two thermoplastic sheets would be used in the new design. The external layer provides the aesthetical finish requirements (painted or ready to paint); UV and environmental protection and the internal sheet will be corrugated to provide the structural stiffness to the cover. The revised conceptual solid model of the thermoplastic AC tank door is presented in Fig. 4.1-9.

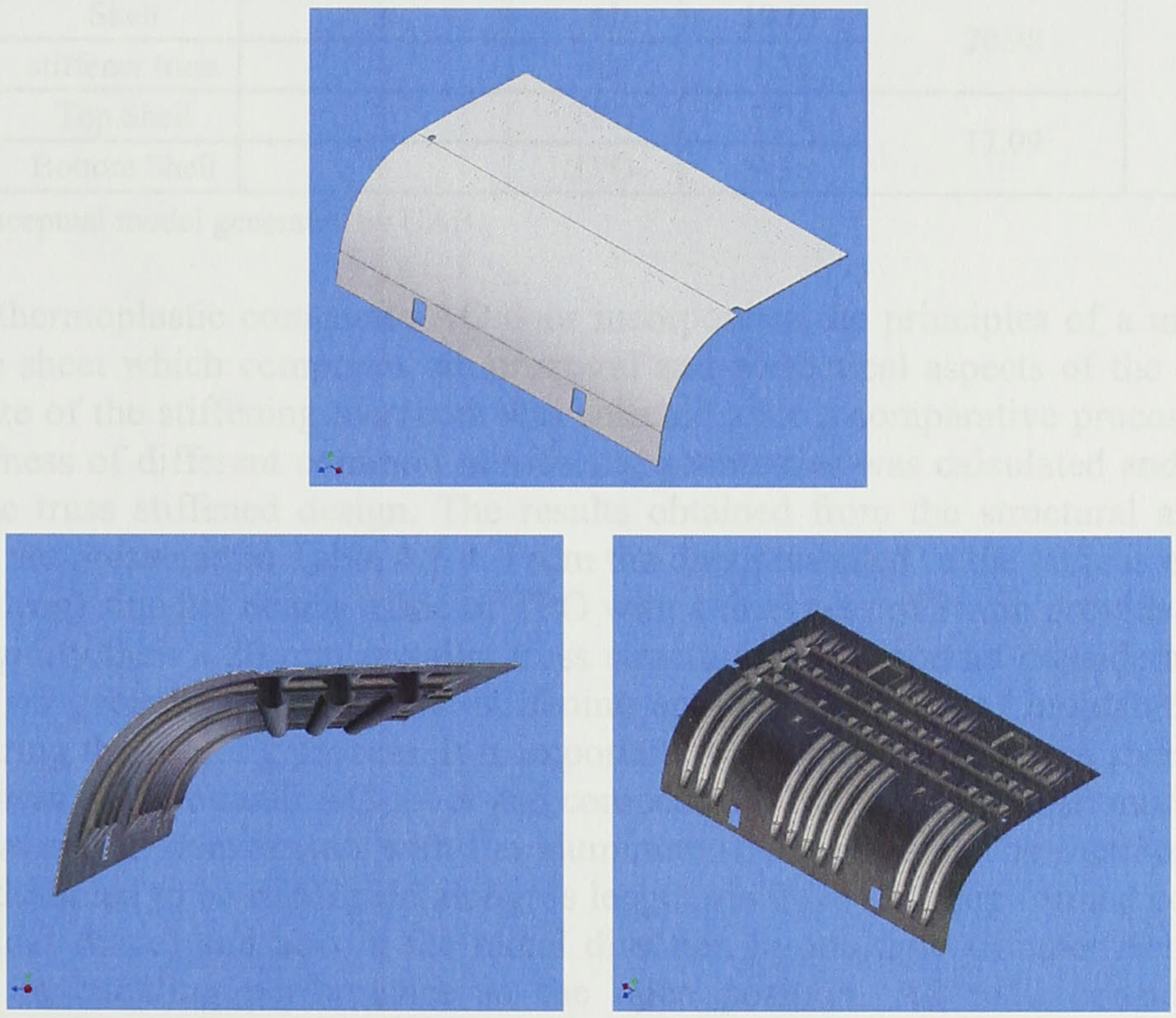

Figure 4.1- 9 External view and internal view of sine-hat stiffened concept for thermoplastic AC cover (solid model)

4.1.3.2 Structural design

The envisioned thermoplastic composite AC door incorporates the principles of a multilayered thermo formable sheet which comprises all structural and aesthetical aspects of the doors. For the structural analysis the initial thickness of each sheet is considered to be 3 mm. The resulting stresses and strains and apparent stiffness of this configuration were the starting point in determining the final thicknesses of the sheets in order to match the stiffness of the aluminum AC door. The structural layer incorporated sinusoidal grooves in the hoop direction to increase the moment of inertia and therefore the stiffness of the section. The incorporation of a longitudinal groove or a series of these increase the stiffness of the door in the longitudinal direction and serve as a replacement of the structural truss existing in the current aluminum design. The weight and volume calculations for the thermoplastic AC door assuming two 3 mm sheets of TPO are shown in Table 4.1-3. It is expected to achieve a considerable labor cost saving and an increase in the rate at which these parts are manufactured by transferring to this technology while also achieving an 18.5% weight savings in comparison to the aluminum structure.

Table 4.1- 3 Thermoplastic AC Cover parameters*

		Thickness (mm)	Material	Mass (kg)	Total Mass (kg)	Weight savings
NABI design	Shell	3	Al	19.63	20.98	18.54%
	stiffener truss	--	Al	1.35		
UAB design*	Top Shell	3	TPO	7.74	17.09	
	Bottom Shell	3	TPO	9.35		

*data based on conceptual model generated by UAB

The envisioned thermoplastic composite AC door incorporates the principles of a multilayered thermo formable sheet which comprises all structural and aesthetical aspects of the doors. The geometry and size of the stiffening members was selected after a comparative process in which the bending stiffness of different common reinforcing geometries was calculated and compared with the baseline truss stiffened design. The results obtained from the structural analysis are summarized and are presented in Table 4.1-4. From the data presented in the table is evident that two (4"/70 mm-deep) sine hat beams made of TPO with a thickness of 3 mm provide almost the same flexural rigidity than a 20 mm metallic truss structure. An important consideration in the selection of the rib geometry was that the stiffening approach had to be "moldable" with the internal sheet during the forming process. It is important to state that the internal sheet enhances the flexural stiffness of the overall AC cover and compensates for the low elastic modulus of the thermoplastic material in comparison with the aluminum/steel baseline. The thermoplastic AC cover door was designed to be reinforced along its length via three (3) deep formed corrugations (7" deep sinusoidal shape) and also in the radial direction by multiple slimmer ribs (2" deep) which increase its buckling performance in the open position. All radii considered were maximized to minimize the probability of wrinkles during the molding of the prototypes.

Table 4.1- 4 Calculated deflections for different beam sections under an assumed flexural loading regime

Case	2D beam	Cross Sectional Area	Maximum deflection	Material Properties
1.	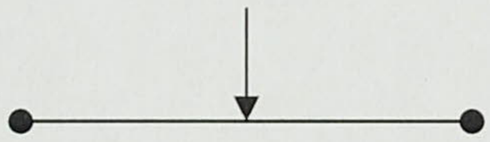	total height = 20 mm	27.8 mm	Al E = 70 GPa
2.		total height = 20 mm	2.9 mm	Al E=70 GPa
3.	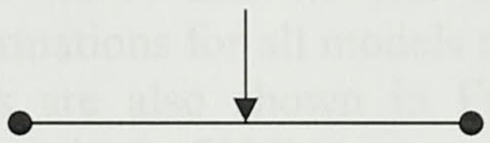	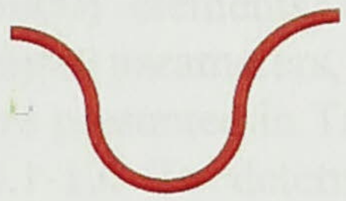 total depth = 39 mm	125.6 mm	PP E=2 GPa
4.	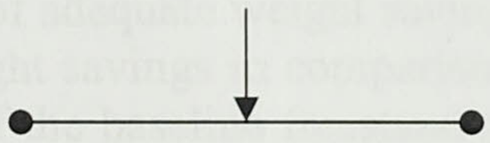	total depth = 39 mm	68.3 mm	PP E =2 GPa
5.		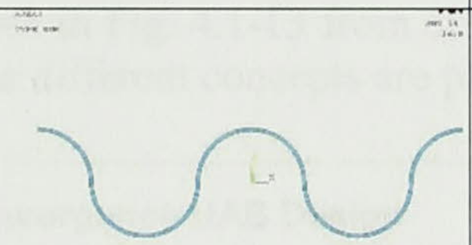 total depth = 70 mm	3.38 mm	PP E=2 GPa

In order to determine the thickness of the two sheets and the expected deformations to a variety of load cases, several finite element models were built to provide detailed information on the considered design as well as in the metallic (Al/steel) baseline. The loading scenario used for these analyses simulates the free-standing deflection observed on the AC cover in its open position (Fig. 4.1-10). This loading scenario includes: inertial loading (a function of the density of the cover's constituents and the action and direction of gravity), and displacement/rotation constraints (at the hinged connections and at the point of attachment of the extender arm) and is shown graphically in Fig. 4.1-10. All the finite element models developed were carefully checked for element shape, aspect ratio and jacobian calculations.

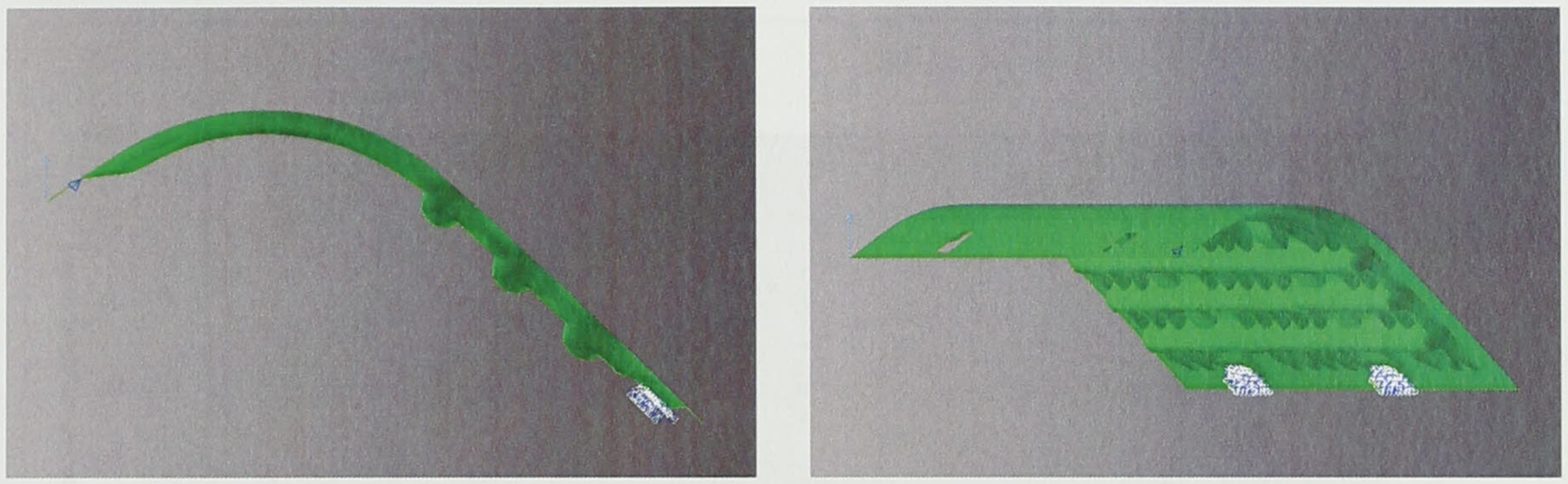

Figure 4.1- 10 Boundary Conditions for structural analysis of AC cover. Translation constraints in blue, rotation constraints in white, Direction of inertial loading in cyan.

Both the baseline design simulations and the new UAB concept simulations were run and analyzed for convergence. The solid design models were generated in Pro/E wildfire. An IGES file of the solid design was inputed to Hypermesh® for meshing. Three different mesh sizes were considered in all cases obtaining solutions to coarse size meshes (~8000 elements) intermediate meshes (~15000) and fine meshes (~35000) elements until deformation convergence was reached (Figs. 4.1-11 and 4.1-12). The input parameters, material properties, total mass and resulting deformations for all models run are presented in Table 4.1-5. The convergence plots for the two cases are also shown in Fig. 4.1-13. To determine the optimum thickness of the individual sheets in the UAB concept, three different thicknesses were evaluated (2 mm, 2.5 mm, and 3 mm). The 3 mm external sheet/3 mm internal sheet combination was found to provide a combination of adequate weight savings vs. low freestanding deflection with a total weight of 15 kg (41% weight savings in comparison with baseline design) and a total deformation of 27 mm almost half of the baseline freestanding deflection of 48 mm. The deformation contours for the baseline design and the UAB concept are shown in Fig. 4.1-13 from different isometric perspectives. The resulting deformations and the total mass of the different concepts are plotted in Fig. 4.1-14.

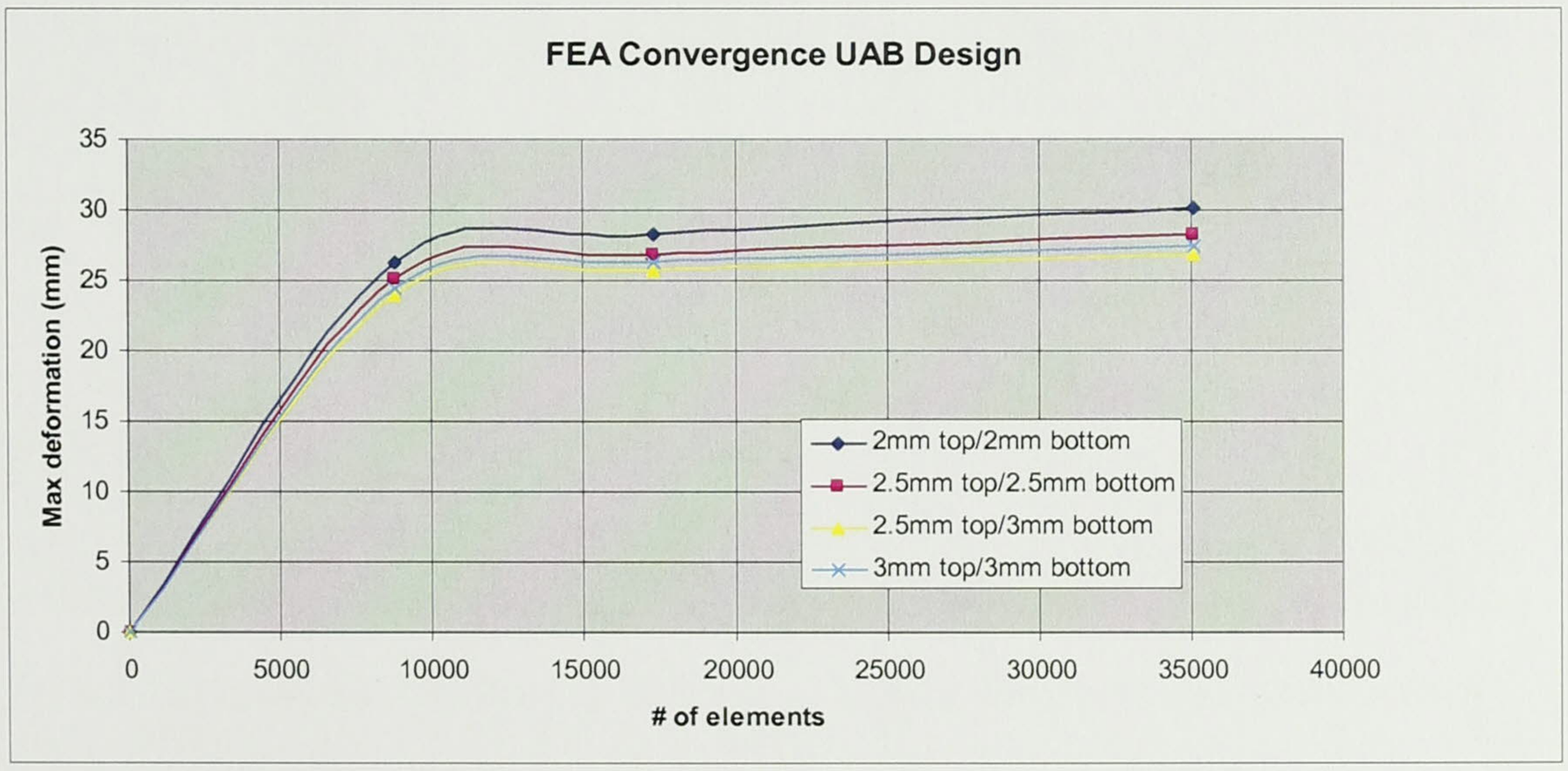

Figure 4.1- 11 Deformation convergence for UAB concept model of AC cover

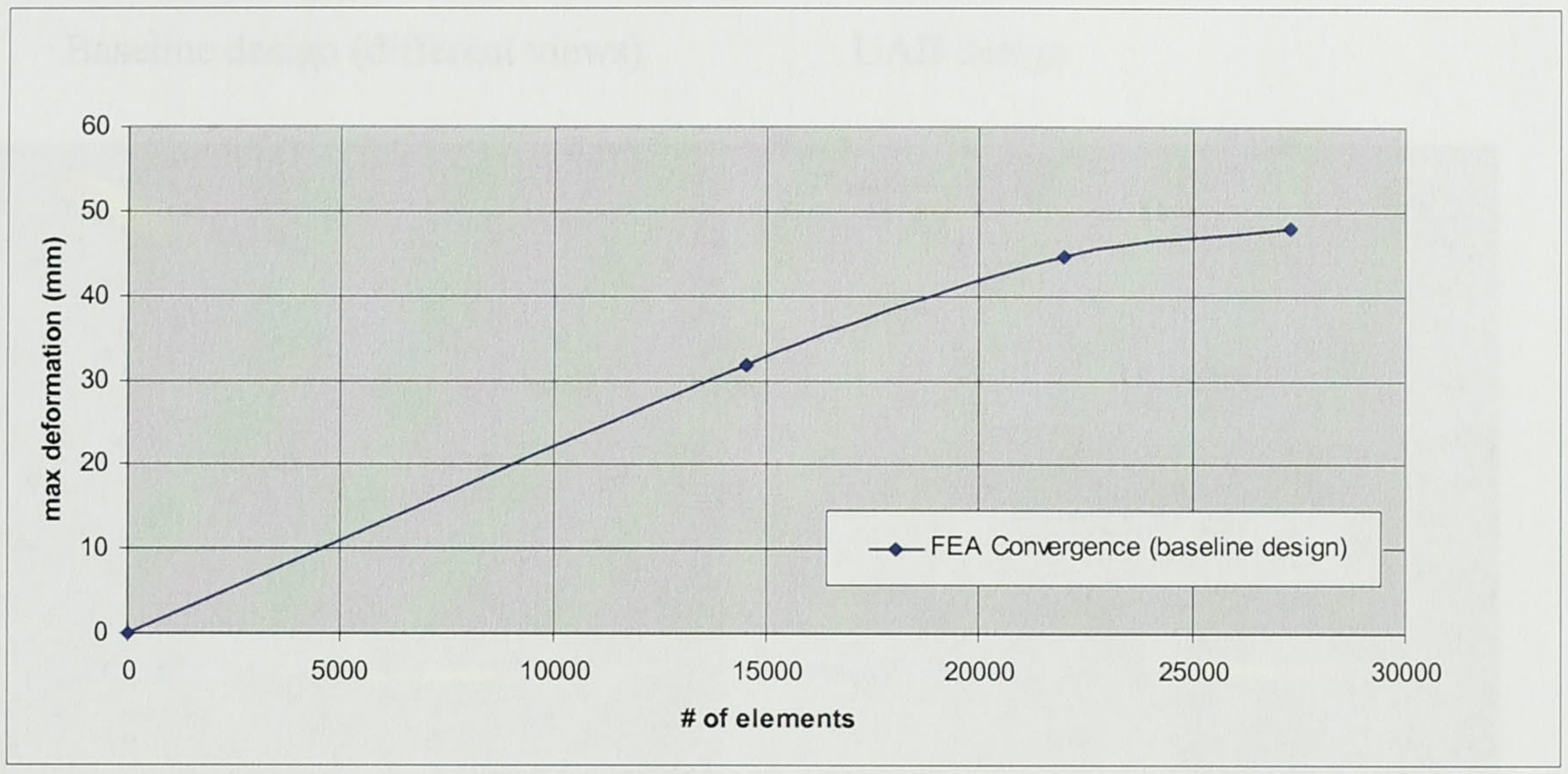

Figure 4.1- 12 Deformation convergence plot for baseline design of AC cover.

Baseline design (different views)

UAB design

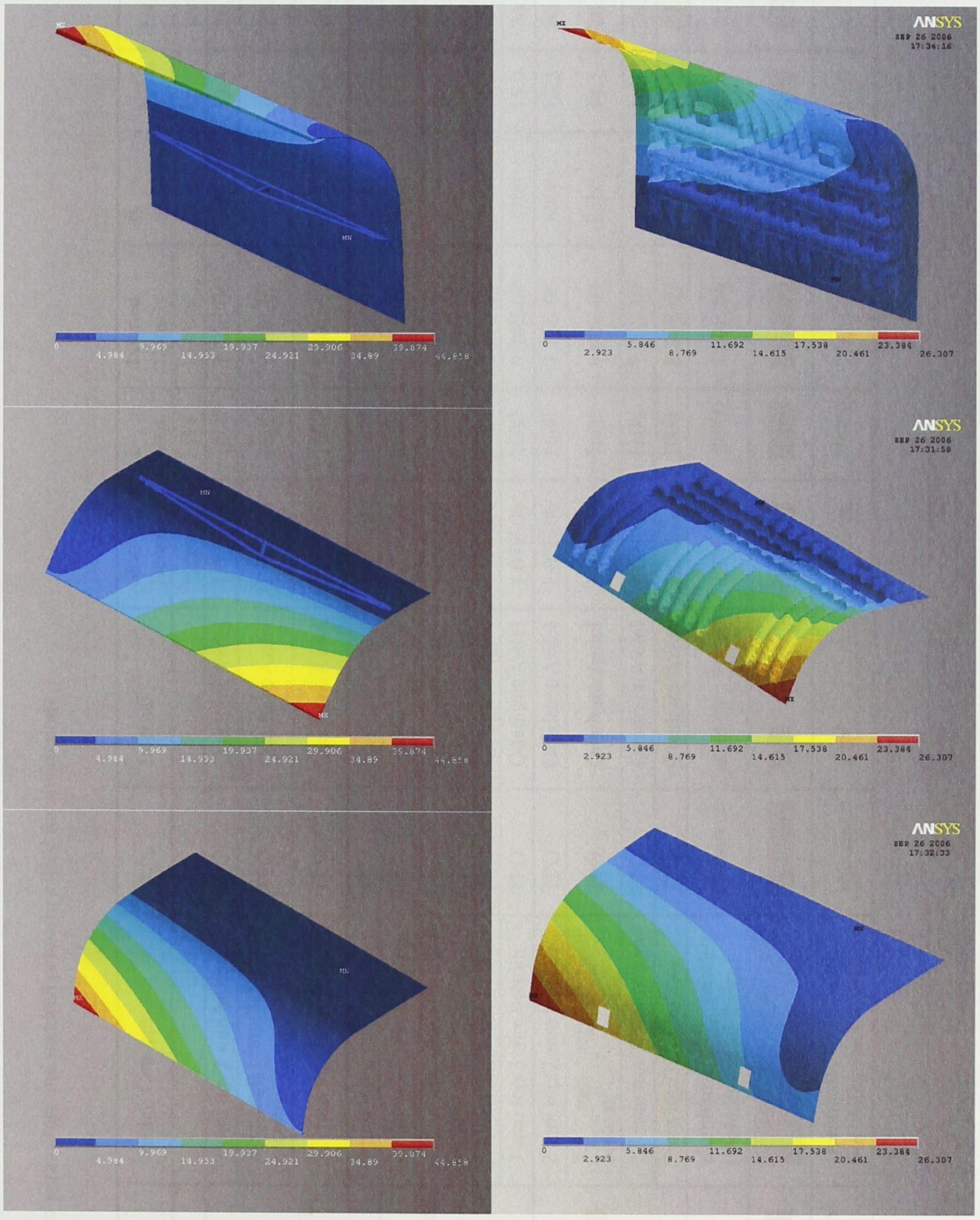

Figure 4.1- 13 Contours of free-standing deflection of baseline design and UAB thermoplastic concept.

Table 4.1- 5 List of parameters and material properties used for simulations

Mesh type (# of elements)	Design Concept	Skin	Internal	Skin Density	E skin	Internal Density	E internal	Mass	Deformation
				kg/mm³	MPa	kg/mm³	MPa	kg	mm
8816 coarse mesh (8816)	2 mm top/2 mm bottom	TPO	Quadrant/Azdel	1.07E-06	1600	1.16E-06	3000	12.3	26.3
	2.5 mm top/2.5 mm bottom	TPO	Quadrant/Azdel	1.07E-06	1600	9.90E-07	2550	14.1	25.1
	2.5 mm top/3 mm bottom	TPO	Quadrant/Azdel	1.07E-06	1600	8.20E-07	2100	14.0	24.0
	3 mm top/3 mm bottom	TPO	Quadrant/Azdel	1.07E-06	1600	8.20E-07	2100	15.3	24.5
intermediate mesh (17272) 17272	2 mm top/2 mm bottom	TPO	Quadrant/Azdel	1.07E-06	1600	1.16E-06	3000	12.3	28.2
	2.5 mm top/2.5 mm bottom	TPO	Quadrant/Azdel	1.07E-06	1600	9.90E-07	2550	14.1	26.9
	2.5 mm top/3 mm bottom	TPO	Quadrant/Azdel	1.07E-06	1600	8.20E-07	2100	14.1	25.7
	3 mm top/3 mm bottom	TPO	Quadrant/Azdel	1.07E-06	1600	8.20E-07	2100	15.3	26.2
fine mesh (35044) 35044	2 mm top/2 mm bottom	TPO	Quadrant/Azdel	1.07E-06	1600	1.16E-06	3000	12.3	30.1
	2.5 mm top/2.5 mm bottom	TPO	Quadrant/Azdel	1.07E-06	1600	9.90E-07	2550	14.1	28.4
	2.5 mm top/3 mm bottom	TPO	Quadrant/Azdel	1.07E-06	1600	8.20E-07	2100	14.1	26.9
	3mm top/3mm bottom	TPO	Quadrant/Azdel	1.07E-06	1600	8.20E-07	2100	15.3	27.4
automesher (14520)	aluminum baseline (including steel frame)	aluminum	steel	2.70E-06	79000	7.90E-06	200000	23.6	31.9
fine mesh (27284)	aluminum baseline (including steel frame)	aluminum	steel	2.70E-06	79000	7.90E-06	200000	26.1	48.0
intermediate mesh (22000)	aluminum baseline (including steel frame)	aluminum	steel	2.70E-06	79000	7.90E-06	200000	26.0	44.7

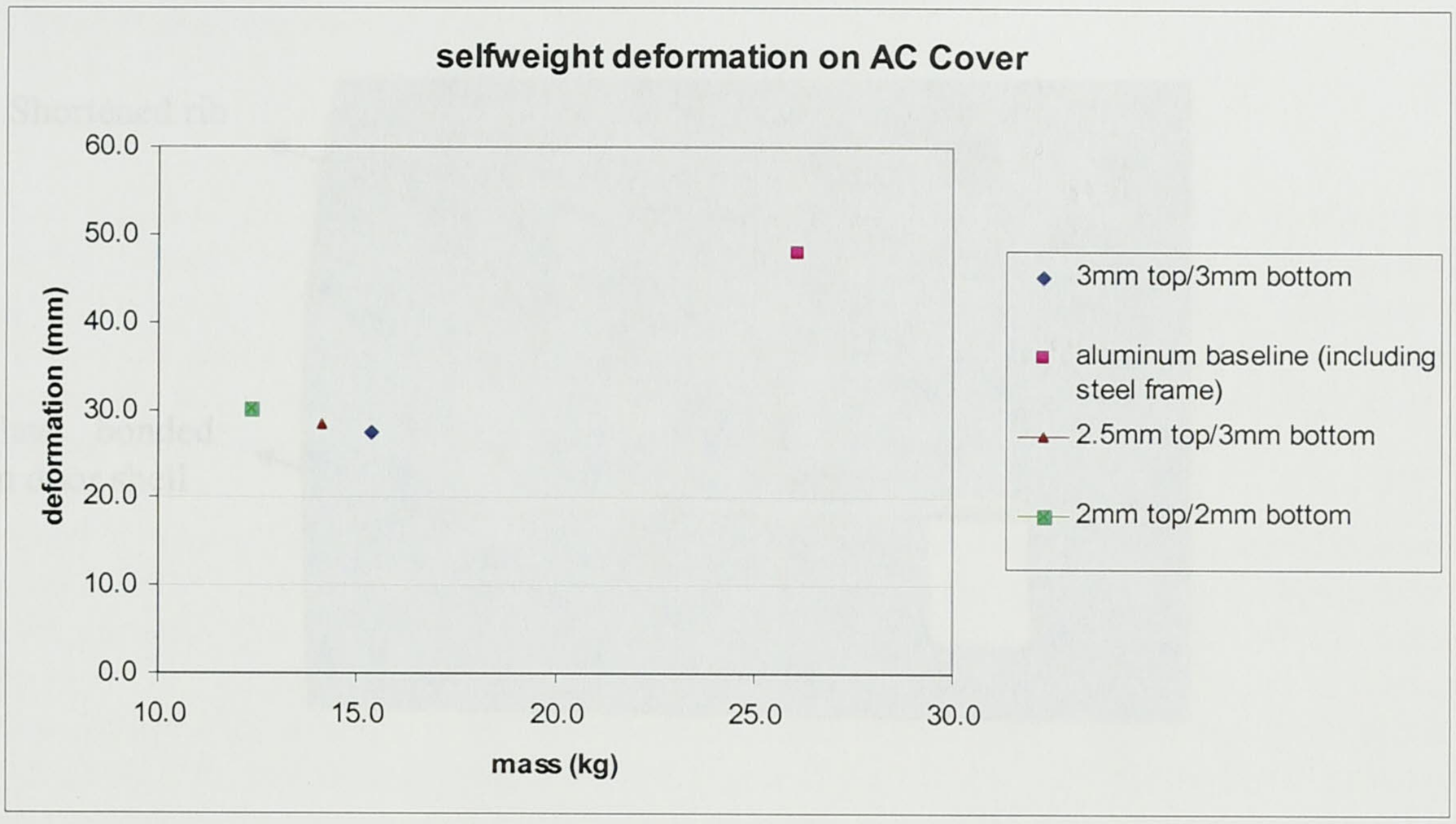

Figure 4.1- 14 Deformation versus total mass for baseline and UAB concepts of AC cover.

4.1.4 Design optimization

The design was optimized in order to accommodate the mounting of the prop. The prop is used for supporting the whole AC door in the NABI bus when the door is open as shown in the Fig. 4.1-15. One end of the prop is connected to the hinge plate which is welded on the door shell. The other end of the prop sits on the bus frame to support the door. Two design options are considered to accommodate the mounting of the prop so that the same hardware on the present NABI bus can be used in the composites door. The position of the prop and the hinge is on one of the ribs. One option is to shorten the rib and the hinge plate can be bonded on the door shell using adhesives as shown in Fig. 4.1-15. The bonding interface is mostly under compressive force instead of destructive shear force when the prop is operating. The other option is to change the rib geometry slightly. A flat area is built on the rib so that the hinge plate can be bolted down to the rib as shown in Fig. 4.1-16.

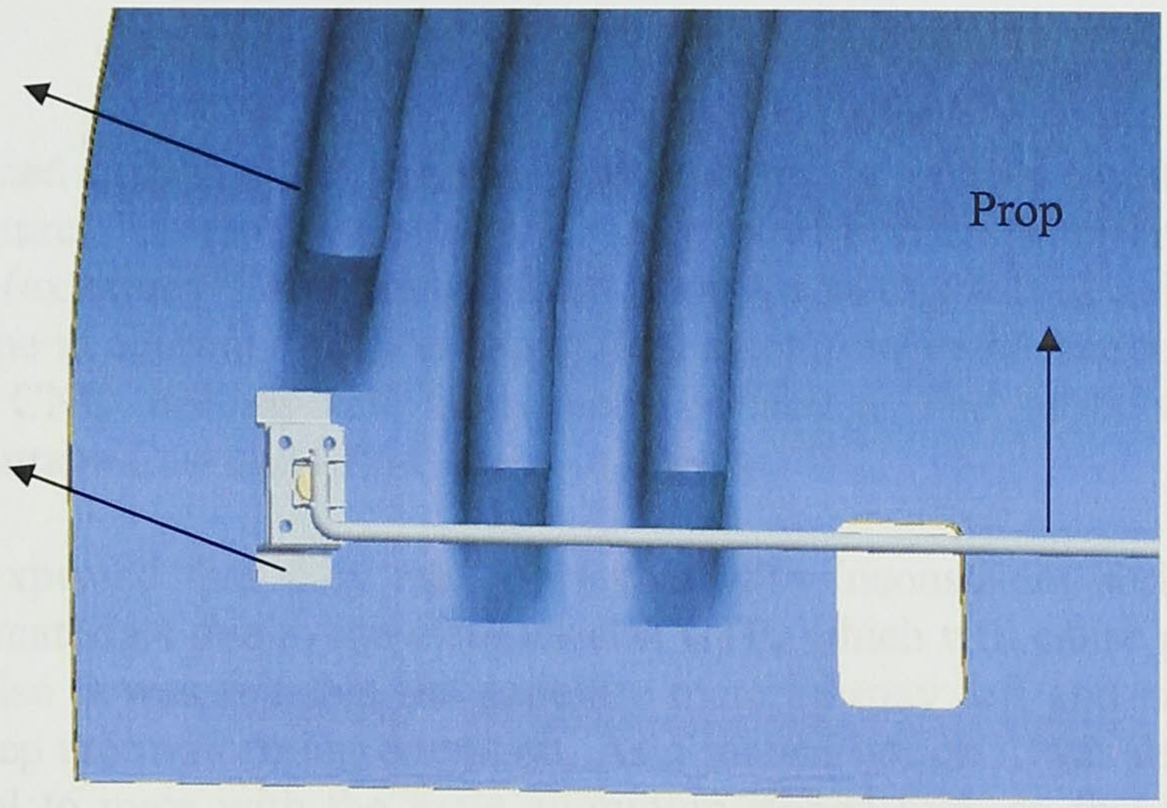

Figure 4.1- 15 The hinge plate and prop bonded on door shell

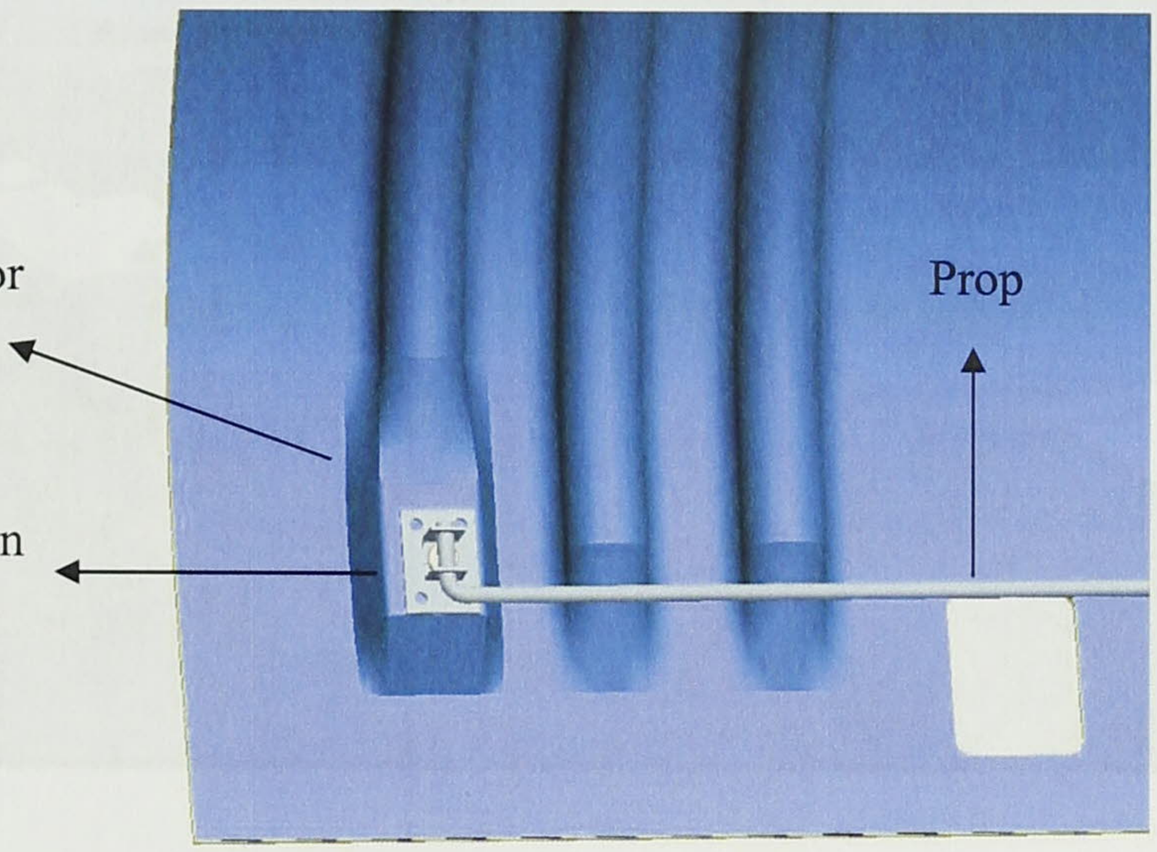

Figure 4.1- 16 The hinge plate and prop bolted on door shell. Note the flat rib area for the bolting.

4.1.5 Tool Design for the AC Cover Door

4.1.5.1 Tool

The tool was designed such that the twin sheet thermoforming process could be used as the first option for manufacture. The tool consisted of a male ribbed portion (interior - azdellite) and the female flat portion (exterior - TPO). The concept is shown in Fig. 4.1-17 below. The tools were cast to near net shape in aluminum 356 and then final machining to surface finish of 100 grit was accomplished via CNC milling and subsequent polishing. The tools were designed and manufactured by Portage Cast and Mold, based in Portage, WI.

However, it was expected that they may be issues with inconsistent shrinkage between the azdellite and TPO materials due to the difference in CTE, which will cause print through on the exterior surface. Also it was felt that the azdellite material may loft and not fully consolidate during the single step thermoforming operation. As a second option it was decided to fabricate a wooden female tool to mate with the male aluminum ribbed tool, so that the ribbed azdellite structure could be heated and compression molded if necessary. This method will involve the ribbed structure being heated and compression molded; the outer TPO skin being thermoformed and thereafter the two sections being bonded. The concept is shown in Fig. 4.1-18.

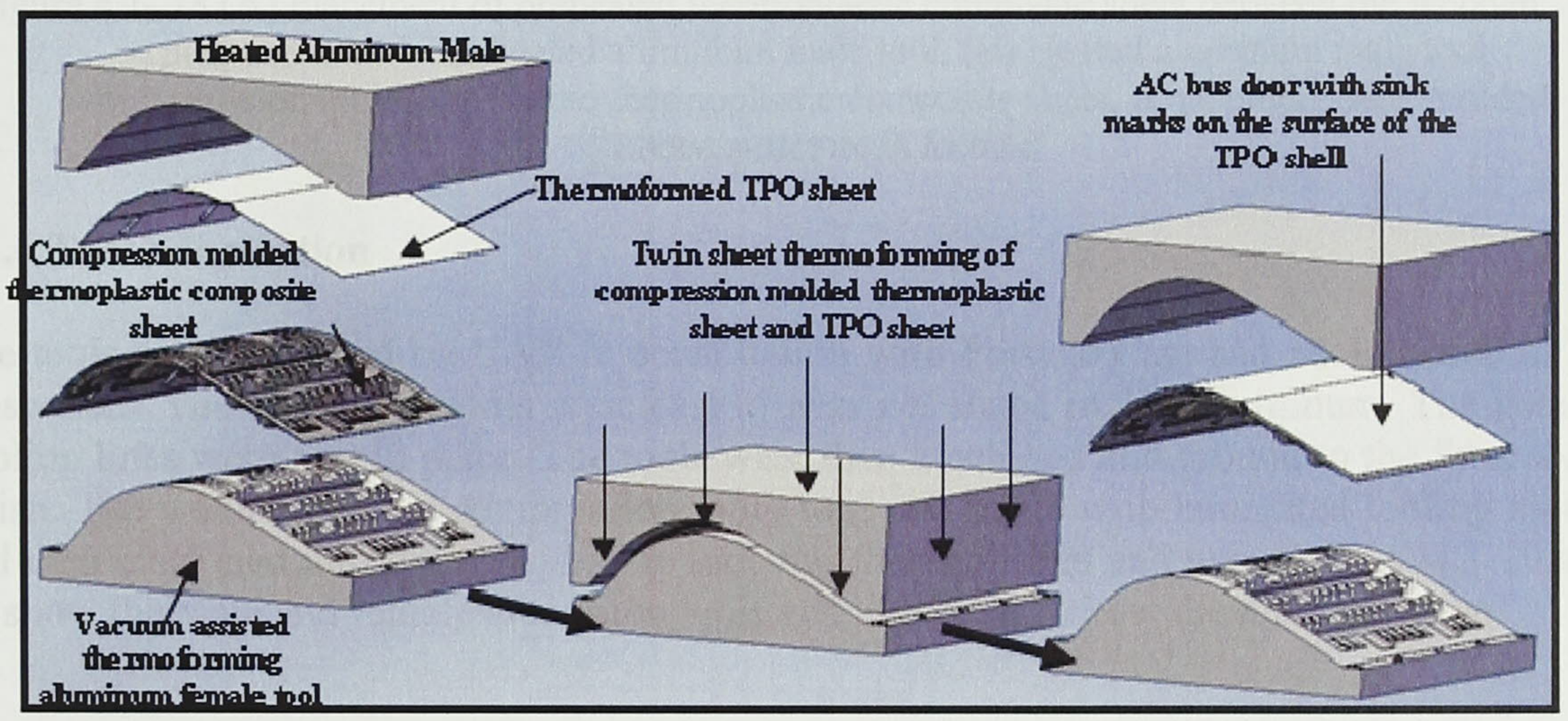

Figure 4.1- 17 Twin sheet thermoforming of thermoplastic composite and TPO sheets.

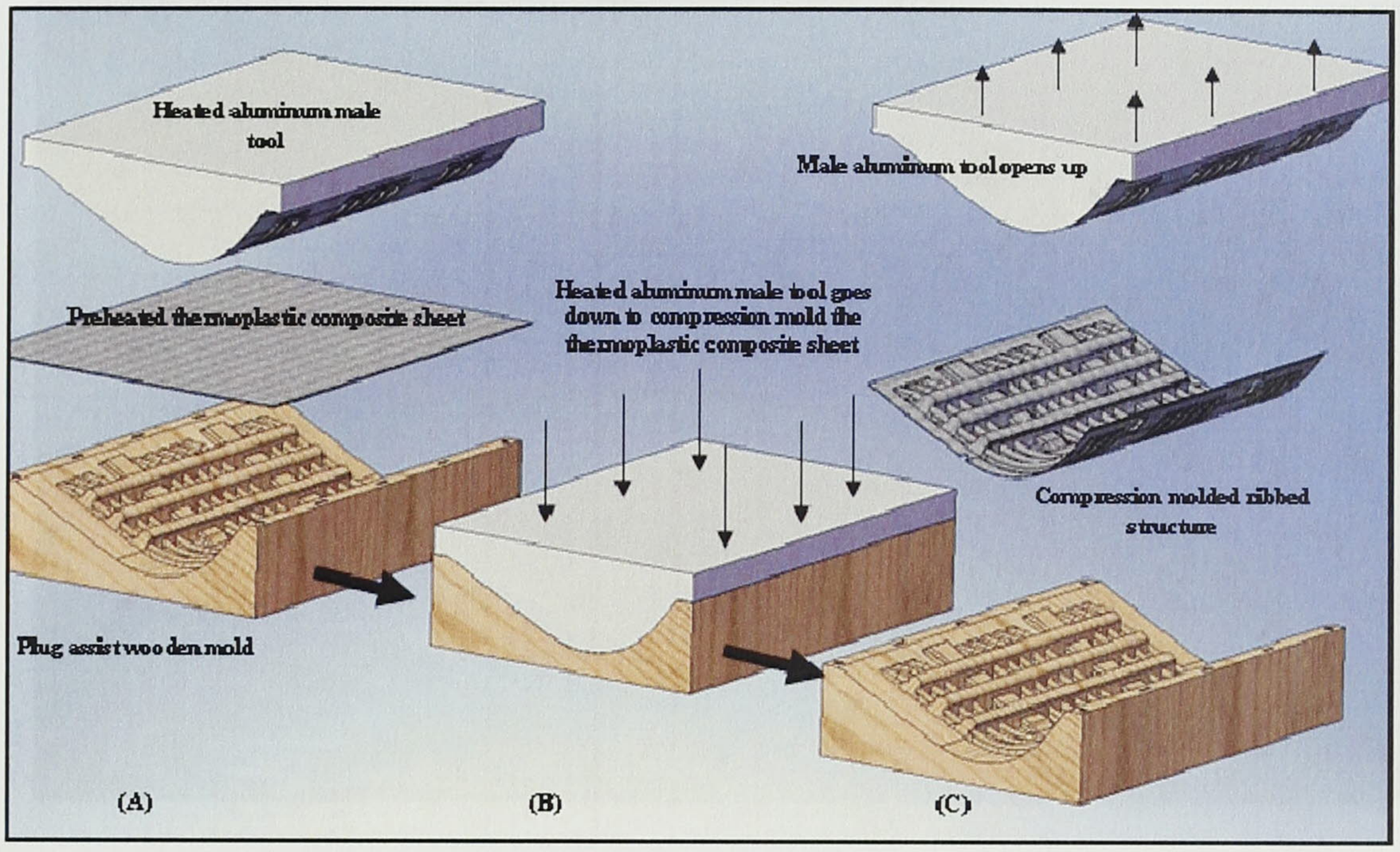

Figure 4.1- 18 (A) Placement of preheated thermoplastic composite sheet between the wooden plug assist tool and heated aluminum male tool, (B) Heated aluminum male tool compression molds the heated thermoplastic composite sheet, (C) Compression molded ribbed structure is formed

4.1.6 Tool Fabrication

The tools were designed by UAB in consultation with Portage Cast and Mold based in Portage Wisconsin. The aluminum tools were cast to near net shape in 356 aluminum. The heating and cooling lines were cast in place. The tools were then machined and ground to the final shape and finish. The wooden female compression mold tool was made with laminated tooling mahogany, and then machined into final shape. The tool was then polished and waxed. Figs. 4.1-19 and 4.1-20 show the male and female aluminum tools and Fig. 4.1-21 show the mahogany tool.

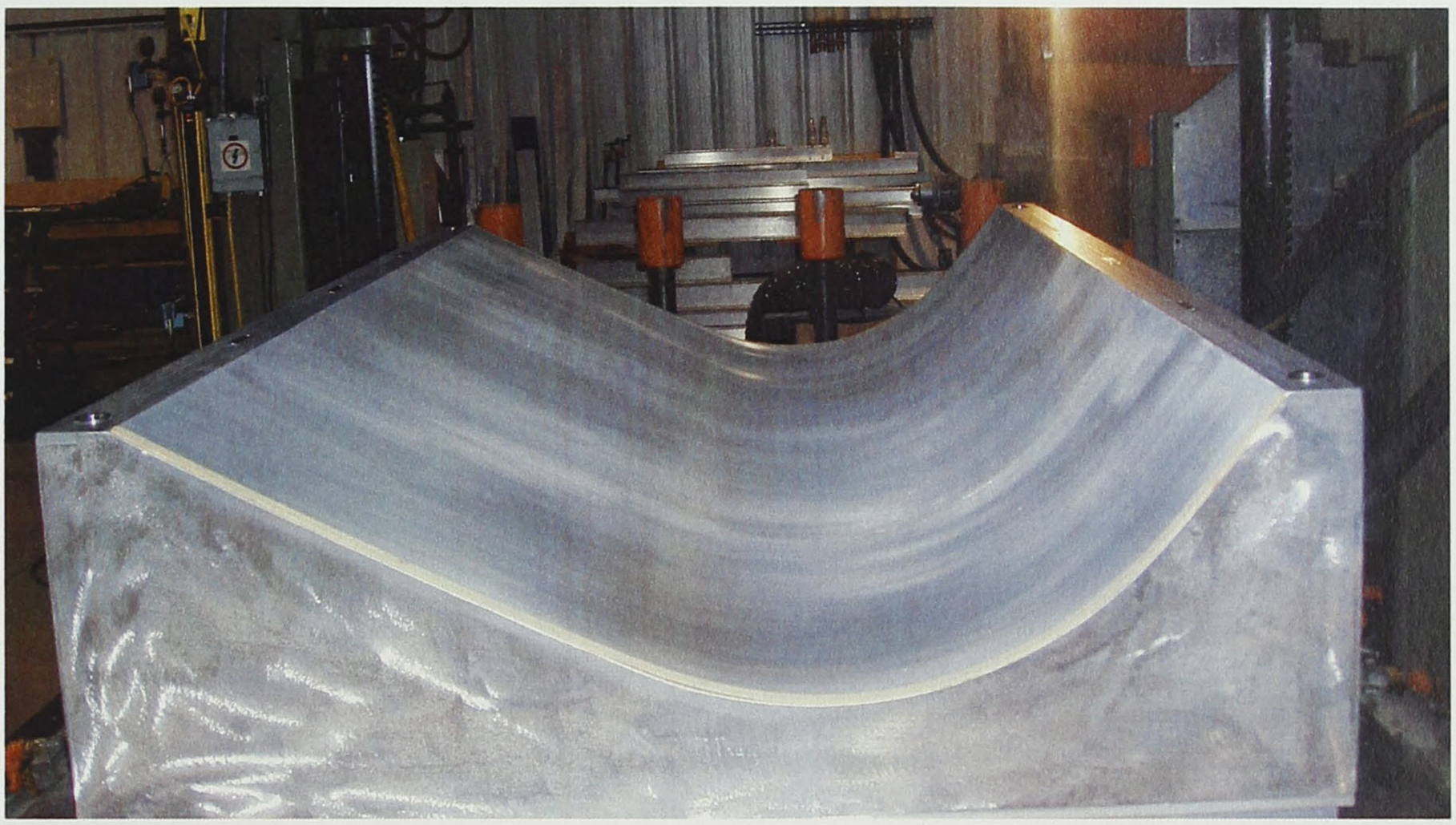

Figure 4.1- 19 Female aluminum tool, for thermoforming of TPO exterior section.

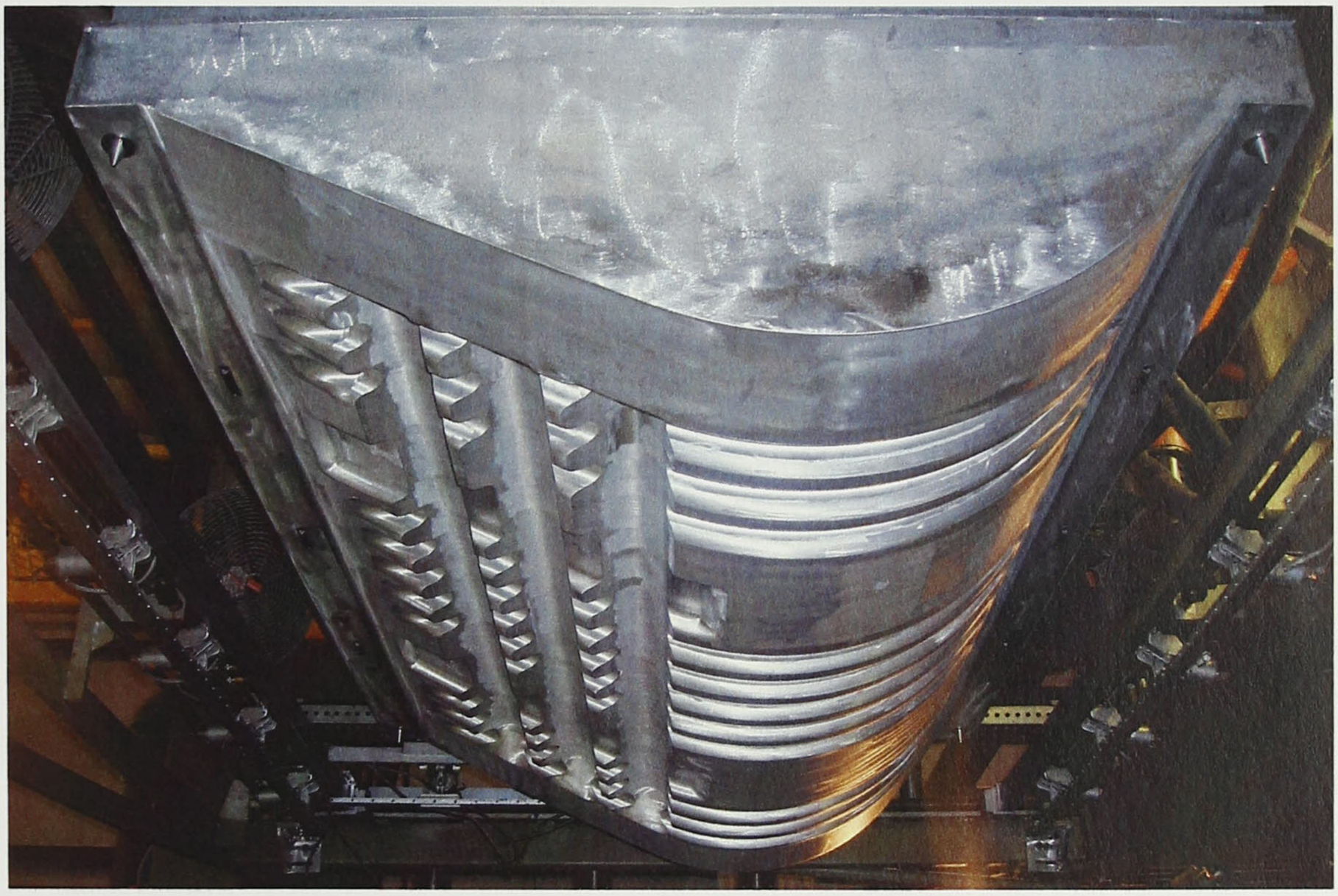

Figure 4.1- 20 Male aluminum tool for thermoforming or compression molding of interior azdellite section

Figure 4.1- 21 Wooden female tool for compression molding of azdellite inner section.

V. Component Demonstration

5.1 Component Fabrication

The manufacture of the final components was carried out the Portage Cast and Mold Technology center. The technology center has two large thermoforming machines, one capable of single sheet thermoforming of up to 10' x 14' sections. The other is a 4 station rotary thermoforming machine capable of twin sheet thermoforming of sections up to 10' x 12'. The rotary machine also has the capacity to compression mold to pressures of up to 60 psi. The machine consists of a material clamping station, followed by two heating stations fitted with 1000 W ceramic heaters, and finally the forming station. The 4 station rotary machine is shown in Fig. 5.1-1.

5.1.1 Twin sheet thermoforming

The initial trial was conducted using the twin sheet thermoforming approach. The TPO sheet was loaded onto the clamps and progressed to the first preheat oven. The sheet is rotated to the first oven between two ceramic heaters. The top heater is 8 inches from the sheet and the bottom heater is 20 inches from the sheet. Heating is achieved through a combination of infrared and convection. While the TPO sheet is in the preheat oven the azdel sheet was clamped to the frame. The azdel sheet was then rotated to the preheat oven at which time the TPO sheet gets transferred into the final heating oven. At the point when the TPO sheet reaches its forming temperature, the sheet is rotated into the forming station as shown in Fig. 5.1-2 (At this time the azdel sheet has been rotated into the final heating oven). The tools close onto the heated TPO sheet. The top tool provides sealing for the vacuum of the bottom forming tool. The TPO sheet is vacuum formed onto the bottom tool. The top tool moves up, while the TPO sheet is still under vacuum on the bottom tool. At this time the azdel sheet reaches its forming temperature. The frame rotates the azdel sheet to the forming section, as shown in Fig. 5.1-3. The top and bottom tools move onto the azdel sheet, with the top tool pulling a vacuum, which draws the azdel sheet into its form. Both sheets are also coined at this stage. After the materials cool to the tool temperatures, the tools are opened and cooling fans are used to cool the exposed part. The formed part is now rotated to the clamping table where it is removed.

The final formed part was removed and inspected. It was found that very good bonding was achieved. However, as anticipated the difference in CTE of the two materials caused uneven shrinkage and subsequent print-through on the TPO outer surface, as can be seen in Fig. 5.1-4. There was also problems with the consolidation of the azdel sheet, there was significant lofting of the material, and the ribs did not have any structural integrity.

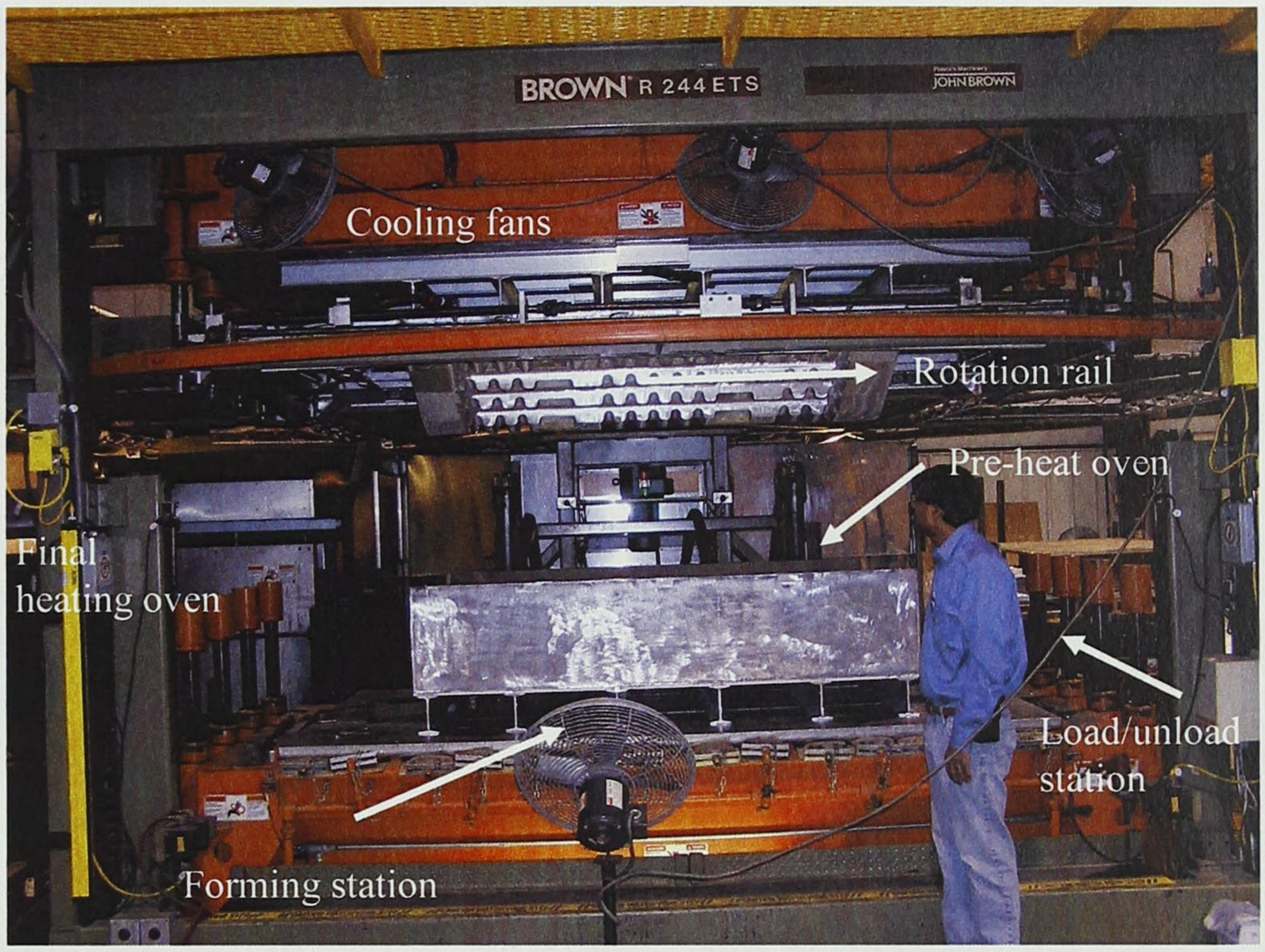

Figure 5.1- 1 Four-station rotary thermoforming machine at Portage Cast and Mold.

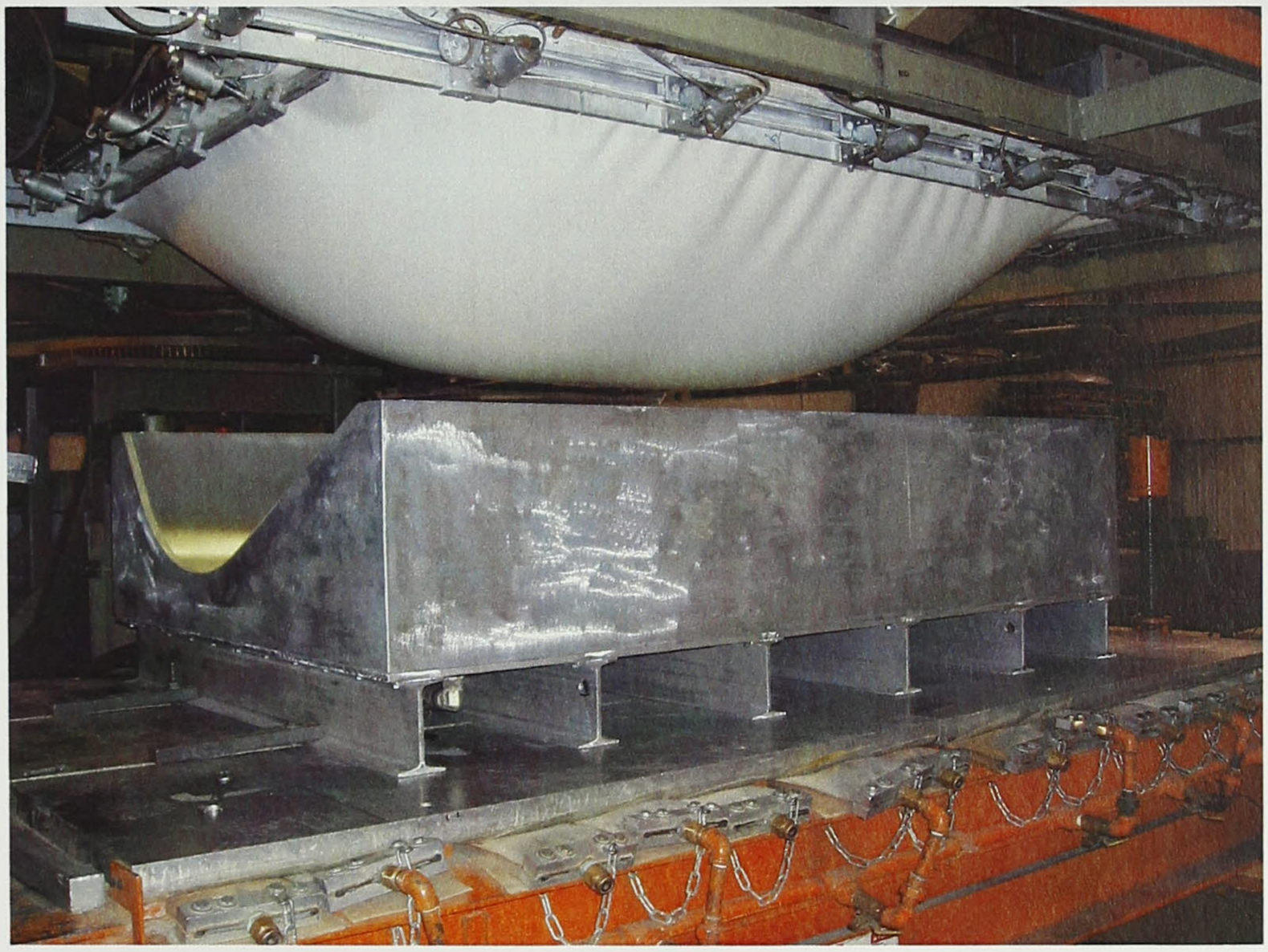

Figure 5.1- 2 TPO sheet heated, moved onto the forming station and ready for tools to close and sheet to be thermoformed.

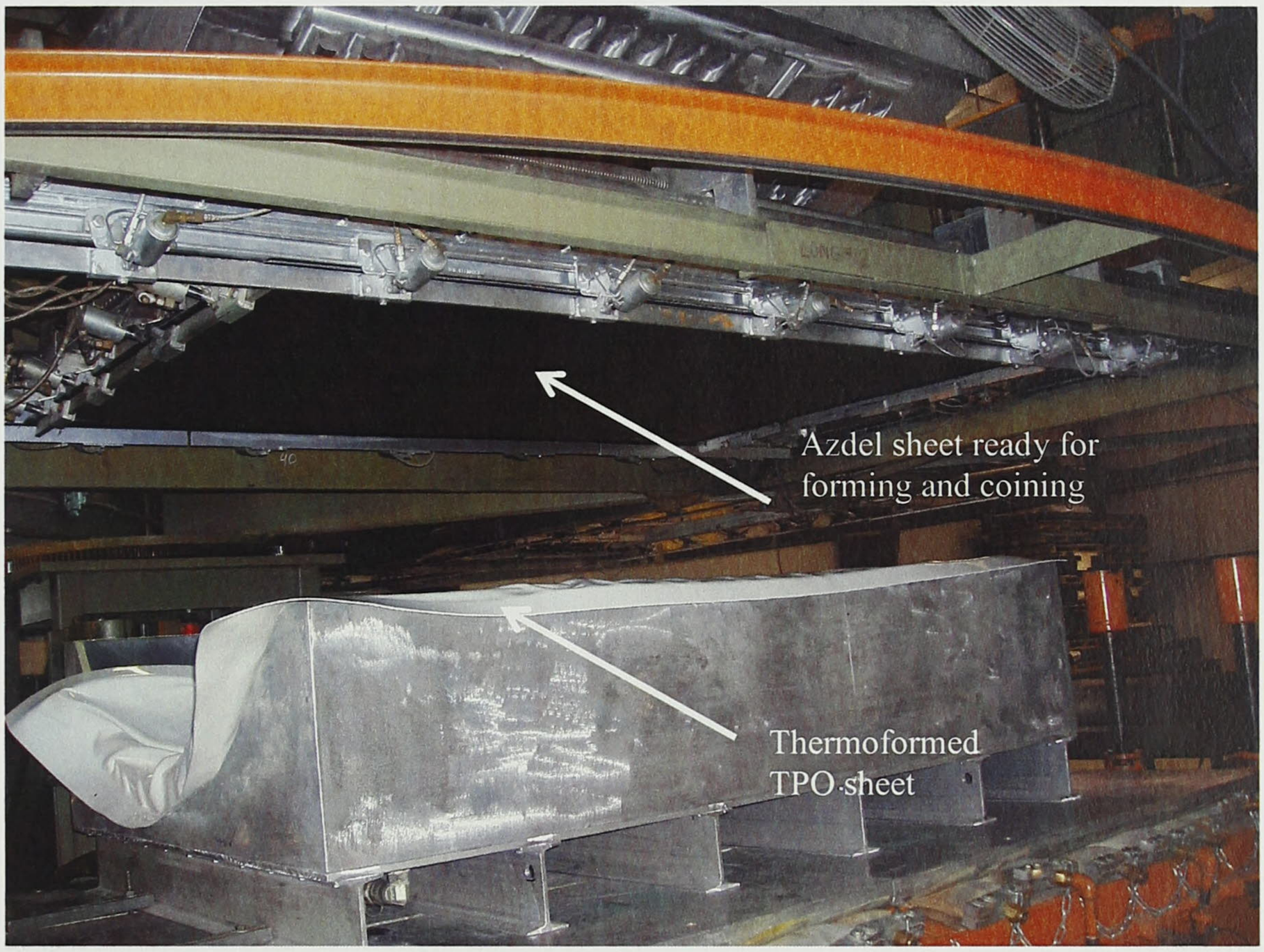

Figure 5.1- 3 TPO sheet thermoformed and azdel sheet ready to be formed and twinned to the TPO sheet.

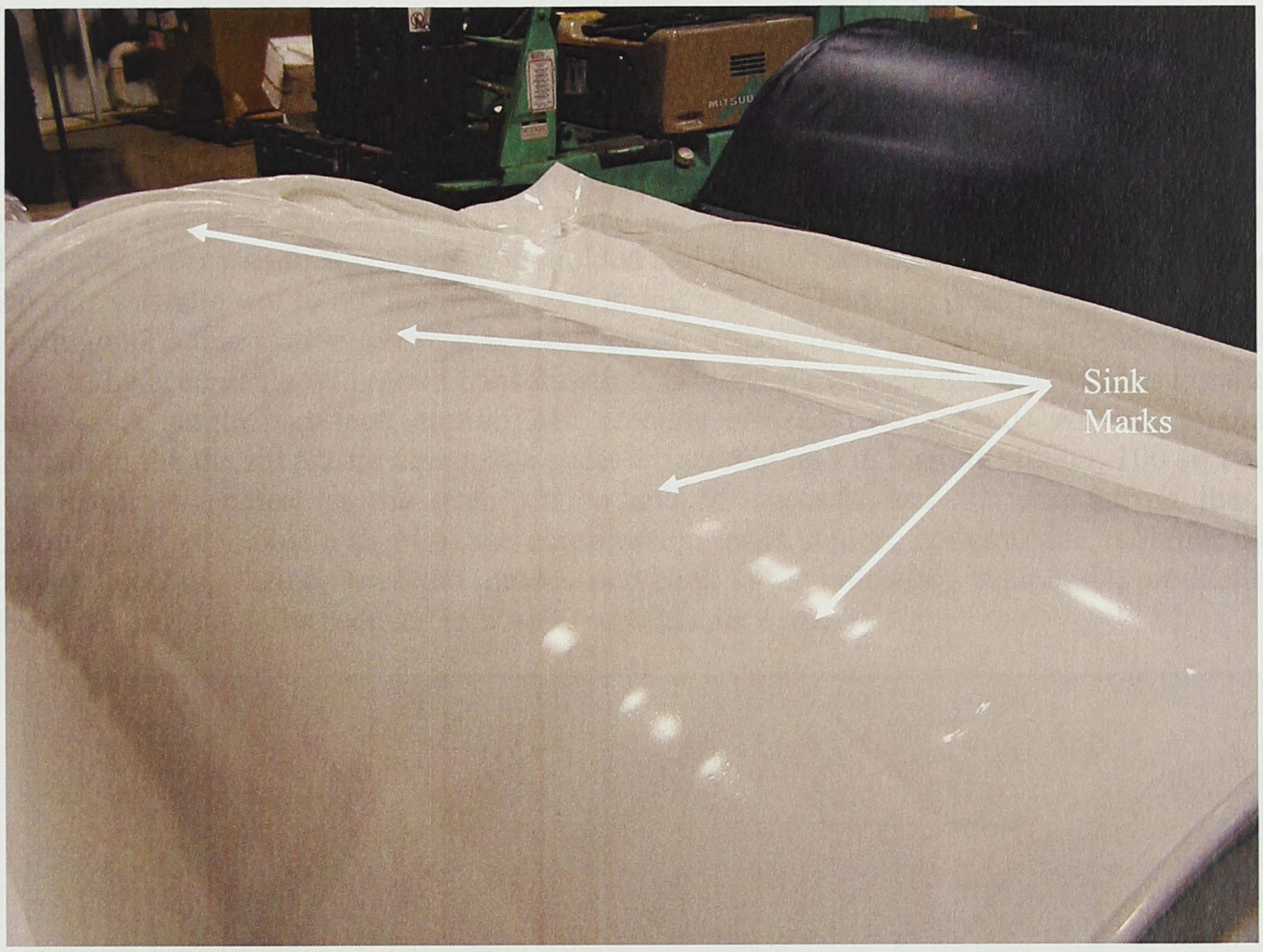

Figure 5.1- 4 Twin sheet formed part, showing sink marks on the exterior TPO side.

5.1.2. Manufacturing option 2

In this option the AC Bus Door is made in three steps.

1. Compression molding of the azdel thermoplastic composite sheet.
2. Thermoforming of thermoplastic olefin (TPO) sheet.
3. Joining of the compression molded thermoplastic sheet and thermoformed TPO sheet

5.1.2.1 Compression molding of thermoplastic composite sheet

The female aluminum tool was removed and the mahogany female ribbed tool was installed at the forming station. The process concept is shown in Fig. 5.1-5. The azdel sheet was loaded and heated to 400° F, as before and transferred to the forming section as shown in Fig. 5.1-6. The aluminum tool was maintained at 125° F and the mahogany tool was maintained below 100° F. The azdel sheet was then compression molded and after a few seconds the mold was opened and the part was allowed to air cool, as shown in Fig. 5.1-7. The formed part then transferred to the loading/unloading station where it is removed for inspection (Fig. 5.1-8). The part was found to have to be acceptable with good consolidation. Several parts were manufactured using the same process. A single part took around 240 seconds of which 45 seconds was for loading and unloading the thermoplastic composite sheet at the loading / unloading station, 100 seconds was for heating the sheet at the oven station and 95 seconds was for transferring the heated thermoplastic composite sheet to the compression mold station, compression molding the TPO part and sending the compression molded part back to the unloading station. On production run, the cycle time could be reduced to 80-100 seconds per cycle.

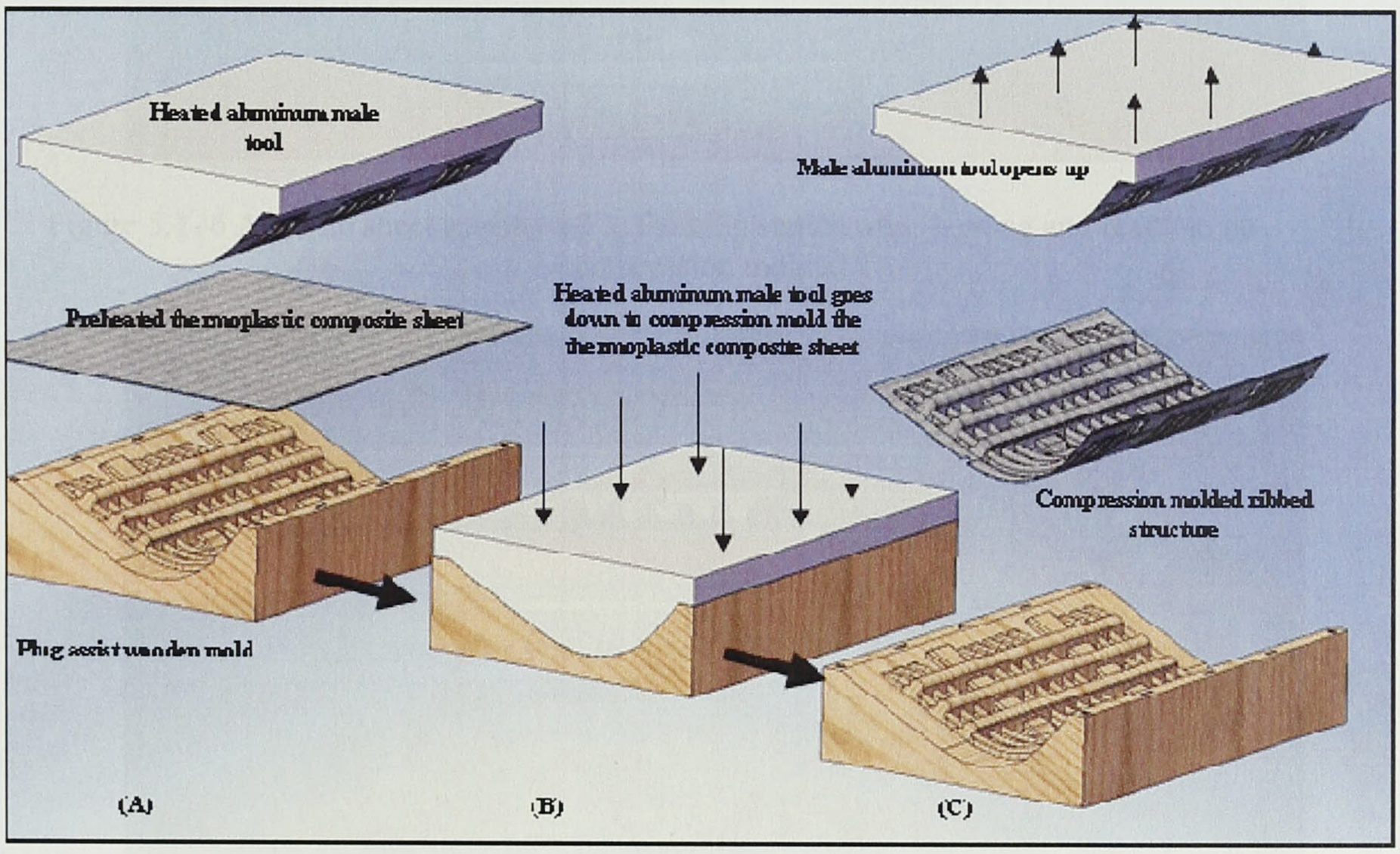

Figure 5.1- 5 (A) Placement of preheated thermoplastic composite sheet between the wooden tool and heated aluminum male tool, (B) Heated aluminum male tool compression molds the heated thermoplastic composite sheet, (C) Compression molded ribbed structure is formed

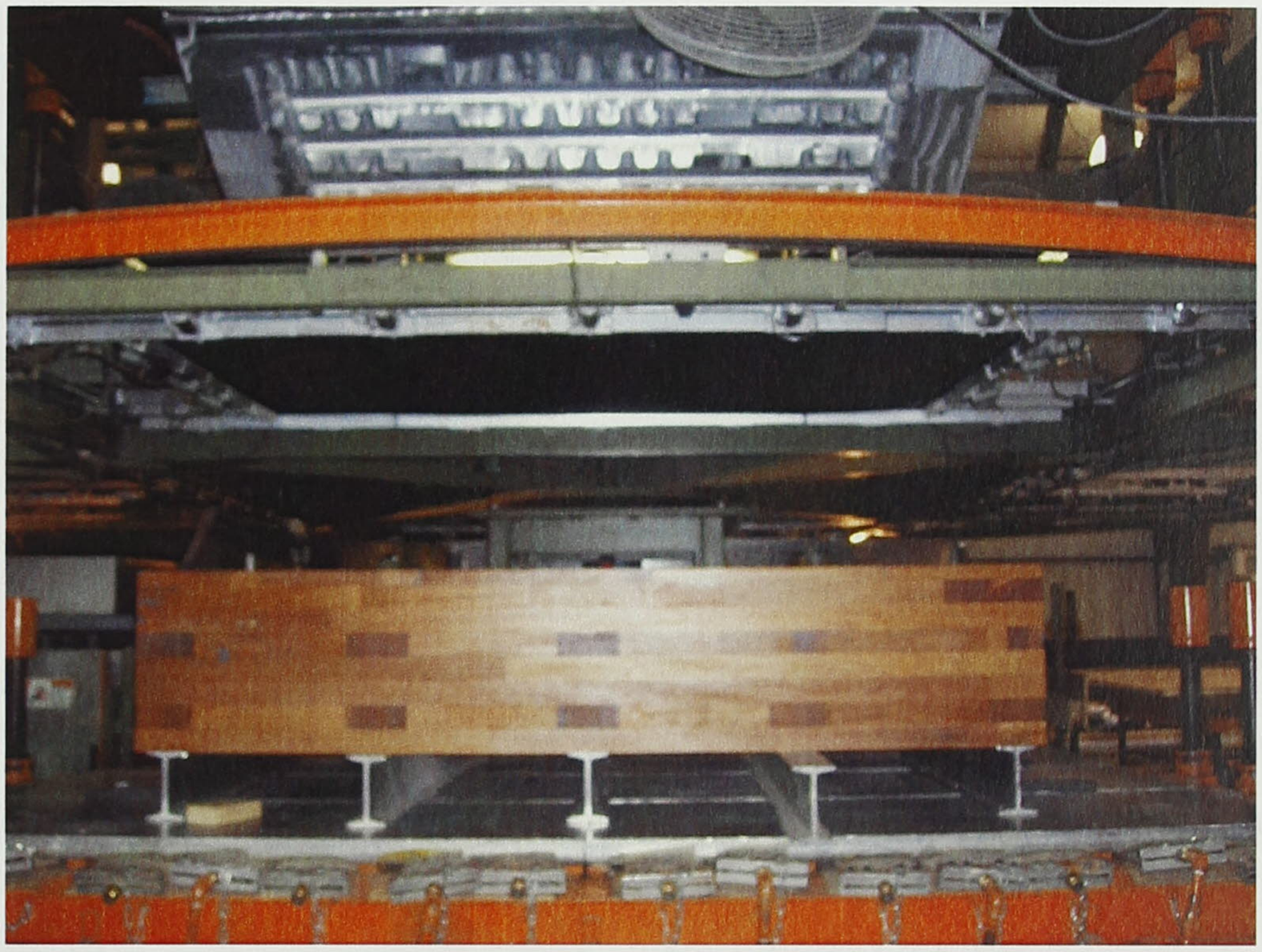

Figure 5.1- 6 Azdelite sheet transferred to forming station after heating and ready to be compression molded.

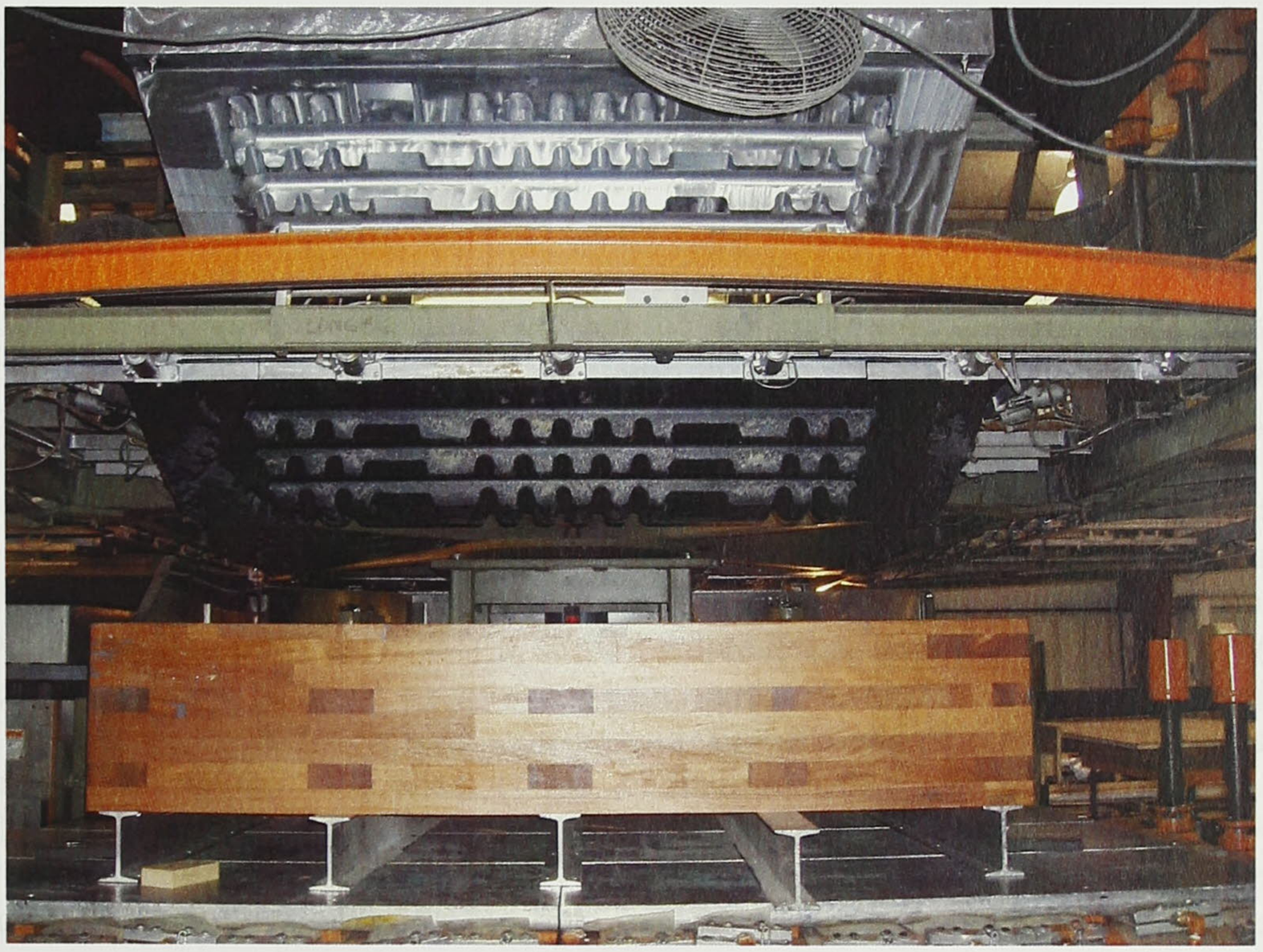

Figure 5.1- 7 Compression molded part, after opening of tools, being air cooled.

Figure 5.1- 8 Part being removed at the loading/unloading station.

5.1.2.2 Thermoforming of thermoplastic olefin (TPO) sheet

The next stage was to thermoform the TPO (outer skin) section. The wooden tool was removed and the female aluminum tool was reinstalled. Wooden side sections were put onto female tool to aid to the forming and vacuum retention between the tool and the TPO sheet. The TPO sheet was installed onto the clamping frame moved through the preheating and heating ovens. When the temperature of the sheet reached the recommended forming temperature (360° to 400° F), the sheet was moved onto the forming section as shown in Fig. 5.1-9. Both the aluminum tools are maintained at 150° -160° F. The tools closed (with the top tool only providing sealing for vacuum), and vacuum was applied through the bottom tool (Fig. 5.1-10). The sheet was allowed to cool to the tool temperature and the tools were then opened and the part was then air cooled. The part was then rotated to the unloading section where it was removed for inspection (Fig. 5.1-11). The part was found to be of acceptable quality and several more parts were manufactured using the same process. A single part took around 300 seconds of which 45 seconds was for loading and unloading the TPO sheet at the loading/unloading station, 100 seconds was for heating the sheet and 155 seconds was for transferring the heated TPO sheet to the thermoforming molds, thermoforming the TPO part and sending the thermoformed part back to the unloading station. On production run, the cycle time could be reduced to 100 seconds per cycle.

Figure 5.1- 9 TPO sheet at compression molding station ready for vacuum thermoforming.

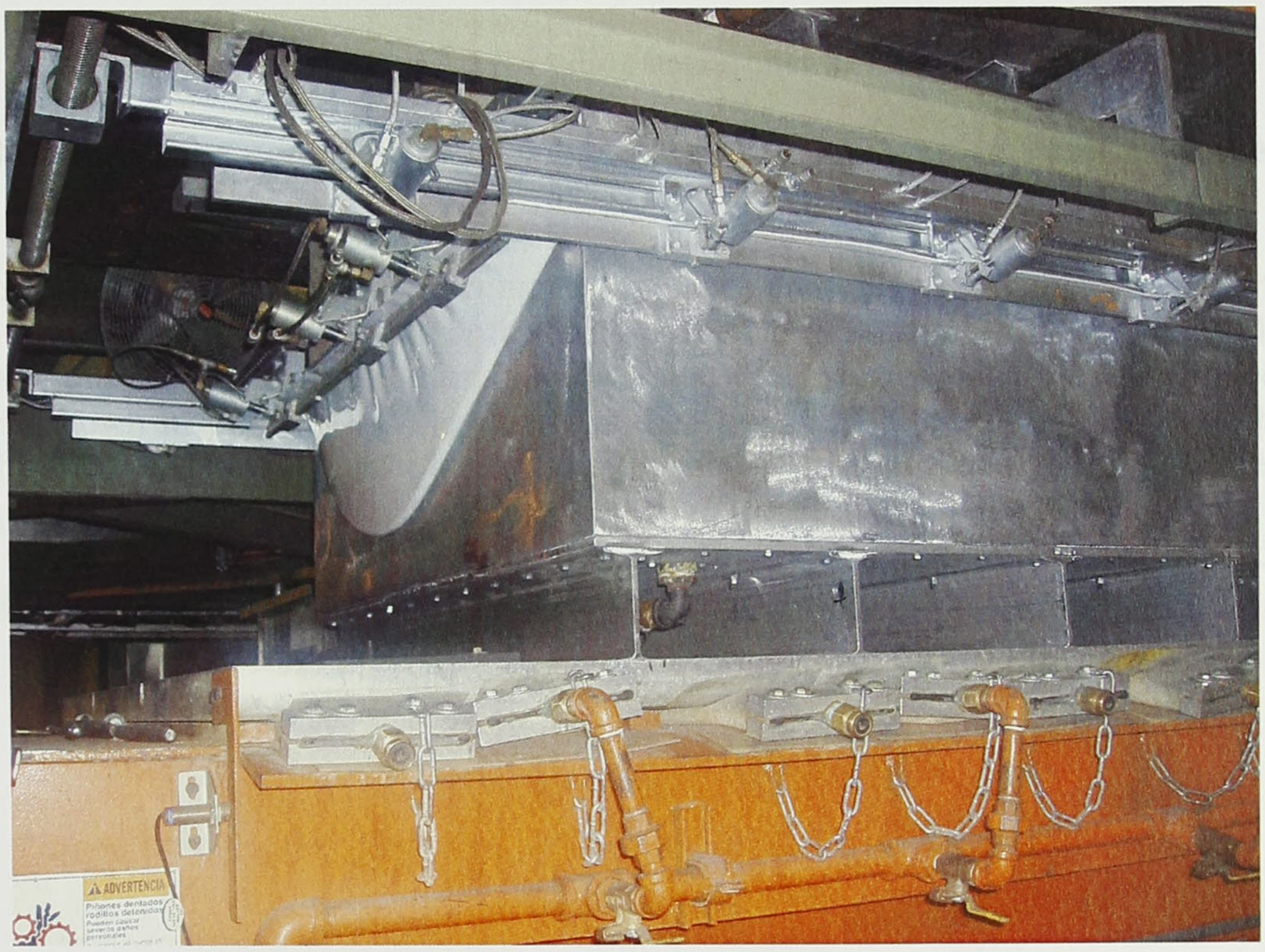

Figure 5.1- 10 TPO sheet during thermoforming.

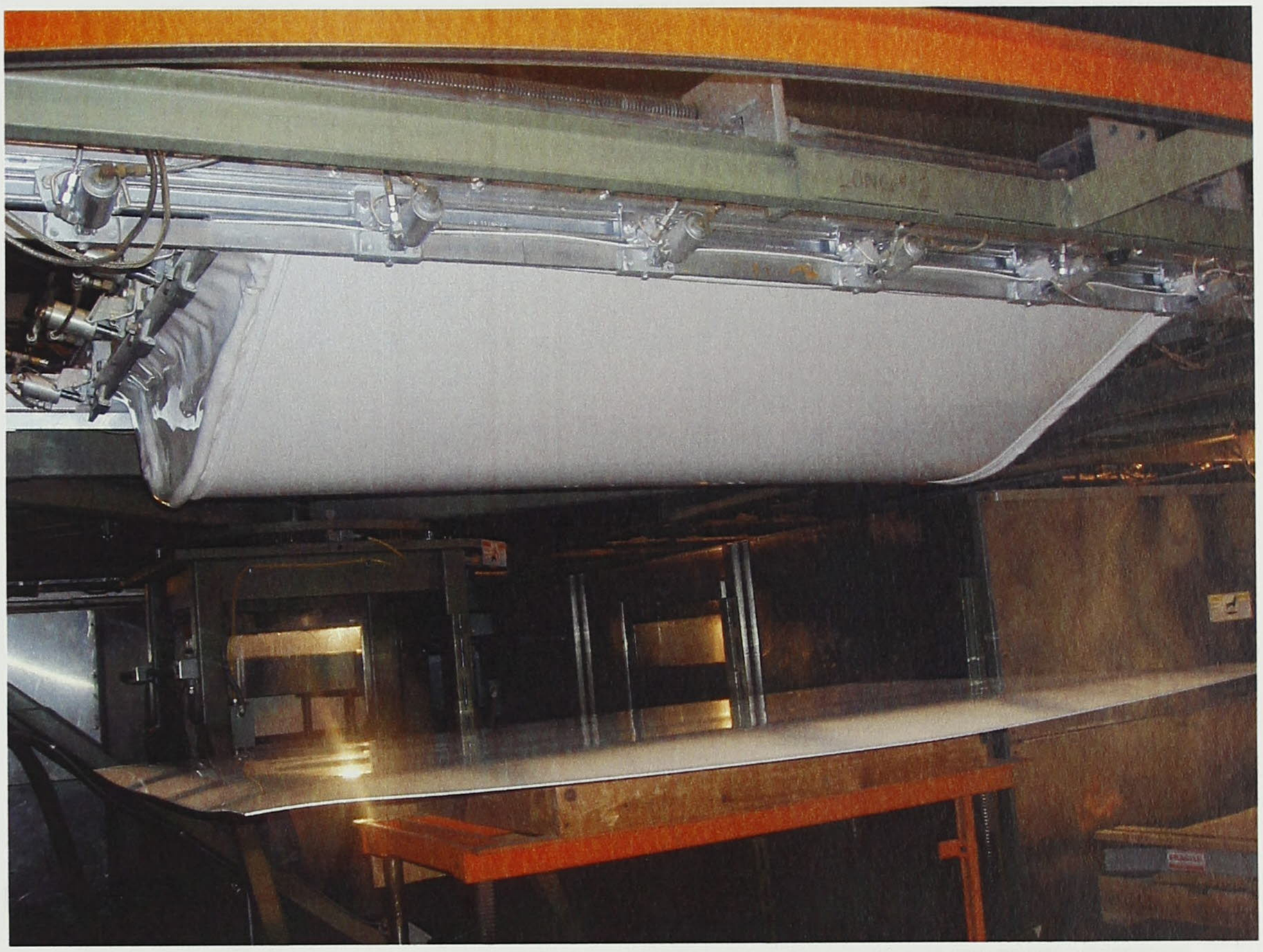

Figure 5.1- 11 TPO sheet at unloading station after thermoforming.

5.1.2.3 Joining of the compression molded thermoplastic sheet and thermoformed TPO sheet

The azdel and TPO parts were then trimmed (by hand) and adhesive primer recommended for use with the 3M tape was applied to both sheets, as shown in Figs. 5.1-12 and 5.1-13. The azdel section was placed on the ribbed aluminum tool and the 3M pressure tape was applied to the section, as shown in Fig. 5.1-14. The tape was then hand rolled to aid bonding onto the azdel sheet. The TPO sheet was then placed onto the ribbed structure and the tools were closed applying a pressure of 13 psi to aid with the bonding. The part was removed after a few seconds and was then ready for trimming (Fig. 5.1-15). The composite section was then placed onto a trimming fixture and trimmed on a 5 axis CNC machine.

Figure 5.1- 12 Primer being applied to formed azdel composite part (after hand trimming).

Figure 5.1- 13 Primer being applied to thermoformed TPO part (after hand trimming)

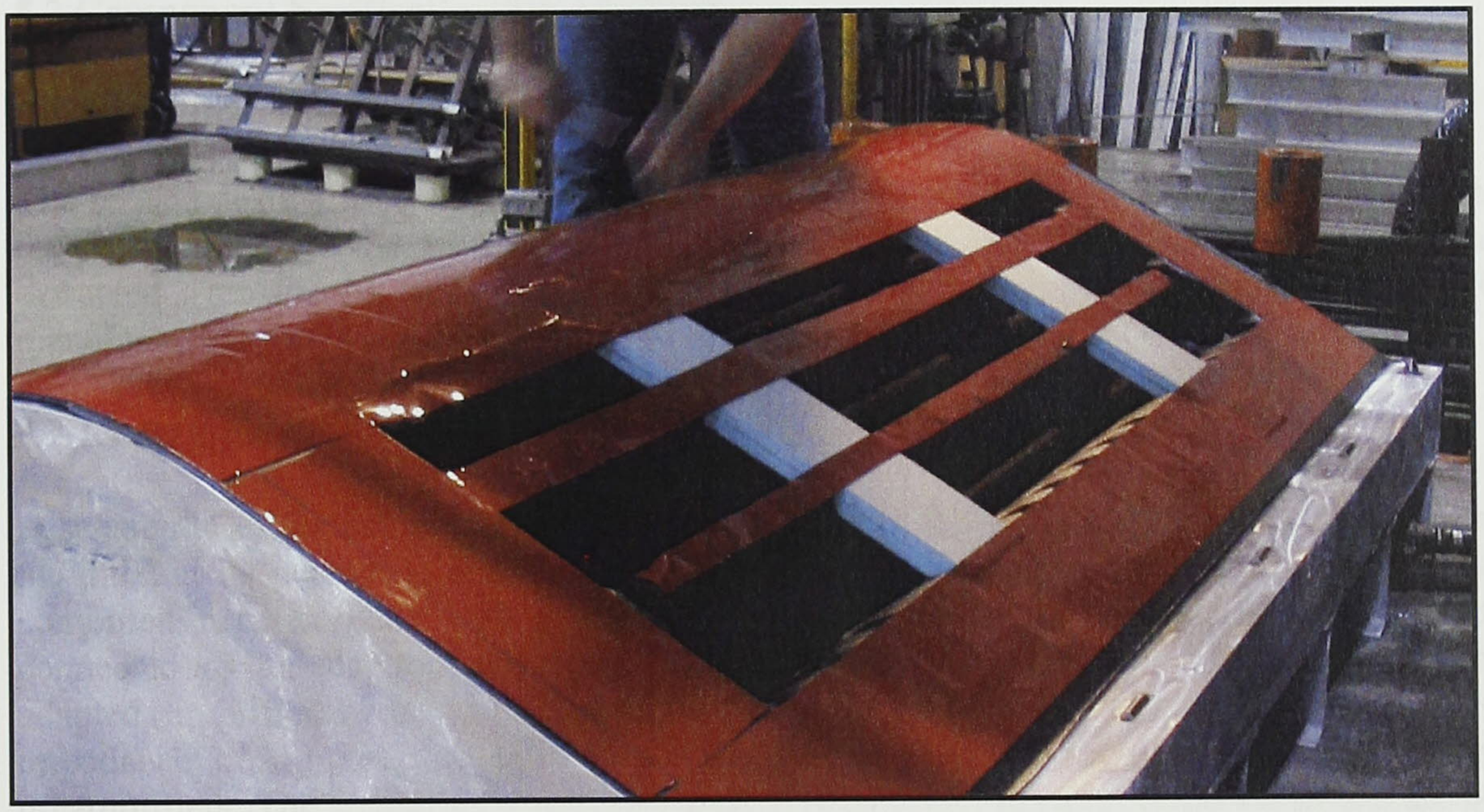

Figure 5.1- 14 3M VHB tape applied to composite sheet and being hand rolled.

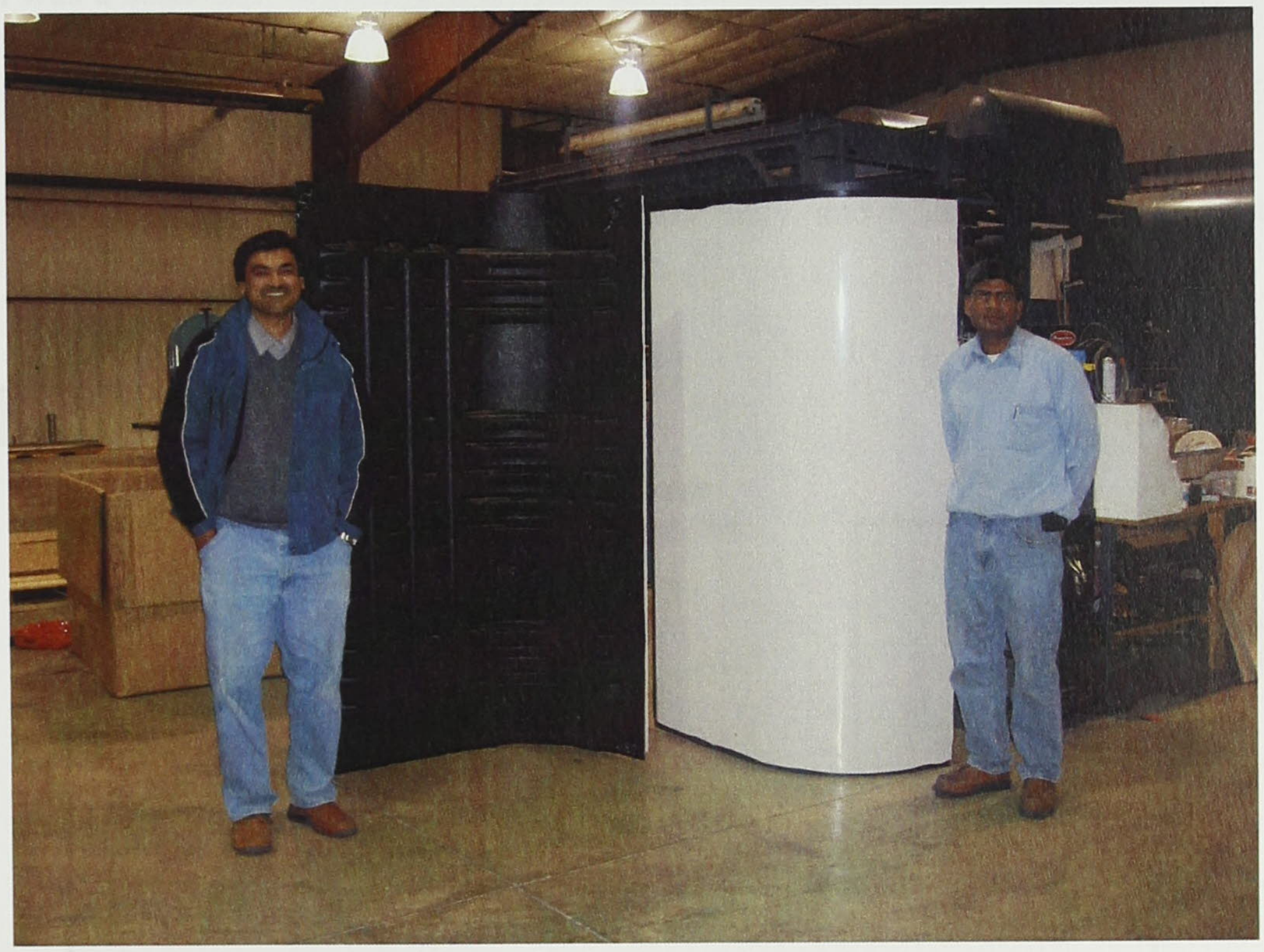

Figure 5.1- 15. Bonded parts ready for CNC trimming.

5.2 Component Verification for AC Door

5.2.1 Testing

The second design option, flat rib area created for bolting the hinge plate and prop, was used for the prototyping (see the processing part for details). Damping testing was conducted on coupons extracted from the AC door manufactured. Deflection testing was conducted on the AC door manufactured.

5.2.1.1 Damping

A schematic of the setup used for vibration testing is shown in Fig. 5.2-1. All specimens were mounted at its geometric center with the help of bees wax on an impedance head, which is a combined accelerometer and force transducer in one single unit. The impedance head is connected to an electrodynamic shaker using a stinger rod. Random noise excitation was adapted, amplified by a power amplifier. The input force and output velocity signals from the impedance head were fed to a dual channel frequency analyzer through two dual mode preamplifiers. The frequency response function (FRF), i.e., the amplitude vs. frequency plot was measured in baseline and zoom modes. The support condition used for mounting the beam specimen was a simulation of a free-free boundary condition. The damping ratio was calculated using the half-power method, given by equation:

$$\xi = (f_2 - f_1)/2f_n \tag{12}$$

where ξ is the damping ratio, f_n is the resonant frequency, and f_1 and f_2 are locations at which response is 3 dB less than the resonant frequency.

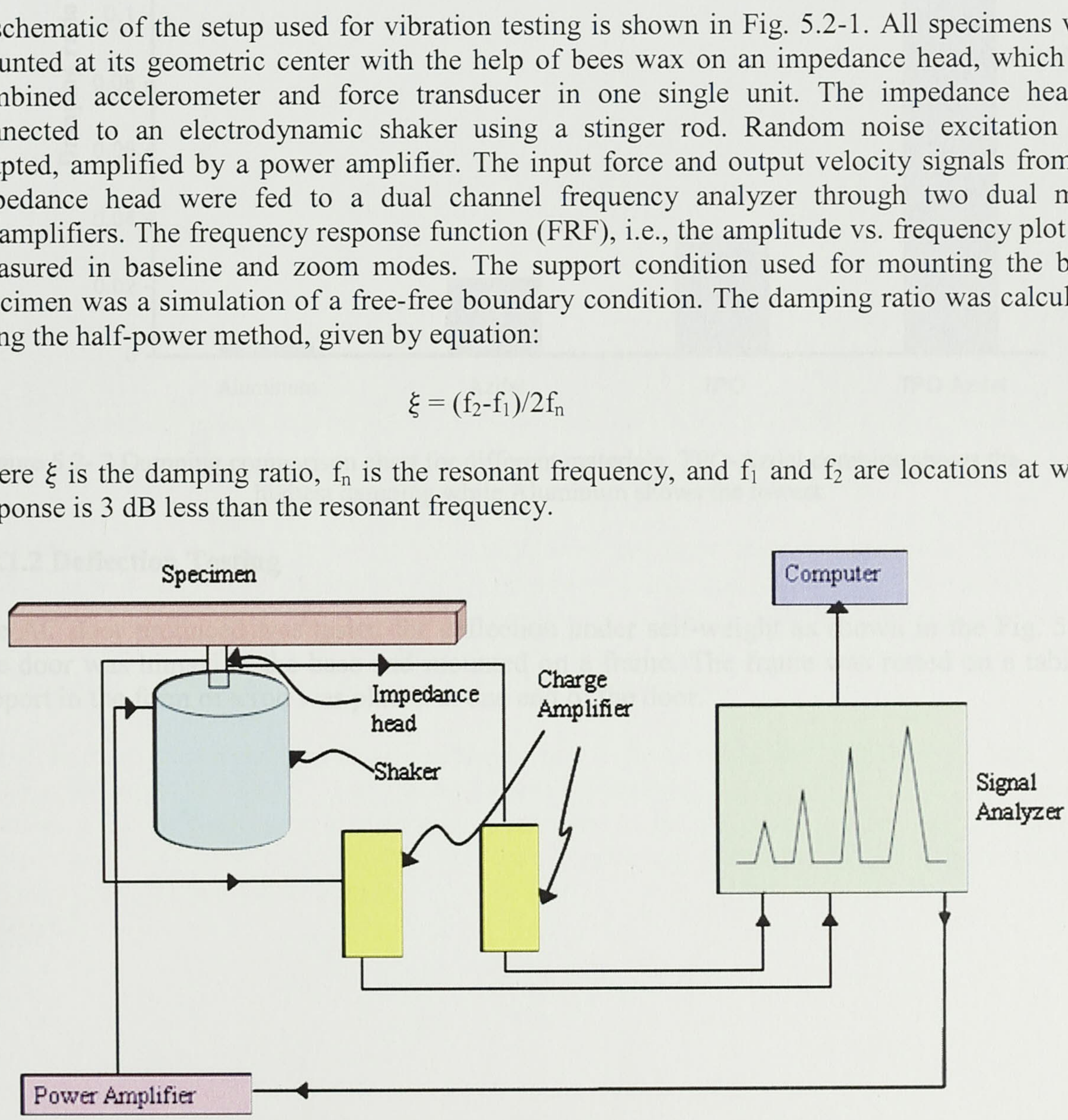

Figure 5.2- 1 A schematic of the experimental setup for vibration testing in free-free boundary conditions.

The materials used were Aluminum which is being currently used for the AC door and Azdel, TPO and Azdel-TPO combine which is the proposed material for the new AC door design. Fig. 5.2-2 shows the damping comparison plot of all the material. It can be seen that TPO-Azdel combine shows the highest damping as compared to Aluminum, Azdel and TPO.

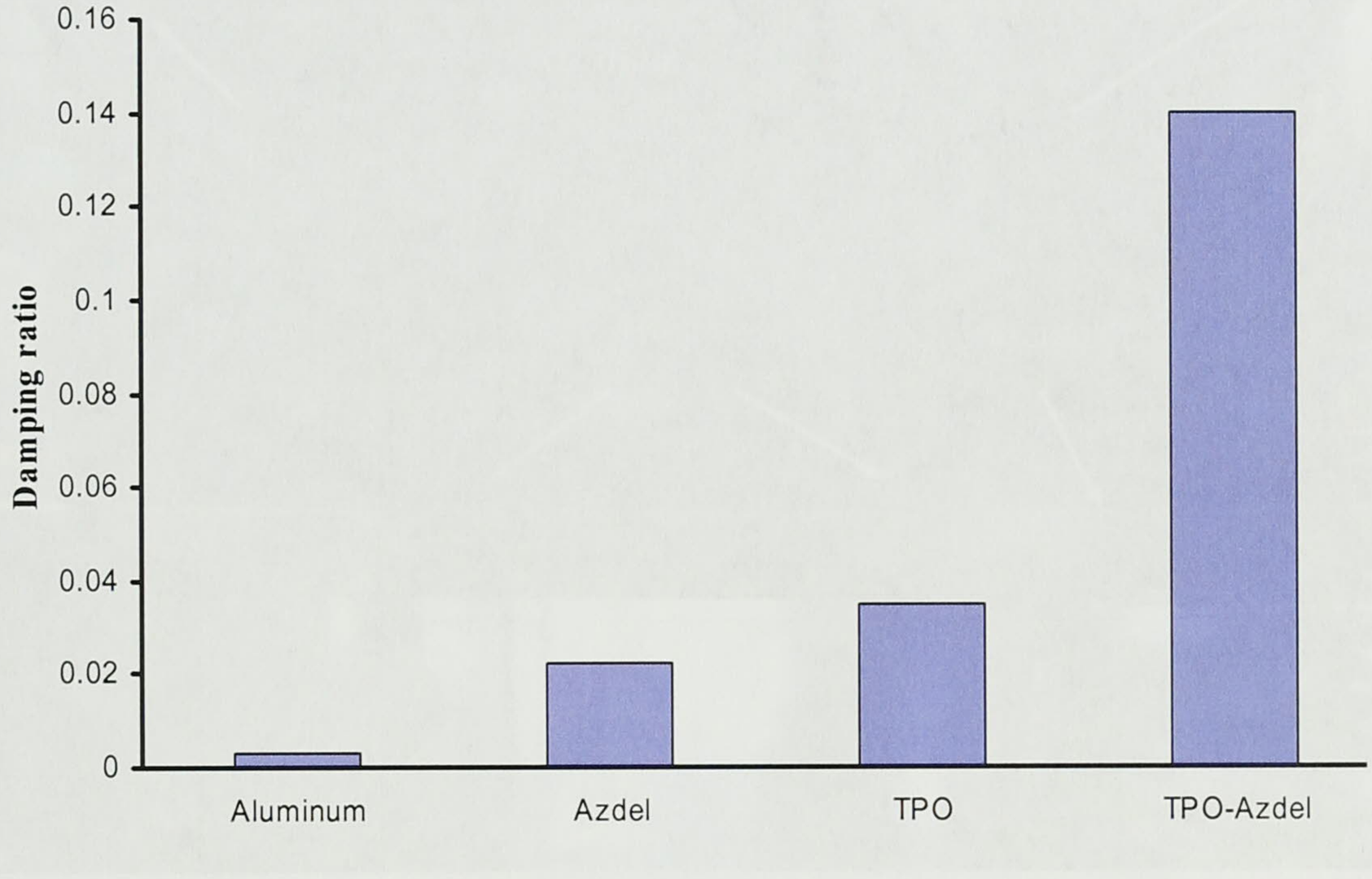

Figure 5.2- 2 Damping comparison chart for different materials. TPO-Azdel combine shows the highest damping while Aluminum shows the lowest.

5.2.1.2 Deflection Testing

The AC door produced was tested for deflection under self-weight as shown in the Fig. 5.2-3. The door was hinged at the base and mounted on a frame. The frame was rested on a table. A support in the form of a rod was placed at one end of the door.

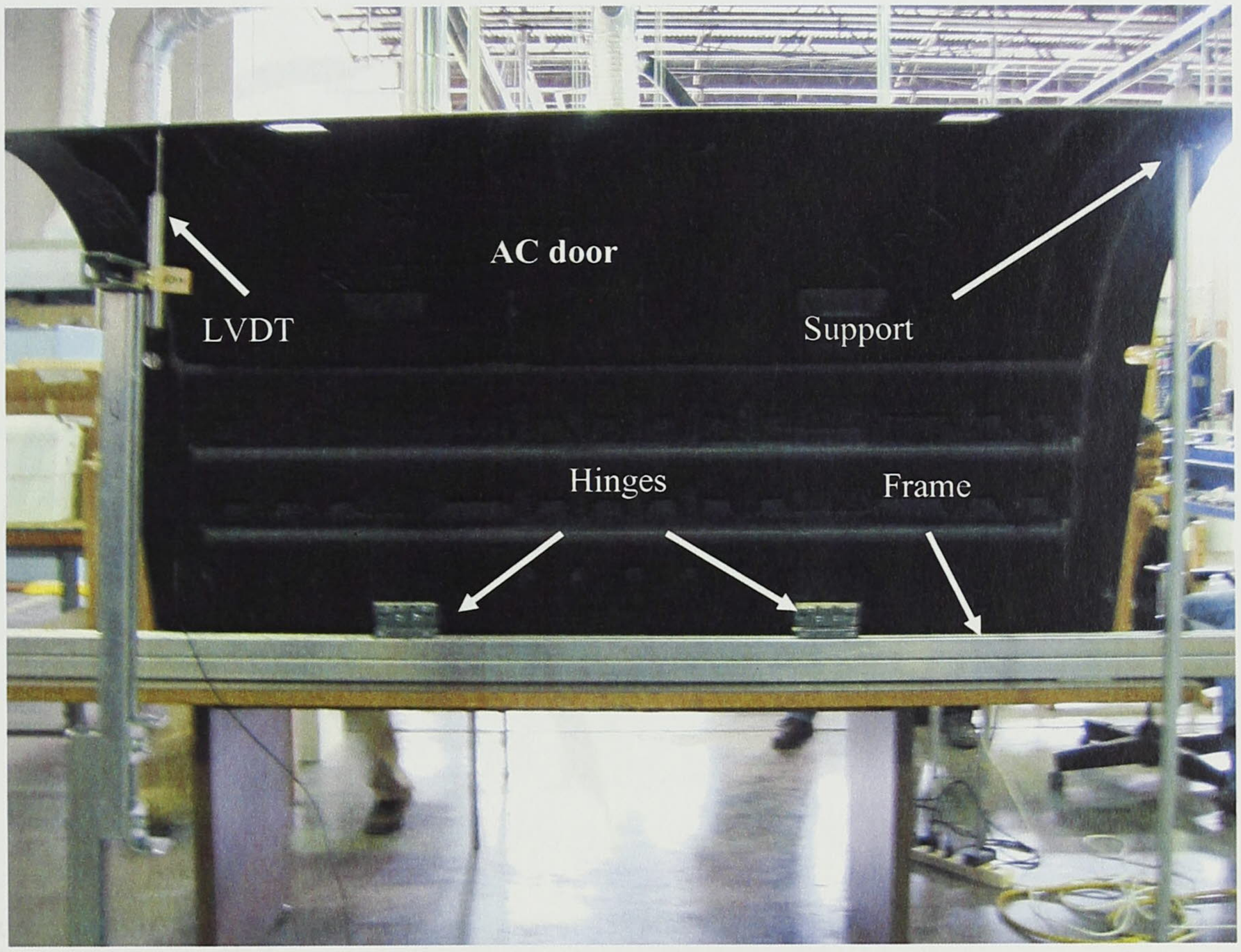

Figure 5.2- 3 AC door mounted on a frame for the deflection testing

The deflection of the door under its self weight was measured with the help of an LVDT. The LVDT was mounted on a Unistrut®, which in turn was mounted on a trolley. The LVDT on the trolley could be moved along the edge of the door so that the deflection could be measured at various points (Fig. 5.2-3). To mimic the door handles on the door, two bolts same as door handle weight on the present NABI bus were placed in the slots.

The deflection was measured at two different positions of the door such that the door would make an angle of 75 and 45° with the horizontal respectively, as shown in Fig. 5.2-4. The open position at 75° angle mimics the fully open position of the AC door in the present NABI bus. The position at 45° was considered in the testing because it generates the maximum magnitude and may cause the largest deflection.

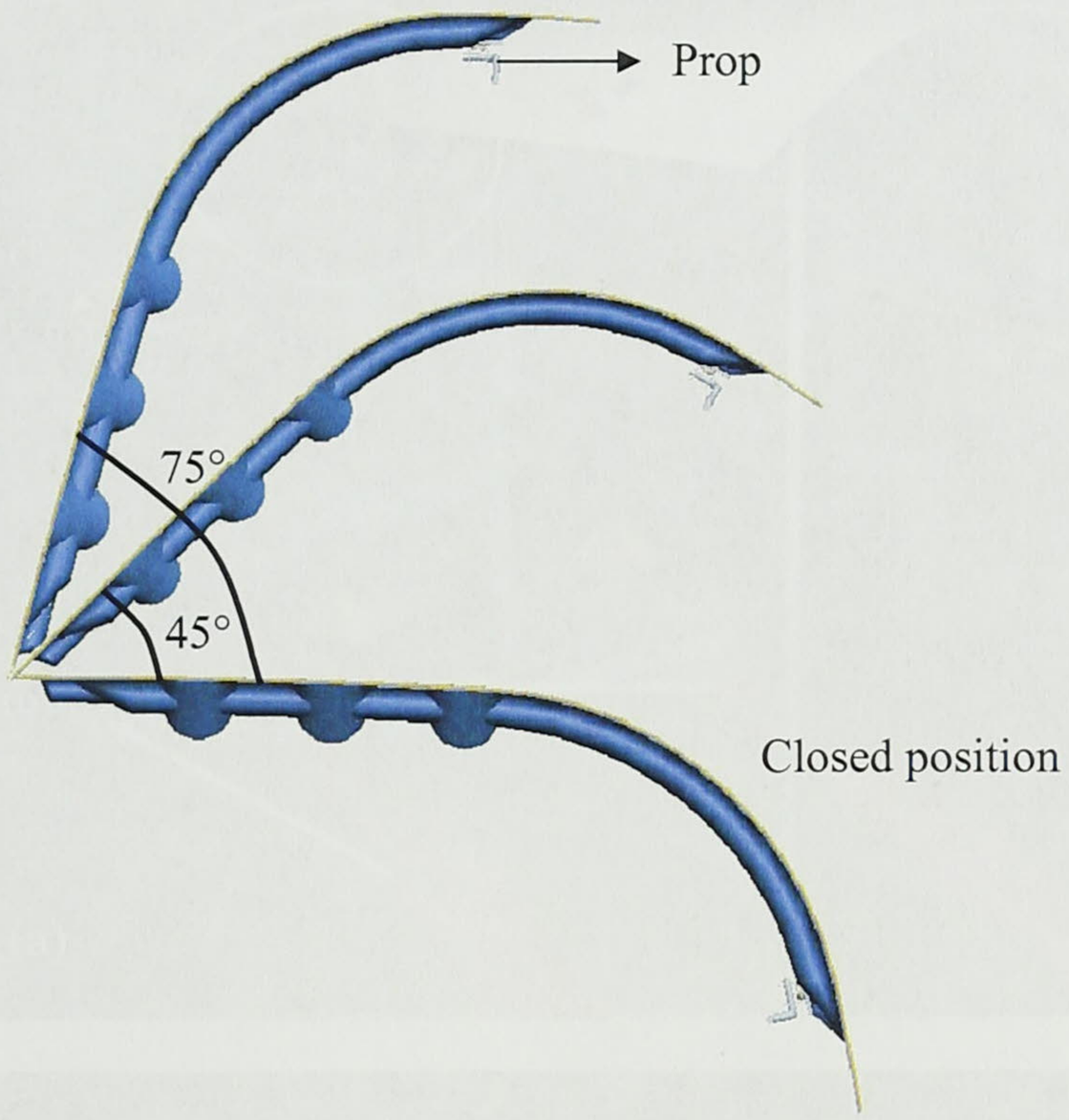

Figure 5.2- 4 AC door at closed position, open at 45° angle and 75° angle (fully open) position.

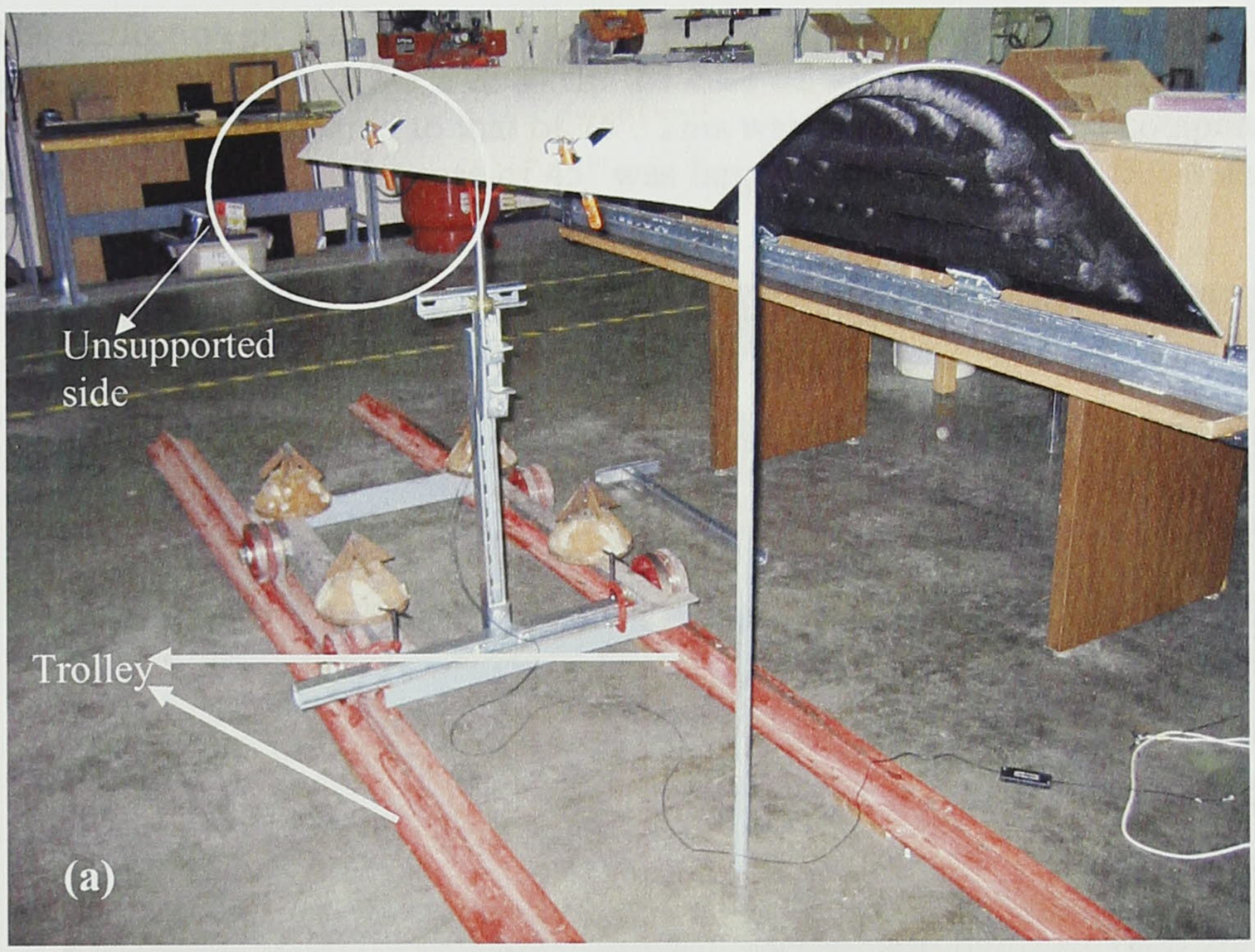

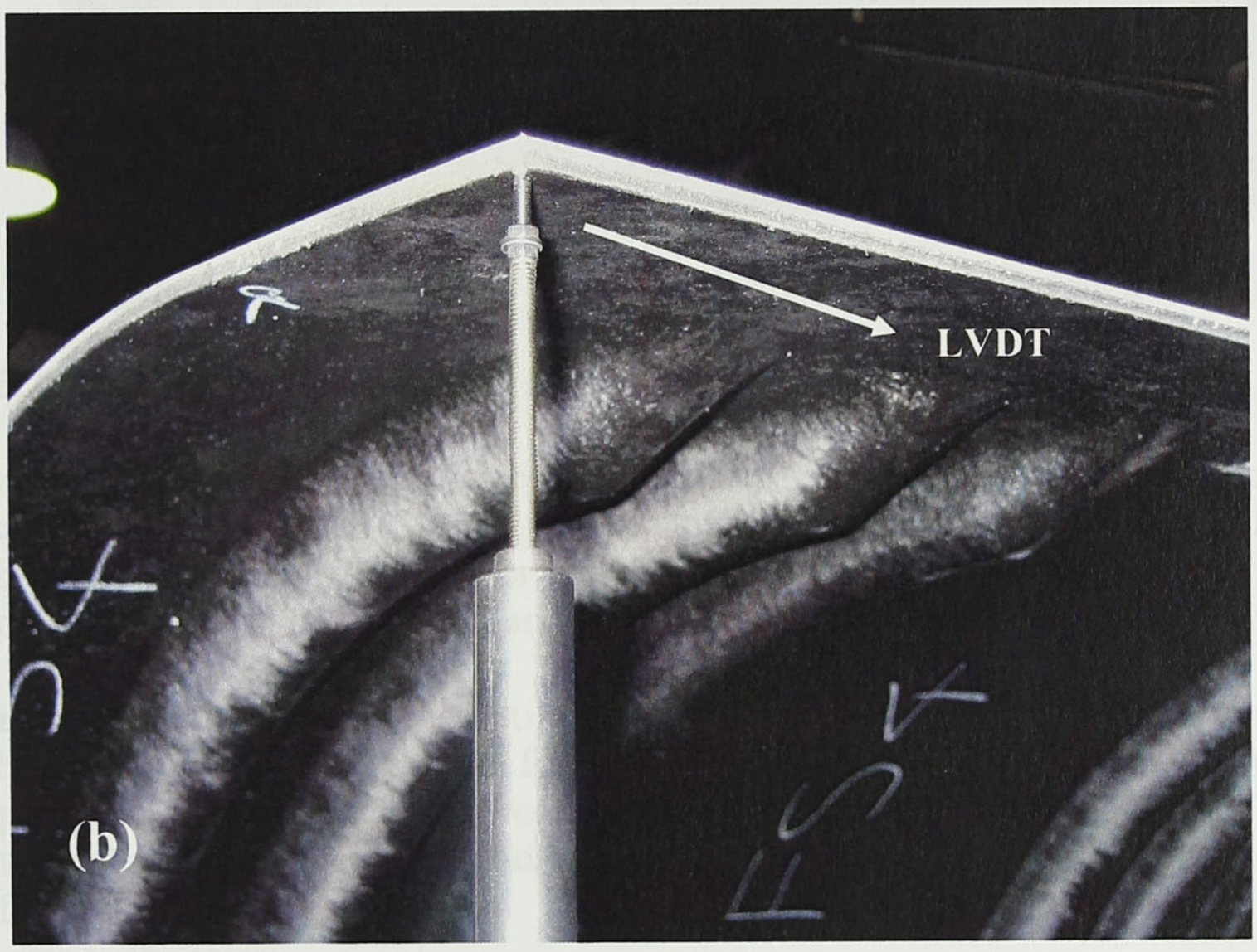

Figure 5.2- 5 AC door testing. (a) The deflection was measured with the help of an LVDT mounted on a trolley. (b) The maximum deflection measured at the corner of the unsupported side.

The deflection of the door, in both the positions, was observed to be the maximum at the non-supported end (Fig. 5.2-5 a & b). In the case of 45° position, the deflection at the unsupported end was more compared to that of 75°. This was because the force component due to the weight acting downwards in the case of 45° was larger in magnitude. Fig. 5.2-6 shows the deflection of the AC door at 45°.

Figure 5.2- 6 AC door under its self weight and door handle weight at an angle of 45°.

5.2.2 Design Verification (AC Door)

A finite element analysis was conducted to validate the test results. The solid Pro/E model was converted to an IGES file and inputed into Hypermesh® for meshing. The mesh density was based on the previous FEA for convergence investigation. A mesh with 25,707 elements was created as shown in Fig. 5.2-7 and imported into ANSYS (Version 10.0) for analysis.

Boundary and loading conditions were determined based on the component testing. The boundary conditions allowed for rotation along the x-axis for the nodes at the door hinge position. Two loading cases were considered, one of which was from self weight and the other was after adding the door handle weights (approximately 2 lbs). The translation in z-axis was fixed at the prop position.

Material properties used for FEA are listed in Table 5.2-1. The tensile modulus of TPO was input from the experimental data generated at UAB (see the details in Materials Technologies part of this report) while the others listed in the table were used from the manufacturer's data. Both TPO and Azdel were considered as isotropic materials.

Table 5.2- 1 Materials properties used for finite element analysis

	Al	TPO	Azdel 1600
Tensile modulus (MPa)	79000	1780	3800
Density (g/cm^3)	2.7	1.07	0.56

Figs. 5.2-7 and 5.2-8 show the loading and boundary conditions and deflection contour for the composites door at fully open position (75°). The comparison between the experimental and FEA is shown in Fig. 5.2-9. Deflections from the current NABI aluminum door and truss were also obtained using finite element method and listed in the table as a baseline.

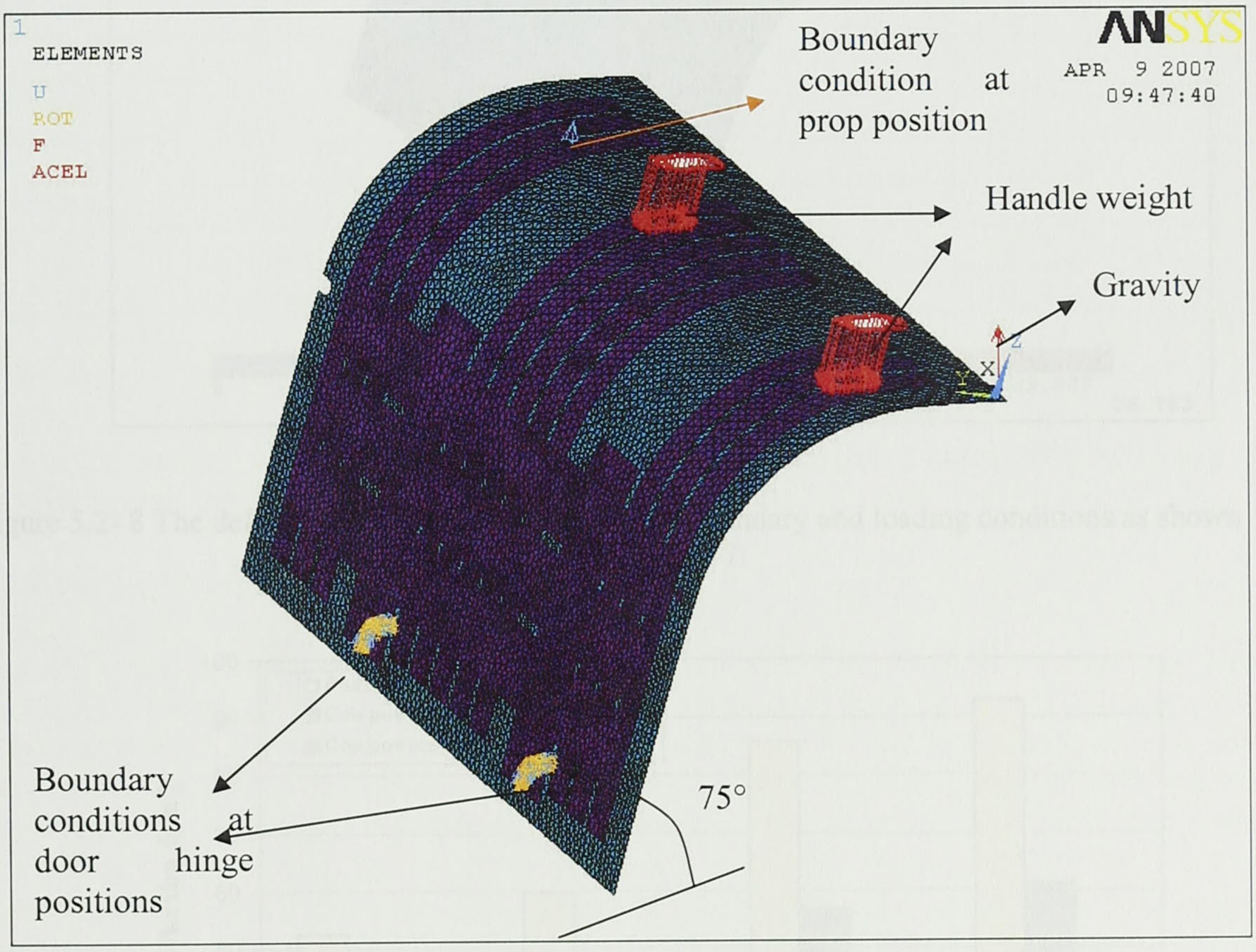

Figure 5.2- 7 The boundary and loading conditions for the fully open AC door.

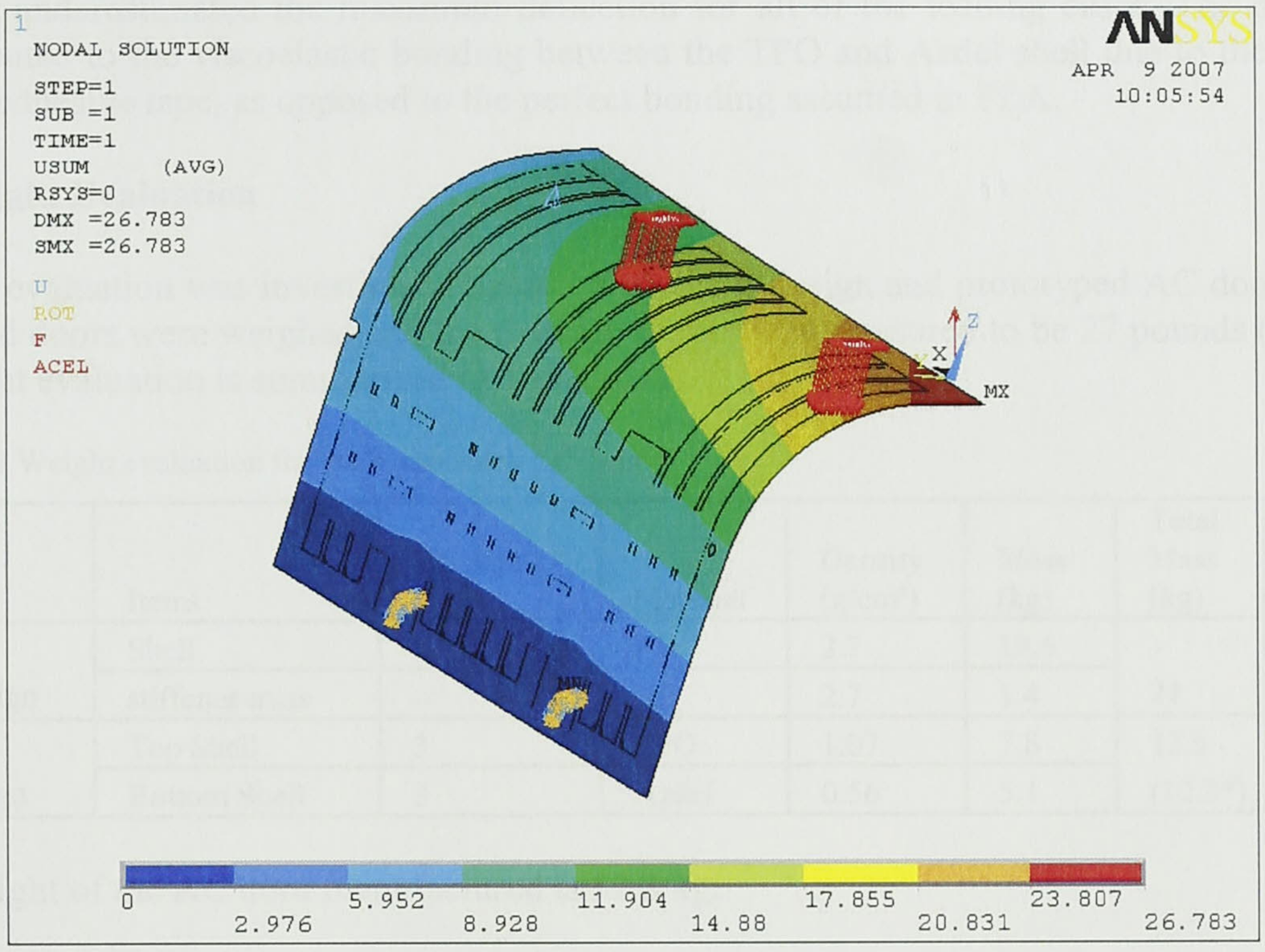

Figure 5.2- 8 The deflection contour resulted from the boundary and loading conditions as shown in Fig. 5.2-7.

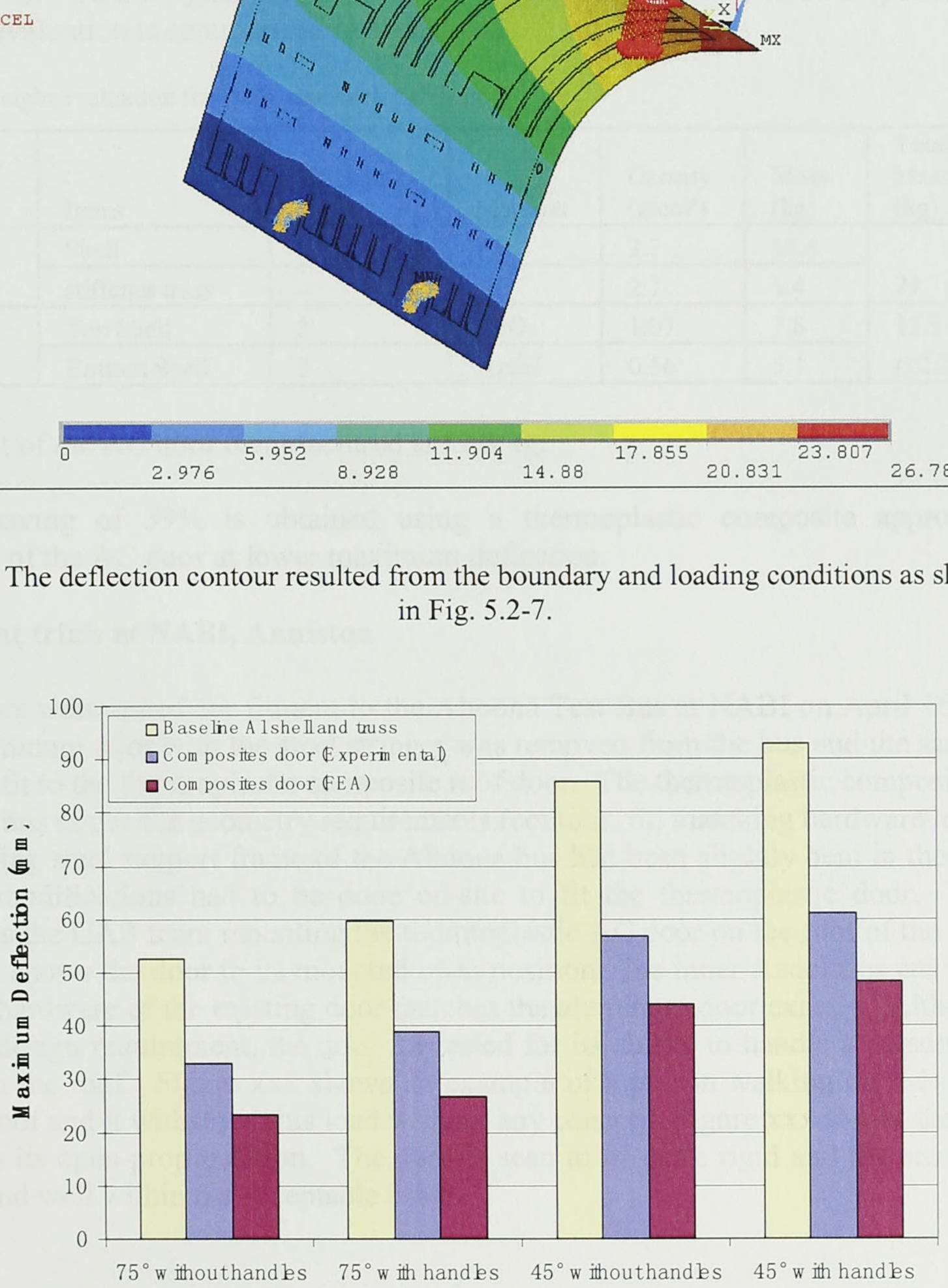

Figure 5.2- 9. The comparison among the baseline Al shell and truss, the composites door in experimental and FEA results for four loading cases.

The FEA underestimated the maximum deflection for all of the loading cases. The difference was attributed to the viscoelastic bonding between the TPO and Azdel shell due to the pressure sensitive adhesive tape, as opposed to the perfect bonding assumed in FEA.

5.2.3 Weight Evaluation

A weight evaluation was investigated based on the final design and prototyped AC doors. Three prototyped doors were weighed and the average weight was measured to be 27 pounds (12.3 kg). The weight evaluation is summarized in Table5.2-2.

Table 5.2- 2 Weight evaluation for the composites AC door

	Items	Thickness (mm)	Material	Density (g/cm^3)	Mass (kg)	Total Mass (kg)	Weight savings
NABI design	Shell	3	Al	2.7	19.6	21	
	stiffener truss	--	Al	2.7	1.4		
UAB design	Top Shell	3	TPO	1.07	7.8	12.9 (12.3*)	39%
	Bottom Shell	3	Azdel	0.56	5.1		

* The weight of the AC door manufactured is 12.3 kg.

A weight saving of 39% is obtained using a thermoplastic composite approach for the construction of the AC door at lower maximum deflection.

5.2.4 Fitment trials at NABI, Anniston

The AC doors were tested for fitment to the Altoona Test Bus at NABI on April 16, 2007. The existing aluminum door with the steel stringer was removed from the bus and the same hardware was used to fit to the thermoplastic composite roof door. The thermoplastic composite door fit to the Altoona bus as per the geometry requirements (contour, fit, matching hardware locations etc). The underlying steel support frame of the Altoona bus had been slightly bent in the Altoona test and minor modifications had to be done on-site to fit the thermoplastic door. Figure xxxx demonstrates the UAB team mounting the thermoplastic AC door on the roof of the Altoona bus. Figure xxxx shows the door in its mounted open position. The inner Azdel ribs are visible in the figure. The hardware of the existing door matches the aluminum door exactly. Although there is a 'no-step' design requirement, the door for tested for its ability to handle a person walking (or stepping) on the roof. Figure xxx shows an example of a person walking on the thermoplastic composite roof and it withstood this load without any concern. Figure xxx shows the door from a side view in its open-prop position. The door is seen to be quite rigid and the unsupported end deflection and well within the acceptable limits.

Figure 5.2- 10 Assembly of the thermoplastic composite door on the NABI Altoona 60 BRT articulated bus.

Figure 5.2- 11 Thermoplastic composite door on the NABI Altoona 60 BRT articulated bus in its open position. Note: Details of ribbing of the door inside visible.

Figure 5.2- 12 Person stepping on the thermoplastic composite door on the NABI Altoona 60 BRT articulated bus.

Figure 5.2- 13 Thermoplastic composite door on the NABI Altoona 60 BRT articulated bus in its open position. Note: Door has excellent rigidity at the unsupported end.

VI. Summary and Conclusions

Continuation of the work was undertaken in the long fiber thermoplastic (LFT) composite areas from 2004-2005 effort. Effect of mechanical and environmental factors such as fatigue, creep, and UV radiation were studied.

In the case of LFTs, it was observed that fiber orientation developed during processing played an important role in the fatigue and tensile properties. Longitudinal LFT showed better tensile and fatigue behavior than the transverse LFTs. S-N curves were generated at various stress amplitudes, frequencies and R-ratios. Samples tested at lower frequency showed higher fatigue life, compared to the samples tested at higher frequency. This is because of the hysteretic heating phenomenon taking place at high frequencies.

A flexural creep testing apparatus was fabricated to test flexural creep response of neat and reinforced thermoplastics in the non-linear viscoelastic regime. It was observed that an increase in reinforcements improves creep resistance while an increase in temperature, stress or both can accelerate the creep process. Non-linear viscoelasticity in neat and long fiber reinforced thermoplastics was modeled using a four-parameter model. Analytical and empirical data matched well and showed stress and time-sensitivity of the creep process.

UV exposure studies showed that the degraded region was mostly confined to a thin region adjacent to the surface. Crystallinity of the degraded region increased with UV exposure time. Nanoindentation results showed that the local modulus of the degraded region was higher compared to the unexposed region. Local modulus values of the PP matrix increased with the exposure time. Nanoindentation results showed a good correlation with FTIR results. In spite of local increase in the modulus values, the overall composite (LFT) showed a decrease with an increase in the exposure time. This was attributed to the formation of surface cracks.

A series of candidate bus components were selected after a visit to NABI, Anniston by the UAB investigators. An air conditioning (AC) cover/roof door was selected for demonstration of advanced thermoplastic composite materials and thermoforming processing technology for the 2005-2006 project. A detailed work comprising of design, analysis, mechanical testing & characterization, prototyping, processing, manufacturing, processing of the AC cover door for the roof of a mass transit bus was undertaken.

Various candidate materials including thermoplastic Polyolefin (TPO), Azdelite, and Quadrant Symalite were evaluated for their thermal, mechanical, and damping properties. TPO and Azdelite were selected as the materials of choice for the manufacturing of the AC door based on their mechanical and damping characteristics and processability. During the processing of the door, the exterior section comprising of TPO was thermoformed and the interior section of the thermoplastic composite, Azdelite, was compression molded. Both the parts were adhesion bonded to form the door.

The complete door assembly was tested for the deflection under its own weight when it is in an open condition and supported at one end. The door was tested at two different angles (45^{o} and 75^{o}) when it's in open condition. It was observed that the deflection was maximum at 45^{o}.

The AC doors were tested for fitment to the Altoona Test Bus at NABI. The thermoplastic composite door fit to the Altoona bus as per the geometry requirements (contour, fit, matching hardware locations etc). Although there is a 'no-step' design requirement, the door was adequate in supporting a person walking (or stepping) on the roof. The unsupported end deflection was not significant indicating the door was rigid enough. The high damping capacity of the thermoplastic door is expected to result in excellent acoustic and noise dampening. The thermoplastic AC doors are 40% lighter than the metal counterpart and can be readily molded in a mass-producible cost-effective manner. A projected weight savings of 500 lbs can be realized if all roof doors on the articulated bus (i.e. AC, CNG and cover doors) adopt the demonstrated thermoplastic composite approach developed in this work.

References

1. Center for Composites Manufacturing, Final Report, December 2006, FTA-AL-26-7022-02.

2. Center for Composites Manufacturing, Final Report, December 2005, FTA-AL-26-7022-02.

3. Center for Composites Manufacturing, Quarterly Report, February 2006, FTA-AL-26-7022-02.

4. Center for Composites Manufacturing, Quarterly Report, June 2006, FTA-AL-26-7022-02.

5. Center for Composites Manufacturing, Quarterly Report, October 2006, FTA-AL-26-7022-02.

6. S.D. Bartus and U.K. Vaidya, Composite Structures 67 (2005) 263.

7. T. Hartness, G. Husman, J. Koenig, and J. Dysterhouse, Composites Part A: Applied Science and Manufacturing 32 (2001) 1155.

8. K.K. Chawla, in "Composite Materials: Science and Engineering". 2 ed (Springer-Verlag, New York, 1998).

9. J.L. Thomason, Mechanical and thermal properties of long glass fiber reinforced polypropylene, in "Polypropylene: An A-Z reference", J. Karger-Kocsis, ed. (Kluwer Academic Publishers, Dordrecht, The Netherlands, 1999).

10. R.W. Hertzberg and J.A. Manson, in "Fatigue of Engineering Plastics" (Academic Press, New York, 1980).

11. H.T. Hahn, Fatigue of Composites, in "Delaware Composites Design Encylopaedia" (Technomic Publishing Company, Lancaster, 1990) pp. 73-126.

12. S.E. Kultural and I.B. Eryurek, Materials and Design 28 (2007) 816.

13. M. Van Den Oever and T. Pejis, Composites Part A: Applied Science and Manufacturing 29A 227.

14. E.K. Gamstedt, L.A. Berglund, and T. Pejis, Composites Science and Technology 59 (1999) 759.

15. A. Pegoretti and T. Ricco, Composites Science and Technology 59 (1999) 1055.

16. D. Grove and H. Kim, Fatigue behavior of long and short glass fiber reiforced thermoplastics, in Proceedings of International Congress and Exposition, Detroit (SAE Technical Paper Series, 1995). pp. 77-83.

17. M.N. Riddell, G.P. Koo, and J.L. O'Toole, Polymer Engineering Science 6 (1966).

18. N. Chawla, Journal of American Ceramic Society 81 (1998) 1221.

19. H.C. Kim, L.W. Glenn, C.S. Ellis, and D.E. Miller, Plastics Engineering 53 (1997) 39.

20. J.I. Kroschwitz and H.F. Mark, eds. in "Encyclopedia of polymer science and technology" (Wiley-Interscience, Hoboken, N.J., 2003).

21. I.M. Ward and J. Sweeney, in "An introduction to the mechanical properties of solid polymers" (Wiley, West Sussex, England, 2004).

22. T.W. Strganac and H.J. Golden, International Journal of Solids and Structures 33 (1996) 4561.

23. S. Yang and W. Chin, Polymer Composites 20 (1999) 207.

24. Annual book of ASTM standards, (1970-2001).

25. S.M. LangfaserverstarktE, Kunststoffe Plast Europe 93 (2003) 53.

26. F.S. Qureshi, M.B. Amin, A.G. Maadhah, and S.H. Hamid, Journal of Polymer Engineering 9 (1990) 67.

27. I. Yakimets, D. Lai, and M. Guigon, Polymer Degradation and Stability 86 (2004) 59.

28. R. Selden, B. Nystrom, and R. Langstrom, Polymer Composite 25 (2004) 543.

29. M.S. Rabello and J.R. White, Polymer 38 (1997) 6379.

30. A. Larena, S. Jiménez DE Ochoa, and F. Domínguez, Polymer Degradation and Stability 91 (2006) 940.

31. A. Hulme, G. Williams, P. Shipton, and M. Philip, Waste and Resources Action Programme. 2004.

32. J.R. White and A. Turnbull, Journal of Materials Science 29 (1994) 584.

33. M.R. Vanlandingham, J.S. Villarrubia, W.F. Guthrie, and G.F. Meyers, Macromolecular Symposium 167 (2001) 15.

34. A.W. Signor, M.R. Vanlandingham, and J.W. Chin, Polymer Degradation and Stability 79 (2003) 359.

35. H. Zhao and R.K.Y. LI, Polymer 47 (2006) 3207.

36. M. Hagenbeek, in "Fibre Metal Laminates". First ed, ed. A. Vlot and J.W. Gunnink (Kluwer academic publisher, Dordrecht, 2001) pp. 409-426.

37. G. Lawcock, L. Ye, and Y.-W. Mai, SAMPE Journal 31 (1995) 23.

38. R. Van Rooijen, J. Sinke, T.J. De Vries, and S. Van Der Zwaag, Material characterisation and optimisation of fibre metal laminates, in Proceedings of First International Conference on Computational Methods in Materials Characterisation, MATERIALS CHARACTERISATION, Nov 5-7 2003, Santa Fe, NM, United States (WIT Press, Southampton, SO40 7AA, United Kingdom, 2004). pp. 55-64.

39. A. Vlot, E. Kroon, and G. La Rocca, Key Engineering Materials 141-143 (1998) 235.

40. L.B. Vogelesang and A. Vlot, Journal of Materials Processing Technology 103 (2000) 1.

41. N. Chawla and K.K. Chawla, in "Metal Matrix Composites". First ed (Springer, New York, 2005) pp. 356-359.

42. Advani and Sozer., Process Modeling in Composites Manufacturing., Marcel Dekker, NY, 2002.

43. www.geimd.com (last accessed January 2007).

44. Jim Allison, Azdel Rail-Lite Composite Brings Superb Fire and Smoke Safety Aboard Metro-North's Passenger Locomotives., AH&M Marketing Communications, www.geplastics.com.

45. www.quadrantplastics.com (last accessed January 2007).

46. T. Czigany, J.Marosfalvi, J. Karger-Kocsis, “An acoustic emission study of the temperature dependent fracture behavior of polypropylene composites reinforced by continuous and discontinuous fiber mats”, Composites science and technology 69, p. 1203-1212, (2000)

47. Advanced glass-mat thermoplastic composite applications for the automotive industry; Quadrant Plastic Composites - Technical Information, March 2007.

48. GM replacing paint with films on some exterior parts., On-line Plastics News Report, April 15, 2007, www.plasticsnews.com/china., Crain Communications Inc.

49. Twin sheet forming has potential for big, rigid parts., British Plastics & Rubber, September, 1993.

50. A Feasibility Study Of Quickstep Processing of an Aerospace Composite Material Victoria Coenen et. al., SAMPE 2005 Technical Conference, CD-ROM Proceedings.

51. Solvay Engineering Polymers., www.solvay.edu (last accessed January 2007)